



UNIVERSITY OF
BIRMINGHAM

ABRASIVE WATERJET AND WIRE ELECTRICAL DISCHARGE
MACHINING OF METAL MATRIX COMPOSITE

By

Lik Soo

A thesis submitted to the
University of Birmingham
for the degree of
DOCTOR OF PHILOSOPHY

Department of Mechanical Engineering

School of Engineering

The University of Birmingham

November 2021

UNIVERSITY OF
BIRMINGHAM

University of Birmingham Research Archive

e-theses repository

This unpublished thesis/dissertation is copyright of the author and/or third parties. The intellectual property rights of the author or third parties in respect of this work are as defined by The Copyright Designs and Patents Act 1988 or as modified by any successor legislation.

Any use made of information contained in this thesis/dissertation must be in accordance with that legislation and must be properly acknowledged. Further distribution or reproduction in any format is prohibited without the permission of the copyright holder.

SYNOPSIS

Metal matrix composites (MMCs) are widely used in many applications such as aerospace and automotive industries for over the past few decades. However, the conventional machining of MMCs causes serious tool wear, poor surface integrity and dimensional deformity due to strain hardening. Three main phases of experimental work were conducted to evaluate the non-conventional machining: Abrasive Waterjet (AWJ) and Wire Electrical Discharge Machining (WEDM) methods on SiC particulate reinforced Al alloy AA2618 matrix composite. The first phase of the experiments focuses primarily on the optimisation of the selected process parameters. The key findings show that traverse rate and pulse-on time are the most important factor in AWJ and WEDM, respectively.

Following an extensive literature review, the effect of wettability based on the surface integrity was studied in Phase 2. The in-depth study of process parameters optimisation of AWJ and WEDM to achieve desirable surface integrity and chemistry has been proven useful in controlling the wettability of Al/SiCp metal matrix composite. Surface wetting properties were characterised by measuring the static contact angle and sessile droplet method was employed. The surface integrity varies significantly across the AWJ machined surfaces, the results show that the surface generated by AWJ

are more hydrophobic compared to by WEDM. The wetting analysis demonstrates the Cassie-Baxter model that the surface roughness increases, contact angle increases due to air pockets entrapment. The anisotropic surface features generated by AWJ contribute to the complex behaviour of wetting property whereas the WEDM surfaces are more isotropic due to the consistency of material removal mechanism. The influence of material removal mechanisms by ploughing effect upon the workpiece subsurface characteristics were explored.

The state-of-the-art of proposed hybrid machining strategy in Phase 3 emphasised on the emerging approaches for generation of hydrophobic to superhydrophobic surface. Hydrophobic surface is crucial in the aerospace application of commonly used MMCs due to anti-icing. The research results revealed that the combination of AWJ rough cutting and dual pass WEDM polishing technique is able to create a close to superhydrophobic surface, with the advantages of time and cost saving as no anti-icing coating or tool adjustment is needed. This methodology is also capable of removing surface defects (striation and ploughing marks) and grits embedments generated by AWJ processes.

In conclusion, the comprehensive study of the AWJ and WEDM machining of this special purpose MMC will impact the future of aerospace industry and generate a research direction in the wettability study.

ACKNOWLEDGEMENTS

The author would like to acknowledge everyone who has contributed their support and advice throughout this research project.

First and foremost, I would like to express my sincere gratitude to my chief supervisor, Dr Carol Kong for providing me a PhD research opportunity and scholarship at the Department of Mechanical Engineering. Her dedicated academic supervision and continuous encouragement over the course of my research and particularly during the Covid-19 outbreak have been a great impact on me. I am also deeply in debt to my co-supervisor, Dr Sein Leung Soo for his valuable knowledge and providing access to laboratory facilities.

I would also like to thank Dr Richard Hood for his effortless guidance regarding to statistical experimental design and analysis. Special thanks go to Andrew Loat (Laboratory Technician) and my fellow colleagues of the Advanced Machining Group for sharing knowledge in experimental setup and technical support such as workpiece preparation and hands-on assistance.

I am very grateful to Prof. Dragos Axinte and his team at the Machining and Condition Monitoring (MCM) Research, University of Nottingham for providing me guidance and access to the state-of-the-art Abrasive Waterjet

machine. Additional thanks go to the following people for their training and facilities support: Prof. Stefan Dimov of Laser Processing Group (Alicona Microscope), Dr Khamis Essa (SEM Microscope), Jacqueline Deans, SciCity research lab of School of Chemical Engineering (Contact Angle Goniometer) and David Morgan, HarwellXPS ESPRC National Facility for X-ray Photoelectron Spectroscopy (XPS).

I would also like to thank Prof. Kyle Jiang (Principal Investigator of H2020-RISE-FabsurfWar Project), for funding my secondment to Changchun University of Science and Technology (CUST) in China. I gained valuable insights and useful discussion into the study of wettability.

Last but not least, my sincerest gratitude to my wife and family, my Achilles' heel for their unconditional love, support and encouragement throughout my PhD study.

TABLE OF CONTENTS

SYPNOSIS.....	(i)
ACKNOWLEDGEMENTS.....	(iv)
TABLE OF CONTENTS.....	(vi)
LIST OF FIGURES	(IX)
LIST OF TABLES	(xv)
LIST OF NOMENCLATURE	(XVIII)
Chapter 1: INTRODUCTION	
1.1 Motivation	1
1.2 Research Gap	2
1.3 Research Aims and Objectives	3
1.4 Thesis Outline	4
Chapter 2: LITERATURE REVIEW	
2.1 Introduction	5
2.2 Overview of Metal Matrix Composites (MMCs)	6
2.3 Particulate Reinforced Metal Matrix Composite (PRMMC)	
2.3.1 Physical and Mechanical Properties of PRMMC	9
2.3.2 Fabrication Process of MMCs	12
2.3.3 Applications of MMC	13
2.3.4 Overview of Machinability of MMCs	18
2.3.5 Critique Analysis	21
2.4 Non-conventional Machining	
2.4.1 Wire Electrical Discharge Machining (WEDM)	23
2.4.2 Abrasive Waterjet Machining (AWJ)	28
2.4.3 Research Gaps and Critique Analysis	33
2.5 Surface Modification of Wettability Characteristics	
2.5.1 Theoretical Background	36
2.5.2 Characterisation Methods	37
2.5.3 Factors Affecting wettability	41
2.5.4 Hydrophobic and Superhydrophobic Surfaces for Aerospace Applications	47
2.5.5 Research Gaps and Critique Analysis	49

Chapter 3: EXPERIMENTAL METHODOLOGY

3.1 Phase One: Process Parameter Optimisation	
3.1.1 Workpiece Material	52
3.1.2 Straight Cutting Machining Equipment	56
3.1.2.1 Abrasive Waterjet Machining (AWJ)	56
3.1.2.2 Wire Electrical Discharge Machining (WEDM)	59
3.1.3 Experimental Procedure	
3.1.3.1 Design of Experiment and test arrays	64
3.1.3.2 ANOVA analysis	67
3.1.4 Characterisation and Measurement Techniques	
3.1.4.1 Cutting Performance: Material Removal Rate	69
3.1.4.2 Investigation of Surface Geometrical Accuracy	70
3.1.4.3 Examination of Surface Quality and Integrity	73
3.1.4.4 Evaluation of Mirco-hardness	77
3.2 Phase Two: Surface Wettability Analysis	
3.2.1 Preliminary Static Contact Angle (CA) Measurement	82
3.2.2 Static Contact Angle Goniometer	83
3.2.3 X-ray Photoelectron Spectroscopy (XPS)	86
3.3 Phase Three: Case Study – Hybrid Machining Strategy	87

Chapter 4: RESULTS

4.1 Preliminary Trials in Wire Selection in WEDM	89
4.2 Phase One: Influence of Process Parameters in AWJ	
4.2.1 Material Removal Rate	92
4.2.2 Kerf Profile Geometry	96
4.2.3 Initial Damage Zone Evaluation	107
4.2.4 Surface Roughness	113
4.2.5 Micro-hardness	125
4.3 Phase One: Influence of Process Parameters in WEDM	
4.3.1 Material Removal Rate	128
4.3.2 Kerf Profile Geometry	133
4.3.3 Surface Roughness	142
4.2.4 Micro-hardness	153
4.4 Evaluation of surface microstructure	156

4.5 Phase Two: Wettability analysis	
4.5.1 Static Contact Angle (CA) Results	167
4.5.2 AWJ Regression Analysis	174
4.5.3 WEDM Regression Analysis	176
4.5.4 XPS Analysis	179
4.5.5 Summary	184
4.6 Phase Three: Case Study – Strategy in creating anti-icing special purpose aircraft surfaces using hybrid machining method	
4.6.1 Design specification of ventral fins and anti-icing systems	185
4.6.2 Proposed machining method combining AWJ and WEDM	186
4.6.3 Results Analysis	187
CHAPTER 5: CONCLUSIONS	191
CHAPTER 6: RECOMMENDATIONS FOR FUTURE WORKS	195
REFERENCES	196
APPENDIX A	214
APPENDIX B	216
APPENDIX C	217

LIST OF FIGURES

Figure 2.1	Different types of continuous and discontinuous reinforcement.	9
Figure 2.2	The effects of volume and form of reinforcement on tensile strength of aluminium matrix composites [16].	12
Figure 2.3	Increase in demand of MMC over the last decade[20].	14
Figure 2.4	Al-SiC composites used in ventral fins and fuel access doors of the F-16 Fighting Falcon and mid-fuselage structure of Space Shuttle Orbiter [30].	17
Figure 2.5	Experimental setup of WEDM[55].	24
Figure 2.6	Insight of AWJ Nozzle Setup[66].	29
Figure 2.7	Contact angle of 3 different liquids[94].	37
Figure 2.8	(a)Young's angle on a flat and homogeneous surface, (b) Wenzel state wetting and (c) Cassie Baxter's wettability model schematic for a water drop resting on a substrate with micro-pillars[96].	38
Figure 2.9	The schematic diagram of sliding angle[97].	40
Figure 2.10	Factors influencing the surface wettability.	41
Figure 2.11	Stir casting with nitrogen gas [106].	43
Figure 2.12	Contact angle illustration of (a) Untreated surface; (b) EDMed surface [118].	46
Figure 2.13	Schematic diagram of hydrophilic and hydrophobic angles [92].	47
Figure 2.14	De-icing of a Boeing-777 aircraft[123].	48
Figure 3.1	Flow chart of experimental procedures of Phase 1 to 3.	51

Figure 3.2	Prepared MMC workpiece.	53
Figure 3.3	Microstructure of the workpiece before experimental trials in (a) longitudinal extruded direction and (b) transverse direction.	54
Figure 3.4	Measurement setup of the four-point probe on the sample surface.	54
Figure 3.5	The diagram of the electrical current flow.	56
Figure 3.6	The main subsystems of the Ormond CNC 5-axis abrasive waterjet machine.	58
Figure 3.7	AgieCharmilles Robofil FI 240 CC machine.	60
Figure 3.8	(a) Workpiece clamped on the mounting table and (b) setup of wire feeding system.	60
Figure 3.9	Wire composition of (a) Charmiles CuZn37 , (b) Bedra Broncocut and (c) Bedra Topas Plus.	61
Figure 3.10	The diagram of spark generation with simultaneous trend of voltage and intensity[129].	63
Figure 3.11	Cutting direction and trials setup.	64
Figure 3.12	Radwag PS 3500/C2 Precision Lab Balance.	70
Figure 3.13	Diagram of kerf width measurement and an example of graph of kerf width against Depth-to-Thickness	71
Figure 3.14	Alicona InfiniteFocus G5 Microscope.	72
Figure 3.15	Mitutoyo Surfptest SJ-210 surface roughness tester setup.	74
Figure 3.16	Setup of JEOL JCM-6000 Plus Neoscope SEM.	76
Figure 3.17	(a) Buehler Simpliment 2 mounting press and (b)	78
Figure 3.17	Buehler Alpha 2 Speed grinder-polisher.	
Figure 3.18	(a) Mitutoyo HM-124 apparatus and (b) Knoop	81

	hardness indentation procedure.	
Figure 3.19	(a) JGW-360A measurement system and (b) static CA measuring system.	83
Figure 3.20	(a) Attension Theta Optical Goniometer and (b) automated CA measuring software.	84
Figure 3.21	The (a) outer and (b) inner view of the Mili-Q water purification system.	85
Figure 3.22	The (a) Kratos Axis Supra, (b) X-ray chamber and (c) sample mounting / ex-situ preparation.	87
Figure: 4.1	Knoop microhardness profile generated by three different wires.	91
Figure 4.2	Main effect plot of S/N for AWJ MRR.	94
Figure 4.3	Main effect plot of Mean for AWJ MRR.	94
Figure 4.4	The Graph of Mean Kerf Width against Trial No. for AWJ Trial 1 to 18.	98
Figure 4.5	Main effect plot of S/N for AWJ Kerf Width.	105
Figure 4.6	Main effect plot of Means for AWJ Kerf Width.	105
Figure 4.7	Top view of the initial damage zone width of AWJ Trial	108
Figure 4.8	17. (a) Top view of cutting zone, (b) initial damage zone of AWJ cutting, (c) zones of kerf geometry and (d) measurement of initial damage width using Alicona 2D measurement of AWJ Trial 17.	108
Figure 4.9	The Graph of width and Ra of IDZ against Trial No. for AWJ Trial 1 to 18.	109
Figure 4.10	Main effect plot of S/N for AWJ IDZ width.	111
Figure 4.11	Main effect plot of Means for AWJ IDZ Width.	111
Figure 4.12	2D measurement of the cutting front surface of AWJ	113

samples.

Figure 4.13	Main effect plot of S/N for AWJ Ra.	116
Figure 4.14	Main effect plot of Means for AWJ Ra.	117
Figure 4.15	Main effect plot of S/N for AWJ Sa.	125
Figure 4.16	Main effect plot of Means for AWJ Sa.	125
Figure 4.17	Main effect plot of S/N for AWJ microhardness.	126
Figure 4.18	Main effect plot of Means for AWJ microhardness.	127
Figure 4.19	Main effect plot of S/N for WEDM MRR.	130
Figure 4.20	Main effect plot of Means for WEDM MRR.	130
Figure 4.21	The graph of mean kerf width against Trial 1 to 18.	134
Figure 4.22	Main effect plot of S/N for WEDM kerf width.	140
Figure 4.23	Main effect plot of Means for WEDM kerf width.	140
Figure 4.24	Main effect plot of S/N for WEDM Ra.	144
Figure 4.25	Main effect plot of Means for WEDM Ra.	144
Figure 4.26	Main effect plot of S/N for WEDM Sa.	151
Figure 4.27	Main effect plot of Means for WEDM Sa.	151
Figure 4.28	Main effect plot of S/N for WEDM microhardness.	154
Figure 4.29	Main effect plot of Means for WEDM microhardness.	154
Figure 4.30	SEM image of WEDM machined surface trial 3 at magnification X150.	156
Figure 4.31	SEM image of WEDM machined surface trial 3 at magnification X1000.	157
Figure 4.32	SEM image of Trial 17 at magnification of (a) X1000 and (b) X2000.	158
Figure 4.33	EDS spectrum of the chemical composition.	159
Figure 4.34	(a) Overlay of Al and SiC X-ray mapping and (b) map topography of Cu and Zn atoms.	160

Figure 4.35	SEM image of WEDM machined surface at magnification X800.	161
Figure 4.36	SEM image of the entrapped aluminium oxide and 3D topography of the analysed area.	161
Figure 4.37	The different zones in the AWJ machined surfaces and deformations mechanism involved in the MMC.	163
Figure 4.38	The EDS analysis using spot analysis and overlay of Al and SiC.	164
Figure 4.39	EDS spectrum of the chemical composition.	164
Figure 4.40	SEM images of the different zones in the AWJ machined surfaces of Trial 6.	166
Figure 4.41	Static contact angle measurement of AWJ Trial 6 and WEDM Trial 3.	167
Figure 4.42	(a) 9 measurements taken on AWJ samples and (b) 6 measurements taken on WEDM samples.	168
Figure 4.43	AWJ Trial 15 and 17 striation marks analysis based on the water droplet diameter.	171
Figure 4.44	(a) WEDM Trial 3 3D surface topography (b) SEM image showing micro-voids (c) general surface EDX spectrum and (d) chemical composition analysis.	173
Figure 4.45	Pareto chart of AWJ variables and their interaction on the CA.	175
Figure 4.46	Pareto chart of WEDM variables and their interaction on the CA.	177
Figure 4.47	XPS Spectra of WEDM Trial 8.	180
Figure 4.48	Ventral fins of an F-16 Fighting Falcon.	185
Figure 4.49	Schematic diagram of the primary and secondary	188

polishing of WEDM.

Figure 4.50 Increment in CA for WEDM rough cutting and dual passes WEDM polishing. 190

Figure 4.51 The 3D topography map of the (a) primary WEDM polishing and (b) secondary WEDM polishing surface. 190

LIST OF TABLES

Table 2.1	The mechanical properties of selected monolithic metal and MMCs [16].	11
Table 2.2	Primary processing routes for aluminium matrix composites[17].	13
Table 2.3	Types of AWJ with different pressure [78].	30
Table 2.4	Static contact angle versus wettability.	39
Table 3.1	Physical Characteristics and Chemical Composition of GMA Garnet [128].	58
Table 3.2	Summary of WEDM wire properties.	62
Table 3.3	Summary of AWJ and WEDM process parameters.	67
Table 3.4	General polishing procedure guide for metal matrix composite [131].	79
Table 3.5	Step by step hybrid machining strategy.	88
Table 4.1	Results analysis of MRR, kerf width and Ra of three types of wires.	90
Table 4.2	Results of data obtained from MRR of AWJ.	93
Table 4.3	ANOVA analysis of AWJ MRR.	95
Table 4.4	Confirmation test results for AWJ MRR.	96
Table 4.5	Graph of Kerf width against Depth-to-thickness Ratio of AWJ.	99
Table 4.6	ANOVA analysis of AWJ kerf width.	106
Table 4.7	Confirmation test results for AWJ kerf width.	106
Table 4.8	ANOVA analysis of AWJ IDZ width.	112
Table 4.9	Confirmation test results for AWJ IDZ width.	112
Table 4.10	AWJ 2D Surface Roughness Results Analysis.	114

Table 4.11	ANOVA analysis of AWJ Ra.	117
Table 4.12	Confirmation test results for AWJ Ra.	118
Table 4.13	Three-d dimensional (3D) topography maps for the AWJ cutting front Trial 1 to 18.	120
Table 4.14	AWJ 3D Surface Roughness Results Analysis.	123
Table 4.15	ANOVA analysis of AWJ Sa.	125
Table 4.16	Confirmation test results for AWJ Sa.	125
Table 4.17	ANOVA analysis of AWJ microhardness.	127
Table 4.18	Results of data obtained from MRR of WEDM.	129
Table 4.19	ANOVA analysis of WEDM MRR.	132
Table 4.20	Confirmation test results for WEDM MRR.	132
Table 4.21	Graph of Kerf width against Depth-to-thickness Ratio of WEDM.	135
Table 4.22	ANOVA analysis of WEDM kerf width.	141
Table 4.23	Confirmation test results for WEDM kerf width.	141
Table 4.24	Summary of the mean 2D surface roughness parameters results.	142
Table 4.25	ANOVA analysis of WEDM Ra.	145
Table 4.26	Confirmation test results for WEDM kerf width.	145
Table 4.27	Summary of the mean 3D surface roughness parameters results.	146
Table 4.28	Three-dimensional (3D) topography maps for the WEDM cutting front Trial 1 to 18.	147
Table 4.29	ANOVA analysis of WEDM Sa.	152
Table 4.30	Confirmation test results for WEDM Sa.	152
Table 4.31	ANOVA analysis of WEDM microhardness.	155
Table 4.32	Confirmation test results for WEDM microhardness.	155

Table 4.33	EDS chemical composition of scanned surface.	159
Table 4.34	EDS chemical composition.	162
Table 4.35	EDS chemical composition of the spot analysis.	165
Table 4.36	Summary of CA measurement of AWJ samples.	169
Table 4.37	Mean CA of WEDM machined samples.	172
Table 4.38	ANOVA analysis of the regression analysis of AWJ.	176
Table 4.39	ANOVA analysis of the regression analysis of WEDM.	178
Table 4.40	Relative concentration ratio of different forms of organic C/%.	180
Table 4.41	Molar content of polar oxygen groups of different samples.	183
Table 4.42	Result analysis of Sa and Sku after rough cutting of AWJ.	187
Table 4.43	Mean Sa and Sku after primary and secondary polishing.	189

LIST OF NOMENCLATURE

A	Pulse on time
Al	Aluminium
AJ	Average Machining Voltage
AlMMC	Aluminium Metal Matrix Composite
ANOVA	Analysis of Variance
AWJ	Abrasive Waterjet
B	Pulse off time
CA	Contact Angle
CFRP	Carbon Fibre Reinforced Plastic
CNC	Computer Numerical Control
Cu	Copper
d_n	Depth-to-Thickness Ratio
DoE	Design of Experiment
D_t	Total Thickness
EDM	Electrical Discharge Machining
EDS	Energy Dispersive Spectroscopy
Fe	Iron
FF	Function of Frequency
FVM	Focus Variation Microscope
HK	Knoop Hardness
HV	High Vacuum Mode
IAL	Ignition Pulse Current
LB	Larger is Better
LV	Low Vacuum Mode
Mg	Magnesium

MMC	Metal Matrix Composite
MRR	Material Removal Rate
NB	Nominal is Better
Ni	Nickel
OA	Orthogonal Arrays
PCD	Polycrystalline Diamond
PCR	Percentage Contribution Ratio
PRMMC	Particulate Reinforced Metal Matrix Composite
Ra	Mean Arithmetic Surface Roughness
Rku	Kurtosis Surface Roughness
Rsk	Skewness Surface Roughness
Sa	3D Mean Arithmetic Surface Roughness
Sku	3D Skewness Surface Roughness
Ssk	3D Skewness Surface Roughness
SB	Smaller is Better
SEI	Secondary Electron Image
SEM	Scanning Electron Microscope
S/N	Signal-to-Noise Ratio
SOD	Standoff Distance
SiC	Silicon Carbide
t	Thickness
WEDM	Wire Electrical Discharge Machining
wt	Weight
W_b	Bottom Kerf Width
W_t	Top Kerf Width
XPS	S-ray Photoelectron Spectroscopy

CHAPTER 1: INTRODUCTION

1.1 Motivation

In recent years, monolithic metallic alloys can be considered as the most widely used materials in mechanical engineering applications. This group of materials can be enhanced by reinforcing with particles (e.g. Sic) to improve their mechanical properties. Particulate reinforced metal matrix composites (PRMMC) are a particularly important class of metal matrix composites for engineering applications. They have been widely used in high performance automotive parts and aerospace industries for the past decades. Compared to monolithic matrix metals, the main advantages of using PRMMC include higher tensile strength, better wear resistance and lower electrical resistivity as reported in many studies. In many research studies, machining of PRMMC was conducted using conventional machining processes such as turning, grinding and drilling. However, it has been noted that the non-conventional machining of non-homogeneous structure metal matrix composite have been established to solve the common problem, such as poor surface integrity and tool wear generated by traditional processing method due to the direct contact of cutting tool and workpiece. While the most applicable and compatible non-conventional machining processes are Abrasive Water Jet (AWJ) and Electrical Discharge Machining (EDM), as it has been noted

that there was commercial hybrid AWJ-EDM machine in the market, it will be very interesting and valuable to conduct research into the potential of hybrid machining application and surface integrity evaluation of the hybrid machined surfaces.

1.2 Research Gaps

It seems that there are many researches were carried out on different MMC, but limited research on this specific AA2618 aluminium matrix reinforced with 15% SiC particulate. There is no report studying the process parameters optimisation of AWJ and WEDM on this particular material. Furthermore, literature reviews showed that the studies on the surface functionality are mainly on metal alloys while there is very limited study of surface functionality on metal matrix composite, particularly in the two recently promising technologies, i.e. abrasive waterjet (AWJ) and wire electrical discharge machining (WEDM). For example, the determination of wetting behaviour is of importance in wider applications such as adhesion, lubrication, coating, self-cleaning and anti-icing applications for aerospace industries.

1.3 Research Aims and Objectives

The overall aim of this research is to identify the optimum operating parameters and investigate the surface integrity of AWJ and WEDM machined MMC workpieces. To evaluate the non-conventional machining: Abrasive Waterjet (AWJ) and Wire Electrical Discharge Machining (WEDM) on SiC reinforced Al MMC, the objectives of the research are as follows:

- To carry out an in-depth literature review on the published work related to AWJ and WEDM of MMCs.
- To determine the baseline operating parameters and identify the optimum process parameters selected based on Taguchi DoE and ANOVA optimization.
- To evaluate the relationship between wettability and cutting process parameters.
- To identify the relationship between static contact angle and surface integrity.
- To propose a hybrid machining strategy combining AWJ and WEDM for creating a hydrophobic surface for special purpose aerospace application.

1.4 Thesis Outline

The thesis comprises six chapters. Following this introduction, the second chapter is a literature review encompassing an overview of metal matrix composite and particularly particulate reinforced MMCs, application of MMCs, WEDM and AWJ process configuration and technology, etc. This chapter also covers the extensive literature review of published research on the aspects of surface functionality, wetting behaviour characterisation and application of hydrophobic surfaces.

Chapter Three consists of the detailed experimental work, introduction relating to the workpiece materials, WEDM and AWJ machines and operating parameters, equipment, Taguchi DoE and ANOVA analysis. Chapter Four details the results and Taguchi analysis of AWJ and WEDM related to MRR, kerf width, Ra, Sa and microhardness. The regression analysis of the effect of factors influencing the static contact angle of MMC and the results relating to the proposed hybrid machining strategy are also presented in this chapter. Chapter Five summarises the conclusion and Chapter Six consist of the recommendations for future work.

CHAPTER 2: LITERATURE REVIEW

2.1 Introduction

This literature review provides an overview of the machinability of metal matrix composites (MMC) with emphasis of aluminium matrix reinforced with silicon carbide particulates due to their present and future dominance in the aerospace and engineering industries. Manufacturers are constantly developing materials to create stronger, lighter and more durable components. There are different combination of matrix and reinforcing material that consists of the metal matrix composites. MMC provides a serious challenge for cutting tool due to their unique combination of mechanical properties such as high tensile strength and stiffness. The comparison of conventional and non-conventional machining of MMC will be explored. One of the major applications of MMC in the aerospace industry is anti-icing in extreme weather conditions. This chapter also provides an in-depth understanding of the surface wettability and characterisation methods.

2.2 Overview of Metal Matrix Composites (MMCs)

Over the last three decades, the demand of research and development of metal matrix composite material characteristics due to higher performance requirement and reduction in weight alternative to conventional engineering alloys. MMC are well known for their attractive physical and mechanical properties. They are basically the combination of the metallic properties (ductility and toughness) with ceramic properties (strength and modulus) resulting in greater strength in shear and compression and higher service temperature capabilities [1] The main significance in lightweight materials with improved performance is less fuel consumption and stricter CO_2 emissions regulations. In addition to reduction in weight, composite materials offer potential advantages of cost reduction in manufacturing processes and capability to be tailored to meet specific design requirements. Owing to strength and thermal stability, MMC has gained great interest in aerospace and automotive industries in last three decades. In the automotive sector, reduction in the mass of engines is a key factor for improving the fuel efficiency. Most manufacturers have replaced cast iron (density= 7.8 g/cm^3) engine blocks with aluminium silicon MMC (density= 2.79 g/cm^3) crankcases with an overall weight reduction of 10% to improve fuel economy by 7% [2].

The distinguishing difference between composite and other multiphasing material is the phase transformation. Composite material is defined as a combination of two or more distinct phases with different physical and chemical properties compared to its constituents: primary and secondary phases. The primary phase is called matrix, which commonly exhibits a continuous character and is more ductile, whereas the secondary phase is called the dispersed (reinforcing) phase[3]. A matrix is a continuous phase and hold the reinforcements chemically bonded together. In terms of the matrix phases, composites can be classified into: metal matrix composites (MMC), ceramic matrix composites (CMC) and polymer matrix composites (PMC).

MMC is made by embedding a reinforcing material into a low-density monolithic metal matrix (most commonly aluminium, magnesium or titanium). Aluminium alloys have been widely investigated as matrix for MMCs due to their low density, resistance to corrosion and abrasion, relative ease of fabrication and ability to accommodate a variety of reinforcing agents[4]. It is difficult to distinguish the mechanical properties of different MMCs due to the number of different MMC system. There is limited information regarding comparison of mechanical properties of different MMCS due to the broad range of MMC systems investigated[5].

The reinforcement material can be divided into: continuous or discontinuous as shown in Figure 2.1[6]. Discontinuous reinforcement is typically particulate or whiskers. Particulate-reinforced composites are isotropic (same mechanical properties in all direction) and better mechanical properties compared to whiskers due to higher reinforcement properties, which provide the advantages of improved affordability[7]. Whereas whiskers have a higher aspect ratio and are brittle. It tends to break up into shorter lengths due to anisotropy properties. Continuous reinforcement can be further divided into wire and long fibre. The most commonly used fibres are carbon and ceramic (alumina and SiC). The surfaces can be coated to prevent chemical reaction with the matrix and improve the strength of the fibres. The most commonly used particulate reinforcements are SiC and Al_2O_3 , but TiC have also been used [8, 9]. Extensive commercialisation of particulate reinforcement MMC has been increased due to availability reinforcement at reasonable costs and availability of metal working processes for these materials[10]. The matrix, reinforcement and interface determine the characteristics of the MMC.

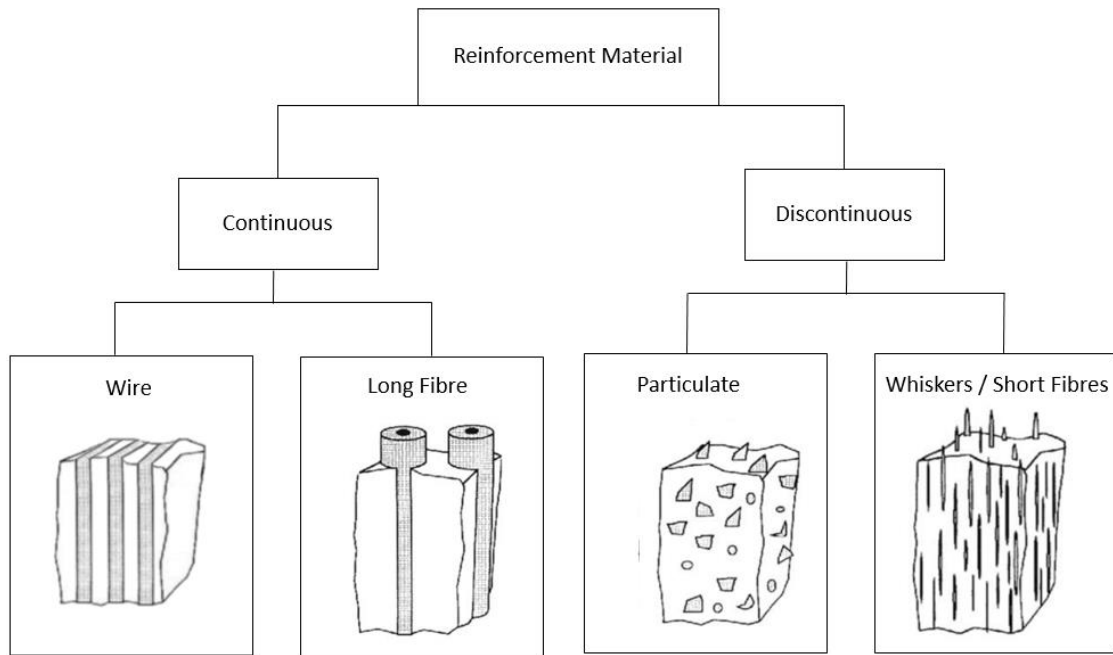


Figure 2.1: Schematic presentation of four different types of continuous and discontinuous reinforcement[6].

2.3 Particulate Reinforced Metal Matrix Composite (PRMMC)

2.3.1 Physical and Mechanical Properties of PRMMC

Table 2.1 shows the detailed properties of some monolithic metals and MMCs. Compared to the monolithic matrix alloy, MMCs have relatively higher strength and stiffness-to-density ratios and lower coefficient of thermal expansion (CTE)[11]. Comparing to basic aluminium alloy, the tensile strength increased from 76 *MPa* to 515 *MPa* by reinforcing with 55% SiC particulate and higher Young's Modulus (175 GPa) while having a comparable density of 2950 kg/m³. The main factors influencing the characteristics of MMCs are matrix properties, reinforcement volume

fraction, properties and geometric arrangement[6]. MMC properties can be tailor-made and varied over appropriate selection of constituents. For example, thermal and electrical conductivity can be adjusted by varying constituent matrix and reinforcement volume fraction (V_f) and morphology as shown in the Table 2.1, generated from data obtained from CES Edupack software. The tensile properties of Al-SiC MMCs are compared with various percentage content of and form of SiC reinforcements shown in Figure 2.2. For an Al matrix with constant 47% of SiC reinforcement, the tensile strength of longitudinal alignment (parallel to the fibre direction) was found to be a factor of two higher than those in the direction perpendicular to the fibre direction. Fibre orientation and its effect on mechanical properties have been investigated in several studies, in particularly SiC reinforcement. The difference in tensile strength was attributed to the strain limiting effects of fibres and matrix shear band formation. Extensive experimental studies were conducted to establish the effect of reinforcement volume fraction and particle size on the mechanical properties behaviour of MMCs[12-14]. In general, an increase in the reinforcement volume fraction and decrease in particle size, the yield strength and fatigue strength increased. Other studies [15] also verified that the decrease in particulate size of SiC reinforcement increases the tensile strength of the Al MMC.

Table 2.1: The mechanical properties of selected monolithic metal and MMCs[16].

Properties	Al S150	Cu C12200	Mg AE42	Al 6061- 55%SiC(p)	Al 6061- 47%SiC(f)
Density, kg/m ³)	2670	8940	1780	2950	2840
Young's Modulus (GPa)	69	120	44	175	202
Compressive Strength (MPa)	28.5	55	135	480	1460
Tensile Strength (MPa)	76	215	180	515	1460
Thermal expansion coefficient $\mu\sigma/^\circ\text{C}$	22.2	16.8	26	10	6.3
Thermal Conductivity (W/m ^{°C})	205	290	83	138	50
Electrical Resistivity (Ωm)	3	1.91	11.5	10	5.62

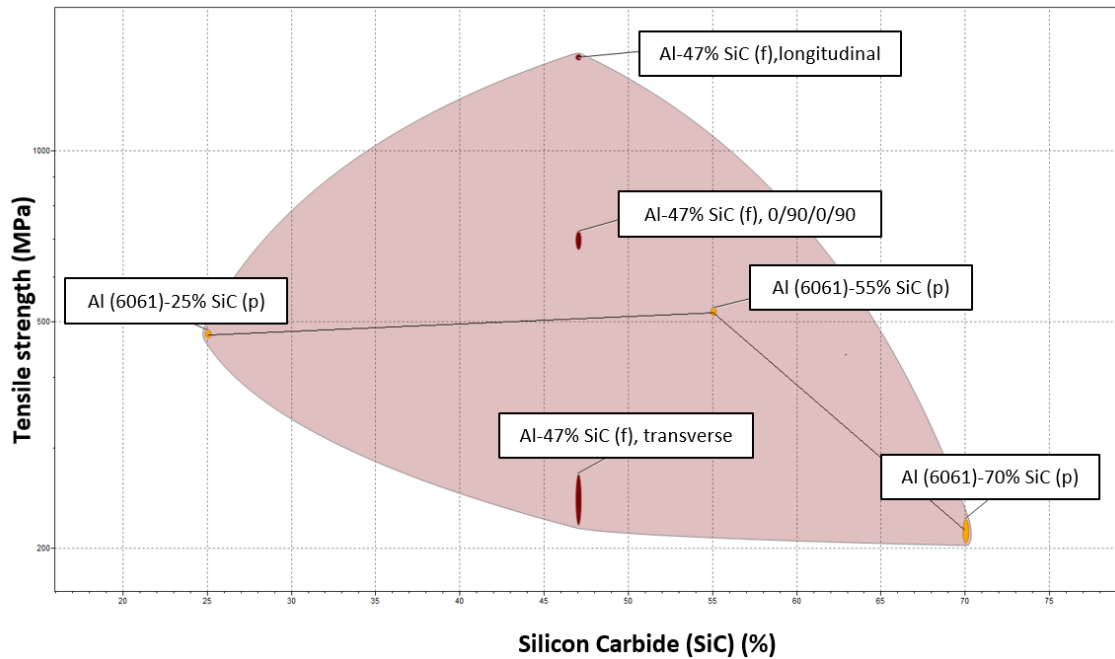


Figure 2.2: The effects of volume and form of reinforcement on tensile strength of aluminium matrix composites[16].

2.3.2 Fabrication Process of MMCs

A variety of detailed processing techniques have been developed, which comprises of primary material production and secondary consolidation or forming operations. The primary fabrication for manufacturing MMC can be classified into three main groups: (1) solid state process, (2) liquid state processes and (3) deposition processes. Solid state processing include powder blending and consolidation, diffusion bonding and physical vapour deposition. Liquid state processes consist of stir casting, infiltration and spray deposition. Stir casting and infiltration processes comprises of the largest volume (~67%) of the primary production market[8]. The selection of

fabrication route of aluminium matrix composite depends on many factors including size, shape and type of reinforcement, the target mechanical properties and the degree of microstructural integrity[6]. Table 2.2 provides the summary of various processing routes feasibility for which a reinforcement can be incorporated into aluminium matrix composites[17].

Table 2.2: Primary processing routes for aluminium matrix composites[17].

Types of AMCs	Blending and consolidation	Diffusion Bonding	Vapour deposition and consolidation	Stir casting/ slurry casting	Infiltration process	Spray deposition and consolidation	<i>In-situ</i> reactive process
Continuous fibre-reinforced AMCs (CFAMCs)	Not in practice	Not in practice	In use	Not in practice	In use	Not in practice	
Mono filament-reinforced AMCs (MFAMCs)	Not in practice	In use	In use	Not in practice	Generally not used	In use	Not in practice
Particle-reinforced AMCs (PAMCs)	In use	Not in practice	In use	In use	In use	In use	In use
Whisker- or short fibre-reinforced AMCs (SAMCs)	In use	Not in practice	In use	Generally not used	Generally not used	In use	Not in practice

2.3.3 Applications of MMC

With the development of the new composite materials, they provide a wide range of possibilities to be used in different applications according to the demand[18]. Among all composites, Aluminium Metal Matrix Composite (AlMMC) possess all these beneficiaries properties but also many other such as higher stiffness and strength and resistive to high temperature. Some researchers found that there is an increase in global demand of AlMMC reported across different sectors: automotive, aerospace, military, etc. from 2007 to 2013 by 4.1 million of kilogram to 5.9 million of kilogram[19]. Figure

2.3 shows that the exploitation of MMCs has been widely used in the automotive industry in which their advantages over traditional materials. Such as in mechanical industry where the light weight, mass production volumes, increase in exploitation time and low manufacturing cost materials are desirable[20].

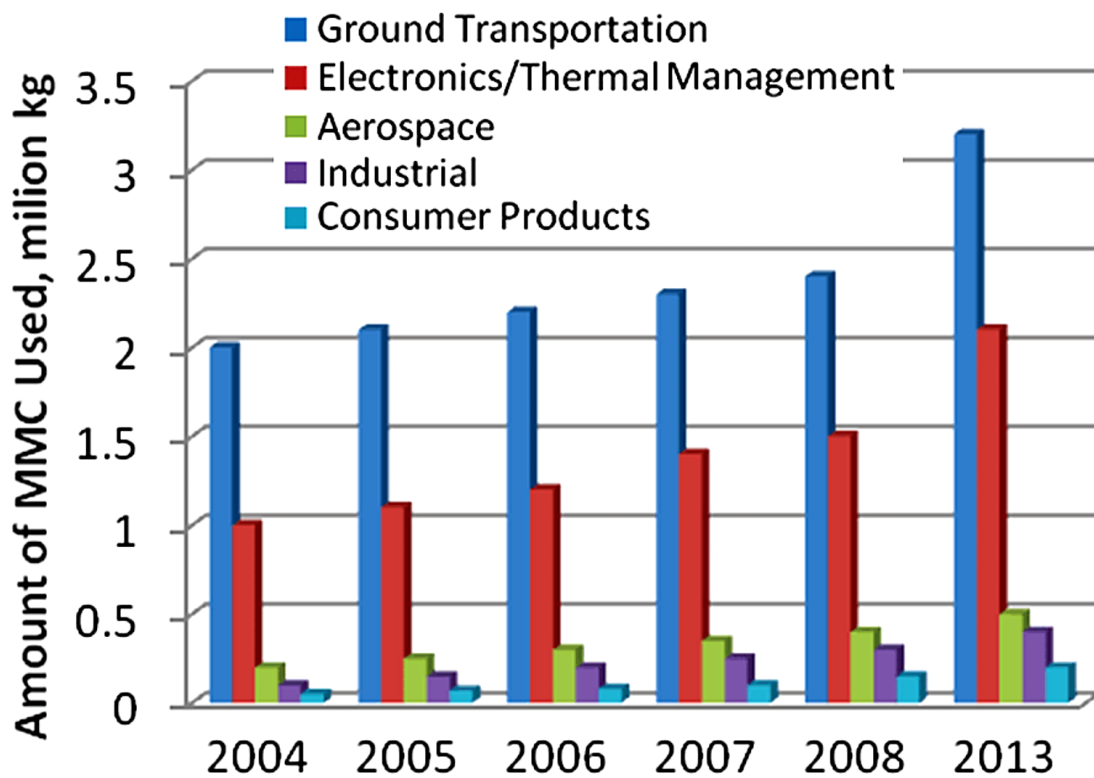


Figure 2.3: Increase in demand of MMC over the last decade[20].

i. Automotive Industry

With reference to [21], more than 50% of the globally produced AlMMC has been used in the automotive industry for the responsible parts of the car such as crankshaft, braking system and engine cylinder etc.[22]. The Toyota

car manufacturer has been using the AlMMC as engine piston since 1983 as it operates in very hard thermal and mechanical conditions with the frequency of 100 Hz where fatigue damages are predominantly [23]. AlMMC has high resistance to wear and improved thermal expansion coefficient making it promising material over conventional alloys.

Likewise, 3M Cooperation has been using the AlMMC with reinforcing material Al₂O₃ for the production of engine pushrods [7]. It provided with 25% higher stiffness and twice higher absorption capacity along with smaller weight and density that result in increased exploitation period as compared to the steel ones [24]. Moreover, an engine connection rod of AlMMC has 57% mass reduction in comparison with steel which results in decrease of fuel consumption along with increase in engine power and production cost [25].

ii. Aerospace and Aircraft Industry

Aluminium alloys are widely used for mass-produced aerostructure parts due to its availability, light weight and strength. Fuel efficiency is the main driving force in the modern aerostructures development and is directly dependent upon the weight of the material used. Based on the objectives set by the High Level Group On Aviation Research in Flightpath 2050, 75%

reduction in CO_2 emissions per passenger kilometre and 90% reduction in NO_x emissions to be achieved by year 2050[26]. This has driven the continuous development of lightweight materials on aircraft and engines and more compact engine design to achieve an enhanced aerodynamic engine cycle and higher thermal efficiency [27, 28]. For example, the ventral fins of the F-16 Fighting Falcon on the fuselage as shown in Figure 2.4 (a), which is used to stabilise the aircraft during high angle ascents and maneuvers. They were originally made of 2024-T4 aluminium and have been replaced with ceramic particle-reinforced Al matrix composite to increase the specific stiffness and fatigue life in order to eliminate cracking problem[29]. Relatively few applications have been established for space application. One of the notable applications is the Al-6061 reinforced with 50% Boron mono-filaments were used for the tubular frame stabilising struts for the mid-fuselage and landing gear drag link of the Space Shuttle Orbiter as shown in Figure 2.4 (b). which reduced weight by 40% compared to Al design[7, 30].

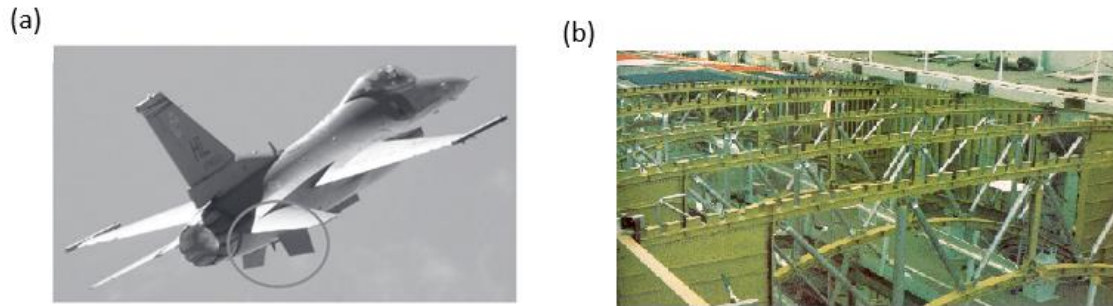


Figure 2.4: Al-SiC composites used in (a) ventral fins and fuel access doors of the F-16 Fighting Falcon and (b) mid-fuselage structure of Space Shuttle Orbiter[30].

iii. Other Novel Applications

Beside the automotive and aerospace industry, AlMMC has been very much in demand in sports, electronic packaging and thermal management[31]. In the sport industry, being light weight and high tensile strength makes AlMMC promising[32]. Whereas in the electrical field, the AlMMC has caught the attention of transmission lines and the enclosed integrated circuit due to its good thermal conductivity, corrosion resistance and high efficiency in conductivity[31]. For example, low coefficient of thermal expansion (CTE) properties of MMCs and thermal characteristics of the interfacial bonding of matrix and reinforcement are significant in manufacturing thermal management components, such as microwave

housing by Lanxide electronic components and printed circuit of Textron Special Material Inc.[33]. Recent data shows that in 2010, shipment of AlMMC has been increases by 13.1 % in electrical applications as an aluminium conductor steel reinforced cable flew 631 million sterling pounds. North America being the fourth largest electrical market of aluminum as a whole with a share of 7.3 % in the aluminum shipment[34].

2.3.4 Overview of Machinability of MMCs

MMC is a combination of the metallic matrix with the hard ceramic reinforcement and aluminium matrix composites have been used extensively due to their low density, low melting cost and cheap to source[35]. However, the fabrication processes of AlMMC remain a challenge due to the high tensile strength and stiffness of the reinforcing phases [36]. Its hardness causes drastic machinability degradation by increasing the cutting force and mechanical power to manufacture which results in an increase in cost of production[37]. With reference to the paper, a wide range of machining and finishing operations has been studied since 1970 and is still improving the process of machining and making it more cost effective[38, 39] .

Machining has been divided into two basic categories conventional i.e. turning, milling, drilling, and grinding and non-conventional method such as electrical discharge machining (EDM), powder mixed EDM, wire EDM, electrochemical machining, and most recent machining technologies, e.g., blasting erosion arc machining [40]. Conventional machining refers to the method of producing MMC uses in the early ages that include turning, milling, drilling, and grinding. These cutting methods were improving by using stronger cutting tool materials, such as diamond coated, Polycrystalline Diamond (PCD) due to its high strength of MMCs [41, 42]. Machining method is directly dependent upon the tool wear and surface quality [43].

Conventional machining processes do not require complex computational optimisation. They involve mechanical force and direct contact of tool and workpiece, which increase in tool wear [44]. Contrary to conventional, non-conventional machining includes many techniques such as Electrical Discharge Machining (EDM) and laser cutting and many new techniques has been under development such as blasting erosion arc machining[45]. The only issue involved in the non-conventional machining is the quality of the surface modification that was not as uniform and attractive, which directly affects the end properties of the MMC [46]. Particle Reinforced Metal Matrix

Composites is a popular material in automotive and aerospace industry[47]. Its manufacturing has been facing the concern of surface quality and the tools efficiency. Hardness and stiffness of MMC has made these popular in the mechanical industry but these qualities has been the core reason for concern in their machining and productivity [48]. Production of the MMC using conventional methods has been cost effective as it mainly refers to the mechanical work[49]. Composite properties of strength, hardness and stiffness has severely affected the tool life of the machining processes. Though many improvements in tools have been made such as PCD, diamond coated and carbide tools being used, it has been unable to improve the tool life[50]. With reference to the paper, it has been found that the PRMMC can be machined using the non-conventional methods such laser cutting, EDM and AWJ. However, all these machining methods have their own effect on surface quality. In EDM, a carter like surface was formed that increases directly with the discharge energy and also the overall process is very slow that cannot be feasible for the high volume production [51]. However, in laser machining the surface is relatively poorer as compared to the EDM as it causes striation patterns on the cut surface and burrs on the exit of the laser. In comparison to the above thermal machining processes, AWJ machined surfaces has poorest surface integrity. AWJ does not induce high

temperature, hence, no heat affected zone within the composite [52]. It is also suitable for rough cut applications as it has high feed rates, but difficult to produce a workpiece with high geometrical accuracy [53].

2.3.5 Critique Analysis

Metal Matrix Composite (MMC) have been used intensively in different industries due to their impressive physical and mechanical properties by ceramic and metallic composites. Addition of different metals and ceramic to form a composite matrix such as Aluminum Metal Composite (Al_2O_3 and SiC) has dominant other PRMMC's due to having versatile properties like the high wear resistance, tensile strength, ductility and light weight, and density. Due to such advances and flexible properties, AMCs are being used in different industries according to the demands. For example, automotive industry find AlMMC's useful due to their light weight and high strength. The aerospace industries are attracted towards Aluminum based MMC's due to their high temperature bearing properties along with being light weight. The Electricity and the Sports industries find AlMMC's advantageous due to their good thermal conductivity. Beside the long list of applications of difficult-to-cut AlMMC's, the machining of such high strength and stiff composites is a great challenge for the manufactures as it cost the degradation of cutting materials. There are many techniques being used for the machining of

PRMMC's: Conventional and non-conventional machining. Conventional machining requires high tooling cost due to low tool life and wastage during material removal processes. The non-conventional machining is the advanced and latest technique and it solves issues faced by conventional machining, which include precise machinability, complexity and surface integrity. It has been established that non-conventional machining is able to manufacture complex property materials with greater strength, higher accuracy and better surface finish in shorter machining time[54]. This technique has improved much with the time such as the Electro Discharge Machining and laser cutting. The EDM technique is efficient in terms of the quality of the product but it consumes much time therefore is not feasible for larger production. The laser cutting is fast but it gives the irregular surface and non-uniformity with a burning edges. In the recent years, researchers are developing new techniques such as Blasting Erosion Arc Machining and Electrochemical-Arc-Machining , which utilises higher energy density compared to EDM spark discharging to achieve high material removal rate and to improve the machinability of difficult-to-cut complex 3D materials[55].

2.4 Non-conventional Machining

2.4.1 Wire Electrical Discharge Machining (WEDM)

Wire electric discharge machining is an electro thermal process consisting of passing current through a wire electrode that can be controlled to cut and shape of an electrically conductive material [56]. The significant advantage of WEDM is it is irrespective of the hardness and strength of the composite materials. So, it will be used for the applications with precise and minor cutting as used in the aerospace and automotive industry. It is a non-contact machining technology as compared to other machining techniques, and does not cause any stresses upon the work piece[57].

In WEDM, the wire electrode that usually employed a range from 0.1-0.3mm in diameter and the gap between the wire and the workpiece being controlled by the path of the cutting. The wire and the workpiece are submerged in a dielectric medium, commonly deionized water. The wire is activated by the voltage up to the level that causes the spark between the wire and workpiece that produces the heat of temperature approximately 15,000-21,000 Fahrenheit, where the workpiece material are melted. The ionized water plays an important role in cooling down the heat produced by the spark and also flushes out the removed material. No burrs are formed as there is no thermal or mechanical stress on the workpiece[58]. This quality

makes it ideal for the delicate and fragile composite workpieces cutting. Also, it been used for cutting the conductive material that cannot used other conventional techniques. While the advanced form of the WEDM is termed, Micro wire electric discharge machining which is used for more the precise and small cutting of the conductive composite materials. Such as in copper wire coated with the zinc and diameter of about 70 μm [59].

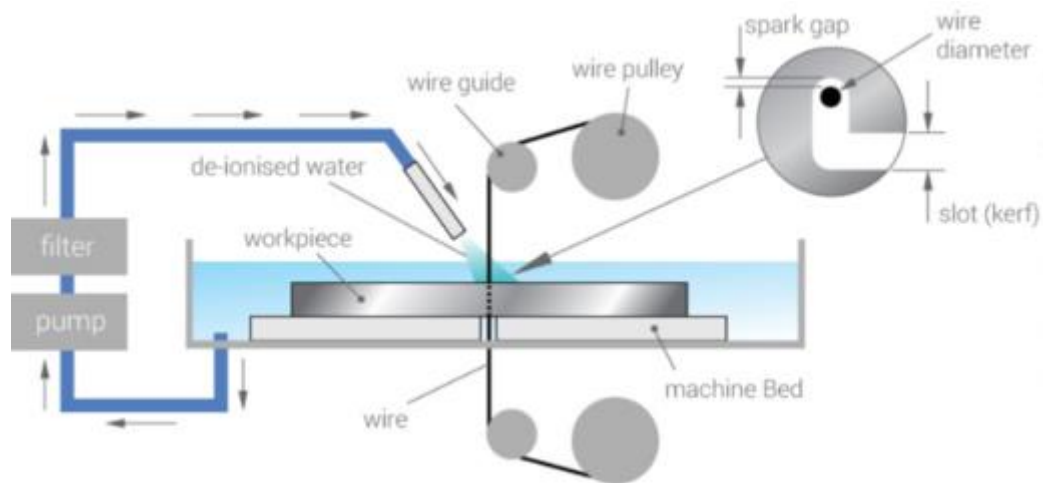


Figure 2.5: Experimental setup of WEDM[55].

In WEDM, the input parameters are pulse on time, pulse off time and peak current with the performance characteristics i.e. material removal rate and surface roughness[60]. Many studies have been conducted based on these parameters and the trends in the influence of process parameters[61]. Some researches [62, 63]conducted experiments to investigate the effect of varying the electrode material on the workpiece in terms of productivity and

surface integrity. Antar et al. [64] discovered that diffusion annealed coated wires increased productivity and reduced the recast layer, but increase the surface roughness.

With reference to paper [57] , the material removal rate and surface roughness has been determined under different values of the pulse-on, pulse-off and peak current values [65]. Three levels were made for the experiment with different values of the input parameters been studied. For MMR, the levels with largest rate is $A_3B_1C_3$ which means that the optimum parameters for better performance is with pulse on time, pulse off time and peak current will be 30 us, 5 us and 3 A respectively. Similarly for the surface roughness is $A_3B_3C_3$ which means that the optimum parameter for better performance is Pon, Poff and peak current will be 30 us, 15 us and 3 A respectively.

Karmakar and maji [66] describe different reinforcement materials like SiC, Al_2O_3 , TiC, TiB_2 , B_4C , ZrO_2 , ZrO_4 , cenosphere and hybrid composites being used and their effects, which show some interesting trends that volume fraction of the reinforcement material and pulse has been very important parameters in terms of machining quality. It has been found that the increasing the weightage percentage of the reinforcement materials

decreases the material removal rate but contrary to that the current applied and pulse on is directly proportional to the surface roughness [67].

Prabhuswamy et. al. [68] also studied the effect of the weightage of the reinforcement material upon the material removal rate; it has been also proved by them that MMR drastically decreases with the increase in the volume of the reinforcement material specifically in case of the SiC deposited on the Al606 MMC's for which 3 %, 6 % and 9 % SiC will have the MMR of 9.15, 9.13 and 9 mm³ min⁻¹, respectively. They also studied the difference in the material removal rate for both the reinforced and unreinforced materials. The unreinforced material has the average of 9.2 mm³ min⁻¹ material removal rate as compared reinforced mentioned above.

In case of the micro-Wire Electro Discharge Machining [59], surface roughness has been studied in terms of the powdered dipped wire and its capacitance which had a great influence. It is found that better surface finish was achieved with higher capacitance and so the surface roughness increased. The optimum level of machining parameters for least surface roughness: Voltage of 80 V, capacitance 0.0001F and powder concentration 0.5 g/l. Using this experimental combination, the minimum surface values (Ra) of 0. 384 μm was achieved. The graphite powdered methodology proved to be enhancing the surface finishing.

Suresh et. Al. [69] showed that with LM25 aluminium alloy/Graphite/Boron Carbide hybrid composites were successfully fabricated using stir casting to study the effect of the surface roughness by changing the input parameters. This study declared that the current applied so more influential parameters than the other two input parameters that is Pulse on and pulse off. The optimal predicated values for material removal rate and surface roughness are 17.11 μm and 3.44 μm respectively. For the surface roughness the current applied and pulse on has significant influence as it ranked. As earlier studies that have also introduced the optimal value of the parameters for LM25 aluminium alloy/Graphite/Boron Carbide hybrid composites for the maximum material removal rate and minimum surface roughness. With the optimal value i.e., current 7A, pulse on 4 ms and pulse off 6ms. The maximum material removal rate can be achieved for the specified composite. With the optimal value i.e., current 15A, pulse on 6 ms and pulse off 5ms, lower surface roughness of 2.33 μm can be achieved for the specified composite[57].

Surface integrity describes the state of the manufactured surface and can be divided into two parts: external aspects of the topography (surface finish) and internal sub-surface (hardness and residual stress) [70]. Surface roughness is the quantitative measurement of the surface finish. An optimal

surface finish post machining is necessary for the overall structural integrity of the machined components. In most cases, increase in surface roughness indicates subsurface damage in the form of cracking of matrix material, fracture of reinforcement particles and debonding between the particulates and matrix material [71].

2.4.2 Abrasive Waterjet Machining (AWJ)

There are two types of waterjet machining: pure waterjet (WJ) and abrasive waterjet (AWJ). Waterjet cutting has been introduced as a machining tool in the early 1970s. WJ can be used to machine a wide range of soft material such as plastics and fibreglass, whereas AWJ is widely used in machining hard materials of large thickness and different applications such as titanium, Inconel and superalloys [72, 73]. The primary difference of WJ and AWJ is that AWJ jet utilises a high-pressure water jet with abrasive powder in suspension to increase its cutting ability [74, 75]. The upmost advantages of the AWJ process are no thermal stress and no heat affected zone compared to other non-conventional processes and operates at very high temperatures. The abrasive material along with the water that has been pressurized by the pump to convert the abrasive material into kinetic energy. This kinetic energy result in high velocity of abrasive

material that strike on the workpiece with the help of the nozzle moving at the speed of 750 m/s to cut holes or shapes [76].

Apart from cutting, it was found [77] that the removal process abrasive water jets have been applied to milling, drilling and polishing with zero tool wear. One of the disadvantages of AWJ is noise pollution due to high pressure stream, water and abrasive high velocity striking to the work piece causing high noise level up to 120 dB and long term in such environment can causes the lung diseases due to exposure to the abrasive particles [78].

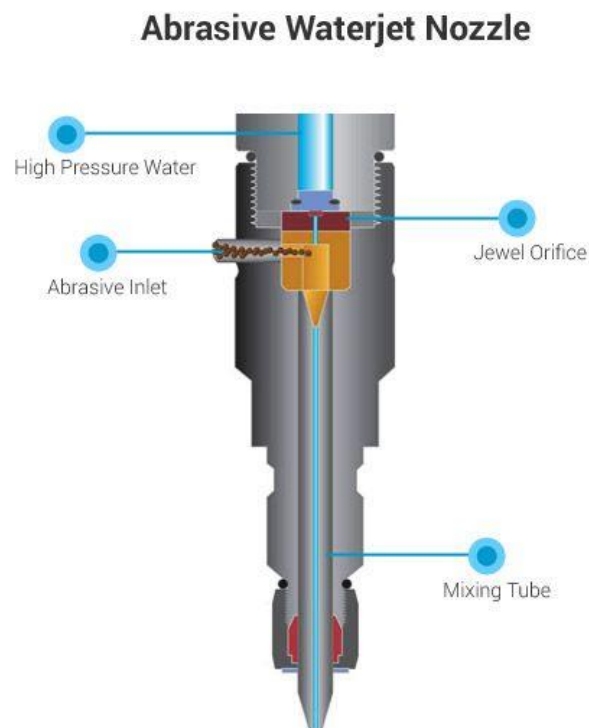


Figure 2.6 : Insight of AWJ Nozzle Setup[66].

Over the years, the AWJ techniques have been improved by increasing the value of pressure. There are different types of the AWJ machining as follows:

Table 2.3: Types of AWJ with different pressure values [78].

Types of AWJ based on pressure range	Pressure (psi)	Pressure (MPa)
High pressure	15,000 psi to 40,000 psi	103 MPa to 276 MPa
Ultrahigh pressure	40,000 psi to 75,000 psi	276 MPa to 517 MPa
Hyper pressure	75,000 psi and above	517 MPa and above

In general, the ultra-high pressure 55,000 psi (379 MPa) to 60,000 psi (412 MPa) and more improvised system operate at hyper pressure of 94,000 psi (650 MPa). The abrasive particles sizes of 0.1-0.5 mm are accelerated at high particle velocities of nearly 1000 m/s , hitting the wall of the mixing tube, rebounds and enter the waterjet again until it travels in the parallel direction of the waterjet and impacting on the cutting surface[79]. The smaller the inner diameter of the mixing tube, the more concentrated the kinetic energy of the abrasive particles hitting on the workpiece surface. In general, the mixing tube diameter is set to be 1mm as the ideal mixing tube diameter should be five times the average diameter of the abrasive particle[80]. The input factors of the process that can be varied in order to

study the trends and developments are abrasive particles, carrier gas, abrasive jet nozzle and work material.

On the other hand, the output aspects that can be observed are material removal rate (MRR), surface roughness of the work piece and nozzle life.

Many research and studies has been conducted on Abrasive Jet Machining, to optimize the parameters by using different method. Most commonly, researchers have used Taguchi approach, Response Surface Method, ANOVA to study the output parameters specifically the surface roughness [81].

Saurabh et. al. [82] described a number of experimental studies conducted on the aluminium ceramic that proved to be very successful for the cutting and processing. They have optimized the input parameters; abrasive flow rate and pressure and study the change in output parameters; material removal rate and surface roughness. It has been observed that the increasing the pressure in abrasive water jet has been directly proportional to the material removal rate and the surface roughness. Surface roughness can be effective on the properties of the composite. So, the maximum MRR of $62.16 \text{ mm}^3 \text{ min}^{-1}$ can be obtained with the minimum roughness of $5.01 \mu\text{m}$ after machining at optimal level of the pressure and abrasive flow rate.

Radovanovic [83] used the Matlab Multi Objective Genetic Algorithm Solver to obtain the optimized parameters by creating the logical equations based upon the dependency of the parameters upon each other. Similarly, they have used the same input parameters abrasive mass flow rate, traverse speed and standoff distance with the optimization of the machining time required to produce a unit of cut surface and its operating cost per meter of cut for carbon steel.

Paul and Mandal [84] used Taguchi approach to optimize the abrasive particle size to analyse the input parameters pressure; stand-off distance and nozzle diameter on outcomes. Abrasive particle size has also been a very effective parameter that can cause a significant change on the output i.e. material removal rate. They have used two different sizes of abrasive particles of $60\ \mu\text{m}$ and $120\ \mu\text{m}$ and study the effect on the output parameter. Where the particle with size of the $120\ \mu\text{m}$ has more contribution in terms of percentage on MRR for each input is 43.85 %, 47.73 % and 6.65 % for nozzle diameter, Stand-off distance and pressure respectively. However, for the abrasive particle size of $60\ \mu\text{m}$, it is 32.04 %, 65.24 % and 2.3 % only. It was determined that the greater the size of the abrasive particle, the higher the material removal rate.

Another important study [85] has explained the surface hardness and roughness of the Al 6063-T₆ alloy composite using the genetic algorithm. Genetic algorithm method was recommended by the author to be most reliable as it has minimum deviation of 0.82 % and maximum deviation of 4.48 %. They have used water jet peening to study the parameters that has increased the surface roughness by 35.9 % and presence of the boundary dislocation was caused due to plastic deformation generated by the deflection of the waterjet stream. The microstructure shows an increased surface roughness up to 26.6% due to smooth and dull surface.

2.4.3 Research Gaps and Critique Analysis

Conventional machining of MMCs is difficult due to the presence of reinforcement materials predominantly harder than cutting tools. From the review of published papers, there is an extensive of research in non-conventional machining of MMCs over the years. A large amount of research has been conducted for the optimization of parameters and the most common optimisation technique was Taguchi DoE [74, 86, 87]. Many machining process parameters were analysed with respect to different machining output. The machinability of different composites require different machining conditions [88]. To date, research has been conducted based on mainly one set of parameters for a process. For example, Taguchi

approach has been studied the input parameters mostly while output parameters have not been studied in detail. Research has performed in the simulation software such as Matlab multi objective genetic algorithm solver[74]. It produced the optimized input parameters for machining but the simulating parameters has not been tested practically for Abrasive Waterjet machining. AWJ proved useful for precise cutting as reported in different studies but the surface roughness could not be controlled and optimized with the other factors such as MRR, pressure and flowrate[68]. The material thickness affects the behaviour of the jet as it exits at the bottom on the workpiece. It was established that the jet lags between the point its first enters into the workpiece and where it exits has a considerable effect on the surface roughness of the workpiece [72].

WEDM has the ability of making complex shapes on harder material and machining more precise and accurate[71, 89].Machining techniques are becoming more efficient, advanced and updated versions of previous techniques. The WEDM is a contactless technique which can be used for minor cutting and shaping of the any kind of composite materials (ductile, conductive and fragile) without causing stress on the workpiece. The efficiency and precision of the WEDM is based on the input parameters (Pulse on/off peak current and material removal rate) optimization

according to the condition of the process. The volume fraction and pulse on/off are decisive parameters for measuring the machining quality.

In conclusion. AWJ cutting shows no thermal deformation and has the ability to cut high thickness material at a relatively high feed rates and low power consumption, but difficult to produce a workpiece with very high geometrical accuracy as in critical standard. Whereas WEDM produces smoother surface finish, but low MRR and can only be used for conductive materials only. Most of the published work focus on WEDM and EDM machining processes. Therefore, a detailed investigation to compare different non-conventional machining methods is needed. Very few studies have been reported on the detailed analysis of the surface integrity analysis of the machined surfaces. In this research, non-conventional machining: Abrasive waterjet (AWJ) and Wire electrical discharge machining (WEDM) of special purpose metal matrix composite will be investigated. In the published literature, no information exists for process parameters optimisation of AWJ and WEDM of this specific metal matrix composite of mechanical and thermal properties.

2.5 Surface Modification of Wettability Characteristics

There are three important features that comprises a MMC i.e. Matrix phase, the solid alloy who will be the host or whose properties needed to be improved; Reinforcement phase, the layer of the carbide formed upon the matrix which enhance and improve the properties of the matrix phase[90]; the interface between the matrix and reinforcement, the most important feature that is directly proportional to the enhancement of the properties of the resulting composite. Composite is the combination of the two material in order to obtain the better properties which totally depends upon the correct selection of the materials and the bonding between the two materials. The stronger the adhesion and the surface bonding between the two metal matrix and the reinforcement material more will be the composite strengthen [91].

2.5.1 Theoretical Background

Wettability refers to the ability of a liquid to wet a solid surface depends on the surface energies of the solid-vapour interface, the liquid-vapour interface and the solid-liquid interface[92]. A material with higher surface energy, have more interaction with water, more hydrophilic, hence has higher wettability [93]. For example, in Figure 2.7, three types of the liquid

i.e. mercury, oil and water has been spread over the solid surface i.e. clean glass plate.

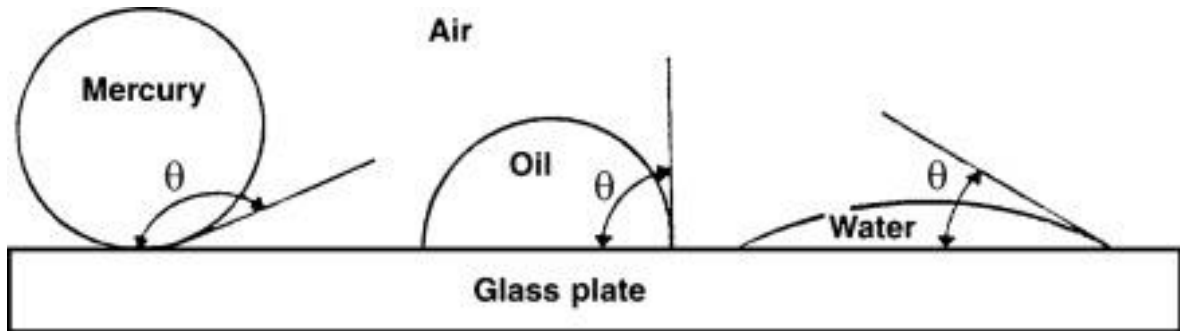


Figure 2.7 : Contact angle of 3 different liquids [94].

As it can be seen, mercury forms the spherical shape and oil forms hemisphere; whereas water spread all over the glass plate. So the tendency of the liquid to be more in contact with solid surface refers to the wetting characteristic. Wettability can be determined by the contact angle between the liquid and solid layer. Contact angle is inversely proportional to the wettability i.e. smaller the contact angle greater will be the wettability. For complete wettability the contact angle should be zero, good wettability will be if the contact angle is less than 90° and above 90° will state as poor wettability[95].

2.5.2 Characterisation Methods

Wettability of the MMC is measured as contact angle or static angle between the liquid usually water and solid phase metal matrix composite. The most

important to determine the wettability between the liquid and solid layer is the static angle and sliding the angle which will as follow:

i. Static Contact Angle

When the liquid comes in contact with the solid surface the molecules of the two phases make a physical contact according to the nature of the material. Greater the liquid spread of the over the solid surface greater will be the physical contact between the two phases and lesser the static angle.

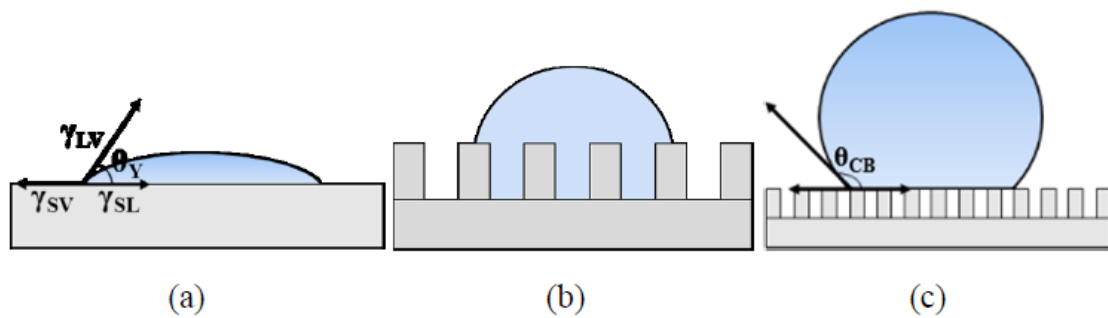


Figure 2.8: (a) Young's angle on a flat and homogeneous surface, (b) Wenzel state wetting and (c) Cassie Baxter's wettability model schematic for a water drop resting on a substrate with micro-pillars[96].

There are three main static contact angle theories showing relationships between contact angle and the surface roughness: Young's model, Wenzel model and the Cassie-Baxter model [97]. At equilibrium, the force exerted by the interfacial tension acts tangent to the surface of the water droplet and its horizontal component. As shown in Figure 2.8(a), contact angle is

defined as the angle formed by applying a tangent line from the intersection of the liquid-solid interface, σ_{SL} and the liquid-vapour interface σ_{VL} , which is defined as the Young's model: $\gamma_{SV} = \gamma_{SL} + \gamma \cdot \cos\theta$. Static angle is inversely proportional to the area in contact and wettability i.e. more the contact area lesser will be the static angle and greater will be the wettability[98]. When the contact angle is $90^\circ \leq \theta < 150^\circ$ and larger than 150° , the surface is considered to be hydrophobic and superhydrophobic respectively, where the interaction strength between the solid and liquid is weak.

Table 2.4: Static contact angle versus wettability.

Contact Angle	Surface	Degree of wetting	Interaction strength solid-liquid
$\theta = 0$	Super hydrophilic	Perfect wetting	Strong
$0 < \theta < 90^\circ$	Hydrophilic	High wettability	Strong
$90^\circ \leq \theta < 150^\circ$	Hydrophobic	Low wettability	Weak
$150^\circ \leq \theta < 180^\circ$	Super hydrophobic	Perfect non-wetting	Weak

ii. Sliding Angle

Another most important characteristic to determine the wettability of the material is sliding angle. This is the angle at which mobility of the liquid droplet over the solid surface occurs called as sliding angle[99]. The sliding angle has also inverse proportional relational with the wettability as static angle i.e. smaller the sliding angle at which liquid droplet run of the solid surface, the wetting behaviour increases [100]. It is a characteristic that exists due to heterogeneous surface chemistry and topography. In a dynamic process, the contact angle formed in front of a forward contact line is called the advancing contact angle, θ_a , while that formed behind a backward contact line is the receding contact angle, θ_r , as schematically shown in Figure 2.9

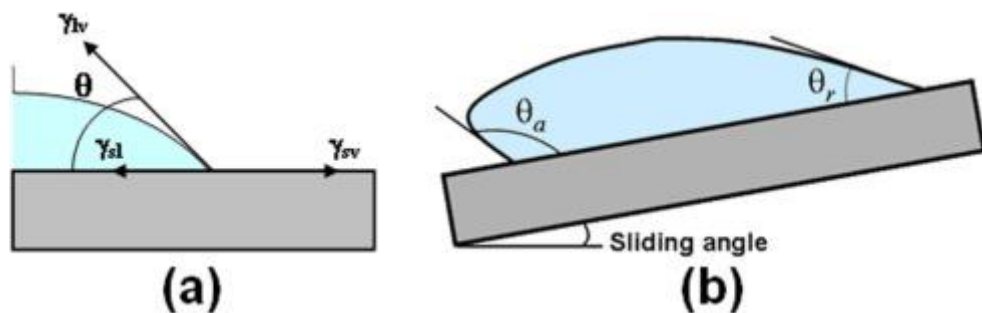


Figure 2.9: The schematic diagram of sliding angle[97].

2.5.3 Factors Affecting Wettability

Factors affecting the wettability have been classified by the author are mainly the surface roughness and surface chemistry of the solid. These factors have a direct effect on the static angle and sliding angle which determine the wettability of the material. Improving these factors will help to achieve the desired wettability and summarised in Figure 2.10.

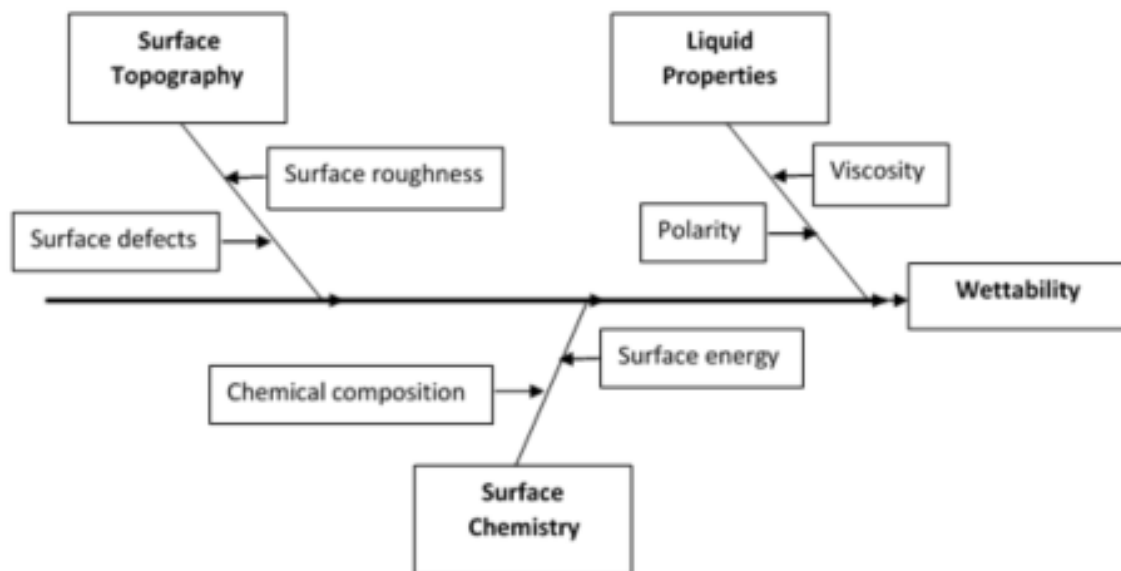


Figure 2.10: Factors influencing the surface wettability.

i. Surface roughness

Surface roughness is commonly used to indicate the surface finish of a manufacturing process and it is the most important outcomes the interface between the two material [101]. The enhancement in the mechanical

properties of the composite depends on the surface formed and their adhesive contact with each other[102]. The uniform and smooth surface formation indicates the improvement in the properties but greater the surface roughness of the composite lesser the properties improved and poorer the wettability [103].

ii. Surface Chemistry

Wettability has been dependent upon another factor that is surface chemistry. Surface chemistry is the nature of the surface of the material i.e. functional, non-functional, acidic and basic[104]. In studies, it has been found that the improving the surface chemistry has a positive influence on the wettability of the composite. Slepickova et. Al. used grafting process to introduce many chemical substances and Nano particle to improve the surface chemistry that not only improved the surface roughness but also has the improvement in the wettability and the properties of the material [105].

In the recent studies of fabrication processes [106], stir casting of the Al composite has been proved as the cause of the poor wettability of the Al alloy and the reinforcement that does not form the uniform surface and adhesive bonding between them that lead to the particle segregation. In this paper, the authors explained many methods to improve the wettability

among which two methods were successful for its improvement; first by subjecting the reinforcement phase to a surface modification process and the melting treatment technique is the second. Surface modification can be achieved by treating them at high temperature which will increase the chemical reaction compatibility of the layers and also adding the wetting agent also stimulate the bonding of the particulate.

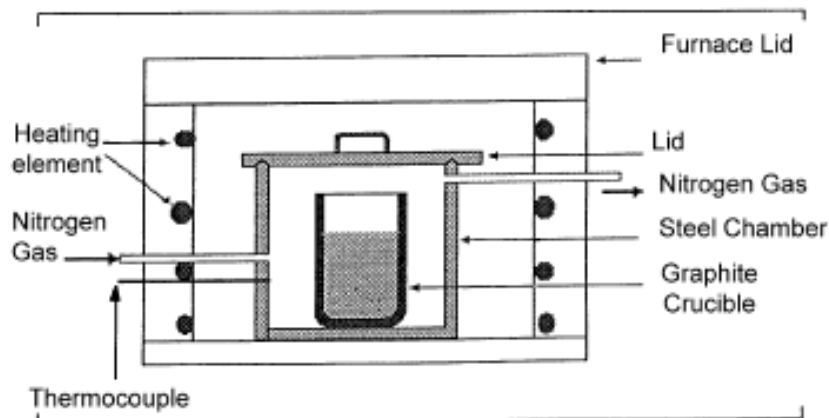


Figure 2.11: Stir casting with nitrogen gas [106].

Similarly in other research[107], mechanical stirring has to be declared important and necessary for the improvement in wettability but the stirring at which point will be effective is discussed. Stirring in fully liquid condition will not allow particulate and matrix to bond strongly that will be effective on the surface chemistry as the bonding will be weak. However, stirring in the slurry is about to solidify form will enhance the chemistry of the bonding.

Decreasing the time of the solidifying will increase the wettability. Also they added Mg as wetting agent to provide the increase in wettability [108].

Other studies [109, 110] have proved that the adding the Mg of 1 % wt. as a wetting agent to increase the solid interfacial energy, which can improve the wettability of the Al composites which have a direct effect upon the mechanical properties of the composites such as tensile strength and the hardness. In this paper [111] , various methods have been developed and discussed in the literature review to enhance the adhesion of the matrix and reinforcement interface and many experiments were conducted to improve the wettability as the following:

- 1) Addition of a wettability agent and fluxes,
- 2) Preheating of the material matrix composites,
- 3) Coating of ceramic particles such as Nickel phosphide coated, silicon nitride particles have been successfully dispersed in Al₆O₆₁ alloy,
- 4) Lowering the casting temperature,
- 5) Adding ceramic particles when the aluminum is in a semi-solid state,
and
- 6) Compo-casting Technique.

It has been investigated and show that stir casting has the poorest wettability as compared to other non-conventional techniques. Kennedy [112] describes the reason of poor wettability is due to formation of the plastic segregating; weak compatibility between the Al matrix and reinforcement in the stir casting has been found. Researches further studies the cause and experimented and observed the stir casting process in detailed[93].

Kumar and Rai [113] concluded that the stirring when the slurry is in liquid state cause the poor bonding between the Al alloy and the reinforcement; however stirring when the slurry start solidifying formed a uniform bonding which will increase the wettability of the Al composite. Also that adding the Mg wetting agent will improve the wettability as it strength the bonding and helps in formation of the smooth surface[114].

In the paper [115] , abrasive flow finishing method is used to study the effect of with reference to surface roughness and wettability using central composite design of aluminium alloy. It has been found that there is a decrease in the surface roughness with minimum roughness of $0.4487 \mu m$ at 8 no. of passes and 55 bar pressure. Wettability has also been studied in this paper showing that the contact angle i.e., static angle has a greater

effect on the wettability. Also that the wettability of the composite can be improved with fined polishing of the surface[116].

Surface wettability has been studied in this paper [117] , where the contact angle has been measured for the both untreated and treated substrate and it has been found that the contact angle of the treated substrate with Electric Discharge Machining technique is smaller than the untreated substrate as shown in Fig. 2.12. The contact angle of the EDM machined substrate change from a base angle of 105.96° to 78.27° , which shows that the surface became more hydrophilic. As discussed earlier, the contact angle is inversely proportional to the measure of the wettability of the material. The smaller the contact angle, the greater the wettability of the material. According to this study, the contact angle has been reduced by using the electric discharge machining[118].

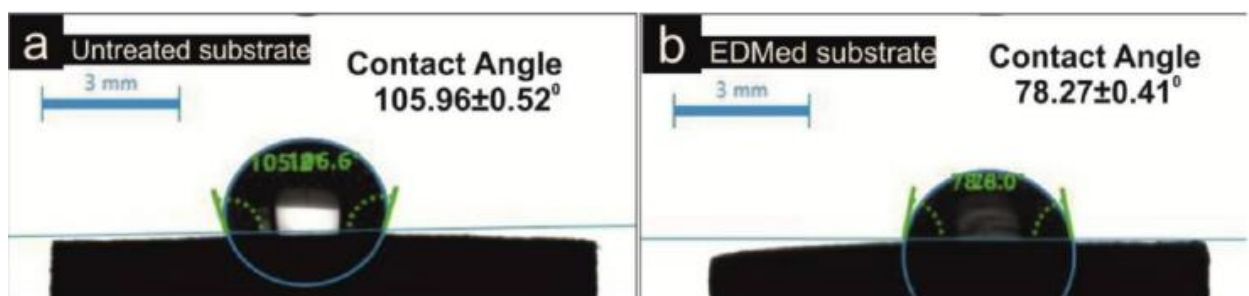


Figure 2.12: Contact angle illustration of (a) Untreated surface; (b) EDMed surface [118].

2.5.4 Hydrophobic and superhydrophobic surfaces for aerospace applications.

Formation of the icing on the surface of the aircraft and air jets is one of the crucial issue faced by the aerospace and defence industries[119]. For the last few decades, many studies have been conducted in removal and deformation of the icing on the aerospace application[120]. As the icing start to be formed on the wings and tails of the aircraft it causes varies in the airflow which reduce the lift force and initiating aerodynamic stall which will be fatal[121]. There are two types of method used to control this formation upon the aerospace applications i.e. de-icing and anti-icing[122].

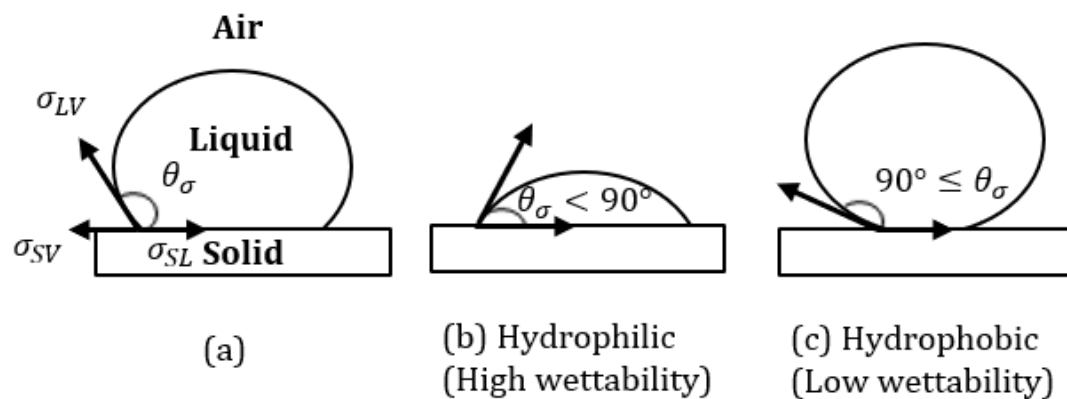


Figure 2.13: Schematic diagram of hydrophilic and hydrophobic angles[92].

De-icing is considered to be old and unsustainable method, where the chemical mainly the mixture of the glycol and water is heated and sprayed

under pressure to melts the icing which will remove and melt the ice but it will not stop the further formation of the icing[123].



Figure 2.14: De-icing of a Boeing-777 aircraft[123].

On other hand, the anti-icing method in order to generate a layer of hydrophobic or superhydrophobic coating surface was evaluated and it was concluded that surface roughness and surface energy are the important factors in controlling the ice-adhesion strength of the coatings[124]. This chemical layer is usually the super hydrophobic layer whose contact angle is above 150° causing low surface energy which repels the water; resisting the surface to adhere to water[125].

2.5.5 Research Gaps and Critique Analysis

Most research investigated the wettability behaviour of surfaces by conducting static contact angle and sliding angle measurements. The factors affecting the surface wettability are surface chemistry and roughness of the solid surfaces. These factors have a direct relation with wettability. The smoother the surface roughness, the smaller the sliding angle and the wettability increases. The surface roughness can be improved by improving the surface chemistry by grafting process using nano particles and other chemical substances. Still there are many research gaps in the field of wettability which need to be covered by exploiting in depth research. The relationship between the surface topography and integrity and the wettability of the machined surfaces should be explored.

One of the main applications of metal matrix composite is aircraft parts such as aerostructure, which requires super hydrophobic or hydrophobic surfaces for anti-icing purpose. Icing formation on an aircraft wings and tails causes airflow variation and can be fatal as it stalls the air jet. While extensive studies on generation of hydrophobic and superhydrophobic surfaces via different methods such as chemical agent addition and ceramic particles coating, there is lack of publication related to the fabrication of

superhydrophobic surfaces via non-conventional machining to eliminate coating processes.

CHAPTER 3: EXPERIMENTAL METHODOLOGY

Based on the critical review and comprehensive discussion on the WEDM and AWJ of MMCs from the previous chapter, the experimental works were performed over three major phases and summarised in Fig.3.1. Particular attention is paid to aluminium matrix composite reinforced with SiC particulates owing to the interest in lightweight aerospace material and mechanical properties.

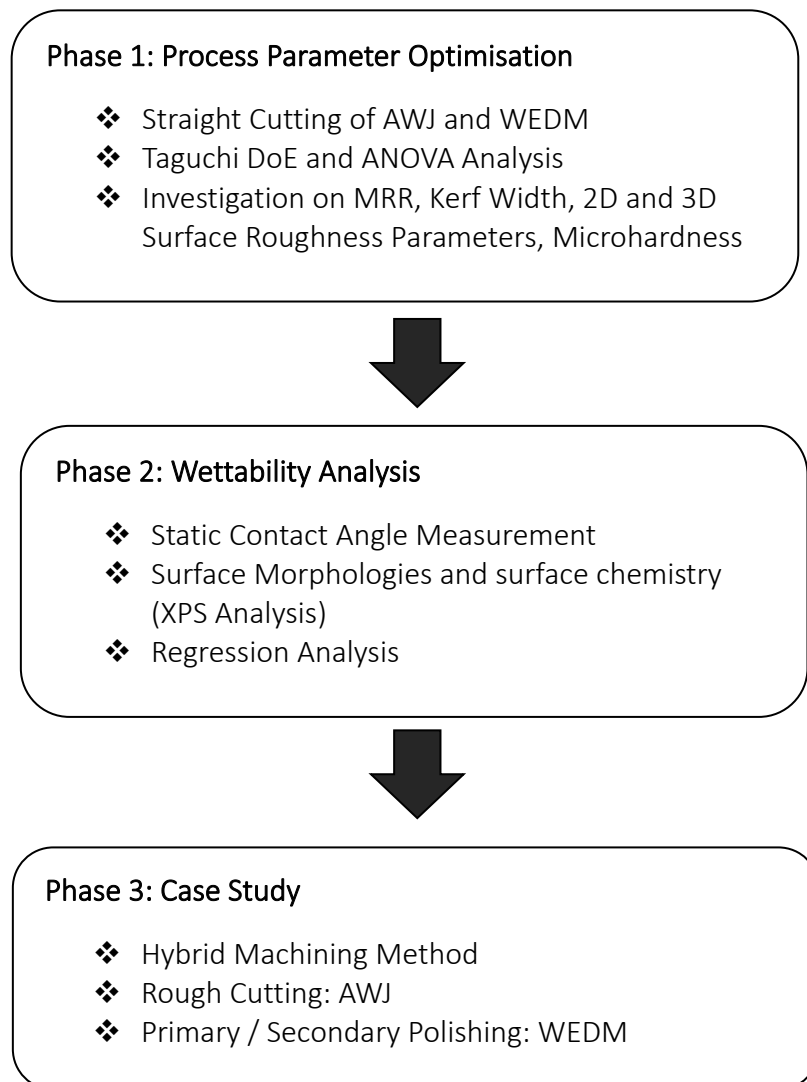


Fig. 3.1: Flow chart of experimental procedures of Phase 1 to 3.

3.1 Phase One: Process Parameter Optimisation

Phase 1 comprises the determination of the process parameters that affect different output parameters. Taguchi DoE was utilised to reduce the number of trials and ANOVA analysis was conducted. The experimental apparatus and step-by-step output parameters analysis procedures are explained in this chapter.

3.1.1 Workpiece Material

The straight cutting of AWJ and WEDM conducted in Phase 1 was carried out on MMC workpiece. The workpiece test specimens was Al/SiCp and supplied by Cospray Ltd., part of Alcan International Ltd. The base alloy matrix was wrought aluminium AA2618 (2.8% Cu, 1.5% Mg, 1.2% Fe, and 1.1% Ni) reinforced with silicon carbide particulate with 15% volume fraction and average nominal size 10-15 μm . The experimental workpiece was produced by spray deposition and fully consolidated via extrusion. The extruded rectangular bars section (24 mm \times 100mm \times 1000 mm) provided by the supplier were cut into blocks of \sim 170 mm in length and skimmed by using PCD tipped facemilling tools to 24 mm thickness as shown in Figure 3.2.

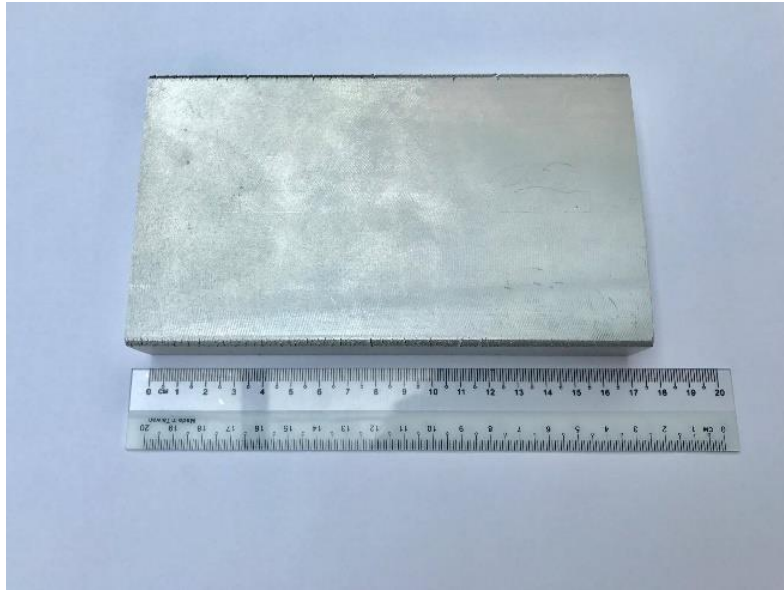


Figure 3.2: Prepared MMC workpiece.

The base material sample had a measured surface roughness $R_a \leq 0.8 \mu m$ and bulk micro-hardness of $\sim 110 HK_{0.005}$. Figure 3.3 shows the optical micrographs under 50 \times magnification of the MMC workpiece in transverse and longitudinal extruded directions by using a Leica microscope. It shows that the typical reinforcement SiC has random particle size and were randomly embedded in the aluminium matrix.

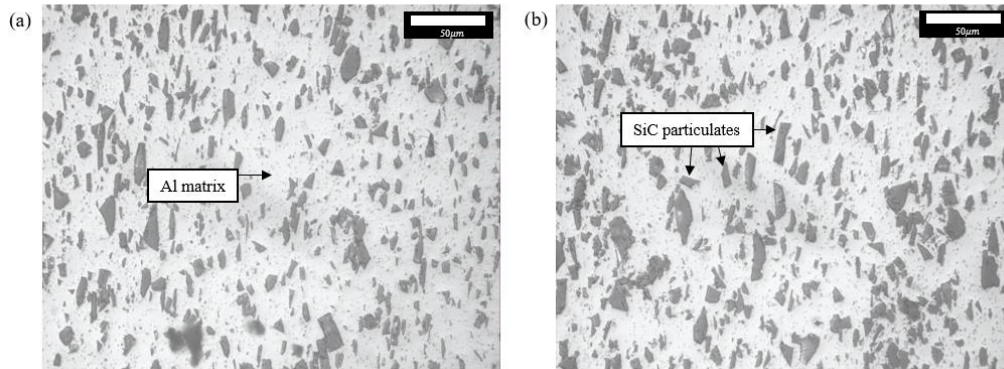
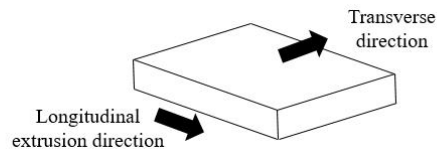


Figure 3.3: Microstructure of the workpiece before experimental trials in (a) longitudinal extruded direction and (b) transverse direction

The electrical conductivity of the workpiece was measured by using the four-point probe method using an ADVANTEST R6552 digital multimeter connected to an ITT Metrix AX-321 adjustable power supply unit (see Figure3.4).

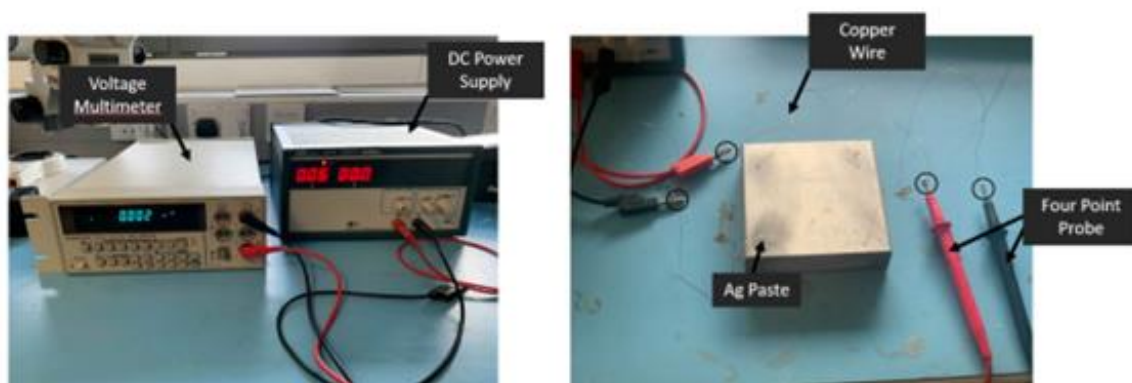


Figure 3.4: Measurement setup of the four-point probe on the sample surface.

Voltage is applied between the two terminal probes connecting the sample with four equal length copper wires. Conductive silver paste was used to fill in the gap between the probe and the material to reduce contact resistance. The measurement was conducted using direct current and under room temperature conditions. The reliability of the data was assessed by repeating measurements at different orientation of the sample. According to Ohm's law ($V = IR$), it allows resistance to be determined assuming the resistance of the silver paste, probe and wires are negligible. Resistivity, ρ_o was evaluated by using the following equation[126]:

$$\rho = G \times \frac{RA}{s} \text{----- Eq. (1)}$$

where ρ is the resistivity in Ωcm , G is the correction factor, A is the cross-sectional area and s is the spacing between the probes.

In this case, the sample is considered as thin sheet as the thickness of the sample, $t < \frac{s}{2}$. The correction factor, G derived in [127] according to geometric sample as below:

$$G = F_0(s) \times F_1\left(\frac{t}{s}\right) = \frac{\pi}{\ln 2} t \text{----- Eq. (2)}$$

Thus, the electrical conductivity, σ was calculated:

$$\sigma = \frac{1}{\rho} \text{----- Eq. (3)}$$

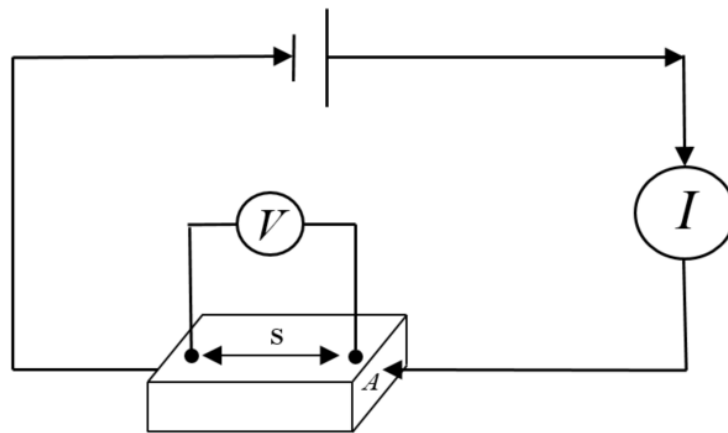


Figure 3.5: The diagram of the electrical current flow.

The calculated conductivity of the MMC sample is $\sim 1002.54 \text{ Scm}^{-1}$.

Compared to other metal alloy, the sample is considered very conductive and the low percentage of non-conductive SiC particles embedded in the aluminium matrix has little influence on the electrical conductivity.

3.1.2 Straight Cutting Machining Equipment

3.1.2.1 Abrasive Waterjet Machining (AWJ)

The experimental trials of AWJ cutting were performed on an Ormond five-axis abrasive waterjet system provided by the Machining and Condition Monitoring research team at the University of Nottingham. Figure 3.5 shows the set up and main subsystems of the built-in waterjet system. The working area for the waterjet operation is within $1.2 \text{ m} \times 0.65 \text{ m}$ and the nozzle

head can be programmed to move on five axes directions: linear (X-, Y- and Z-) and rotary (B and C axis). The pressure of the pump can be adjusted manually on the KMT streamline SL-V100D ultra-high pressure (UHP) pump controller from 10,000 to 60,000 psi. The orifice diameter that can be used ranges from 0.05 to 0.4mm whereas the nozzle diameter depends on the selected tool manufacturer. It is recommended that the ratio of orifice diameter to mixing tube/ nozzle diameter is 1:3. The most common nozzle diameter and used in this research was 10mm and the nozzle was kept at right angles to the sample being cut as shown in Figure 3.6. The mesh size of the abrasive grit that is appropriate for the abrasive feeder is between 60 mesh (200 – 400 μ m) and 220 mesh (70 – 100 μ m). The sub angular shape GMA Garnet with 80 mesh size (300-150 μ m) was selected as it is recommended for high precision machining and suitable for orifice size of 0.305 – 0.330 mm. The physical characteristics and chemical composition of the garnet is tabulated in Table 3.1. MasterCAM 9.0, a third-party software is used for jet path generation. The main role of MasterCAM is to create a jet path and generate numerical codes to enable communication between the control unit and the AWJ machine such as the dwell time. Unlike conventional machining, AWJ uses no actual cutting tool but employs a time-

dependant jet to erode workpiece material. Hence, dwell time is significant as it affects the degree of erosional depth in AWJ machining.

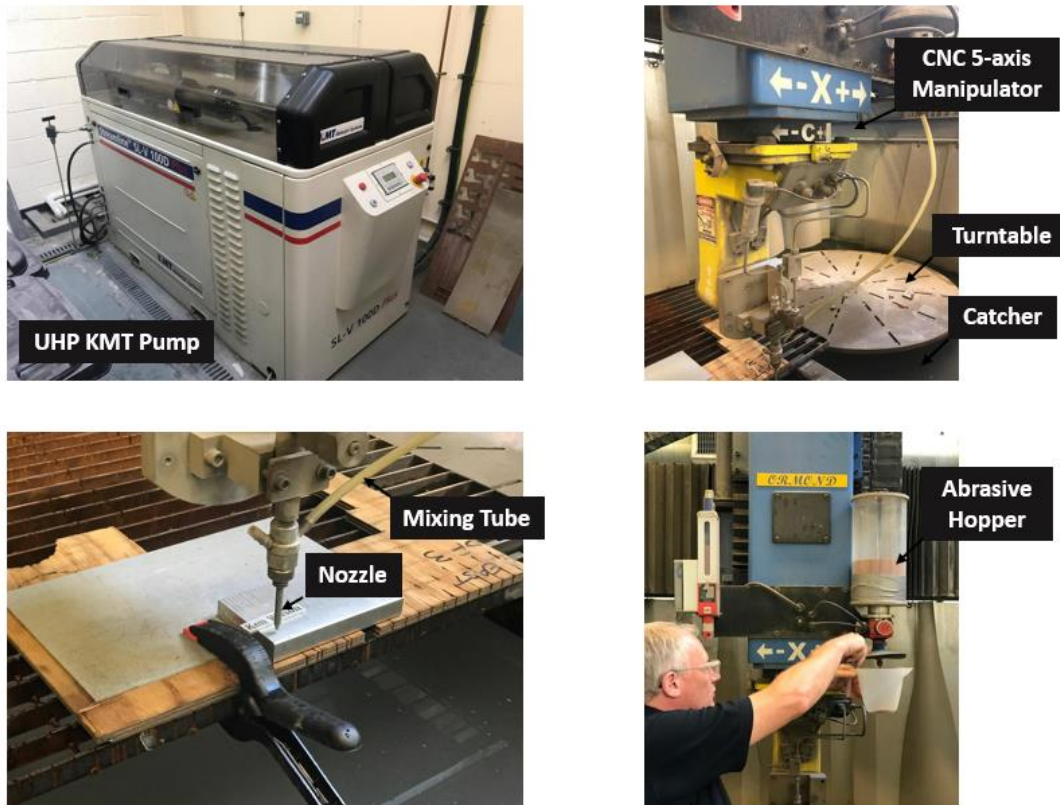


Figure 3.6: The main subsystems of the Ormond CNC 5-axis abrasive waterjet machine.

Table 3.1: Physical Characteristics and Chemical Composition of GMA Garnet [128].

Physical Characteristics	
Hardness (Mohs / Knop)	7.5-8.0 (~1350 kg/mm^2)
Melting Point	1250°C

Average Chemical Composition	
Chemical Name	Proportion (weight %)
Almandine Garnet $Fe_3Al_2(SiO_4)_3$	>97%
Ilmenite $FeTiO_3$	<2.0%
Calcium Carbonate $CaCO_3$	<1.5%
Zircon $ZrSiO_4$	<0.2%
Quartz SiO_2 (<i>Crystalline Silica</i>)	<0.2%

3.1.2.2 Wire Electrical Discharge Machining

The machining trials were conducted on an AgieCharmilles Robofil FI 240 CC supplied by GF Machining Solutions based in Machining Research lab at University of Birmingham as shown in Fig.3.7. It was a five axis CNC submerged wire cutting system facilitated with high speed spark generator and anti-electrolysis protection for minimum damage. The max. workpiece dimensions is $1000 \times 550 \times 220$ (mm). It is able to accommodate wires of diameter ranging from 0.10mm to 0.33mm and equipped with automatic re-threading facilities in case of wire breakage. Deionised water was used as dielectric fluid.



Figure 3.7: AgieCharmilles Robofil FI 240 CC machine.

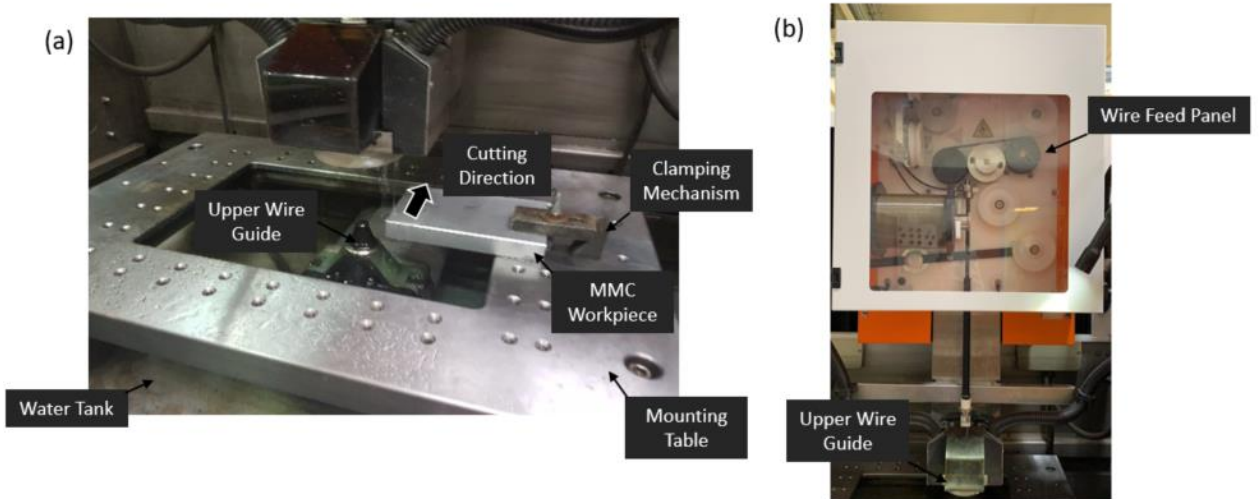


Figure 3.8: (a) Workpiece clamped on the mounting table and (b) setup of wire feeding system.

Three different types of 0.25 mm wires were selected based on their tensile strength to evaluate the optimum wire electrode for process parameter optimization as shown in Figure 3.9. To assess the effectiveness of each wire, the wires with different material composition and tensile strength (see Table 3.2) were tested and compared for desirable optimum outputs. Results were obtained for material removal rate (MRR), kerf profile, surface roughness and microhardness and the preferred wire was found to be Bedra Broncocut, which consisted of a brass core (80%Cu20%Zn) with a dual layer coating containing β (50%Cu50%Zn) and γ (35%Cu+65%Zn) phases. The wire composition provided high tensile strength (800 MPa) and electrical conductivity appropriate for machining high resistivity materials such as CFRP. The conductivity of the deionised water dielectric was maintained at $\sim 8\mu\text{S}/\text{cm}$.

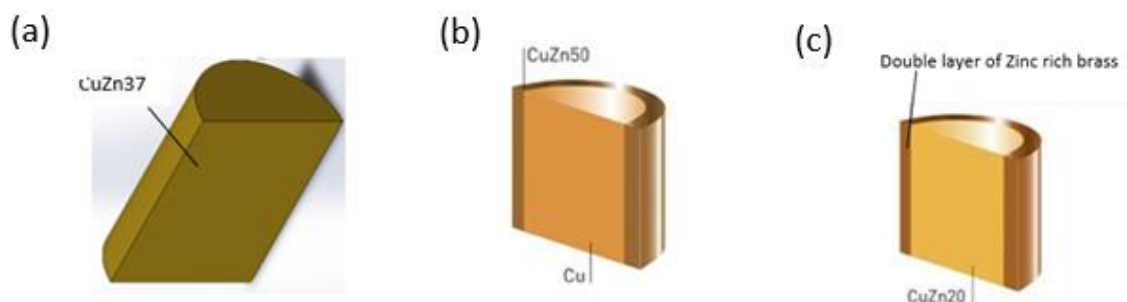


Figure 3.9: Wire composition of (a) Charmiles CuZn37 , (b) Bedra Broncocut and (c) Bedra Topas Plus.

Table 3.2: Summary of WEDM wire properties.

Wire Type / Brand	Core Material Composition	Coating Layer	Tensile Strength (MPa)
Charmiles CuZn37	Cu 63% Zn 37%	-	490
Bedra Broncocut	Pure Cu	Cu 50% Zn 50%	520
Bedra Topas Plus	Cu 80% Zn 20%	Double layer of Zn rich Brass	800

There are two different voltages in WEDM settings: Gap Voltage (V) and Servo Voltage (AJ). The influence of Gap Voltage and Servo Voltage will be studied. Servo voltage refers to the reference voltage to control the advancement and retraction of the wire. The smaller the set value, the narrower the mean gap, the increase in number of electric sparks results in higher machining rate. The gap voltage also known as the open circuit voltage. The greater the gap voltage, the greater electric discharge, the peak current increases.

The Function of Frequency, FF in relationship to the pulse on time, A and pulse off time, B is defined as:

$$F = \frac{1}{(A+B+Td)} \dots\dots\dots \text{Eq. (4)}$$

where Td is the delay time in the region of 1μs and (A+B+Td) is the pulse period in the region of 1 to 25μs. The Function of Frequency can be adjusted in the range of 1 to 100 to generate electric sparks in between 40,000 to 1 million sparks per second[129].

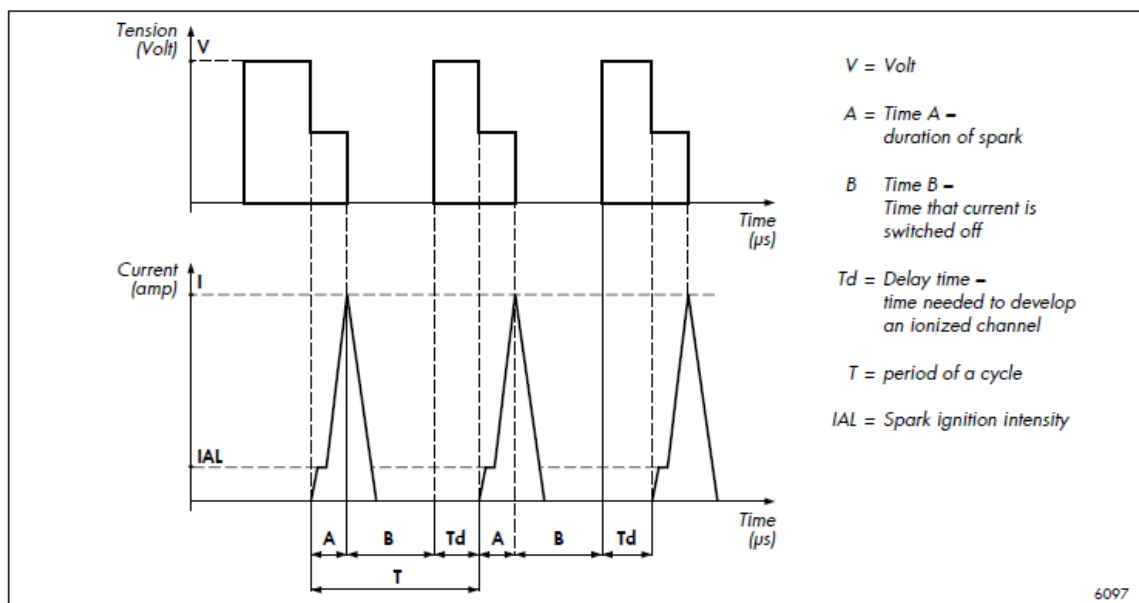


Figure 3.10: The diagram of spark generation with simultaneous trend of voltage and intensity[129].

3.1.3 Experimental Procedure

A number of preliminary cutting experiments and literature surveys were initially undertaken to investigate the main parameters in affecting the machinability of AWJ and WEDM processes. The main objectives of the work are to investigate and compare the influence of process parameters

in WEDM and AWJ machining of MMC in terms of material removal rate, kerf profile geometry, surface roughness and microhardness.

For both AWJ and WEDM straight cutting, a 20mm depth in the traverse direction was carried out as shown in Figure. 3.11. A 5mm gap was left in between trials.

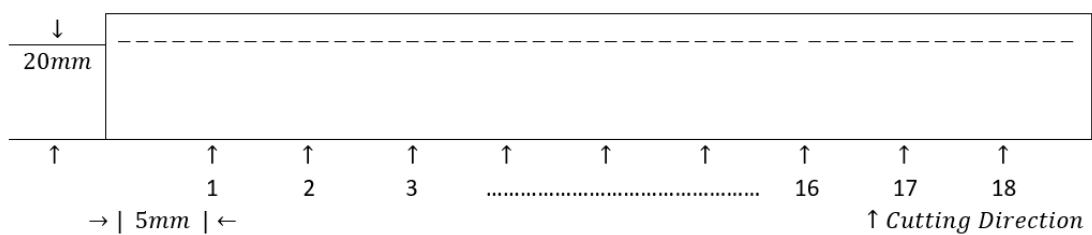


Figure 3.11: Cutting direction and trials setup.

3.1.3.1 Design of Experiment and test arrays

Taguchi Design of Experiment (DoE) was employed to minimize the experimental variation and sensitivity to noise (uncontrollable factors). The orthogonal arrays (OA) used in Taguchi DoE produces the effect of combination of the process parameters and the levels at which they varied. Taguchi method offers a great advantage in reducing time and test runs from 162 runs to 18 runs, compared to full factorial experimental design. The test orthogonal arrays were designed and the output responses was analysed with Minitab 19 software. Taguchi method utilizes signal-to-noise ratio, which is defined as the ratio of mean value (signal) to standard

deviation (noise) to determine the effect of each independent variable on the output parameters. There are three categories of S/N ratio: Smaller is better (SB), Larger is better (LB) and Nominal is best (NB). The S/N ratio for each level of factor parameters is computed based on the equations and adopted to obtain desirable optimum output given by Eq. (5) – (7).

$$\text{Smaller is better: } \frac{S}{N} = -10 \log \frac{1}{n} (\sum y^2) \quad \text{----- Eq. (5)}$$

$$\text{Larger is better: } \frac{S}{N} = -10 \log \frac{1}{n} \left(\sum \frac{1}{y^2} \right) \quad \text{----- Eq. (6)}$$

$$\text{Nomianl is best: } \frac{S}{N} = -10 \log \frac{1}{n} \left(\sum \frac{\bar{Y}}{S_Y^2} \right) \quad \text{----- Eq. (7)}$$

where n is the number of observations, y is the observed data and \bar{Y} is the average of the observed data.

Main effect plots were determined to identify the significant factors and levels. The operating parameters and the baseline set of levels for each factors were selected based on literature review, recommendation from manufacturer and preliminary straight cutting analysis. For most AWJ cases , it was found that the jet traverse speed is the most significant factor affecting the jet penetration of AWJ[130]. The 4 factors are selected: pump pressure, abrasive flow rate, stand-off distance (each with 3 levels) and traverse rate with 5 different levels. It was found that the pulse on time

and pulse current are the most significant factors affecting the cutting performances of the WEDM[89]. It has been observed that most researches concentrated only on investigating the influence of process parameter of either servo voltage / average machining voltage or servo gap voltage. The relationship between both voltages are not well established. The influence of Function of Frequency (FF) was explored. 5 factors each with 3 different levels were selected: pulse on time, average machining voltage, ignition pulse current, open gap voltage and function of frequency. To select an appropriate orthogonal array for the experiments, the total degrees of freedom need to be computed. There are 11 degrees of freedom (DOF) $3 \times (3-1) + 1 \times (6-1) = 11$ for AWJ and 9 degree of freedom (DOF) $4 \times (3-1) + 1 \times (2-1) = 9$ for WEDM process. 18 levels orthogonal array is selected for both AWJ and WEDM processes, assuming there is no interaction between the factors. The range of process parameters is selected carefully so that it reflects the entire range of the AWJ machine settings. The detailed process parameters for abrasive waterjet machining and wire electrical discharge machining are summarised in Table 3.4.

Table 3.3: Summary of AWJ and WEDM process parameters.

Process	Parameter	Value
AWJ	Pump pressure , P(kpsi)	30, 40, 50
	Traverse rate, Vf (mm/min)	5,10, 20, 30, 40, 50
	Abrasive flow rate, Va (kg/min)	0.158,0.340, 0.402
	Stand-off distance, SOD (mm)	1, 3, 5
WEDM	Pulse on time, A (μ s)	0.1, 0.7
	Average machining voltage, AJ (V)	15, 30, 45
	Ignition pulse current, IAL (A)	10, 20, 30
	Open gap voltage, V (V)	80, 100, 120
	Function of frequency, FF (%)	10, 50, 100

3.1.3.2 ANOVA Analysis

Furthermore, a statistical analysis of variance (ANOVA) with confidence level of 95% was performed to determine the contribution of each process parameters to the output. F ratio corresponding to the ratio of two mean

square and the contribution proportions from each of the control factors. It is used to determine whether the factor has a significant effect on the quality characteristic. If the f ratio is bigger than the critical F value F_{α} at the α significance level found in the F table, it means the null hypothesis is rejected. F ratio in ANOVA also determines the p value. The p value confirms the statistical importance of each process parameter and gives the percentage contribution to reduce the variation of the process parameters. The parameter is considered statistically significant when the p value $\leq \alpha = 0.050$. Percentage Contribution Ratio (PCR) was calculated. Finally, confirmation tests for each output parameters were conducted to verify the Taguchi DoE analysis and to validate the optimal process parameters obtained from the parameter design. The confirmation experiment is performed by conducting a test with the optimum combination of machining parameters. The predicted S/N ratio using the optimal levels can be calculated as:

$$n_1 = \bar{T} + (\overline{A_n} - \bar{T}) + (\overline{B_n} - \bar{T}) + (\overline{C_n} - \bar{T}) + \dots \text{----- Eq. (8)}$$

where n is the predicted mean, \bar{T} is the overall mean of the considered response and $\overline{A_n B_n C_n \dots}$ is the mean response for factors at designated levels.

3.1.4 Characterisation and Measurement Techniques

3.1.4.1 Cutting Performance: Material Removal Rate

There are different methods in determining Material Removal Rate (MRR). Eq.(9) was used by measuring the mass difference of workpiece prior and after each straight cutting trials and calculating the time taken in s. The Radwag PS3500/C2 Precision Lab Balance as shown in Figure 3.12. was used for mass measurement. Prior to measurement, the sample was dried using air drier to prevent interference of reading and the scale was calibrated. The balance is internally calibrated with minimum load of 0.5g, readability of 0.01g and accuracy of 0.01g. The workpiece was dried using air pressure before mass measurement and three readings were taken and averaged to maintain consistency.

$$MRR = \frac{(m_1 - m_2)}{\rho_1 t_1} \dots\dots\dots \text{Eq. (9)}$$



Figure 3.12: Radwag PS 3500/C2 Precision Lab Balance.

3.1.4.2 Investigation of Surface Geometrical Accuracy

Kerf width measurement, the distance between the two cutting fronts, is used to determine the geometrical accuracy of the machined part. In order to conduct straight cutting of parts with high accuracy and tolerance, it is important to understand the characteristics of the kerf profile in terms of the kerf width and taper angle. There are a number of reported research work in kerf width analysis, mainly investigating the effect of process parameters on the top and bottom kerf width. It has been found that the kerf width may vary along the depth of the workpiece based on the thickness and material. The average kerf width and kerf angle generated

between the jet entrance and exit of AWJ and top and bottom of the spark gap generated by WEDM do not represent the entire kerf profile. In this research, 11 readings were measured and plotted on the graph for each kerf with Depth-to-Thickness Ratio, $d_n = \frac{1}{10}$ of total thickness, D_t as shown in Figure 3.13. Standard deviation, σ_w of the kerf width measurements was calculated to determine the straightness of the kerf profile.

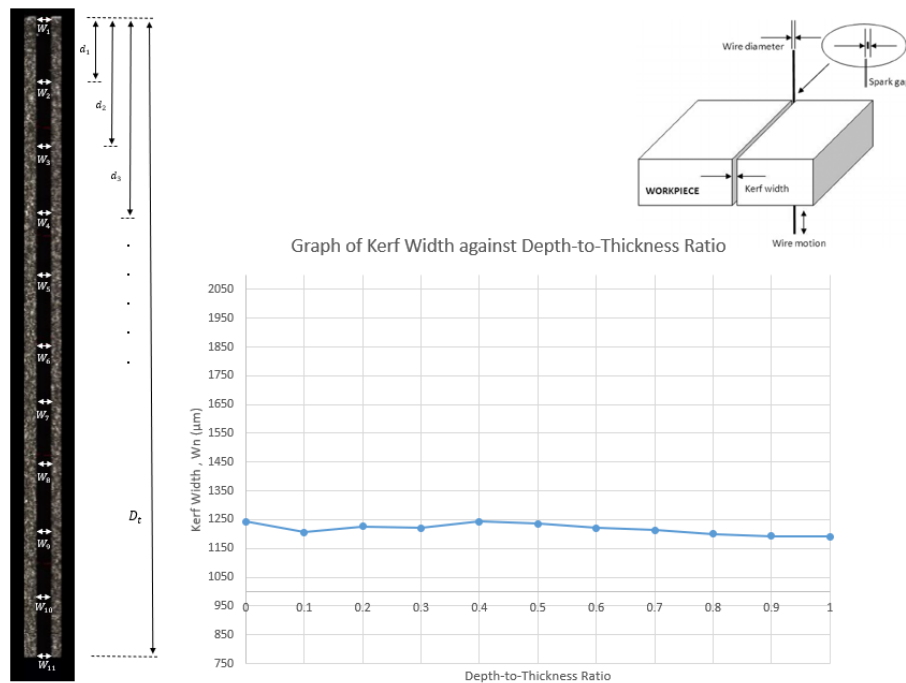


Figure 3.13. Diagram of kerf width measurement and an example of graph of kerf width against Depth-to-Thickness Ratio of WEDM sample.

Kerf taper angle was calculated using equation and illustrated in Figure 3.13.:

$$\theta = \tan^{-1} \frac{(W_t - W_b)}{2t} \text{ ----- Eq. (10)}$$

where W_t is the top kerf width , W_b is the bottom kerf width and t is the thickness of the workpiece.

The Alicona InfiniteFocus G5 focus variation microscope (FVM) based in the Laser Machining Lab (Advanced Machining Group) as shown in Figure 3.12. was used to evaluate the kerf profile. It is a powerful focus variation measuring equipment up to 5-axis measurement. A 10x objective magnification with working distance of 17.5mm and lateral measurement range of 1.62mm in X- and y- direction was selected to scan the 2D microscopic image of the kerf profile.



Figure 3.14: Alicona InfiniteFocus G5 Microscope.

3.1.4.3 Examination of Surface Quality and Integrity

i. 2D and 3D Areal Surface Roughness

After geometrical inspection, the WEDM and AWJ machined samples were cross sectioned $\sim 12\text{mm}$ from the front view / point of entry to analyse the cutting front surface. This was carried out by using WEDM on the Robofil FI 240. The cut samples were initially cleaned in ultrasonic bath tank (James Product Ltd. ULTRA 8050D-H) for 180s and then dried and packed in individual sealable bags with water absorbent to avoid contamination.

Two-dimensional (2D) and Areal (3D) surface topography were measured on two different contact and non-contact equipment: Mitutoyo SJ-310 SurfTest tester and Alicona InfiniteFocus G5 Microscope respectively. There are several techniques employed to measure surface roughness. The 2D surface roughness were parameterized based on ISO1997 and several parameters: R_a , R_q , R_{sk} and R_{ku} were selected. A cut-off length, λ_c of 0.8mm and sampling length, λ_s of $2.5\mu\text{m}$ were utilised with 3 measurements repeated on different evaluated positions and mean values were calculated. Due to the anisotropic surface generated by AWJ, 3 locations are categorised: upper, middle and bottom with 6mm, 12mm and 18mm from the top of the surface in the direction of the jet. The 3D Areal

surfaces are scanned and 3D parameters are measured at top and bottom zones (approx. 7mm × 10mm) for WEDM samples and top, middle and bottom zones (approx. 10mm × 6mm) for AWJ samples. The comparison between the 2D and 3D surface roughness is carried out to study the quantitative relevancy between the topography and machining process parameters.

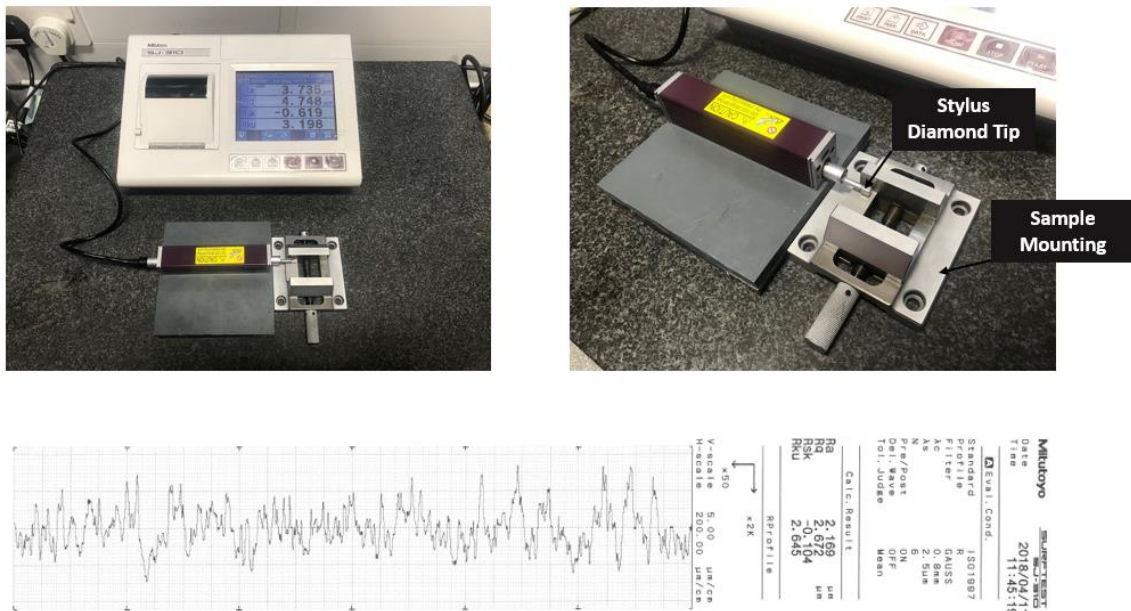


Figure 3.15: Mitutoyo SurfTest SJ-210 surface roughness tester setup.

ii. SEM and Energy Dispersive Spectroscopy (EDS) Analysis

Selected machined work piece samples were characterised by using the JEOL JCM-6000 Plus Neoscope SEM. The SEM is a benchtop base unit connected to a PC, rotary pump and power supply box as shown in Figure

3.16 (a). It can fit a maximum sample size of 70mm diameter X 50mm height and working distance (distance the beam is focused on the sample) of 19 mm. The sample was placed on the carbon specimen block and the height is adjusted to match the observation surface with the holder height (see Figure 3.16 b). There are two modes: Low Vacuum Mode (LV) and High Vacuum Mode (HV). Secondary Electron Image (SEI) in HV mode was selected to reveal fine structure of conductive material and facilitates high magnification observation in the range of $\times 10$ to $\times 60,000$ magnification. Scanning of MMC workpiece typically do not require additional sample preparation prior to examination as the base material is conductive. However, a thin layer of metallic conductive tape was placed in between the workpiece sample and carbon specimen block to increase the electrostatic charge in high vacuum operation to facilitate the charging of low conductive material such as SiC and garnet grit. The sample was placed on the holder and into the vacuum column through an air tight chamber door. The conditions of the imaging were set according to: Accelerating voltage =15 kV, Filament Current = High and Probe Current= High. When an electron beam irradiates the sample surface, the secondary electrons excited from the k-orbitals of the atoms with specific wavelength. The composition of the surface atoms obtained by analysing the detection

of X-ray emitted from the sample. The energy dispersive X-ray (EDS) elemental analysis was carried out to study the grit embedment for AWJ and wire diffusion for WEDM. It supports qualitative/quantitative analysis and mapping (elemental distribution) function. The quantitative maps results show 2-dimensional distribution of the constituent elements, which is useful in identifying additional elements on the surfaces. Some of the elements such as Fe and Ca only occur in the garnet can be considered as a mean to identify the amount of grit embedment on the AWJ machined surfaces. In order to identify the wire diffusion from WEDM, Cu and Zn are used as reference. The chemical composition from EDS analysis was used to evaluate the percentage contribution of wire diffusion and grit embedment at different regions.

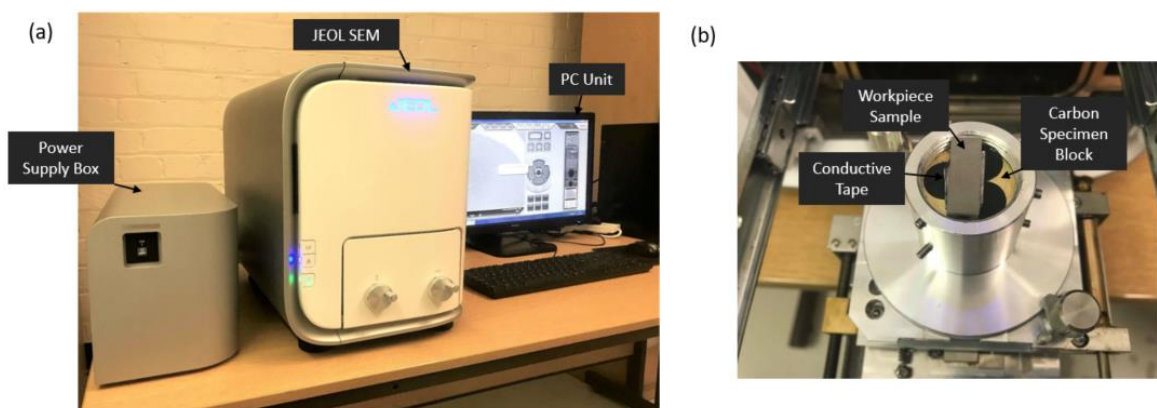


Figure 3.16: Setup of JEOL JCM-6000 Plus Neoscope SEM.

3.1.4.4 Evaluation of Micro-hardness.

i. Sample Preparation (Mounting, Grinding and Polishing)

In order to avoid metallurgical alterations prior to microhardness and microstructure analysis, all of the sectioned AWJ and WEDM machined samples were hot-mounted using Buehler Supliment 2 mounting press as shown in Figure 3.17. Buehler EpoxiCure epoxy resin (phenolic powder) and edge retentive powder were used at conditions of pressure up to $\sim 30 \text{ MPa}$, temperature $\sim 120^\circ\text{C}$ and duration ~ 10 minutes. The mounted samples were then ground and polished according to Buehler's procedure for metal matrix composite using a Buehler Alpha grinder / polisher. The bundle used for aluminium alloy composites includes 3 premium cloths and 3 suspensions. The 3 premium cloths are the UltraPol™ Cloth, TriDent™ Cloth and ChemoMet® Cloth as shown in Table 3.4. The 3 suspensions are the $9\mu\text{m}$ MetaDi® Supreme Diamond Suspension, $3\mu\text{m}$ MetaDi Supreme Diamond Suspension and MasterPrep® Alumina Suspension as shown in Table 3.4 shows the grinding procedure for the mounted samples to remove minimum of $500\mu\text{m}$ material from the workpiece surface until a plane surface with minimal scratches was achieved as follows: SiC paper (400 grit) until plane using 25N load and 240-300rpm (water cooled),

followed by 600 grit, 1200 grit and 2400 grit papers using same load and speed.

The detailed polishing methodology is outlined in Table 3.4. The orientations of the cross-sectioned samples were observed when being placed in the mounting press and a metal engraver was used for marking indentation.

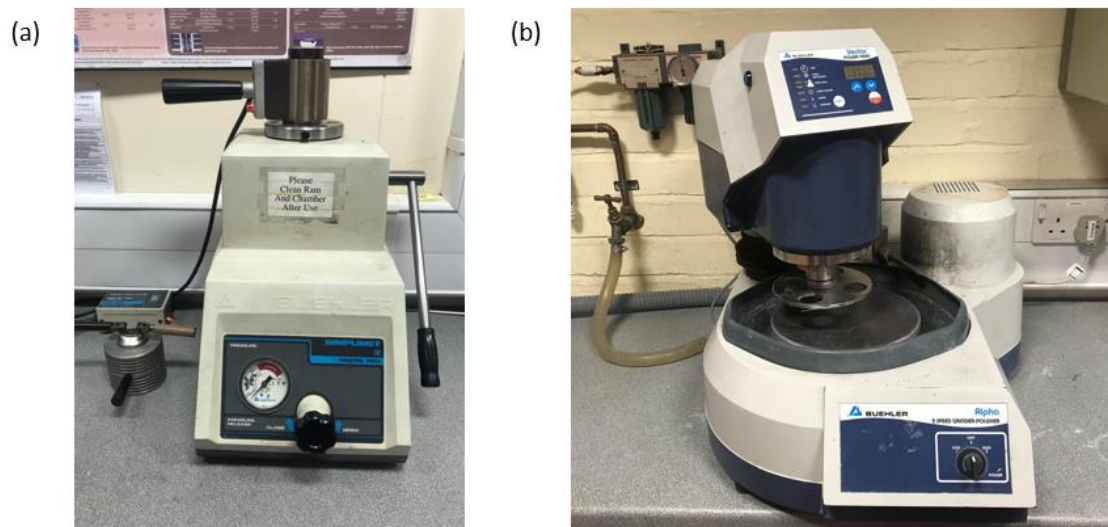


Figure 3.17: (a) Buehler Simpliment 2 mounting press and (b) Buehler Alpha 2 Speed grinder-polisher.

Table 3.4: General polishing procedure guide for metal matrix composite[131].

Material Preparation Procedure Guide: Metal Matrix Composite				
Surface	Abrasive / Size	Load Lb. (N)/ Specimen	Base Speed (rpm)/ Direction	Time (min)
Apex®DGB	30µm diamond	5 (22)	240-300 Contra	Until Plane
UltraPol™ Cloth	9µm MetaDi® Supreme Diamond	5 (22)	150-180 Contra	4:00
TriDent™ Cloth	3µm MetaDi Supreme Diamond Suspension	6(27)	120-150 Comp.	3:00
ChemoMet® Cloth	MasterPrep® Alumina Suspension	6 (27)	120-150 Contra	2:00

The settings of the polishing apparatus and suspension used was established. During the grinding process, water is dispersed onto the platen to prevent scratching and material loss from the sample surfaces. The mounted samples were cleaned with acetone then placed in an ultrasonic bath tank (James Product Ltd. ULTRA 8050D-H) for 180s with deionised

water to remove debris and organic impurities. The samples were then cleaned with isopropanol and dry off to remove acetone residual and contaminants.

ii. Micro-hardness Assessment

The Knoop microhardness (depth profile) test was used to measure the changes in microhardness along the depth below the machined surface.

The measurements were carried out on the Mitutoyo HM-124 with a load range of 0.05-500g as shown in Figure 3.18 (a). A diamond Knoop indenter with a load of 5g and 15s indentation time were selected in this experiment. Figure 3.18 (b) shows the measurement of the Knoop hardness along the depth direction of $10\mu\text{m}$ from the top of the machined surfaces to avoid edge bulging. Knoop hardness with low load of 5g were selected to give indent diagonal lengths of approximately 5 to $10\mu\text{m}$ across the sample in order to avoid the SiC particulates and potential interference of other indentations along the depth. The average diagonal length was used to determine the hardness value as shown in Eq. (11). To ensure repeatability and statistical accuracy, three indentations were taken at depths of 10, 20, 30, 40, 50, 75, 100, 150, 250, 500 and $1000\mu\text{m}$ below the

machined surface. The mean result of each depth was calculated and plotted to describe a profile of the change in microhardness.

$$HK = \frac{P}{C_p L^2} \text{----- Eq. (11)}$$

where L: Length of the long axis indentation,

C_p : Correction factor,

P : Load.

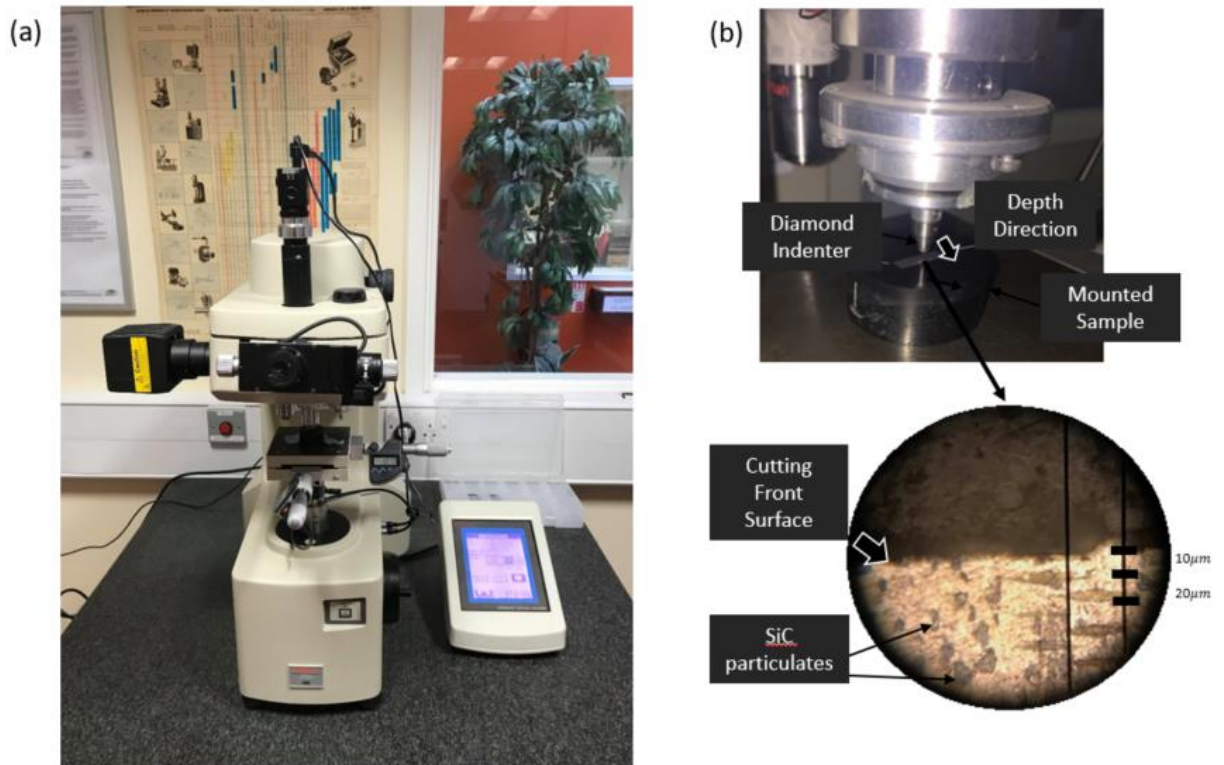


Figure 3.18: (a) Mitutoyo HM-124 apparatus and (b) Knoop hardness indentation procedure.

3.2 Phase Two: Surface Wettability Analysis

The wetting properties of the machined samples were evaluated by measuring the static contact angle (CA) of water on the machined surfaces. Regression analysis between the CA and the output parameters results determined in Phase 1 were carried out. The correlation between the CA and output parameters were determined by the Pareto Chart with confidence level of 95%. Two different sessile drop apparatuses were used and the methodology are outlined in the sections below.

3.2.1 Preliminary Static Contact Angle (CA) Measurement

In order to determine the surface wettability properties of the AWJ and WEDM machined surfaces, a preliminary static contact angle measurement was conducted. The intrinsic contact angle of the MMC samples before machining and selected individual AWJ and WEDM machined samples were measured by employing a JGW-360A measurement system connected to a Nikon optical microscope (see Figure 3.19) with an accuracy of 1° based in Changchun University of Science and Technology (CUST) China, as part of the H2020-RISE-FabSurfWar project. A syringe was filled with 10 μ l of deionised water and mounted above the 3-axis platform holder. 6 μ l of water was dropped on the surface of the specimen manually and the image was frozen to measure the contact angle. The samples were cleaned by

using compressed air to remove debris and no chemical product was used to avoid surface chemistry modification.

The calculation of the wetting CA, $\cos \theta$ is based on drawing a straight line using the software to determine the width, d and drop height, h using the formula:

$$\cos \theta = \frac{(d/2)^2 - h^2}{(d/2)^2 + h^2} \text{-----Eq. (12)}$$

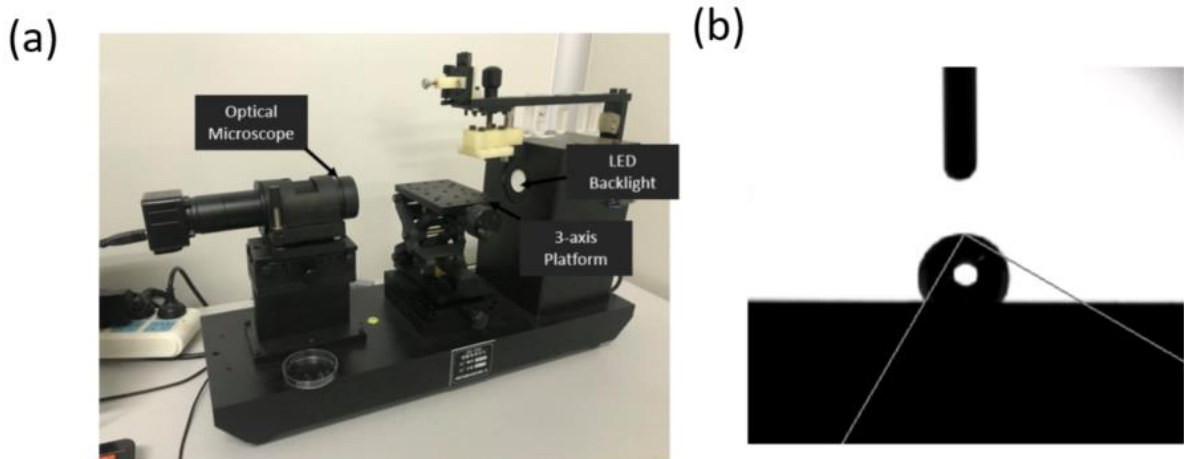


Figure 3.19: (a) JGW-360A measurement system and (b) static CA measuring system.

3.2.2. Static Contact Angle Goniometer

Based on the results achieved in the preliminary investigation, a more in-depth investigation of factors affecting wettability of AWJ and WEDM machined specimens was carried out. The regression analysis with Pareto Chart was performed. The contact angle measuring device, Attension Theta

Optical Goniometer (see Figure 3.20) was used in this experiment based in the SciCity research lab, School of Chemical Engineering. It deployed a video based optical contact angle measuring system, which uses an algorithm to calculate the mean contact angle. A $6 \mu\text{l}$ of Milli-Q water droplets were dispensed on the sample surfaces under atmospheric conditions with the automatic dispenser system. The value of the static contact angle CA was computationally calculated after stabilisation of 5 seconds by analysing droplet images recorded at 10 frames per second (fps).

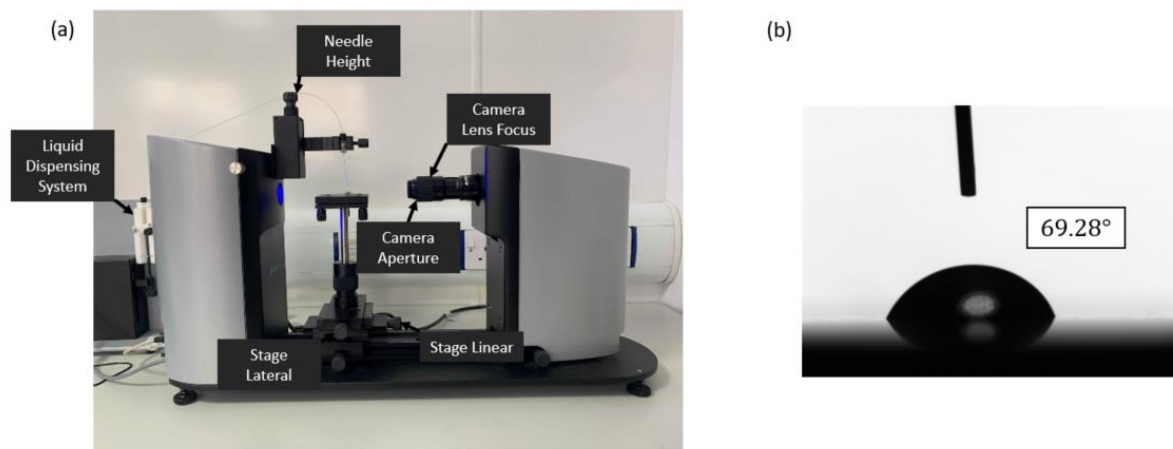


Figure 3.20: (a) Attension Theta Optical Goniometer and (b) automated CA measuring software.

Milli-Q water trademarked by Millipore Corporation by producing ultrapure water of Type 1 (ISO 3696) by using a filtration system (see Figure). It utilises resin filters and deionization process to achieve a purity characterized in terms of 18.2 resistivity at 25 °C [$M\Omega\cdot cm$] and very low total organic carbon of $10\mu g/l$.

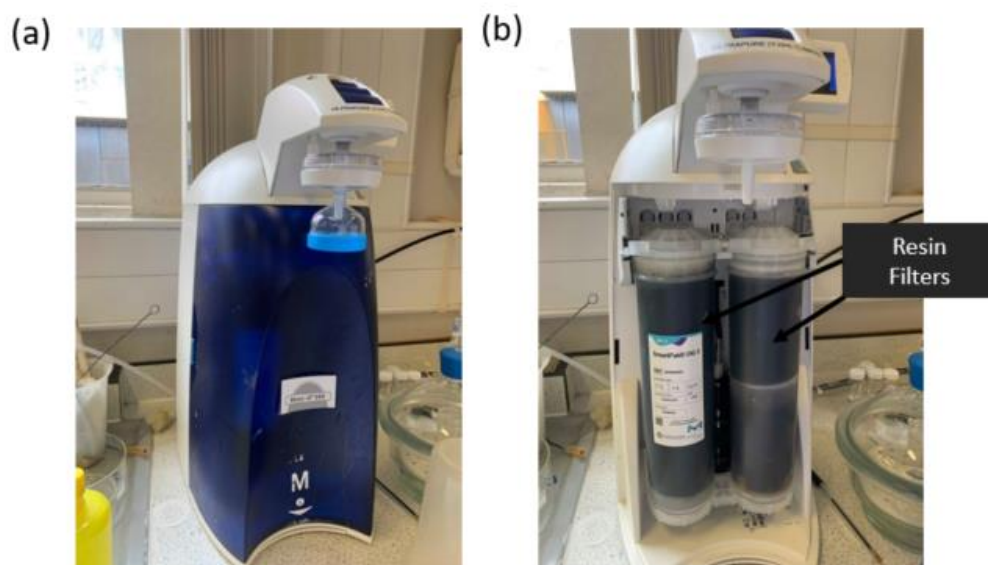


Figure 3.21: The (a) outer and (b) inner view of the Mili-Q water purification system.

Calibration is required every time when it is switched on. A ball on a magnetic circle is placed on the stage exactly under the needle. The zoom ring of the camera and the position of the ball are adjusted until a clear image appears and the software shows the size of the ball is 4.00039. The intrinsic / reference contact angle of the base material is 69.28° , which

indicates that the Al/SiC MMC is hydrophilic due to the high energy of bulk material Al metal.

3.2.3 X-ray Photoelectron Spectroscopy (XPS)

X-ray Photoelectron Spectroscopy is a surface sensitive and quantitative spectroscopic technique to analyse chemical bonds within 10nm depth. The chemical composition of the sample surface and oxygen-containing functional groups were characterized by a multifunctional X-ray photoelectron spectrometer, Kratos Analytical Axis Supra based in the ESPRC National Facility for XPS (Harwell XPS) as shown in Figure 3.22 (a). The equipment operates under a power of 150W with at a pressure in the UHV region (between 10^{-8} and 10^{-9} *mbar*). It works at minimum beam spot diameter of 15 μ m with X-ray excitation source of Al K α monochromatic radiation. The binding energies are calibrated using C1s peak with a reference of 284.8eV. The samples were cleaned with compressed air and mounted on conductive copper sticking tape (see Figure 3.22 c). Due to the elimination of inorganic oxygen, the contact angle is only influenced by oxygen-containing polar group (C-OH, COO), which are the indicator on wettability. Narrow scan of carbon was acquired and the XPS Spectrogram at 1s is split and the survey spectra recorded with a step size of 0.1 eV were quantified with CasaXPS software.

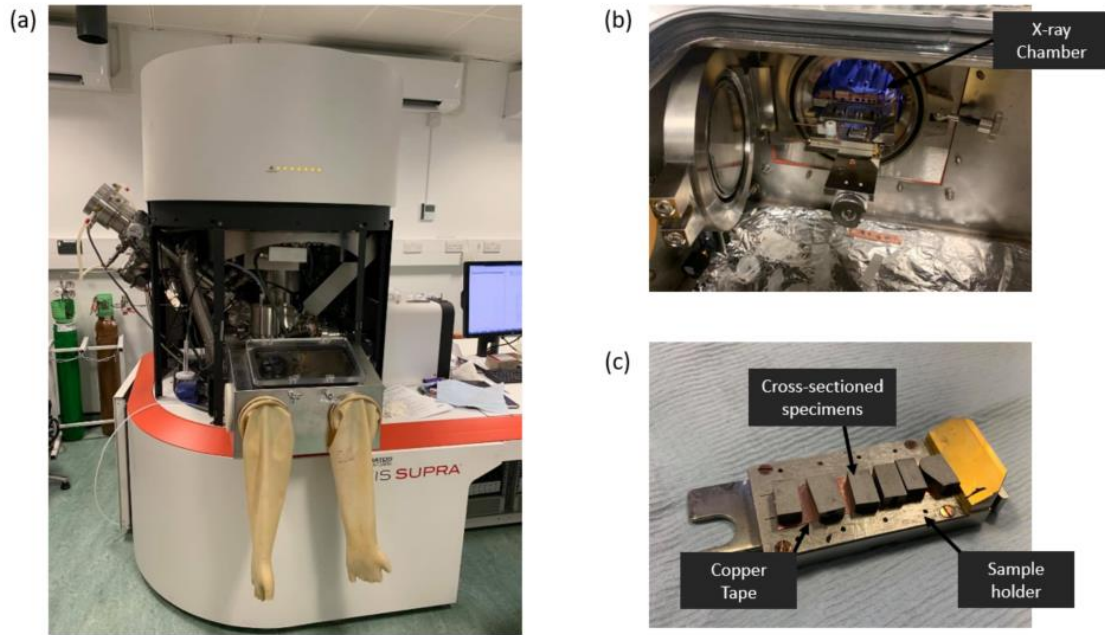


Figure 3.22: The (a) Kratos Axis Supra, (b) X-ray chamber and (c) sample mounting / ex-situ preparation.

3.3 Phase Three: Case Study - Hybrid Machining Strategy

Phase three of this research explore the feasibility of a proposed hybrid machining method of combining abrasive waterjet and wire electrical discharge machining; this has not been reported by any researchers. The optimisation of process parameters and factors influencing the wettability of MMC have been explored in the previous chapter. WEDM generates a homogeneous and good surface finish but low MRR; whereas AWJ has high MMR but processes low surface integrity due to generation of striation marks. As discussed in the previous chapter, surface roughness S_a is the dominant factor in influencing the surface hydrophobicity. High material

removal rate is desirable in the manufacture of key components, required for time saving. The strategy proposed in this chapter is to generate a hydrophobic surface by conducting rough cutting using AWJ and two passes / primary and secondary polishing using WEDM to develop micro-scale features exhibiting metallic hydrophobic surfaces.

In this experiment, the rough cutting of MMC was conducted using the optimum parameters for MRR in AWJ and optimum parameters for SA in EDM were utilised for finishing process as summarised in Table 3.5.

Table 3.5: Step by step hybrid machining strategy.

Step	Application Process	Parameters
1	Rough Cutting (AWJ)	V_f 50 mm/min ; P 50 kpsi; V_a 0.402 kg/min; SOD 5mm
2 and 3	Primary / Secondary Polishing (WEDM)	A 0.1 μ s; AJ 15 V; I_{AL} 30 A; V 120V; FF 10 %

A critical analysis of the proposed hybrid machining method will be explored. The post analysis of surface topography of different stages of the machined surfaces will be explored.

CHAPTER 4: RESULTS

4.1 Preliminary Trials in Wire Selection in WEDM

The investigations were performed in order to evaluate the optimum wire for the following process parameters optimisation. A total of three 12mm cuts into the workpiece were carried out for each wires outlined in Section 3.2.2: Charmiles CuZn36, Bedra Broncocut and Bedra Topaz Plus. The machining parameters of the WEDM was fixed: Current (10A), Gap Voltage (30V) and Spark on time ($0.1\mu s$). The weight of the workpiece and machining time were measured. The mean MRR, kerf width and mean arithmetic surface roughness Ra were recorded and presented in Table 4.1 for the analysis. The results obtained shows that a significant trend that the Topaz Plus wire comprising a high tensile strength core and coating has the highest MRR, kerf width and Ra. This significant increase attributed to higher tensile strength of the wire induces more heat, more material is removed with higher machining rate. This is due to that zinc has a lower melting point than copper which prevents heat to enter the zinc coated brass wire and break.

Table 4.1: Results analysis of MRR, mean kerf width and Ra of three types of wires.

Wire	MRR(mm^3/min)	Mean Kerf Width (μm)	Ra (μm)
Charmilles	49.58	364	2.75
Broncocut	51.84	368	3.07
Topaz Plus	68.52	378	3.16

The kerf width of the slot after machining is generally larger than the diameter of the wire electrode due to the spark gap generated. A slight increase in the kerf width generated by Bedra Topaz Plus. Comparatively, Charmilles CuZn37 generated best surface quality in terms of Ra considering the low discharge energy level. The higher the discharge energy level, more material was removed and larger craters were formed, which results in higher surface roughness.

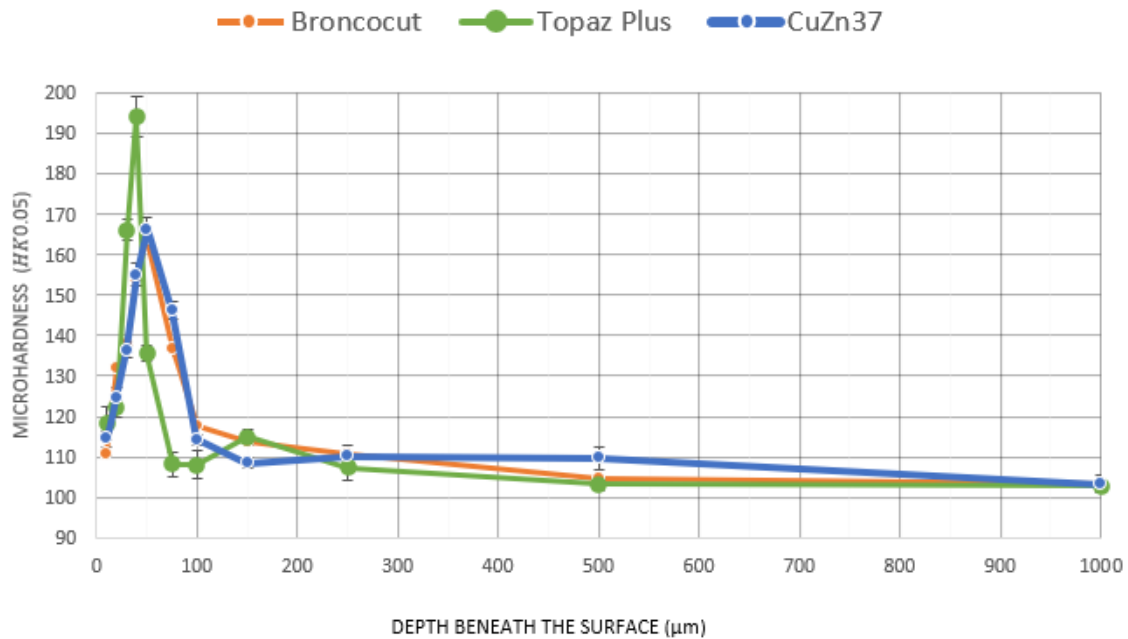


Figure 4.1: Knoop microhardness profile generated by three different wires.

The microhardness profile in Figure 4.1 shows that there is an increase of microhardness on the surface of the MMC up to a depth of $50\mu m$ below the machined surface. The microhardness analysis shows that the microhardness decreases to its bulk microhardness of $110 HK_{0.05}$. The intense heating of the material and rapid cooling by the dielectric fluid form a recast layer on the machined surface, which results in the increase of the microhardness. For Topaz plus wire, the highest peak of microhardness was obtained $194.1 HK_{0.05}$ whereas the microhardness obtained from the Broncocut and CuZn37 are similar, 164.4 and $166.3 HK_{0.05}$ respectively. In general, the selection of wire electrode for further experimental work was

based on the results obtained and literature research. Although Topaz Plus has the highest MRR, the surface integrity generated is not ideal. In this case, Broncocut wire was selected due to its optimal results and more cost effective compared to Topaz Plus.

4.2 Phase One: Influence of Process Parameters in AWJ

4.2.1 Material Removal Rate

The experimental results as shown in Table 4.2 are analysed using Taguchi method. The signal-to-noise ratio was calculated using larger-the-better criterion. The main effect plots of S/N ratio and optimum setting of AWJ process parameters obtained for MRR are shown in Figure 4.2. The maximum value of the S/N ratio determine the optimal performance for MRR can be obtained at traverse speed, V_f 50 mm/min (level 6), Pressure, P 50 kpsi (level 3), abrasive mass flow rate, V_a 0.402 kg/min (level 3) and stand-off distance, SOD 5mm (level 3). Hence, the optimal combination of these process parameters for MRR is $A_6B_3C_3D_3$. The mean value of MRR at each level of the process parameters is shown in Figure 4.3. It can be seen from that the trend of effect of the process parameters on MRR is constant.

Table 4.2 : Results of data obtained from MRR of AWJ.

Trial No.	Vf <i>mm/min</i>	P <i>kpsi</i>	Va <i>kg/min</i>	SOD <i>mm</i>	Mass (m_1) <i>g</i>	Mass (m_2) <i>g</i>	Machining Time <i>s</i>	MRR mm^3 <i>/min</i>
1	5	30	0.158	1	938.38	936.76	240	142.05
2	5	40	0.340	3	945.19	943.10	240	183.27
3	5	50	0.402	5	950.75	945.13	240	492.80
4	10	30	0.158	3	936.76	935.16	120	280.60
5	10	40	0.340	5	943.10	941.10	120	350.75
6	10	50	0.402	1	952.69	950.75	120	340.22
7	20	30	0.340	1	935.16	933.81	60	473.51
8	20	40	0.402	3	955.80	954.03	60	620.82
9	20	50	0.158	5	932.40	930.80	60	561.19
10	30	30	0.402	5	957.33	955.80	40	804.96
11	30	40	0.158	1	941.10	939.77	40	699.74
12	30	50	0.340	3	948.13	946.60	40	804.96
13	40	30	0.340	5	933.81	932.40	30	989.11
14	40	40	0.402	1	954.03	952.69	30	940.00
15	40	50	0.158	3	938.38	936.76	30	1136.42
16	50	30	0.402	3	958.89	957.33	24	1367.91
17	50	40	0.158	5	939.77	938.38	24	1218.85
18	50	50	0.340	1	946.60	945.19	24	1236.38

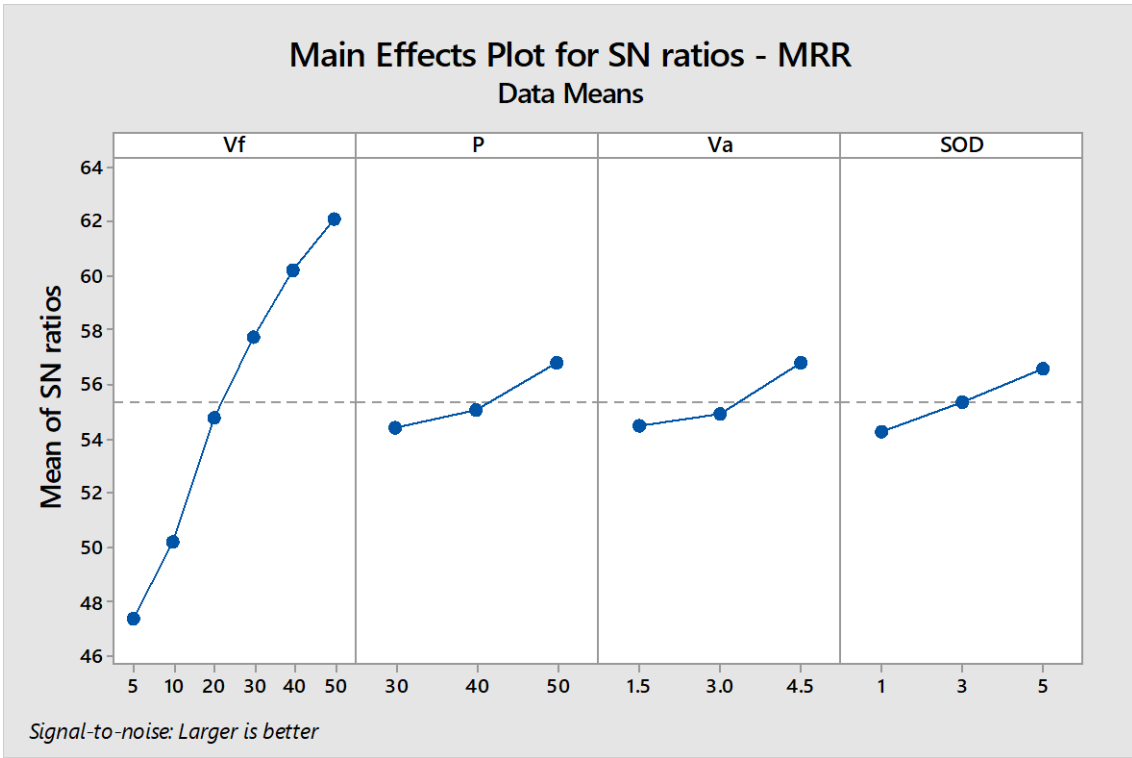


Figure 4.2: Main effect plot of S/N for AWJ MRR.

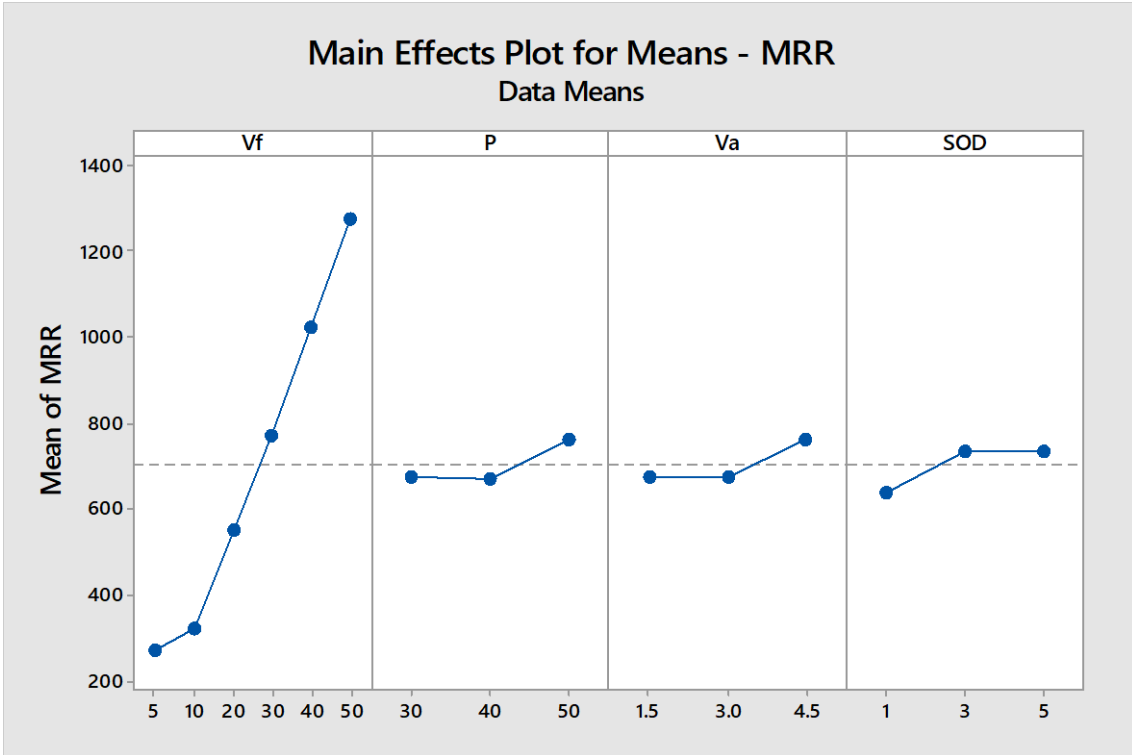


Figure 4.3: Main effect plot of Means for AWJ MRR.

The ANOVA was performed at a confidence level of 95% and the result in S/N ratio of MRR is give in Table 4.3. It is observed that the p value of the traverse speed, V_f is less than 0.05. This indicates that the traverse speed is the most significant factor in affecting the MRR of AWJ. The traverse speed increases, the nozzle moves faster penetrating the workpiece, hence, the machining time reduces. The higher the jet pressure increases the energy of the abrasive particles and the larger amount of abrasive particles contributed towards more efficient cutting and reducing the localized effects of higher feed rate.

Table 4.3: ANOVA analysis of AWJ MRR.

Factor Symbol	DOF	SS	MS	F-value	P-value	Contribution (%)
V_f <i>mm/min</i>	5	2353078	470616	96.90	0.000	94.81
P <i>kpsi</i>	2	32113	16056	3.31	0.108	1.29
V_a <i>kg/min</i>	2	31013	15506	3.19	0.114	1.25
SOD <i>mm</i>	2	36644	18322	3.77	0.087	1.48
Error	6	29171	4857			1.17
Total	17	2481988				100

Confirmation test was carried out to verify the results. Table 4.4 details the predicted and experimental values of mean and S/N ratio for the optimum parameters. The percentage of error between the S/N ratio obtained for the

predicted and experimental mean MRR is 3.45%, which is smaller than 5%. It shows that the values obtained for the performance parameters are within 95% confidence interval range, it confirms the accuracy of Taguchi DoE.

Table 4.4: Confirmation test results for AWJ MRR.

Response	Mean		S/N ratio (dB)		Error %
	Predicted	Experiment	Predicted	Experiment	
MRR	1426.51	1543.29	66.05	63.77	3.45

4.2.2 Kerf Profile Geometry

It is important to understand the characteristics of the kerf profile geometry as it affects the accuracy and tolerance in machining parts. The variance between the top and bottom kerf width do not follow a trend. In order to evaluate the straightness of the kerf profile quantitatively, 11 readings based on the depth-to-thickness ratio were measured and plotted (see Table 4.5) as the kerf profile may not be symmetrical due to jet tail back effect. All the trails were cut with full penetration over a length of 30mm.

From the graph in Figure 4.4, trial 1 has the straightest kerf with a mean kerf width of 1215 μm and SD of 15.27. The mean kerf width of trial 17 is considered closest to the diameter of the nozzle: 1mm, 1003.25 μm and SD

of 137.19. The high value of SD shows that the kerf width along the thickness is not consistent and large variation, hence it is important to observe the entire kerf geometry profile rather than the top and bottom kerf width only, which are used by most researches to represent the kerf width. It is observed that first reading on the top of the kerf inconsistent large deviation initial damage zone (IDZ) further analysed and discussed in Section 4.2.3. All of the trials exhibited convergent tapes as the water jet loses kinetic energy penetrating the workpiece. The centre of the water jet is a higher energy zone which shows a convergent profile, while the outer part of the jet is lower energy zone which display a divergent profile.

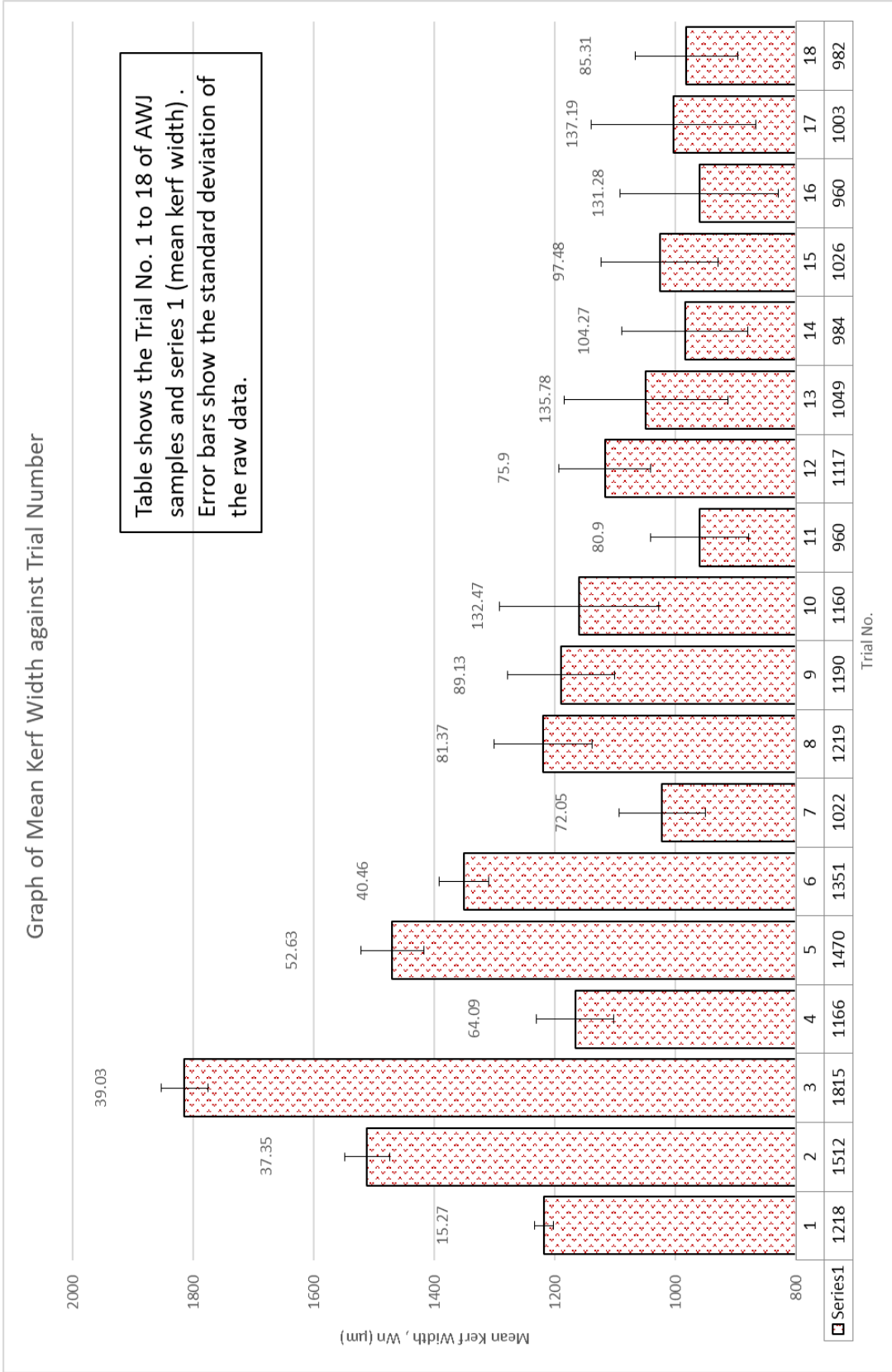
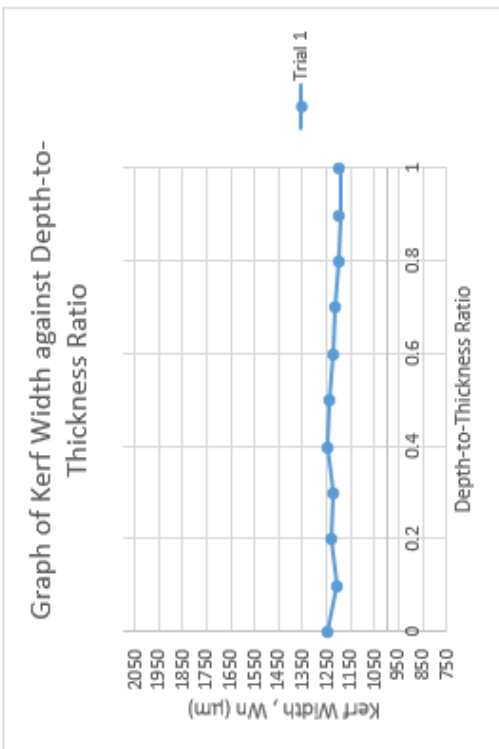
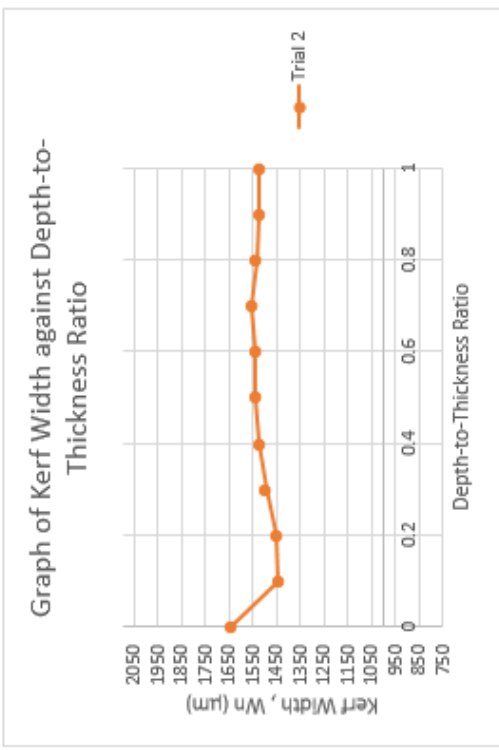
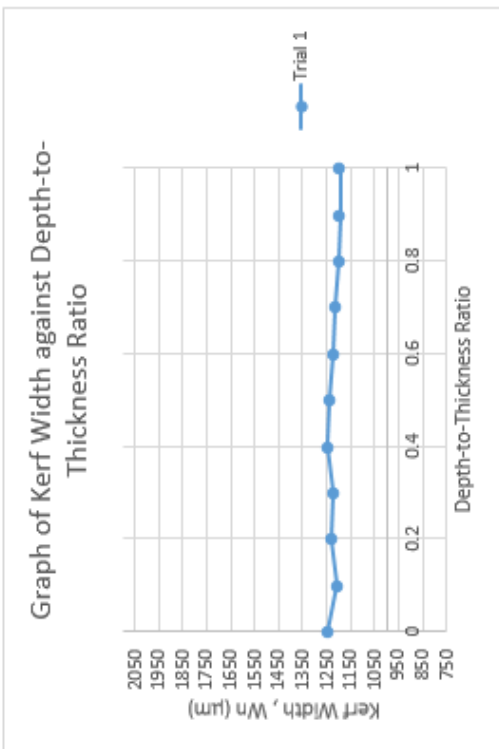
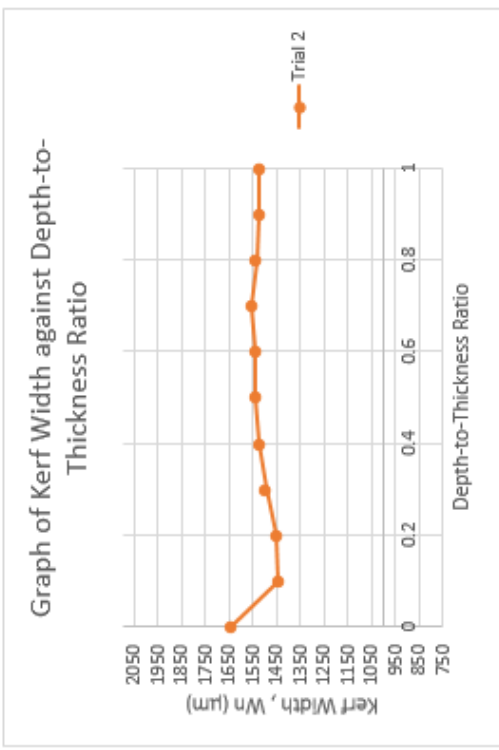

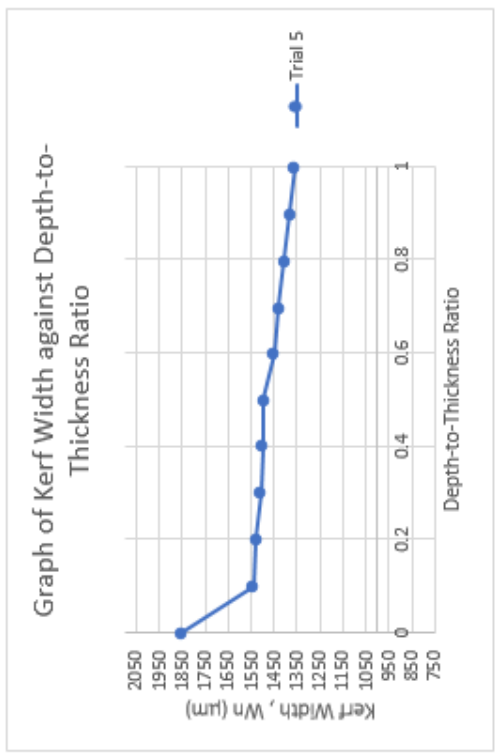

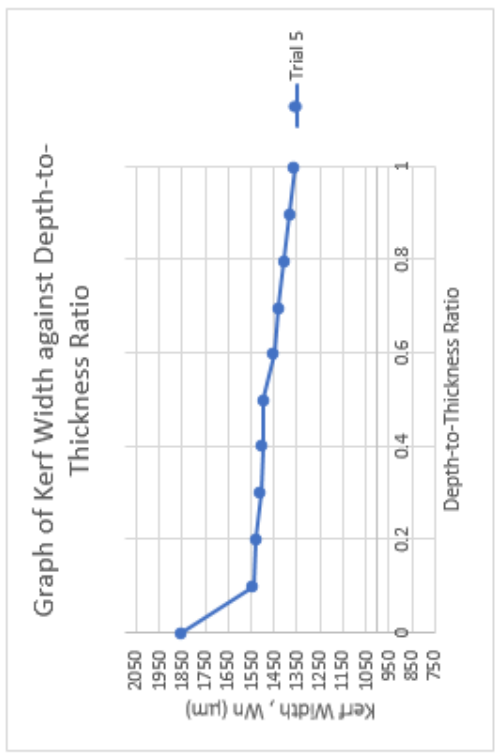

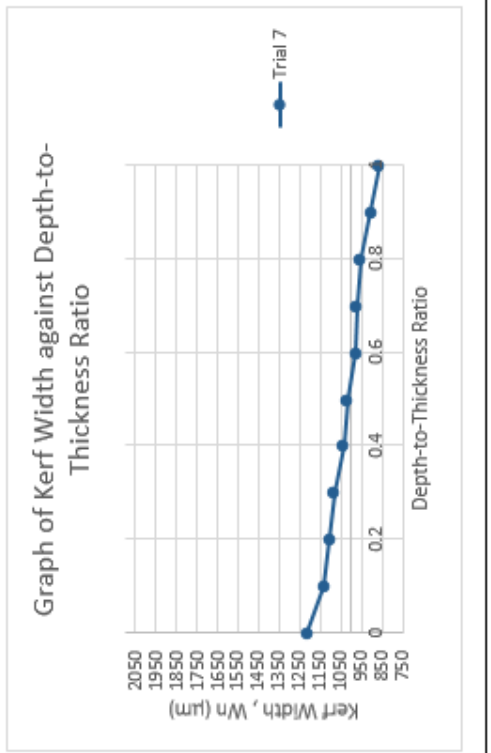

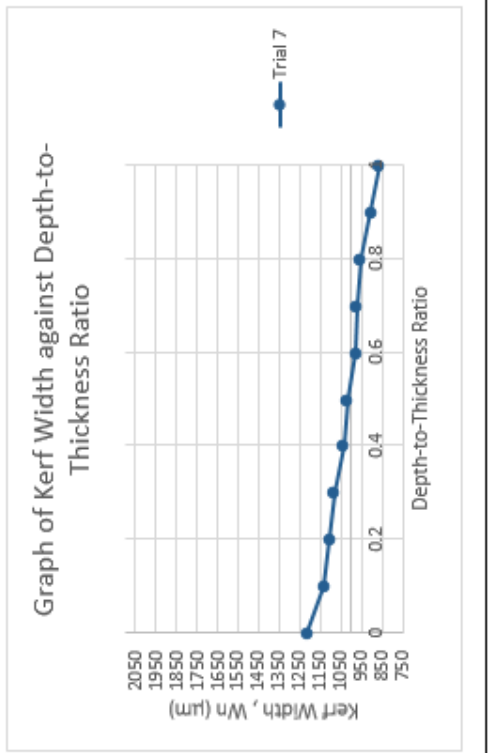


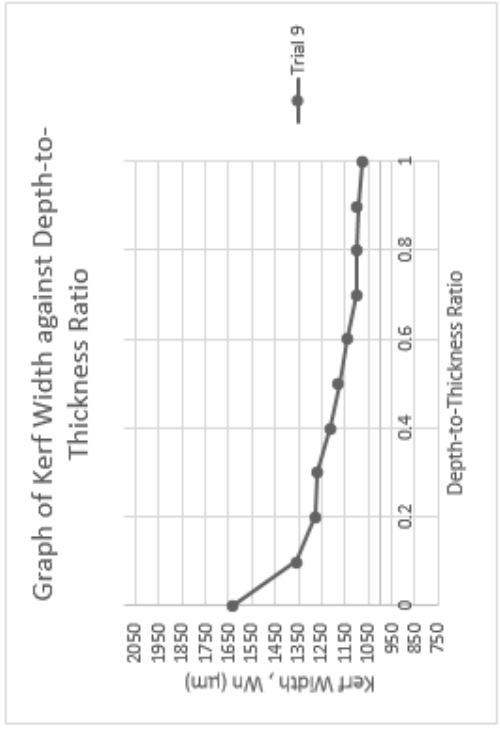
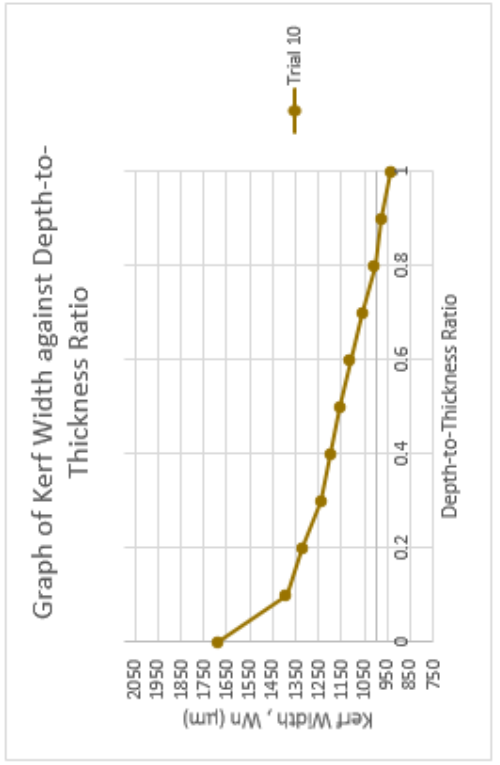


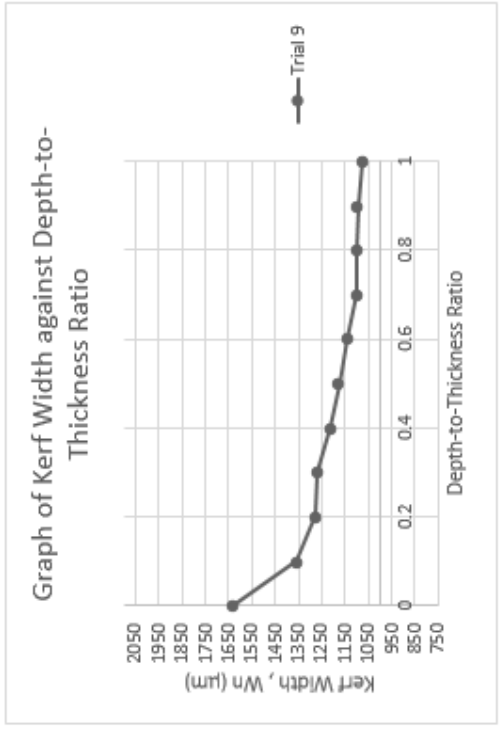
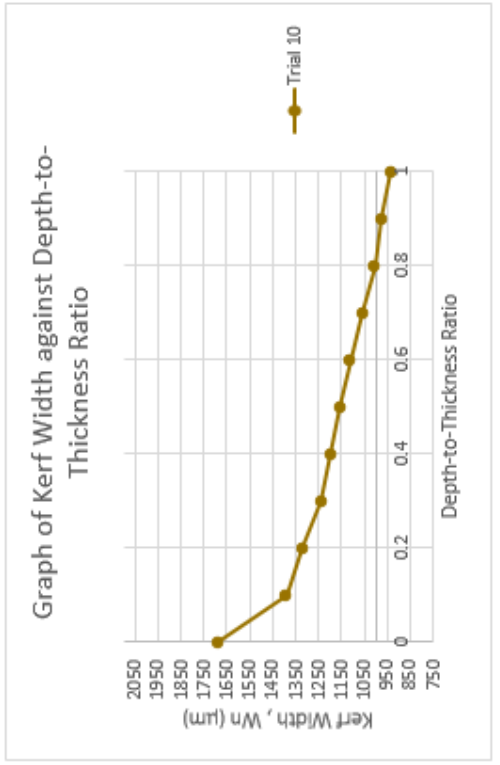


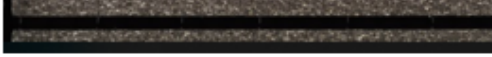


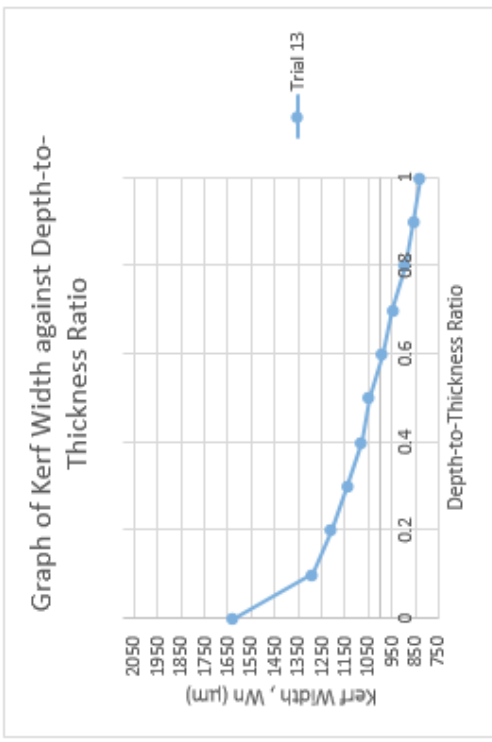
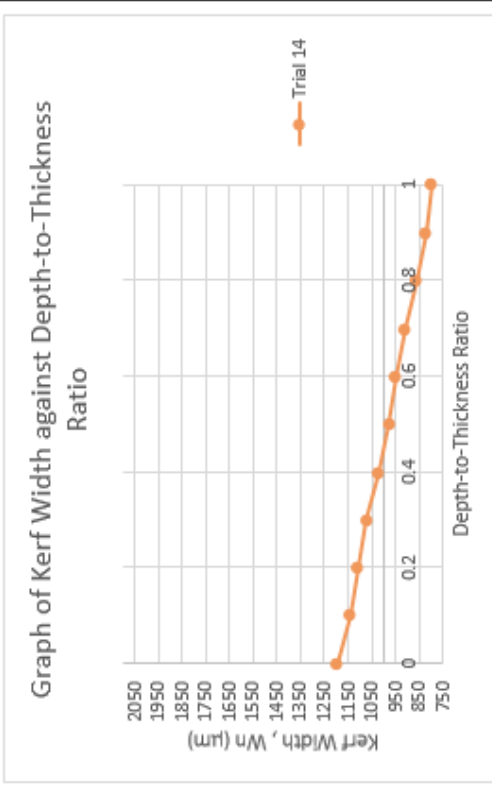
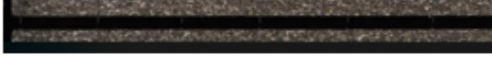


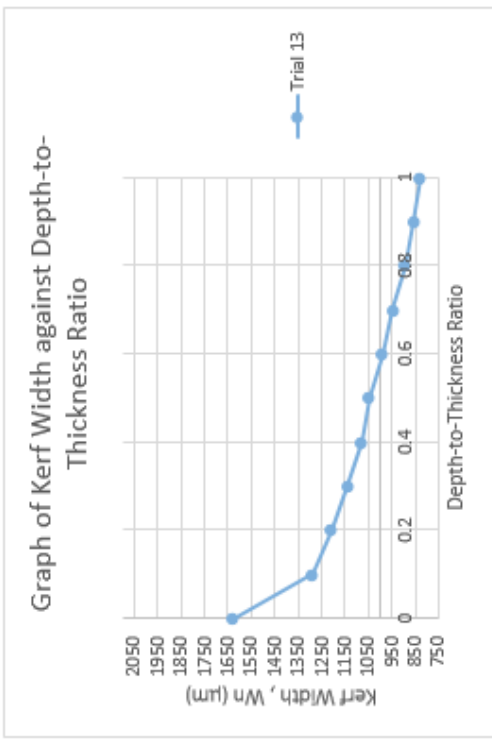
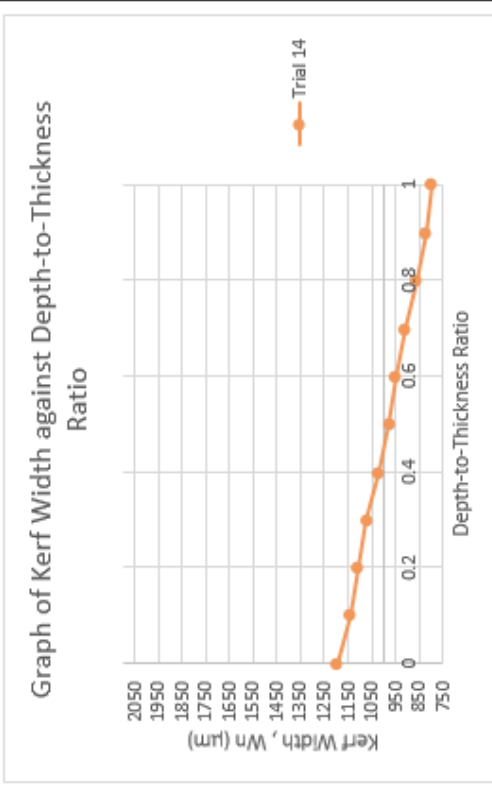
Figure 4.4: The Graph of Mean Kerf Width against Trial No. for AWJ Trial 1 to 18.


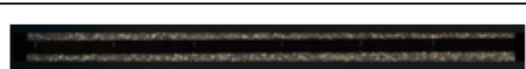
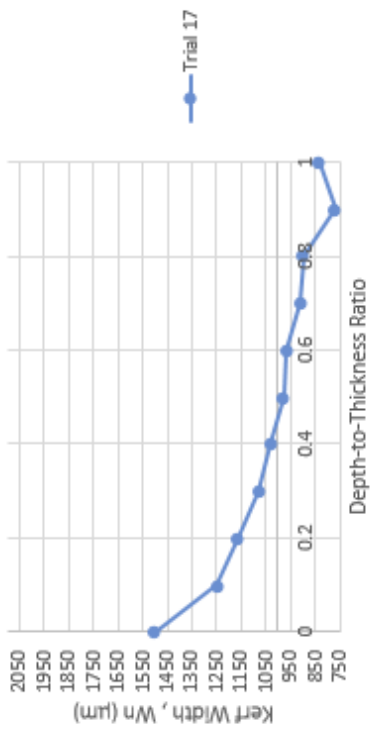
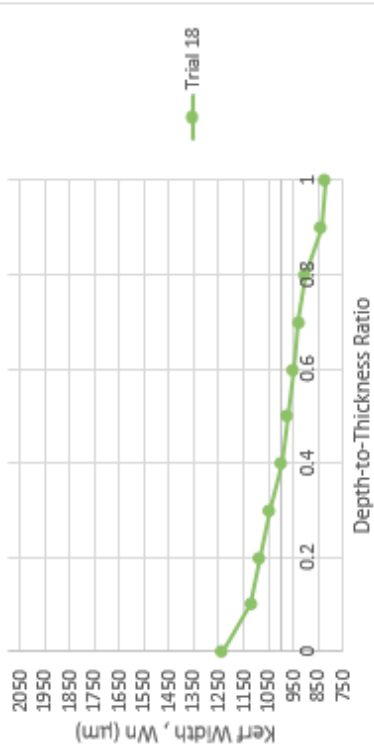
Table 4.5: Graph of Kerf width against Depth-to-thickness Ratio of AWJ.

Trial 1		Trial 2	
Trial 3		Trial 4	

<p>Trial 5</p> 	<p>Trial 5</p> 
<p>Trial 6</p> 	<p>Trial 6</p> 
<p>Trial 7</p> 	<p>Trial 7</p> 
<p>Trial 8</p> 	<p>Trial 8</p> 

Trial 9		Trial 10																																															
<p>Graph of Kerf Width against Depth-to-Thickness Ratio</p>  <table border="1"> <caption>Data for Trial 9</caption> <thead> <tr> <th>Depth-to-Thickness Ratio</th> <th>Kerf Width, Wn (µm)</th> </tr> </thead> <tbody> <tr><td>0.0</td><td>1650</td></tr> <tr><td>0.1</td><td>1450</td></tr> <tr><td>0.2</td><td>1250</td></tr> <tr><td>0.3</td><td>1150</td></tr> <tr><td>0.4</td><td>1050</td></tr> <tr><td>0.5</td><td>1000</td></tr> <tr><td>0.6</td><td>950</td></tr> <tr><td>0.7</td><td>900</td></tr> <tr><td>0.8</td><td>850</td></tr> <tr><td>0.9</td><td>800</td></tr> <tr><td>1.0</td><td>750</td></tr> </tbody> </table>	Depth-to-Thickness Ratio	Kerf Width, Wn (µm)	0.0	1650	0.1	1450	0.2	1250	0.3	1150	0.4	1050	0.5	1000	0.6	950	0.7	900	0.8	850	0.9	800	1.0	750	<p>Graph of Kerf Width against Depth-to-Thickness Ratio</p>  <table border="1"> <caption>Data for Trial 10</caption> <thead> <tr> <th>Depth-to-Thickness Ratio</th> <th>Kerf Width, Wn (µm)</th> </tr> </thead> <tbody> <tr><td>0.0</td><td>1650</td></tr> <tr><td>0.1</td><td>1450</td></tr> <tr><td>0.2</td><td>1250</td></tr> <tr><td>0.3</td><td>1150</td></tr> <tr><td>0.4</td><td>1050</td></tr> <tr><td>0.5</td><td>1000</td></tr> <tr><td>0.6</td><td>950</td></tr> <tr><td>0.7</td><td>900</td></tr> <tr><td>0.8</td><td>850</td></tr> <tr><td>0.9</td><td>800</td></tr> <tr><td>1.0</td><td>750</td></tr> </tbody> </table>	Depth-to-Thickness Ratio	Kerf Width, Wn (µm)	0.0	1650	0.1	1450	0.2	1250	0.3	1150	0.4	1050	0.5	1000	0.6	950	0.7	900	0.8	850	0.9	800	1.0	750
Depth-to-Thickness Ratio	Kerf Width, Wn (µm)																																																
0.0	1650																																																
0.1	1450																																																
0.2	1250																																																
0.3	1150																																																
0.4	1050																																																
0.5	1000																																																
0.6	950																																																
0.7	900																																																
0.8	850																																																
0.9	800																																																
1.0	750																																																
Depth-to-Thickness Ratio	Kerf Width, Wn (µm)																																																
0.0	1650																																																
0.1	1450																																																
0.2	1250																																																
0.3	1150																																																
0.4	1050																																																
0.5	1000																																																
0.6	950																																																
0.7	900																																																
0.8	850																																																
0.9	800																																																
1.0	750																																																
Trial 11		Trial 12																																															
<p>Graph of Kerf Width against Depth-to-Thickness Ratio</p>  <table border="1"> <caption>Data for Trial 11</caption> <thead> <tr> <th>Depth-to-Thickness Ratio</th> <th>Kerf Width, Wn (µm)</th> </tr> </thead> <tbody> <tr><td>0.0</td><td>1650</td></tr> <tr><td>0.1</td><td>1450</td></tr> <tr><td>0.2</td><td>1250</td></tr> <tr><td>0.3</td><td>1150</td></tr> <tr><td>0.4</td><td>1050</td></tr> <tr><td>0.5</td><td>1000</td></tr> <tr><td>0.6</td><td>950</td></tr> <tr><td>0.7</td><td>900</td></tr> <tr><td>0.8</td><td>850</td></tr> <tr><td>0.9</td><td>800</td></tr> <tr><td>1.0</td><td>750</td></tr> </tbody> </table>	Depth-to-Thickness Ratio	Kerf Width, Wn (µm)	0.0	1650	0.1	1450	0.2	1250	0.3	1150	0.4	1050	0.5	1000	0.6	950	0.7	900	0.8	850	0.9	800	1.0	750	<p>Graph of Kerf Width against Depth-to-Thickness Ratio</p>  <table border="1"> <caption>Data for Trial 12</caption> <thead> <tr> <th>Depth-to-Thickness Ratio</th> <th>Kerf Width, Wn (µm)</th> </tr> </thead> <tbody> <tr><td>0.0</td><td>1650</td></tr> <tr><td>0.1</td><td>1450</td></tr> <tr><td>0.2</td><td>1250</td></tr> <tr><td>0.3</td><td>1150</td></tr> <tr><td>0.4</td><td>1050</td></tr> <tr><td>0.5</td><td>1000</td></tr> <tr><td>0.6</td><td>950</td></tr> <tr><td>0.7</td><td>900</td></tr> <tr><td>0.8</td><td>850</td></tr> <tr><td>0.9</td><td>800</td></tr> <tr><td>1.0</td><td>750</td></tr> </tbody> </table>	Depth-to-Thickness Ratio	Kerf Width, Wn (µm)	0.0	1650	0.1	1450	0.2	1250	0.3	1150	0.4	1050	0.5	1000	0.6	950	0.7	900	0.8	850	0.9	800	1.0	750
Depth-to-Thickness Ratio	Kerf Width, Wn (µm)																																																
0.0	1650																																																
0.1	1450																																																
0.2	1250																																																
0.3	1150																																																
0.4	1050																																																
0.5	1000																																																
0.6	950																																																
0.7	900																																																
0.8	850																																																
0.9	800																																																
1.0	750																																																
Depth-to-Thickness Ratio	Kerf Width, Wn (µm)																																																
0.0	1650																																																
0.1	1450																																																
0.2	1250																																																
0.3	1150																																																
0.4	1050																																																
0.5	1000																																																
0.6	950																																																
0.7	900																																																
0.8	850																																																
0.9	800																																																
1.0	750																																																

Trial 13		Trial 14																																																	
	<p>Graph of Kerf Width against Depth-to-Thickness Ratio</p>  <table border="1"> <caption>Data for Trial 13</caption> <thead> <tr> <th>Depth-to-Thickness Ratio</th> <th>Kerf Width, Wn (μm)</th> </tr> </thead> <tbody> <tr><td>0.0</td><td>1650</td></tr> <tr><td>0.1</td><td>1350</td></tr> <tr><td>0.2</td><td>1250</td></tr> <tr><td>0.3</td><td>1150</td></tr> <tr><td>0.4</td><td>1050</td></tr> <tr><td>0.5</td><td>950</td></tr> <tr><td>0.6</td><td>850</td></tr> <tr><td>0.7</td><td>750</td></tr> <tr><td>0.8</td><td>750</td></tr> <tr><td>0.9</td><td>750</td></tr> <tr><td>1.0</td><td>750</td></tr> </tbody> </table>	Depth-to-Thickness Ratio	Kerf Width, Wn (μm)	0.0	1650	0.1	1350	0.2	1250	0.3	1150	0.4	1050	0.5	950	0.6	850	0.7	750	0.8	750	0.9	750	1.0	750	Trial 14	<p>Graph of Kerf Width against Depth-to-Thickness Ratio</p>  <table border="1"> <caption>Data for Trial 14</caption> <thead> <tr> <th>Depth-to-Thickness Ratio</th> <th>Kerf Width, Wn (μm)</th> </tr> </thead> <tbody> <tr><td>0.0</td><td>1250</td></tr> <tr><td>0.1</td><td>1150</td></tr> <tr><td>0.2</td><td>1050</td></tr> <tr><td>0.3</td><td>950</td></tr> <tr><td>0.4</td><td>850</td></tr> <tr><td>0.5</td><td>750</td></tr> <tr><td>0.6</td><td>750</td></tr> <tr><td>0.7</td><td>750</td></tr> <tr><td>0.8</td><td>750</td></tr> <tr><td>0.9</td><td>750</td></tr> <tr><td>1.0</td><td>750</td></tr> </tbody> </table>	Depth-to-Thickness Ratio	Kerf Width, Wn (μm)	0.0	1250	0.1	1150	0.2	1050	0.3	950	0.4	850	0.5	750	0.6	750	0.7	750	0.8	750	0.9	750	1.0	750
Depth-to-Thickness Ratio	Kerf Width, Wn (μm)																																																		
0.0	1650																																																		
0.1	1350																																																		
0.2	1250																																																		
0.3	1150																																																		
0.4	1050																																																		
0.5	950																																																		
0.6	850																																																		
0.7	750																																																		
0.8	750																																																		
0.9	750																																																		
1.0	750																																																		
Depth-to-Thickness Ratio	Kerf Width, Wn (μm)																																																		
0.0	1250																																																		
0.1	1150																																																		
0.2	1050																																																		
0.3	950																																																		
0.4	850																																																		
0.5	750																																																		
0.6	750																																																		
0.7	750																																																		
0.8	750																																																		
0.9	750																																																		
1.0	750																																																		
Trial 15		Trial 16																																																	
	<p>Graph of Kerf Width against Depth-to-Thickness Ratio</p>  <table border="1"> <caption>Data for Trial 15</caption> <thead> <tr> <th>Depth-to-Thickness Ratio</th> <th>Kerf Width, Wn (μm)</th> </tr> </thead> <tbody> <tr><td>0.0</td><td>1450</td></tr> <tr><td>0.1</td><td>1350</td></tr> <tr><td>0.2</td><td>1250</td></tr> <tr><td>0.3</td><td>1150</td></tr> <tr><td>0.4</td><td>1050</td></tr> <tr><td>0.5</td><td>950</td></tr> <tr><td>0.6</td><td>850</td></tr> <tr><td>0.7</td><td>750</td></tr> <tr><td>0.8</td><td>750</td></tr> <tr><td>0.9</td><td>750</td></tr> <tr><td>1.0</td><td>750</td></tr> </tbody> </table>	Depth-to-Thickness Ratio	Kerf Width, Wn (μm)	0.0	1450	0.1	1350	0.2	1250	0.3	1150	0.4	1050	0.5	950	0.6	850	0.7	750	0.8	750	0.9	750	1.0	750	Trial 16	<p>Graph of Kerf Width against Depth-to-Thickness Ratio</p>  <table border="1"> <caption>Data for Trial 16</caption> <thead> <tr> <th>Depth-to-Thickness Ratio</th> <th>Kerf Width, Wn (μm)</th> </tr> </thead> <tbody> <tr><td>0.0</td><td>1450</td></tr> <tr><td>0.1</td><td>1350</td></tr> <tr><td>0.2</td><td>1250</td></tr> <tr><td>0.3</td><td>1150</td></tr> <tr><td>0.4</td><td>1050</td></tr> <tr><td>0.5</td><td>950</td></tr> <tr><td>0.6</td><td>850</td></tr> <tr><td>0.7</td><td>750</td></tr> <tr><td>0.8</td><td>750</td></tr> <tr><td>0.9</td><td>750</td></tr> <tr><td>1.0</td><td>750</td></tr> </tbody> </table>	Depth-to-Thickness Ratio	Kerf Width, Wn (μm)	0.0	1450	0.1	1350	0.2	1250	0.3	1150	0.4	1050	0.5	950	0.6	850	0.7	750	0.8	750	0.9	750	1.0	750
Depth-to-Thickness Ratio	Kerf Width, Wn (μm)																																																		
0.0	1450																																																		
0.1	1350																																																		
0.2	1250																																																		
0.3	1150																																																		
0.4	1050																																																		
0.5	950																																																		
0.6	850																																																		
0.7	750																																																		
0.8	750																																																		
0.9	750																																																		
1.0	750																																																		
Depth-to-Thickness Ratio	Kerf Width, Wn (μm)																																																		
0.0	1450																																																		
0.1	1350																																																		
0.2	1250																																																		
0.3	1150																																																		
0.4	1050																																																		
0.5	950																																																		
0.6	850																																																		
0.7	750																																																		
0.8	750																																																		
0.9	750																																																		
1.0	750																																																		

Trial 17																									
Trial 18																									
	<p data-bbox="470 392 542 896">Graph of Kerf Width against Depth-to-Thickness Ratio</p>  <table border="1" data-bbox="566 1153 941 1904"><thead><tr><th>Depth-to-Thickness Ratio</th><th>Kerf Width, Wn (µm)</th></tr></thead><tbody><tr><td>0</td><td>1450</td></tr><tr><td>0.1</td><td>1250</td></tr><tr><td>0.2</td><td>1150</td></tr><tr><td>0.3</td><td>1050</td></tr><tr><td>0.4</td><td>950</td></tr><tr><td>0.5</td><td>850</td></tr><tr><td>0.6</td><td>850</td></tr><tr><td>0.7</td><td>850</td></tr><tr><td>0.8</td><td>850</td></tr><tr><td>0.9</td><td>850</td></tr><tr><td>1.0</td><td>850</td></tr></tbody></table> <p data-bbox="742 1153 766 1276">Trial 17</p>	Depth-to-Thickness Ratio	Kerf Width, Wn (µm)	0	1450	0.1	1250	0.2	1150	0.3	1050	0.4	950	0.5	850	0.6	850	0.7	850	0.8	850	0.9	850	1.0	850
Depth-to-Thickness Ratio	Kerf Width, Wn (µm)																								
0	1450																								
0.1	1250																								
0.2	1150																								
0.3	1050																								
0.4	950																								
0.5	850																								
0.6	850																								
0.7	850																								
0.8	850																								
0.9	850																								
1.0	850																								
	<p data-bbox="470 392 542 896">Graph of Kerf Width against Depth-to-Thickness Ratio</p>  <table border="1" data-bbox="566 257 941 1008"><thead><tr><th>Depth-to-Thickness Ratio</th><th>Kerf Width, Wn (µm)</th></tr></thead><tbody><tr><td>0</td><td>1250</td></tr><tr><td>0.1</td><td>1150</td></tr><tr><td>0.2</td><td>1050</td></tr><tr><td>0.3</td><td>950</td></tr><tr><td>0.4</td><td>850</td></tr><tr><td>0.5</td><td>850</td></tr><tr><td>0.6</td><td>850</td></tr><tr><td>0.7</td><td>850</td></tr><tr><td>0.8</td><td>850</td></tr><tr><td>0.9</td><td>850</td></tr><tr><td>1.0</td><td>850</td></tr></tbody></table> <p data-bbox="742 257 766 380">Trial 18</p>	Depth-to-Thickness Ratio	Kerf Width, Wn (µm)	0	1250	0.1	1150	0.2	1050	0.3	950	0.4	850	0.5	850	0.6	850	0.7	850	0.8	850	0.9	850	1.0	850
Depth-to-Thickness Ratio	Kerf Width, Wn (µm)																								
0	1250																								
0.1	1150																								
0.2	1050																								
0.3	950																								
0.4	850																								
0.5	850																								
0.6	850																								
0.7	850																								
0.8	850																								
0.9	850																								
1.0	850																								

The analysis of the experimental results obtained for kerf width was also carried out using Taguchi and ANOVA analysis. The main effect plot of the S/N ratio value and mean kerf width for each parameter at all levels as shown in Figure 4.5 and Figure 4.6. The values of the S/N ratio revealed that the optimal performance for kerf width can be obtain at traverse speed, V_f 50 mm/min (level 6), Pressure, P 30 kpsi (level 1), abrasive mass flow rate, V_a 0.158 kg/min (level 1) and stand-off distance, SOD 1mm (level 1). The optimum condition of design parameters for kerf width is defined as $A_6B_1C_1D_1$.

The ANOVA results of the kerf width is given in Table 4.6 and it is observed that all the parameters are statistically significant at the 95% confidence level based on the percentage of contribution in the order of: traverse speed and stand-off distance. The larger the contribution of a factor to the total sum of squares, the larger the ability of the factor to influence the output.

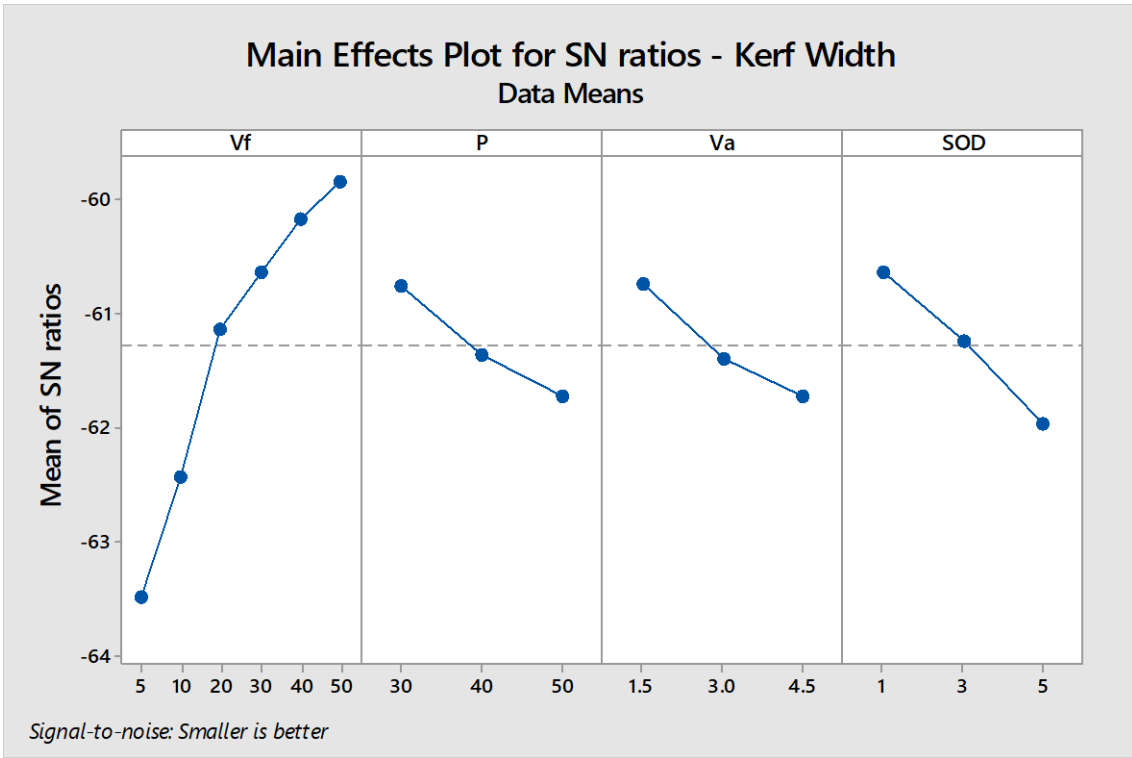


Figure 4.5: Main effect plot of S/N for AWJ kerf width.



Figure 4.6: Main effect plot of Means for AWJ kerf width.

Table 4.6: ANOVA analysis of AWJ kerf width.

Factor Symbol	DOF	Sum of Square	Mean of Square	F-value	P-value	Contribution (%)
<i>Vf mm/min</i>	5	631481	126296	51.10	0.000	69.69
<i>P kpsi</i>	2	70389	35195	14.24	0.050	7.77
<i>Va kg/min</i>	2	73466	36733	14.86	0.050	8.11
<i>SOD mm</i>	2	115906	57953	23.45	0.001	12.79
Error	6	14830	2472			1.64
Total	17	906073				100

Table 4.7 details the predicted and experimental values of mean and S/N ratio of the confirmation trials to validate the optimum operating parameters. The S/N ratio of kerf width by the predictive equation was found to be -58.13 and from the experiment the value of S/N ratio was found to be -57.85. An error of 0.48% for the S/N ratio is observed, which indicates that the accuracy of Taguchi DoE is acceptable.

Table 4.7: Confirmation test results for AWJ kerf width.

Response	Mean		S/N ratio (dB)		Error %
	Predicted	Experiment	Predicted	Experiment	
Kerf width	722.63	780.35	-58.13	-57.85	0.48

4.2.3 Initial Damage Zone (IDZ) Evaluation

The formation of Initial Damage Zone (IDZ) IDZ located at the top kerf width is due to the expansion of the waterjet prior to impingement as shown in Figure 4.8 (a). IDZ was noted at the jet entrance on all the trials conducted. The IDZ width, W_{IDZ} from the top surfaces were measured using Alicona Microscope and plotted along the measured mean Ra in Figure 4.8 (d). A 2D measurement analysis of surface topography on the top view of the initial damage width, see Figure 4.7 presents a random distribution of craters and valleys generated by abrasive particles bombardment from the outlet of waterjet. The abrasive particles are formed by a mixture of sizes with different kinetic energy generated by the waterjet pressure. They were not able to penetrate the workpiece and a small quantity of material was removed and generating valleys and craters before re-entrained in the abrasive slurry. In addition, Figure 4.7 (b) exhibits the trajectories wear tracks created by singular abrasive particles propelled on the workpiece surfaces at different angles. The 2D Ra roughness profiles are not symmetrical and the profile variation is random.

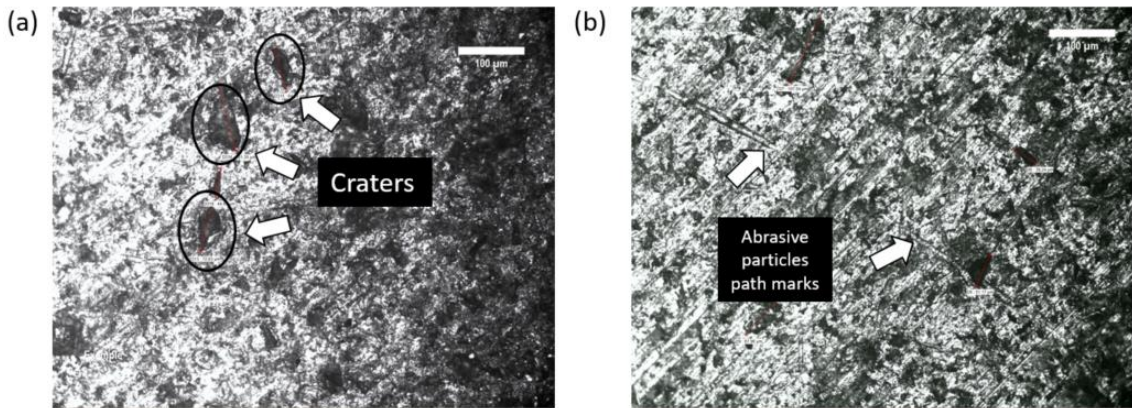


Figure 4.7: Top view of the initial damage zone width of AWJ Trial 17.

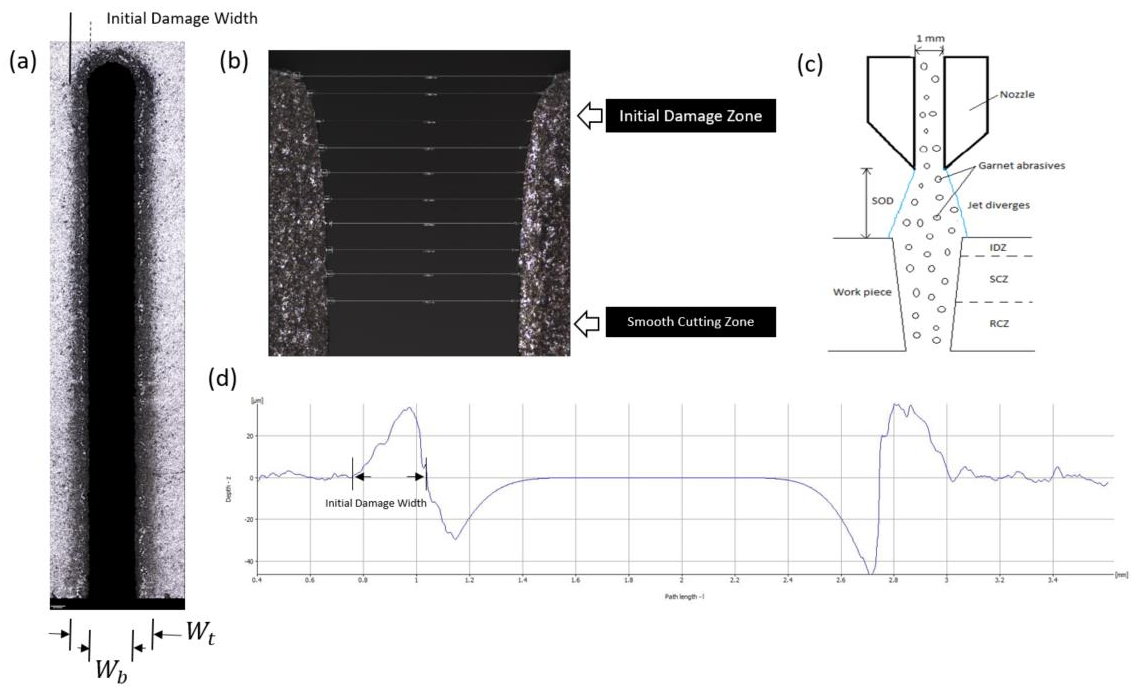


Figure 4.8: (a) Top view of cutting zone, (b) initial damage zone of AWJ cutting, (c) zones of kerf geometry and (d) measurement of initial damage width using Alicona 2D measurement of AWJ Trial 17.

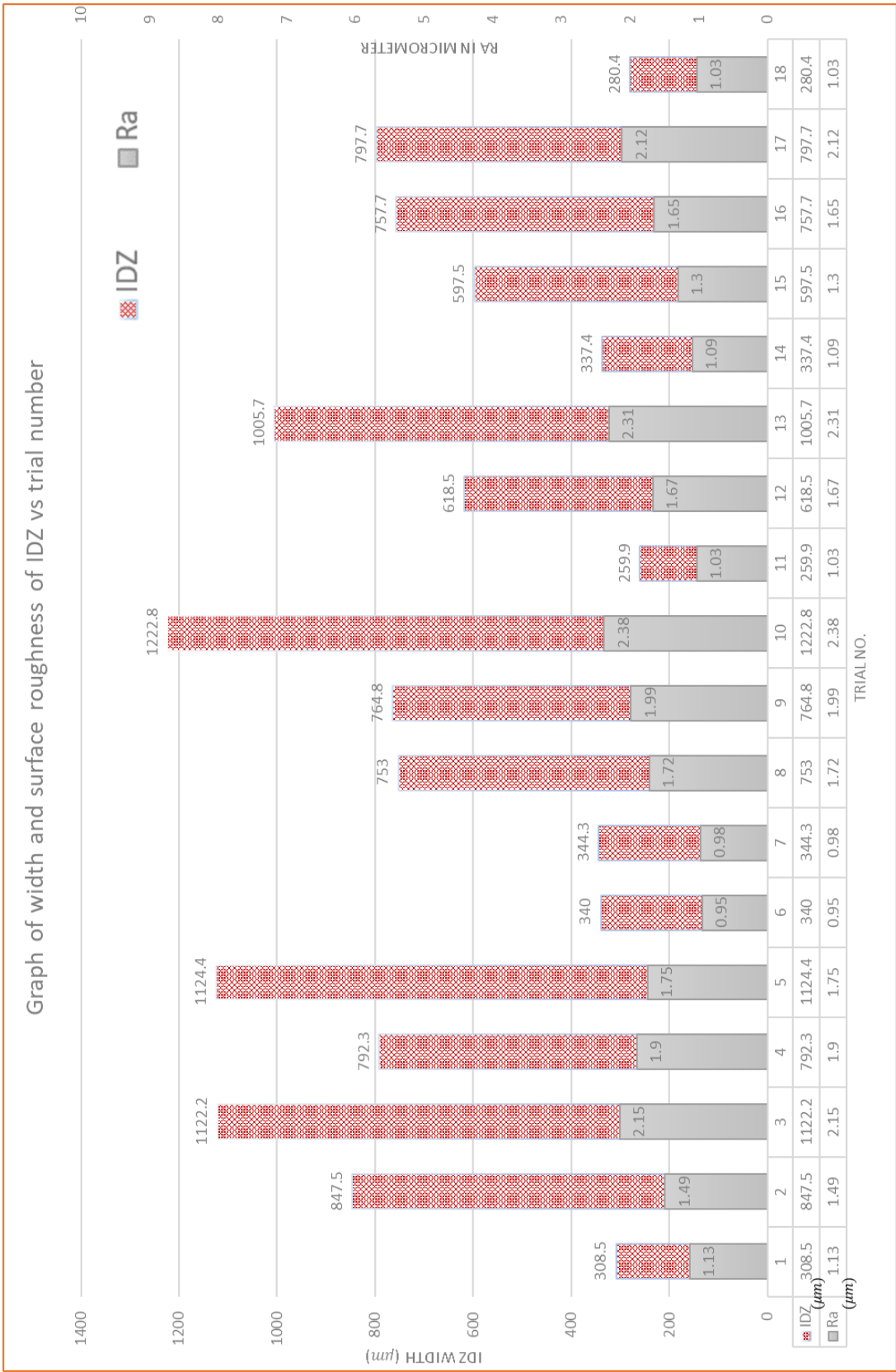


Figure 4.9: The Graph of width and Ra of IDZ against Trial No. for AWJ Trial 1 to 18.

The results of the IDZ width were analysed using Taguchi analysis. The results show that the optimal performance for minimal initial damage width can be obtained at traverse speed, V_f 50 mm/min (level 6), Pressure, P 50 kpsi (level 3), abrasive mass flow rate, V_a 0.158 kg/min (level 1) and stand-off distance, SOD 1mm (level 1). The optimum condition of design parameters for kerf width is defined as $A_6B_3C_1D_1$. ANOVA results suggested that the features were primarily influenced by standoff distance, SOD with PCR of 86.38% followed by abrasive mass flow rate V_a with PCR of 7.43%. Trial 11 exhibited the smallest W_{IDZ} measured on top of the specimens was 259.90 μm whereas the largest 1222.8 μm was measured on Trial 10, which was measured with higher V_a and SOD.

The degree of IDZ width and depth at jet entry can be minimized with a low standoff distance. Generally, higher standoff distance allows the jet to expand before impingement which may increase vulnerability to external drag from the surrounding environment. Therefore, decrease in the standoff distance results in minimizing jet diameter as cutting is initiated and increases the kinetic energy of the jet at impingement, which results in reduction of W_{IDZ} . The results of the confirmation tests conducted with the optimum design parameters proved that the Taguchi analysis is valid.

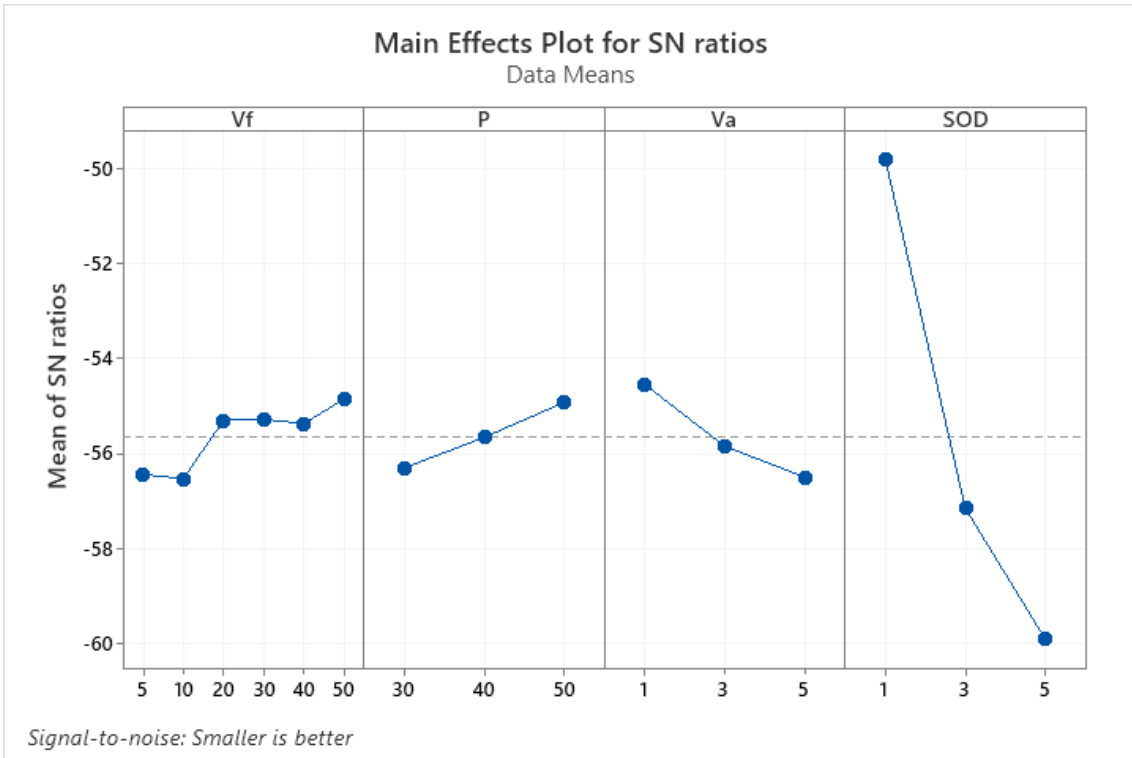


Figure 4.10: Main effect plot of S/N for AWJ IDZ width.

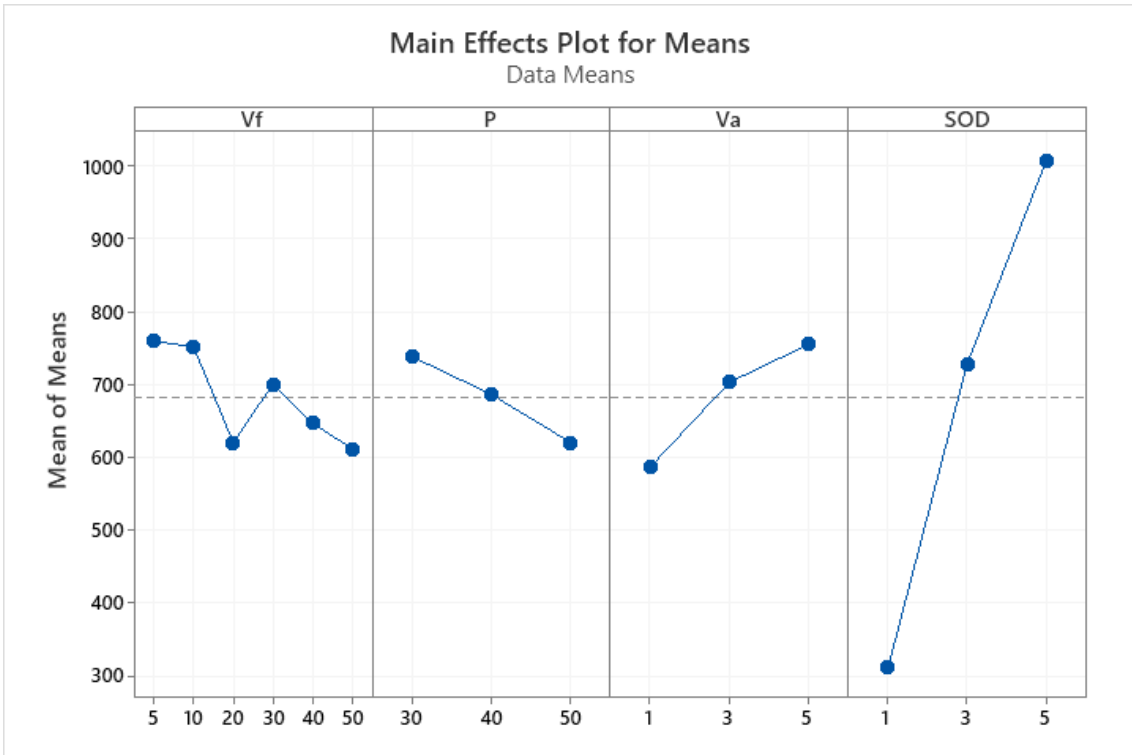


Figure: 4.11: Main effect plot of Means for AWJ IDZ width.

Table 4.8: ANOVA analysis of AWJ IDZ width.

Factor Symbol	DOF	Sum of Square	Mean of Square	F-value	P- value	Contribution (%)
<i>Vf mm/ min</i>	5	63490	12698	2.11	0.196	3.74
<i>P kpsi</i>	2	41961	20981	3.48	0.099	2.47
<i>Va kg/min</i>	2	89590	44795	7.43	0.024	5.28
<i>SOD mm</i>	2	1465962	732981	121.53	0.000	86.38
Error	6	36187	6031			2.13
Total	17	1697190				100

Table 4.9: Confirmation test results for AWJ IDZ width.

Response	Mean		S/N ratio (dB)		Error %
	Predicted	Experiment	Predicted	Experiment	
IDZ Width	85.27	98.07	-38.62	-39.83	0.53

4.2.4 Surface Roughness

The 2 dimensional and 3D Areal surface topography were analysed and studied. Three measurements were taken each at 2mm, 12mm and 22mm from the top of the cutting front for each specimen as shown in Figure 4.12. The results of mean Ra, Rq, Rsk and Rku were recorded in Table 4.10. The Ra measured at the bottom part of the cutting front was found to be higher than the upper section, which is due to the loss in kinetic energy of abrasive particles.

1. Two dimensional 2D surface topography analysis

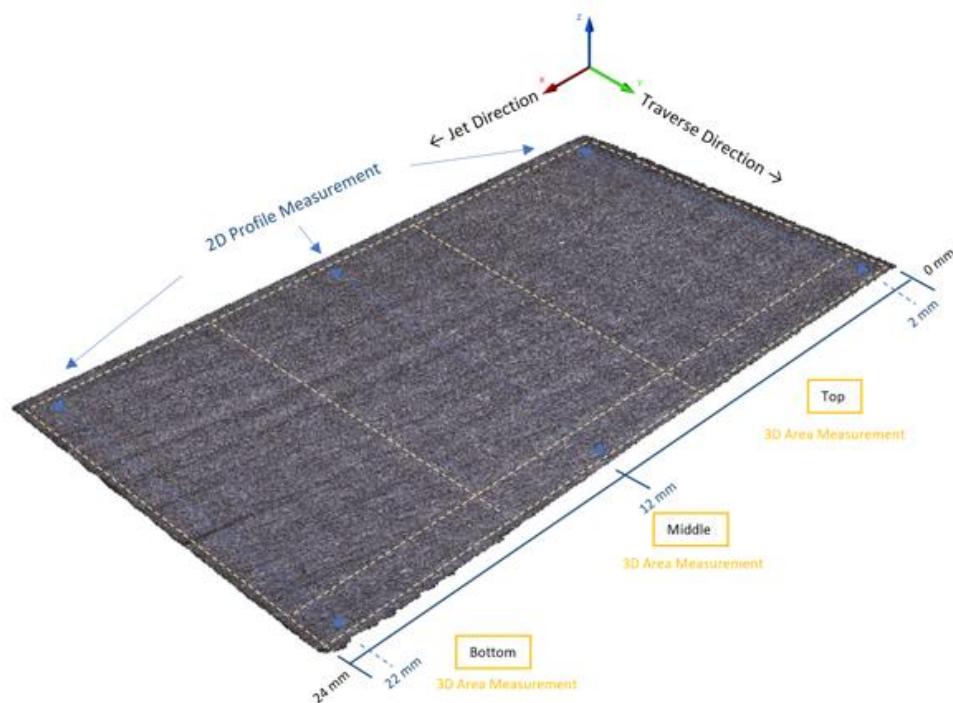


Figure 4.12: 2D measurement of the cutting front surface of AWJ samples.

Table 4.10: AWJ 2D Surface Roughness Results Analysis.

Trial No.	Vf <i>mm/min</i>	P <i>kpsi</i>	Va <i>kg/min</i>	SOD <i>mm</i>	Ra (μm)				Mean		
					2mm	12m m	22m m	Mean	Rsk	Rku	Rq
1	5	30	0.158	1	2.45	2.78	3.17	2.80	-0.39	3.06	3.50
2	5	40	0.340	3	2.79	2.47	2.78	2.68	-0.3	3.03	3.37
3	5	50	0.402	5	2.55	2.55	2.79	2.63	-0.34	2.96	3.29
4	10	30	0.158	3	3.45	3.17	3.57	3.40	-0.38	2.99	4.28
5	10	40	0.340	5	3.25	3.1	2.85	3.07	-0.28	3.05	3.84
6	10	50	0.402	1	2.24	2.37	2.87	2.49	-0.37	3.03	3.10
7	20	30	0.340	1	2.86	3.05	3.31	3.07	-0.37	3.17	3.90
8	20	40	0.402	3	2.72	2.87	2.99	2.86	-0.31	3.09	3.60
9	20	50	0.158	5	4.24	3.81	4.54	4.20	-0.21	2.96	5.22
10	30	30	0.402	5	3.63	3.32	3.38	3.44	-0.26	2.95	4.29
11	30	40	0.158	1	2.79	3.61	4.26	3.55	-0.28	2.98	4.43
12	30	50	0.340	3	3.37	3.63	3.83	3.61	-0.22	2.77	4.46
13	40	30	0.340	5	4.54	3.90	3.78	4.07	-0.22	2.78	5.05
14	40	40	0.402	1	2.40	3.00	3.50	2.97	-0.26	2.91	3.69
15	40	50	0.158	3	3.5	4.49	4.99	4.33	-0.19	2.99	5.42
16	50	30	0.402	3	4.48	4.70	5.13	4.77	-0.3	2.86	5.93
17	50	40	0.158	5	4.59	4.04	4.68	4.44	-0.24	2.83	5.53
18	50	50	0.340	1	2.61	3.70	4.37	3.56	-0.39	3.12	4.47

Figure 4.13. explains the main effects plot of process parameters of surface roughness of AWJ machined samples. The results show that the optimal performance for Ra can be obtained at traverse speed, V_f 5 mm/min (level 1), Pressure, P 40 kpsi (level 2), abrasive mass flow rate, V_a 0.402 kg/min (level 3) and stand-off distance, SOD 1mm (level 1). The optimum condition of design parameters for kerf width is defined as $A_1B_2C_3D_1$. The ANOVA analysis indicates that traverse speed (PCR=58.36%) is the most important factor influencing the Ra followed by standoff distance (PCR=15.32%) and abrasive mass flow rate (PCR=14.335). The lower the traverse speed, the contact between the waterjet and workpiece increases, more abrasive particles take part in cutting. Abrasive mass flow rate increases, the number of particles impacting on the surface increases, smoother surface generated results in decreases in the Ra value. The Ra increases with the increase in standoff distance as the standoff distance increases, the material surface is exposed to the diverged downstream of the jet, loses its coherence and kinetic energy

An analysis of skewness (Rsk) showed all values were negative, indicating that the machined surfaces were typically dominated by deep valleys. From Table 4.10, the high kurtosis (Rku) >3 suggested the surface is leptokurtic, which indicates the presence of sharp peaks on the measured profiles. These

suggested that the AWJ machined surfaces dominated by narrowly distributed valleys due to the 'ploughing' effect of abrasive particles. The predicted and measured results of confirmation tests are presented in Table 4.12. The percentage of error is 4.09%, which is lower than 5%, which indicates the accuracy of the Taguchi experiment is acceptable.

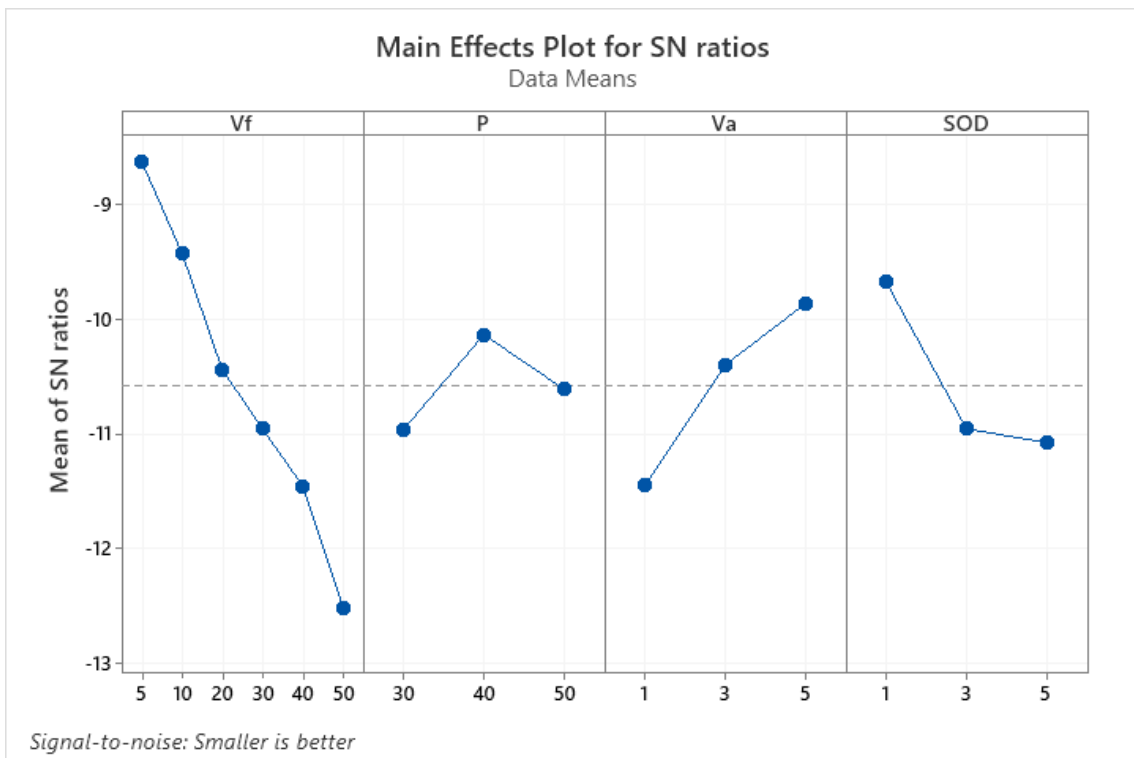


Figure 4.13: Main effect plot of S/N for AWJ Ra.

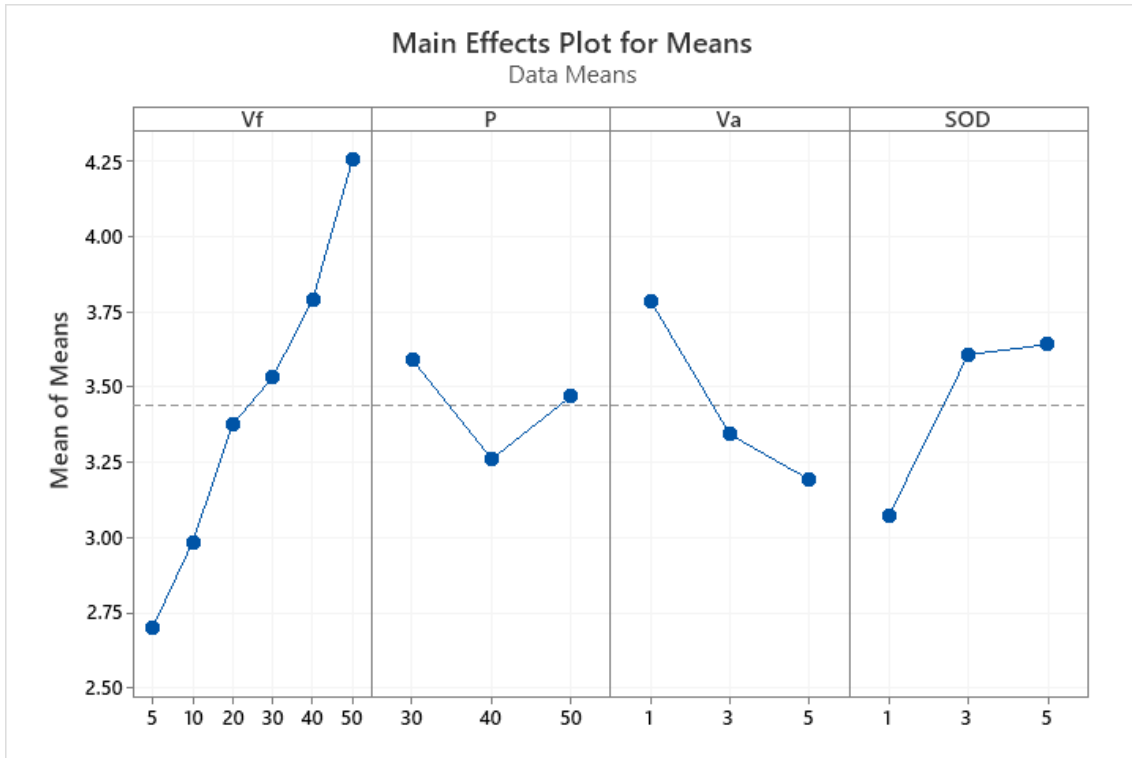


Figure 4.14: Main effect plot of Means for AWJ Ra.

Table 4.11: ANOVA analysis of AWJ Ra.

Factor Symbol	DOF	Sum of Square	Mean of Square	F- value	P- value	Contribution (%)
Vf <i>mm/min</i>	5	4.6510	0.9302	8.98	0.009	58.36
P <i>kpsi</i>	2	0.3342	0.1671	1.61	0.275	4.19
Va <i>kg/min</i>	2	1.1422	0.5711	5.52	0.044	14.33
SOD <i>mm</i>	2	1.2207	0.6103	5.89	0.038	15.32
Error	6	0.6213	0.1035			7.80
Total	17	7.9694				100

Table 4.12: Confirmation test results for AWJ Ra.

Response	Mean		S/N ratio (dB)		Error %
	Predicted	Experiment	Predicted	Experiment	
Ra	1.91	1.86	-5.62	-5.39	4.09

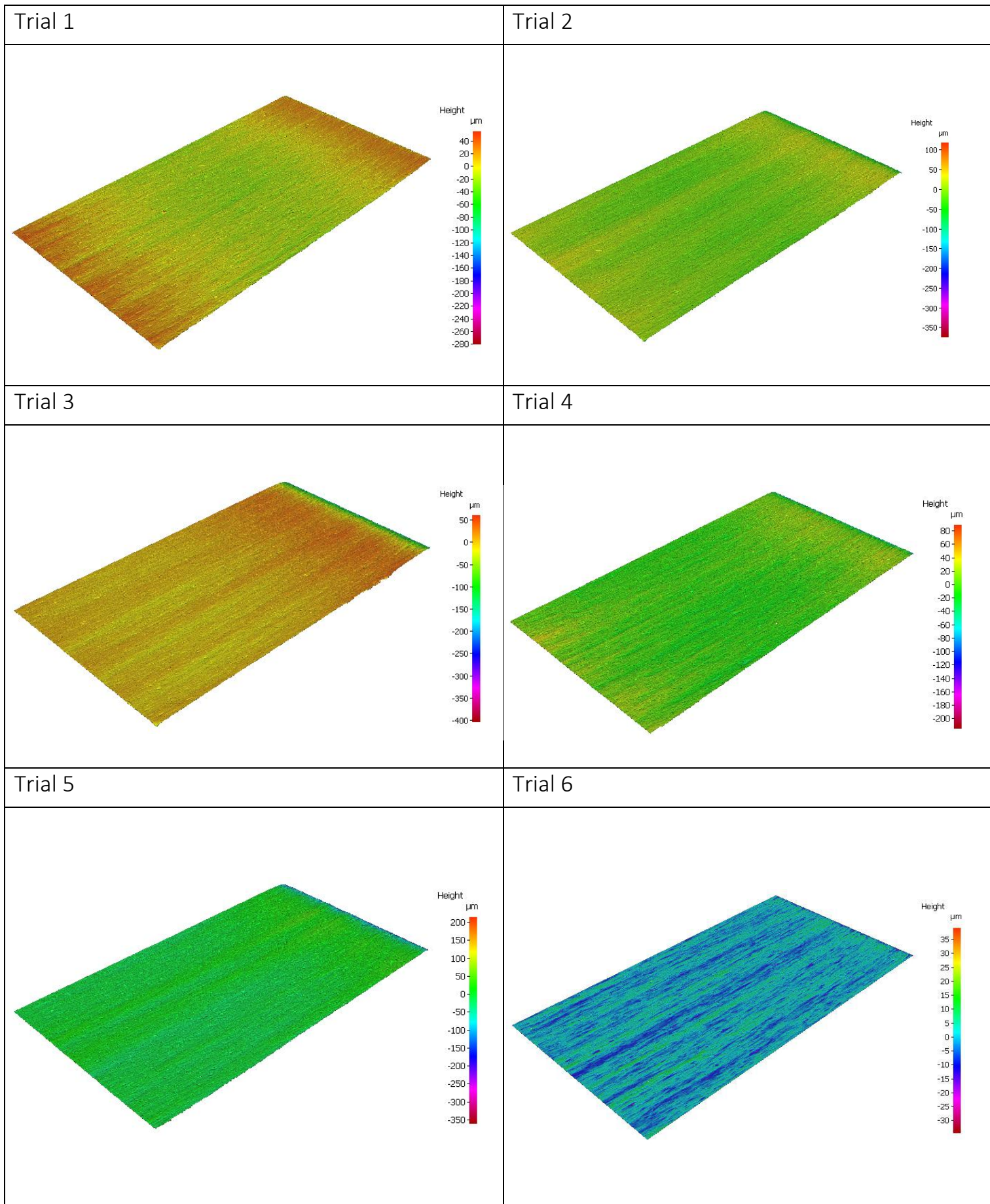
2. Three-dimensional 3D surface topography analysis

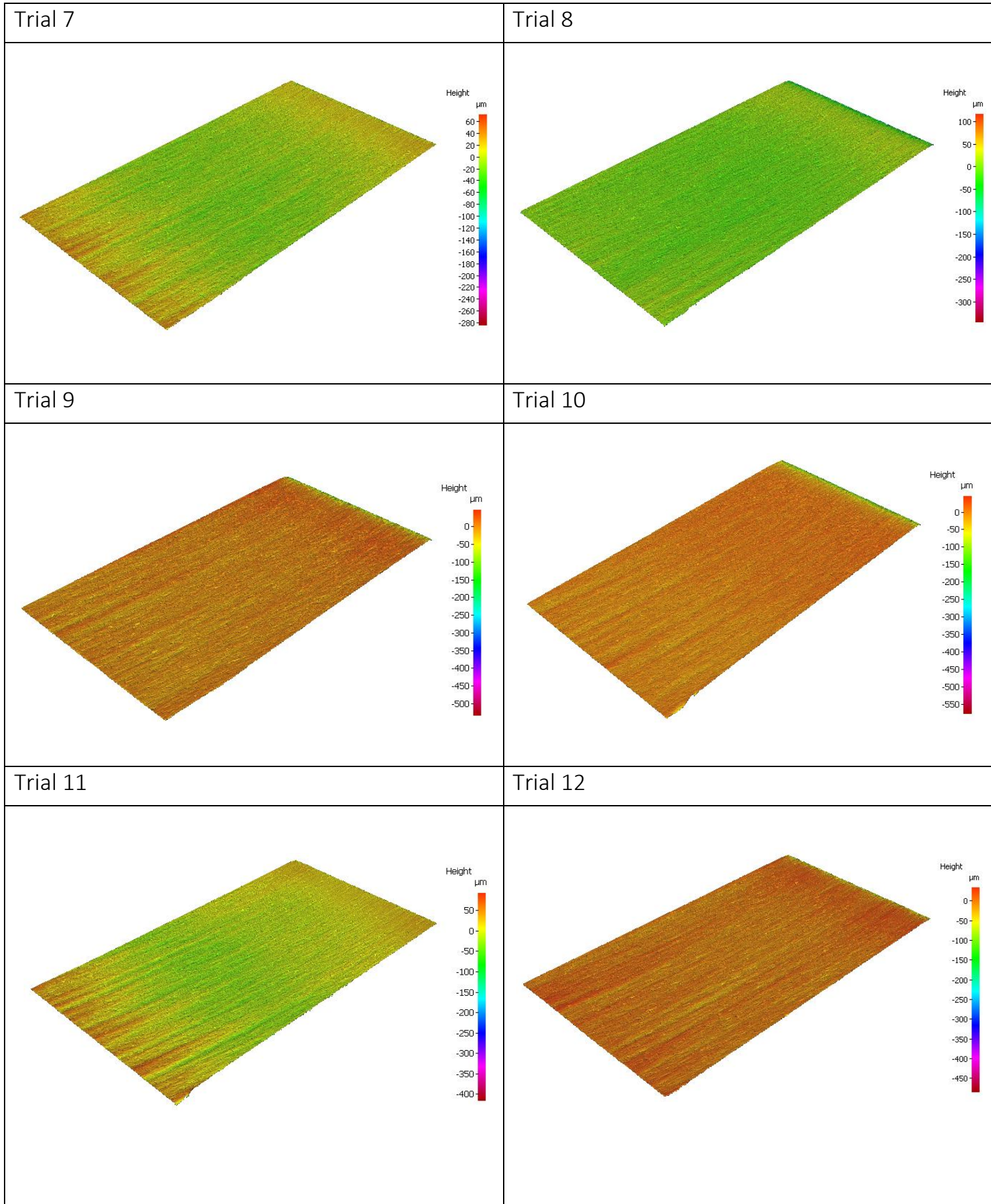
It was suggested that 3D reflects better surface topography reality compared to 2D surface roughness parameters[132]. Table 4.13 details 3D surface roughness values (S_a) recorded at the upper, middle and bottom of the cutting front, with associated surface topography map outlined in Table 4.13. Sku kurtosis refers to qualifying the flatness of the height distribution. All the trials have negative Ssk and higher Sku compared with the original surface. The negative skewness Ssk and Sku larger than 3 represent that the AWJ generated surfaces are dominated by deep valleys. It is suggested that the material removal process of AWJ consists of ploughing of abrasive particles, which generate a surface with deep valleys. The abrasive particles at this penetration depth have a high energy with maximum potential for material removal. It can be seen that the machined surfaces at deeper penetration depth appears to be rougher. The results show that the optimal

performance for S_a can be achieved at traverse speed, V_f 5 mm/min (level 1), Pressure, P 30 kpsi (level 1), abrasive mass flow rate, V_a 0.402 kg/min (level 3) and stand-off distance, SOD 1mm (level 1). The optimum condition of design parameters for kerf width is defined as $A_1B_1C_3D_1$. The ANOVA analysis indicates that traverse speed (PCR=53.7%) is the most important factor followed by abrasive mass flow rate (PCR=28.99%) and stand-off distance (PCR= 12.1%). The confirmation test experiment was carried out and it suggested that the Taguchi Analysis of S_a is valid as the percentage of error is $\sim 5\%$.

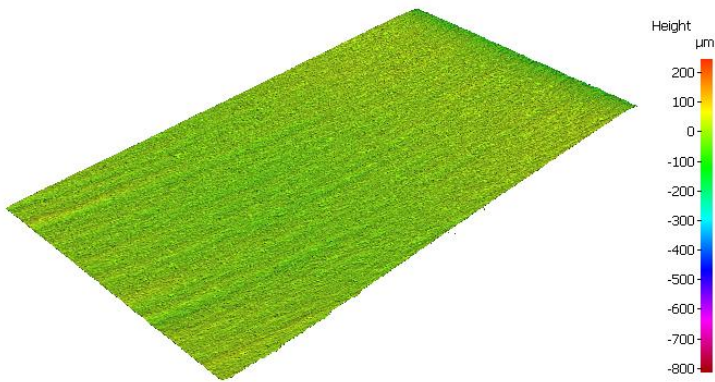
Table 4.13: Three-dimensional (3D) topography maps for the AWJ cutting

front Trial 1 to 18.

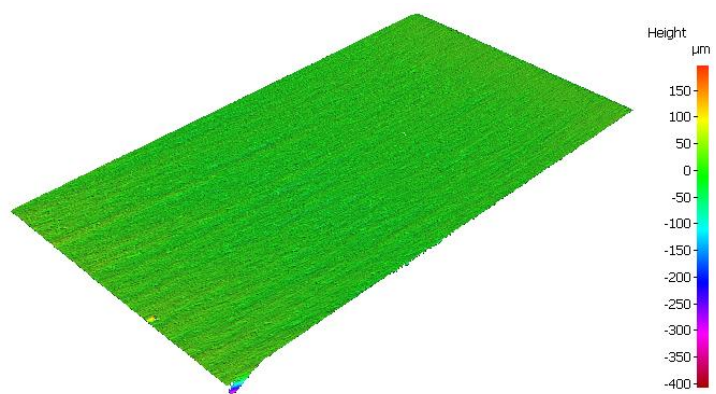




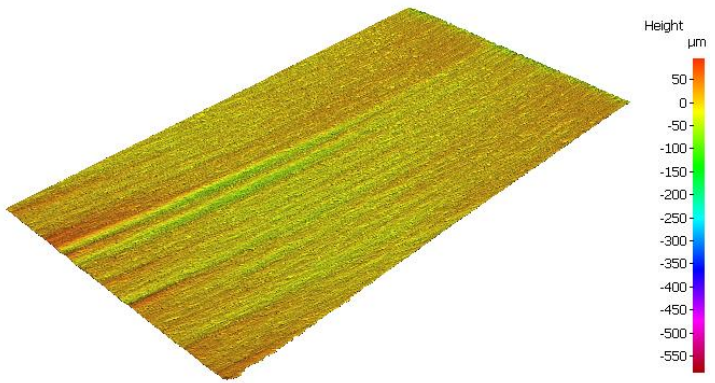
Trial 13



Trial 14



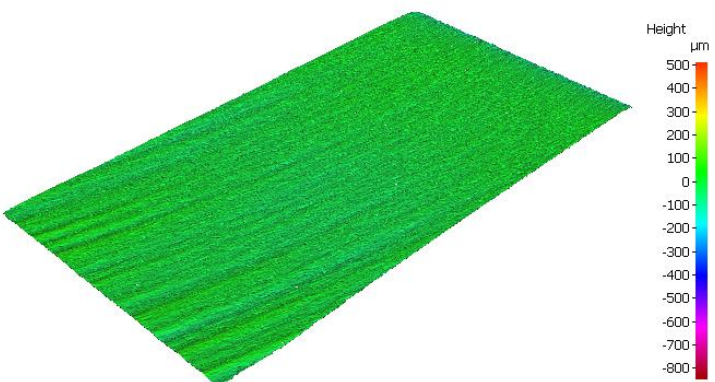
Trial 15



Trial 16



Trial 17



Trial 18



Table 4.14: AWJ 3D Surface Roughness Results Analysis.

Trial No.	Vf <i>mm/min</i>	P <i>kpsi</i>	Va <i>kg/min</i>	SOD <i>mm</i>	Sa (μm)				Mean		
					Upper	Middle	Bottom	Mean	Ssk	Sku	Sq
1	5	30	0.158	1	3.2	3.42	3.89	3.5	-0.49	4.99	4.52
2	5	40	0.340	3	3.73	3.5	3.35	3.53	-0.34	5	4.52
3	5	50	0.402	5	4.14	3.27	3.23	3.55	-0.32	4.45	4.61
4	10	30	0.158	3	4.35	4.12	4.68	4.38	-0.31	4.96	5.59
5	10	40	0.340	5	5.15	4.19	4.34	4.56	-0.25	4.04	5.88
6	10	50	0.402	1	2.62	2.84	3.14	2.87	-0.05	14.4	3.72
7	20	30	0.340	1	3.42	3.88	4.62	3.97	-0.52	3.9	5.09
8	20	40	0.402	3	3.64	3.53	3.85	3.67	-0.49	4.05	4.7
9	20	50	0.158	5	5.56	4.85	5.67	5.36	-0.43	4.22	6.89
10	30	30	0.402	5	4.68	4.18	4.93	4.6	-0.27	3.49	5.82
11	30	40	0.158	1	3.78	5.04	7.52	5.45	-0.41	3.77	6.94
12	30	50	0.340	3	4.46	4.69	5.42	4.86	-0.42	4.06	6.22
13	40	30	0.340	5	5.51	5.22	6.37	5.7	-0.29	3.66	7.24
14	40	40	0.402	1	3.42	4.03	4.94	4.13	-0.35	4.54	5.28
15	40	50	0.158	3	5.37	6.94	9.22	7.18	-0.46	4.1	9.34
16	50	30	0.402	3	4.24	4.66	6.36	5.09	-0.27	3.34	6.41
17	50	40	0.158	5	5.81	6.52	9.25	7.19	-0.21	3.43	9.17
18	50	50	0.340	1	3.72	5.14	6.59	5.15	-0.44	3.81	6.6

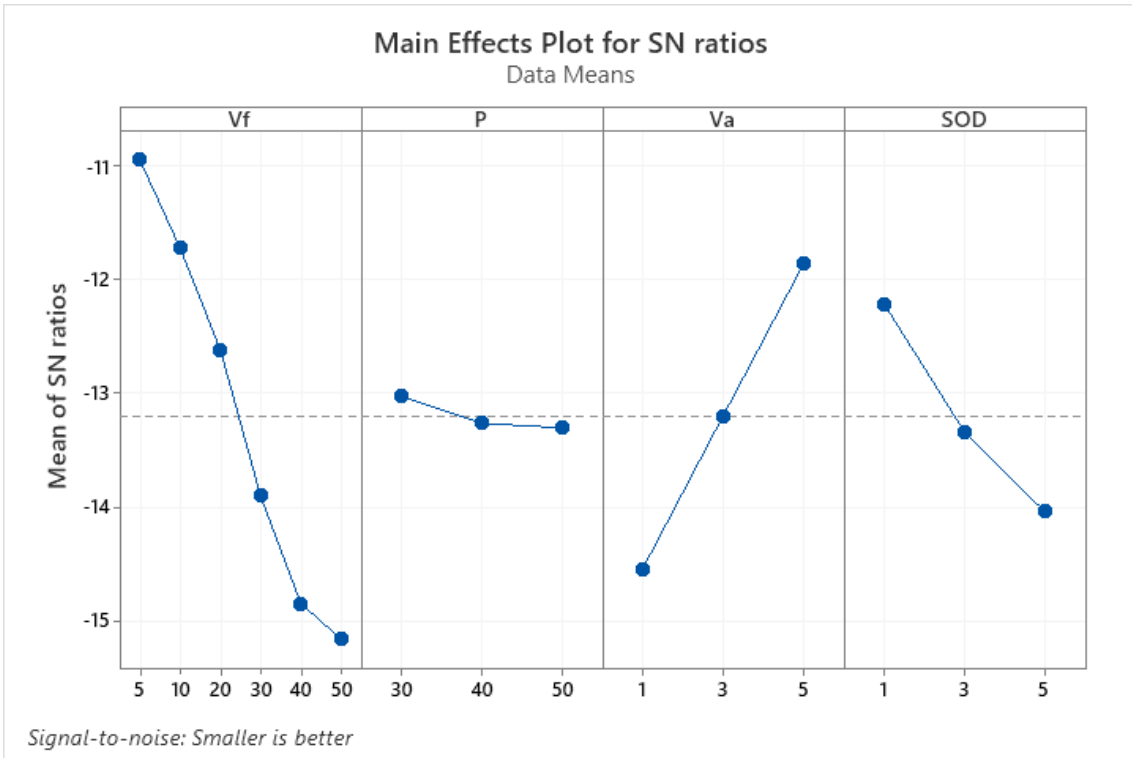


Figure 4.15: Main effect plot of S/N ratio for AWJ Sa.

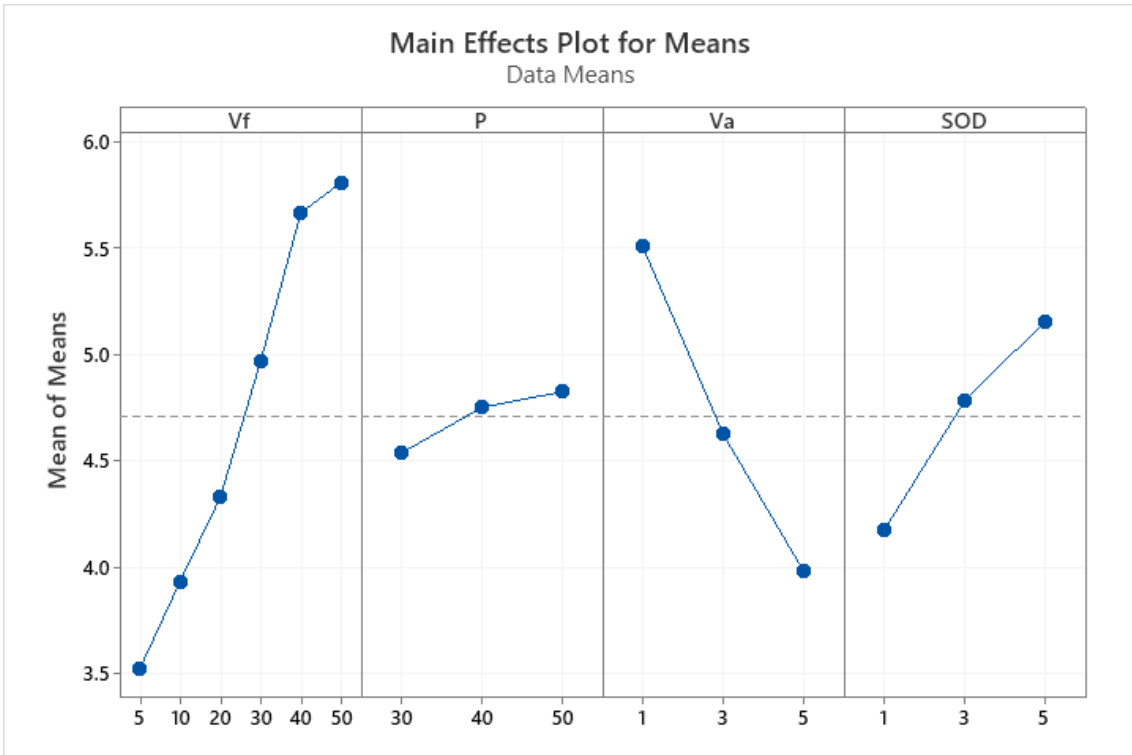


Figure 4.16: Main effect plot of means for AWJ Sa.

Table 4.15: ANOVA analysis of AWJ Sa.

Factor Symbol	DOF	Sum of Square	Mean of Square	F- value	P- value	Contribution (%)
<i>Vf mm/min</i>	5	13.0181	2.6036	15.74	0.002	53.66
<i>P kpsi</i>	2	0.2695	0.1347	0.81	0.487	1.11
<i>Va kg/min</i>	2	7.0337	3.5168	21.25	0.002	28.99
<i>SOD mm</i>	2	2.9447	1.4723	8.90	0.016	12.14
Error	6	0.9928	0.1655			4.09
Total	17	24.2587				100

Table 4.16: Confirmation test results for AWJ Sa.

Response	Mean		S/N ratio (dB)		Error %
	Predicted	Experiment	Predicted	Experiment	
Sa	2.11	2.20	-6.49	-6.85	5.26

4.2.5 Micro-hardness

The Knoop microhardness measurements were carried out in three different regions of the machined specimens. Each microhardness values in the profile graph represents an average value of 9 measurements in order to ensure repeatability and the reproducibility of the results. The variation in mean microhardness of each trial was plotted against depth as shown in Appendix

A. The microhardness depth profile results showed that there is a presence of a strain hardened surface in all trials, irrespective of cutting parameters. The hardness increased by approximately $\sim 90 \text{ HK}_{0.05}$ above the bulk hardness ($\sim 110 \text{ HK}_{0.05}$) which was due to strain hardening / plastic deformation as a result of high-impact of abrasive particles. Some of the samples showed increase in microhardness up to the depth of $1000 \mu\text{m}$. The increase in microhardness can be accounted for increase in localised strain due to the presence of grit embedment and striation marks formed during the cutting process. The grit particles were pushed into the surface creating a surface of strained aluminium alloy matrix.

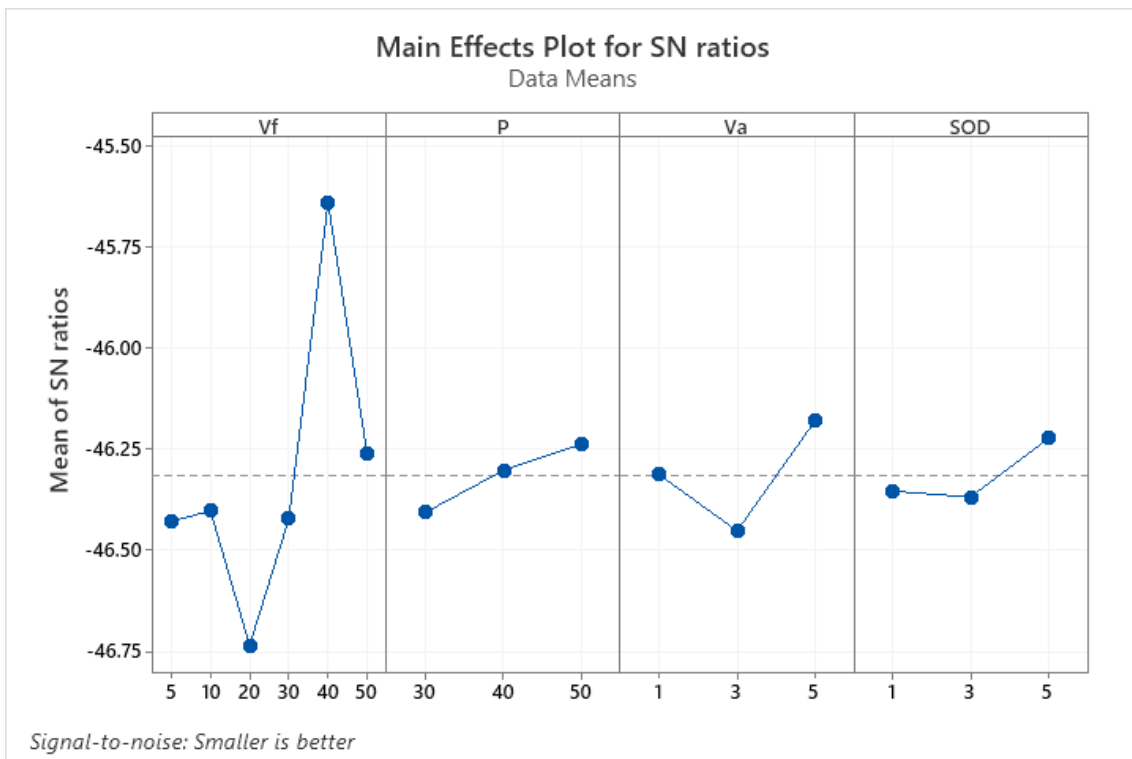


Figure 4.17: Main effect plot of S/N for AWJ microhardness.

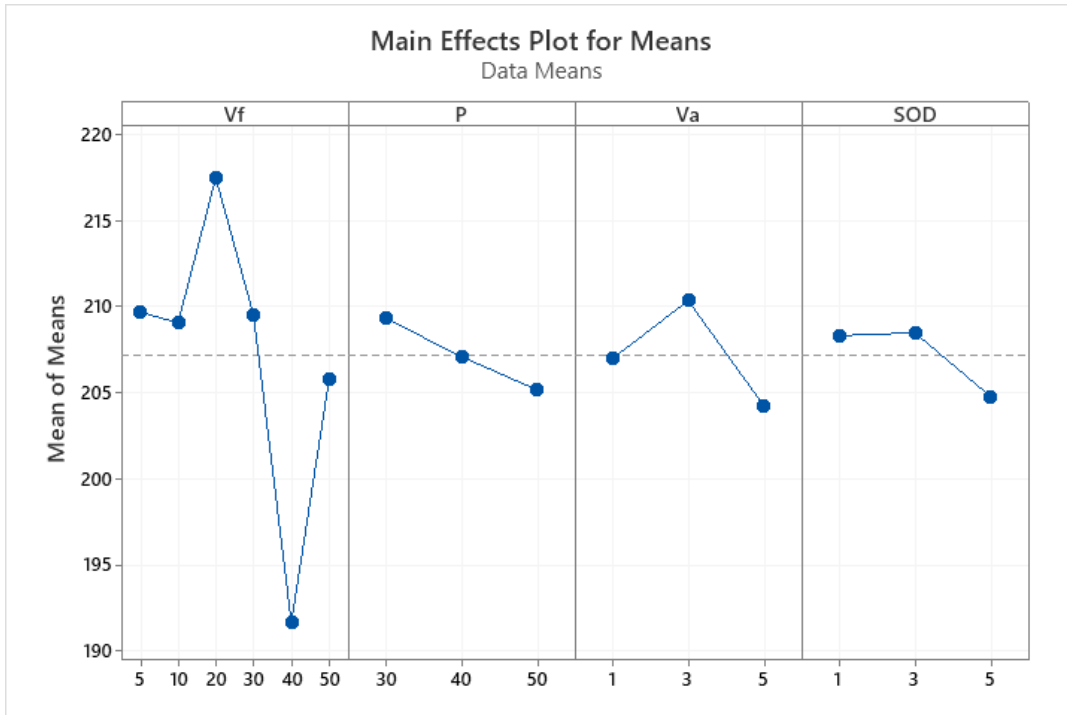


Figure 4.18: Main effect plot of means for AWJ microhardness.

According to the main effect plot shown in Figure 4.18 and ANOVA analysis, it is suggested that the process parameters have no significant effect on the microhardness as all the p -value > 0.05 .

Table 4.17: ANOVA analysis of AWJ microhardness.

Factor Symbol	DOF	Sum of Square	Mean of Square	F- value	P- value	Contribution (%)
Vf <i>mm/min</i>	5	109.80	218.56	1.91	0.227	54.75
P <i>kpsi</i>	2	51.75	25.87	0.23	0.804	2.59
Va <i>kg/min</i>	2	112.03	56.02	0.49	0.636	5.61
SOD <i>mm</i>	2	52.40	26.20	0.23	0.802	2.63
Error	6	687.02	114.50			34.42
Total	17	1996.00				100

4.3 Phase One: Influence of Process Parameters in WEDM

4.3.1 Material Removal Rate

The material erodes and vaporised from the workpiece by a series of discrete electrical discharges, which are then flushed away in dielectric fluid. The calculated material removal rate in mm^3/min is summarised in Table 4.18.

Observation shows that the material removal rate increases dramatically comparing trial 1 to 9 and 10 to 18, mainly due to the increase in pulse on time. According to the main effect plots of MRR, the optimal performance can be achieved at pulse on time, A 0.7 μs (level 2), average machining voltage, AJ 45 V (level 3), ignition pulse current, IAL 10 A (level 1), open gap voltage, V 80 V (level 1) and function of frequency, FF 100 % (level 3). The optimum condition of design parameters for kerf width is defined as $A_2B_3C_1D_1E_3$.

Table 4.18: Results of data obtained from MRR of WEDM.

Trial No.	A μs	AJ V	IAL A	V V	FF %	Mass 1 (g)	Mass 2 (g)	Time (min)	MRR(mm^3/min)
1	0.1	15	10	80	10	886.61	886.35	10.58	8.62
2	0.1	15	20	100	50	886.35	886.07	4.23	23.22
3	0.1	15	30	120	100	886.07	885.81	4.05	22.52
4	0.1	30	10	80	50	885.81	885.55	3.17	28.77
5	0.1	30	20	100	100	885.55	885.29	2.88	31.66
6	0.1	30	30	120	10	885.29	885.06	18.68	4.32
7	0.1	45	10	100	10	885.06	884.76	16.43	6.40
8	0.1	45	20	120	50	884.76	884.5	4.65	19.61
9	0.1	45	30	80	100	884.5	884.26	2.65	31.77
10	0.7	15	10	120	100	884.26	883.94	2.18	51.49
11	0.7	15	20	80	10	883.94	883.66	3.8	25.84
12	0.7	15	30	100	50	883.66	883.36	2.48	42.43
13	0.7	30	10	100	100	883.36	883.06	1.42	74.10
14	0.7	30	20	120	10	883.06	882.76	4.55	23.13
15	0.7	30	30	80	50	882.76	882.49	1.47	64.42
16	0.7	45	10	120	50	882.49	882.18	1.47	73.97
17	0.7	45	20	80	100	882.18	881.87	1.15	94.55
18	0.7	45	30	100	10	881.87	881.54	3.97	29.16

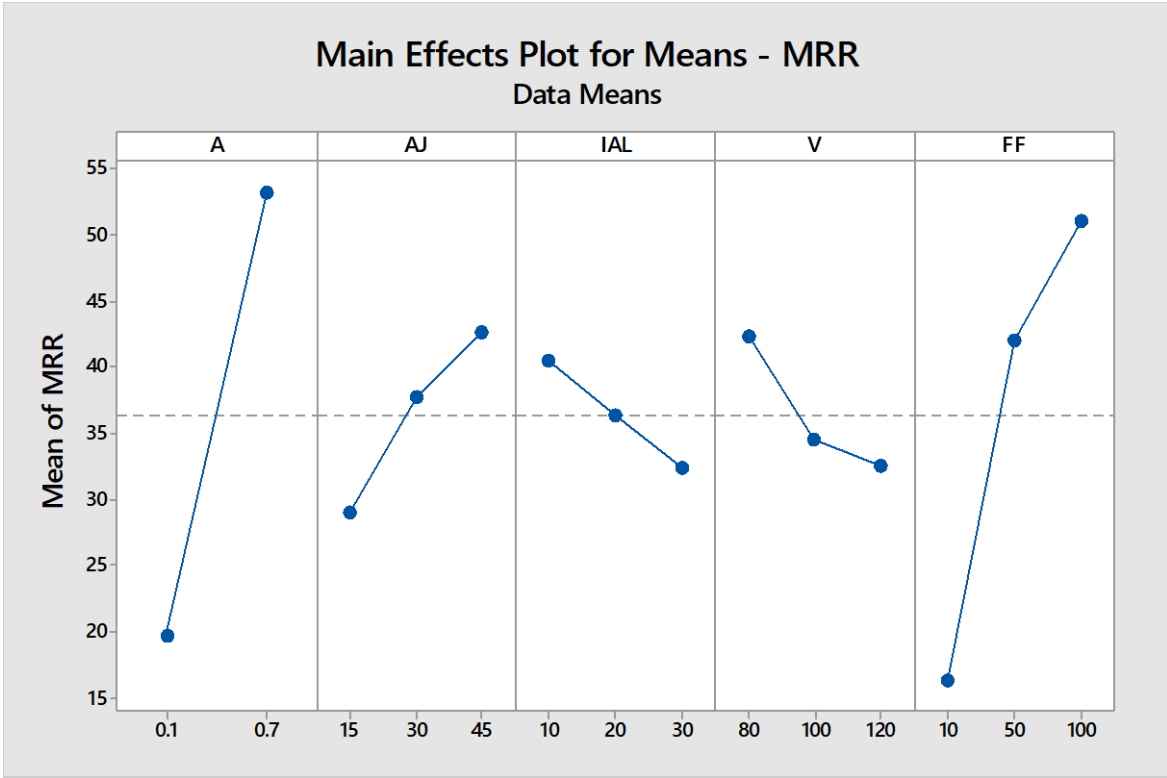


Figure 4.19: Main effect plot of S/N for WEDM MRR.

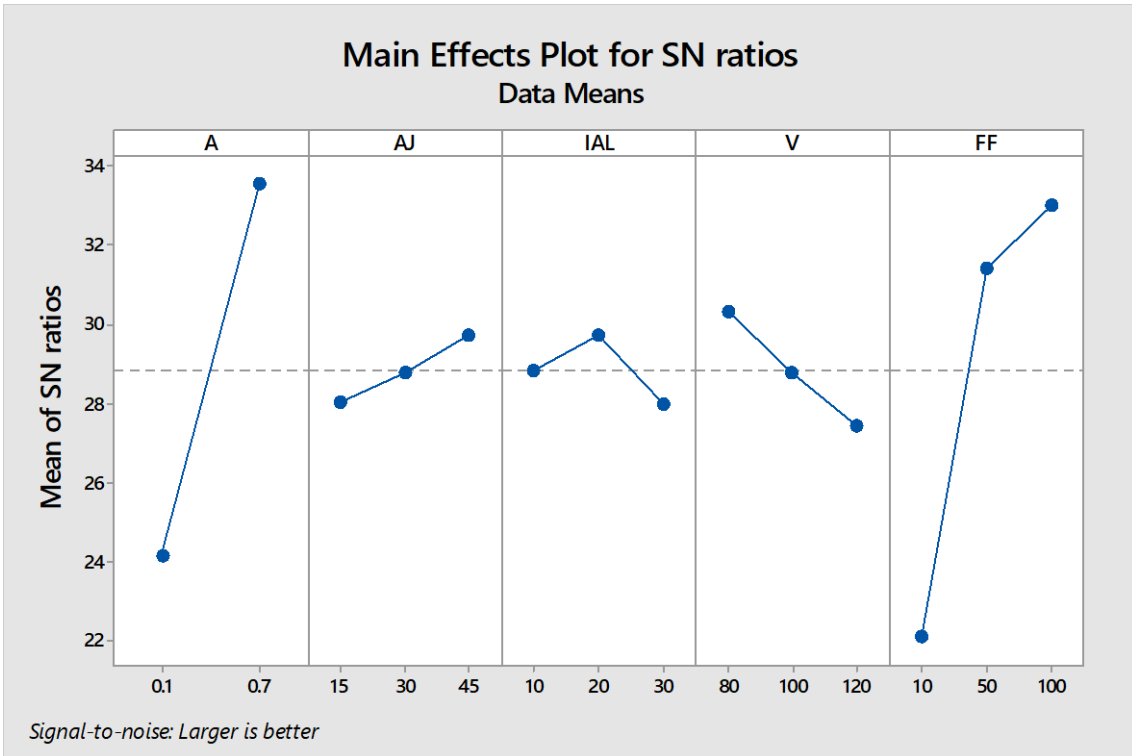


Figure 4.20: Main effect plot of Means for WEDM MRR.

The increase in pulse-on time and average machining voltage increases the material removal rate as the number of electrons striking on the work surface in the electric discharge increases thus more material is eroded from the workpiece surface. The function of frequency increases, the delay time decreases, material removal rate increases. The machining speed increases with decreases in open gap voltage, the mean gap becomes narrower, which leads to an increase in number of electric sparks. The material removal rate decreases with increases in ignition pulse current as the current in each pulse increases may contribute to the rise in molten material in the spark gap caused by increase in discharge energy, which leads to unstable machining.

The ANOVA analysis showed that pulse on time (PCR=45.90) is the most significant factor in influencing the material removal rate followed by function of frequency (PCR=35.39%). This is similar to the trends widely reported in literature[53, 133, 134].

Table 4.19: ANOVA analysis of WEDM MRR.

Factor Symbol	DOF	Sum of Square	Mean of Square	F-value	P-value	Contribution (%)
A μs	1	5073.6	5073.6	41.36	0.000	45.90
AJ V	2	566.3	283.16	2.31	0.162	5.12
IAL A	2	198.0	99.00	0.81	0.479	1.79
V V	2	323.6	161.78	1.32	0.320	2.93
FF %	2	39118	1955.90	15.94	0.002	35.39
Error	8	981.4	122.67			8.88
Total	17	11054.6				100

The results of experimental confirmation tests using optimal machining parameters are shown in Table 4.20. The error value between the predicted and experimental data is 4.96, which is within the 5% threshold set, hence the Taguchi experiment is valid.

Table 4.20: Confirmation test results for WEDM MRR

Response	Mean		S/N ratio (dB)		Error %
	Predicted	Experiment	Predicted	Experiment	
MRR	83.94	80.56	40.11	38.12	4.96

4.3 .2 Kerf Profile Geometry

From the variation in the kerf width measured along the cut length shown in Figure 4.21, it is observed that the kerf width is improved by decreases in the pulse on time. The graphs of all the trails shown in Table 4.21 show that the kerf geometries are relatively straight.

The main effect plots in Figure 4.23 revealed that the optimal performance can be achieved at pulse on time, A 0.1 μ s (level 1), average machining voltage, AJ 15 V (level 1), ignition pulse current, IAL 20 A (level 2), open gap voltage, V 80 V (level 1) and function of frequency, FF 50 % (level 2).

The optimum condition of design parameters for kerf width is defined as $A_1B_1C_2D_1E_2$. The mean kerf width decreases with decreases in pulse-on time and average machining voltage, decreases in electric discharge, less material is removed. The mean kerf width decreases with smaller open gap voltage. When a smaller open gap voltage / reference voltage is set, the number of electric sparks increases resulting in higher machining rate, hence the mean gap becomes narrower. Surprisingly, moderate ignition pulse current and function of frequency are desirable due to stable machining.

The ANOVA analysis shown in Table 4.22 demonstrated that pulse on time was the only significant factor with a corresponding PCR of 85.64%.

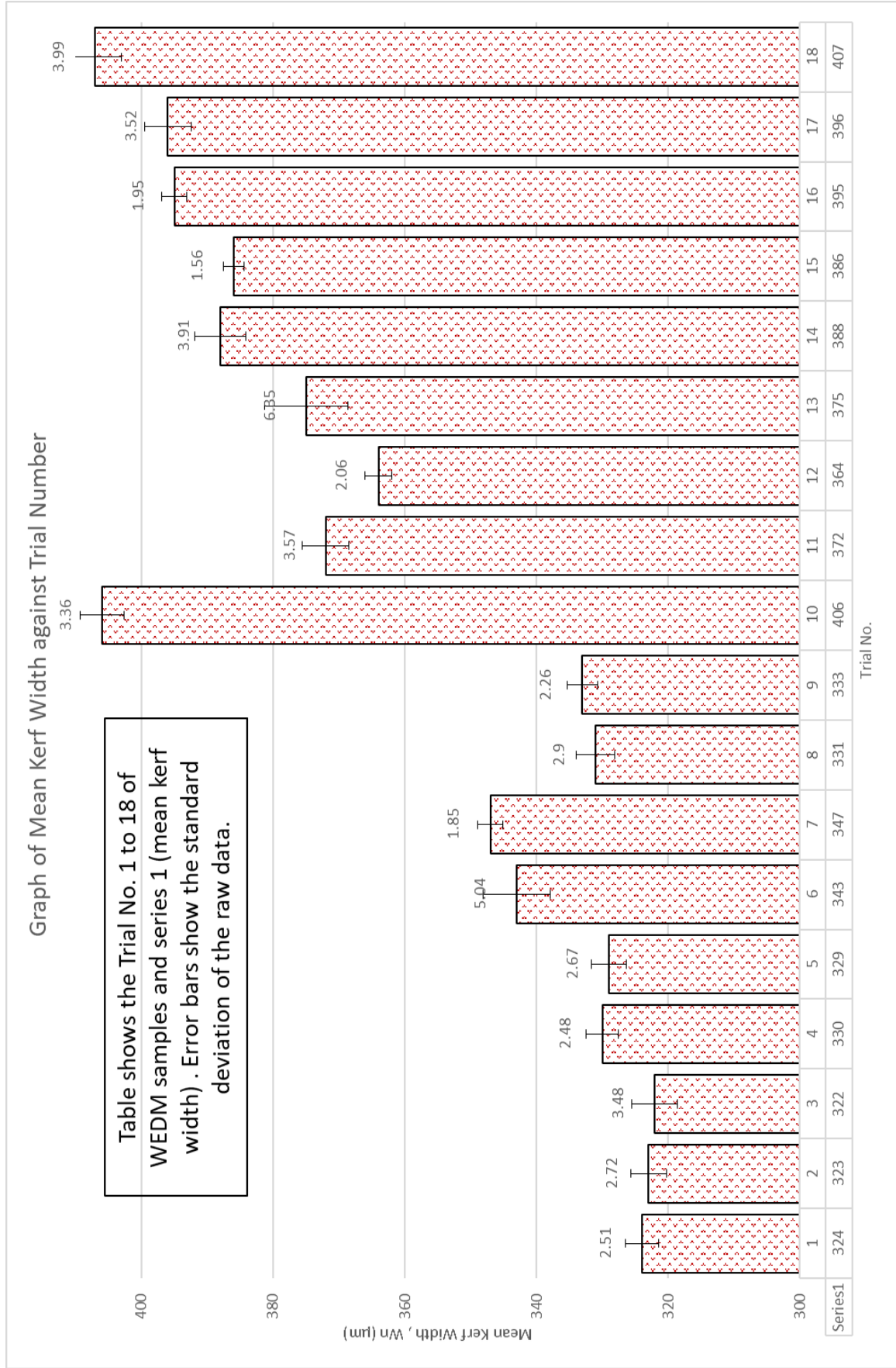

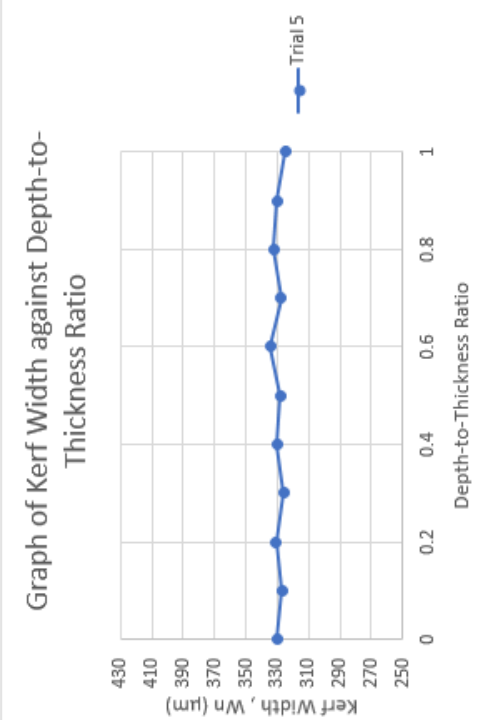
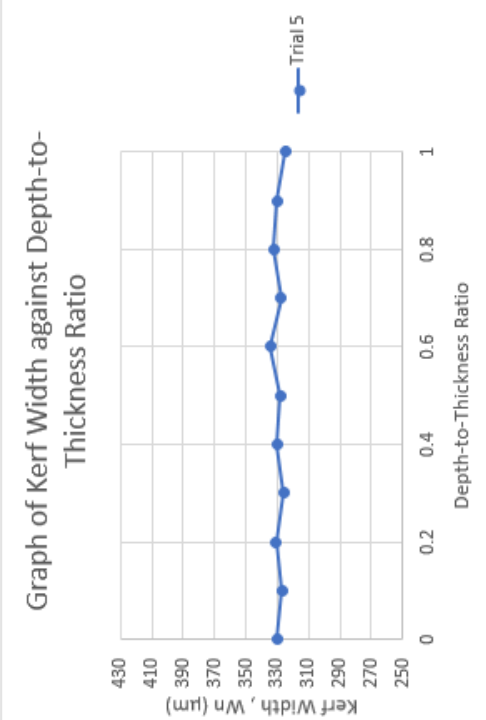
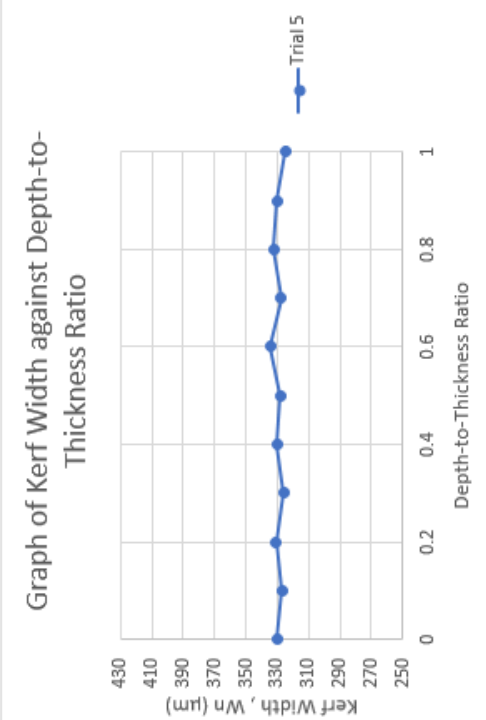

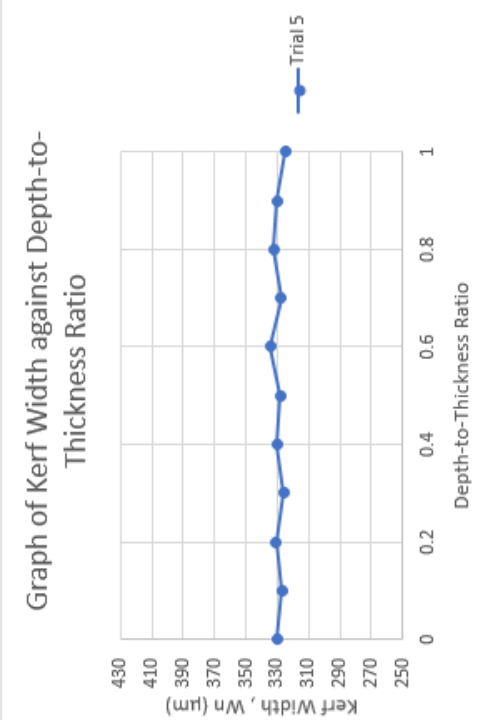
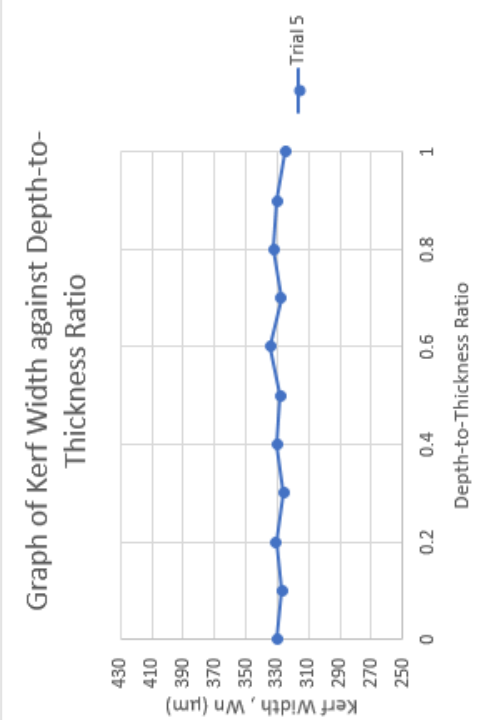
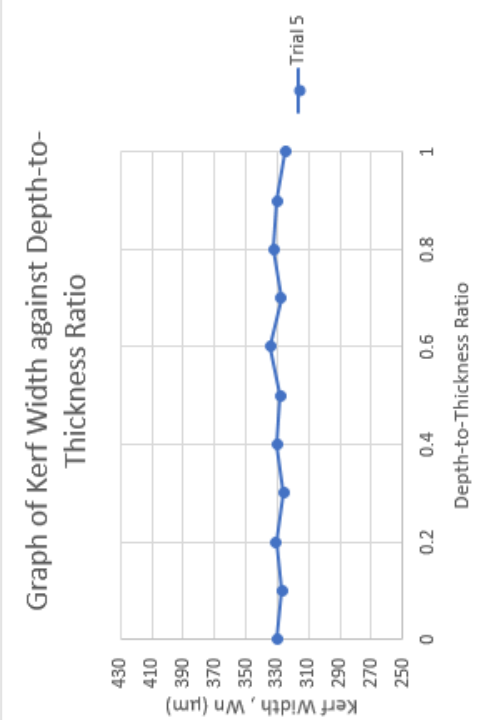
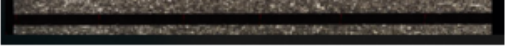

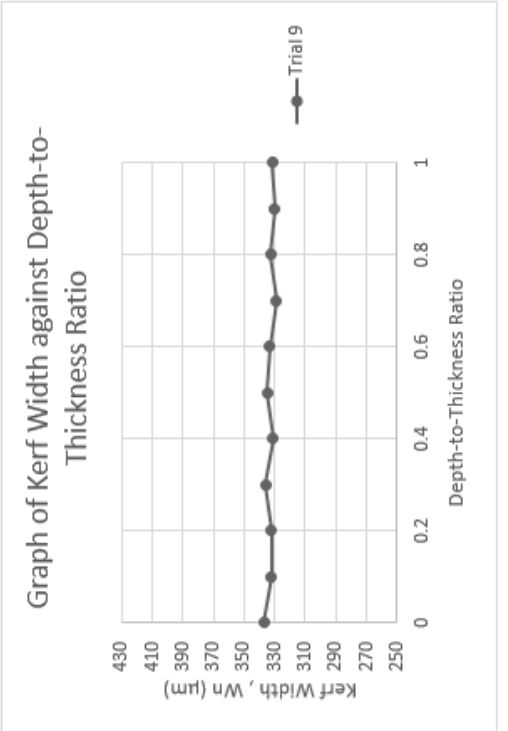
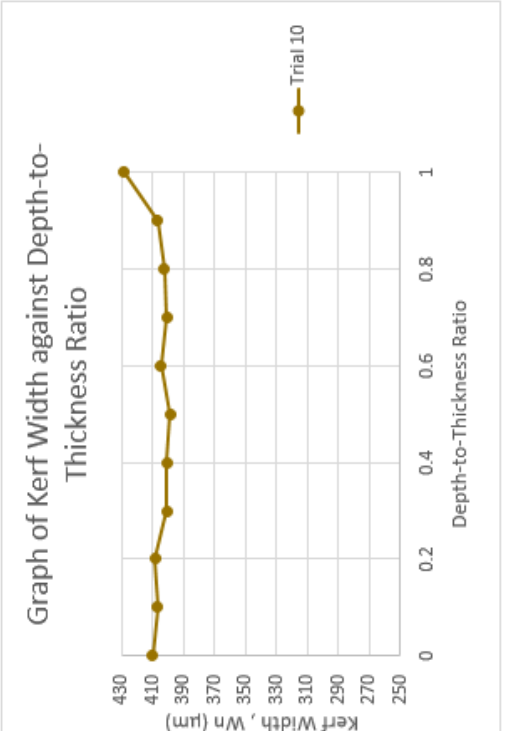
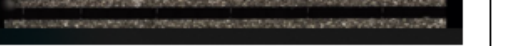

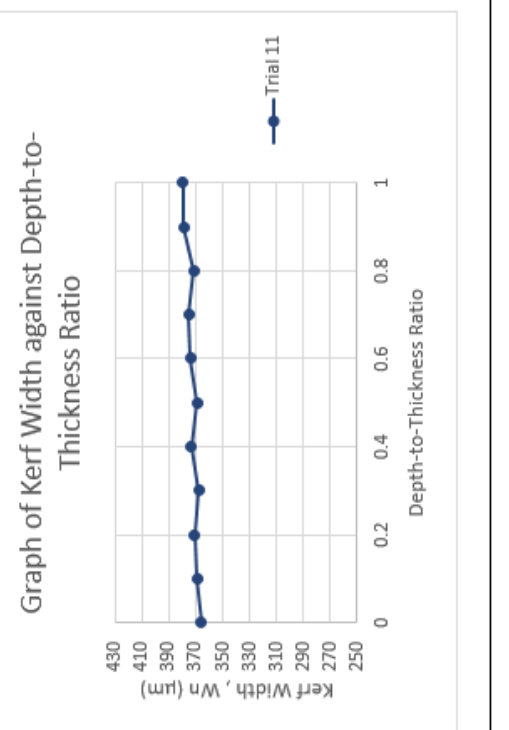
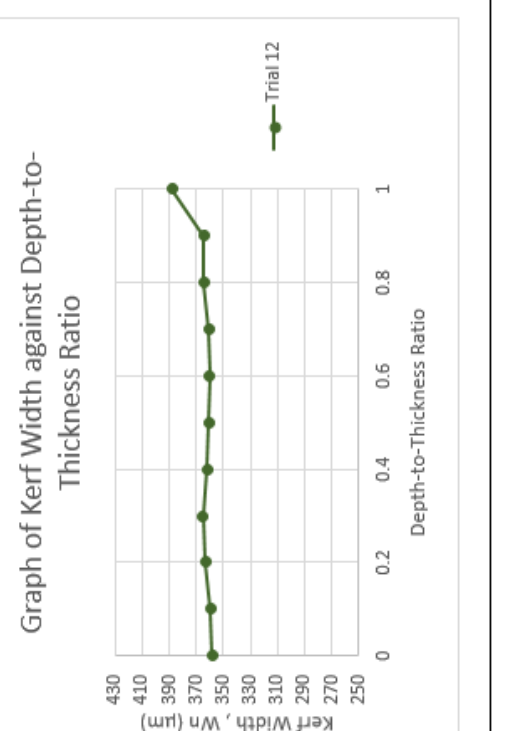


Figure 4.21: The Graph of mean kerf width against Trial 1 to 18.


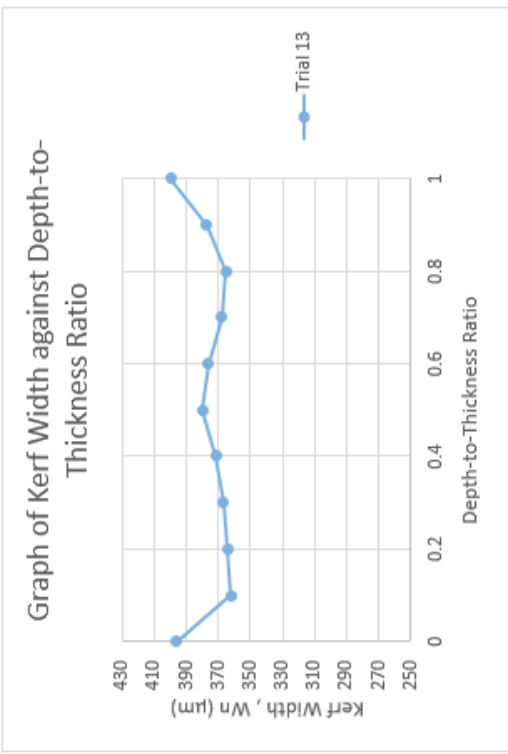
Table 4.21: Graph of Kerf width against Depth-to-thickness Ratio of WEDM.

Trial 1	<p>Graph of Kerf Width against Depth-to-Thickness Ratio</p>	Trial 2	<p>Graph of Kerf Width against Depth-to-Thickness Ratio</p>
Trial 3	<p>Graph of Kerf Width against Depth-to-Thickness Ratio</p>	Trial 4	<p>Graph of Kerf Width against Depth-to-Thickness Ratio</p>

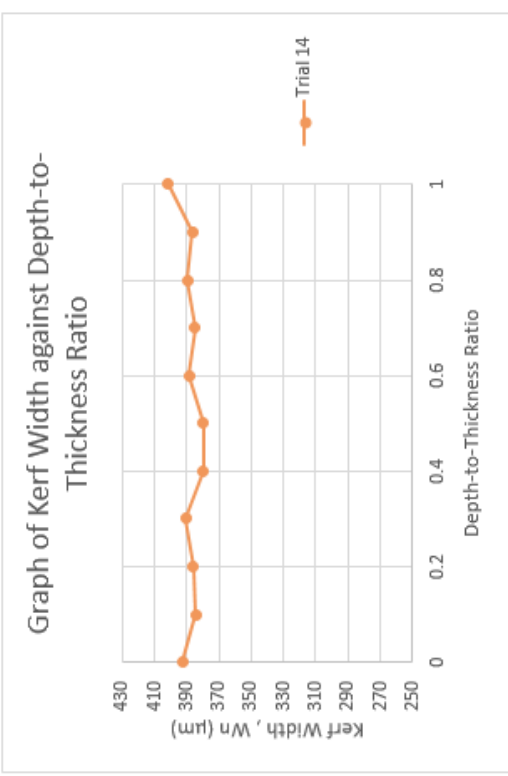
Trial 5		Trial 6	
<p>Graph of Kerf Width against Depth-to-Thickness Ratio</p> 	<p>Graph of Kerf Width against Depth-to-Thickness Ratio</p> 		
Trial 7		Trial 8	
<p>Graph of Kerf Width against Depth-to-Thickness Ratio</p> 	<p>Graph of Kerf Width against Depth-to-Thickness Ratio</p> 		

<p>Trial 9</p> 	<p>Trial 10</p> 																																																
<p>Graph of Kerf Width against Depth-to-Thickness Ratio</p>  <table border="1"> <thead> <tr> <th>Depth-to-Thickness Ratio</th> <th>Kerf Width, Wn (µm)</th> </tr> </thead> <tbody> <tr><td>0.0</td><td>330</td></tr> <tr><td>0.1</td><td>330</td></tr> <tr><td>0.2</td><td>330</td></tr> <tr><td>0.3</td><td>330</td></tr> <tr><td>0.4</td><td>330</td></tr> <tr><td>0.5</td><td>330</td></tr> <tr><td>0.6</td><td>330</td></tr> <tr><td>0.7</td><td>330</td></tr> <tr><td>0.8</td><td>330</td></tr> <tr><td>0.9</td><td>330</td></tr> <tr><td>1.0</td><td>330</td></tr> </tbody> </table> <p>Trial 9</p>	Depth-to-Thickness Ratio	Kerf Width, Wn (µm)	0.0	330	0.1	330	0.2	330	0.3	330	0.4	330	0.5	330	0.6	330	0.7	330	0.8	330	0.9	330	1.0	330	<p>Graph of Kerf Width against Depth-to-Thickness Ratio</p>  <table border="1"> <thead> <tr> <th>Depth-to-Thickness Ratio</th> <th>Kerf Width, Wn (µm)</th> </tr> </thead> <tbody> <tr><td>0.0</td><td>410</td></tr> <tr><td>0.1</td><td>410</td></tr> <tr><td>0.2</td><td>410</td></tr> <tr><td>0.3</td><td>410</td></tr> <tr><td>0.4</td><td>410</td></tr> <tr><td>0.5</td><td>410</td></tr> <tr><td>0.6</td><td>410</td></tr> <tr><td>0.7</td><td>410</td></tr> <tr><td>0.8</td><td>410</td></tr> <tr><td>0.9</td><td>410</td></tr> <tr><td>1.0</td><td>410</td></tr> </tbody> </table> <p>Trial 10</p>	Depth-to-Thickness Ratio	Kerf Width, Wn (µm)	0.0	410	0.1	410	0.2	410	0.3	410	0.4	410	0.5	410	0.6	410	0.7	410	0.8	410	0.9	410	1.0	410
Depth-to-Thickness Ratio	Kerf Width, Wn (µm)																																																
0.0	330																																																
0.1	330																																																
0.2	330																																																
0.3	330																																																
0.4	330																																																
0.5	330																																																
0.6	330																																																
0.7	330																																																
0.8	330																																																
0.9	330																																																
1.0	330																																																
Depth-to-Thickness Ratio	Kerf Width, Wn (µm)																																																
0.0	410																																																
0.1	410																																																
0.2	410																																																
0.3	410																																																
0.4	410																																																
0.5	410																																																
0.6	410																																																
0.7	410																																																
0.8	410																																																
0.9	410																																																
1.0	410																																																
<p>Trial 11</p> 	<p>Trial 12</p> 																																																
<p>Graph of Kerf Width against Depth-to-Thickness Ratio</p>  <table border="1"> <thead> <tr> <th>Depth-to-Thickness Ratio</th> <th>Kerf Width, Wn (µm)</th> </tr> </thead> <tbody> <tr><td>0.0</td><td>370</td></tr> <tr><td>0.1</td><td>370</td></tr> <tr><td>0.2</td><td>370</td></tr> <tr><td>0.3</td><td>370</td></tr> <tr><td>0.4</td><td>370</td></tr> <tr><td>0.5</td><td>370</td></tr> <tr><td>0.6</td><td>370</td></tr> <tr><td>0.7</td><td>370</td></tr> <tr><td>0.8</td><td>370</td></tr> <tr><td>0.9</td><td>370</td></tr> <tr><td>1.0</td><td>370</td></tr> </tbody> </table> <p>Trial 11</p>	Depth-to-Thickness Ratio	Kerf Width, Wn (µm)	0.0	370	0.1	370	0.2	370	0.3	370	0.4	370	0.5	370	0.6	370	0.7	370	0.8	370	0.9	370	1.0	370	<p>Graph of Kerf Width against Depth-to-Thickness Ratio</p>  <table border="1"> <thead> <tr> <th>Depth-to-Thickness Ratio</th> <th>Kerf Width, Wn (µm)</th> </tr> </thead> <tbody> <tr><td>0.0</td><td>350</td></tr> <tr><td>0.1</td><td>350</td></tr> <tr><td>0.2</td><td>350</td></tr> <tr><td>0.3</td><td>350</td></tr> <tr><td>0.4</td><td>350</td></tr> <tr><td>0.5</td><td>350</td></tr> <tr><td>0.6</td><td>350</td></tr> <tr><td>0.7</td><td>350</td></tr> <tr><td>0.8</td><td>350</td></tr> <tr><td>0.9</td><td>350</td></tr> <tr><td>1.0</td><td>350</td></tr> </tbody> </table> <p>Trial 12</p>	Depth-to-Thickness Ratio	Kerf Width, Wn (µm)	0.0	350	0.1	350	0.2	350	0.3	350	0.4	350	0.5	350	0.6	350	0.7	350	0.8	350	0.9	350	1.0	350
Depth-to-Thickness Ratio	Kerf Width, Wn (µm)																																																
0.0	370																																																
0.1	370																																																
0.2	370																																																
0.3	370																																																
0.4	370																																																
0.5	370																																																
0.6	370																																																
0.7	370																																																
0.8	370																																																
0.9	370																																																
1.0	370																																																
Depth-to-Thickness Ratio	Kerf Width, Wn (µm)																																																
0.0	350																																																
0.1	350																																																
0.2	350																																																
0.3	350																																																
0.4	350																																																
0.5	350																																																
0.6	350																																																
0.7	350																																																
0.8	350																																																
0.9	350																																																
1.0	350																																																

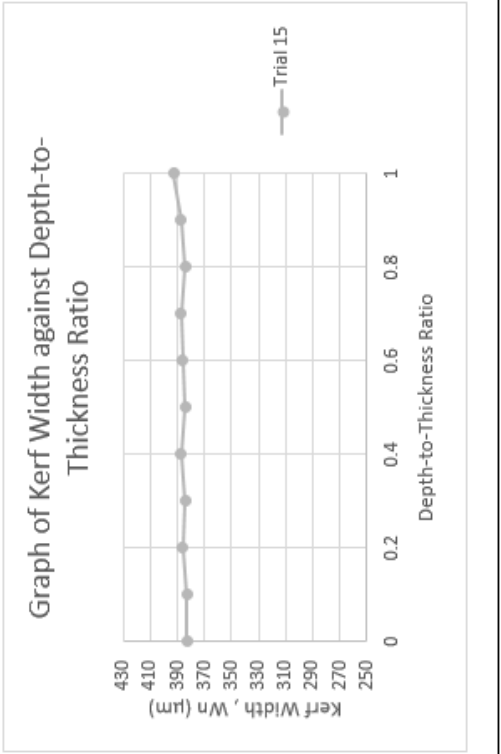
Trial 13

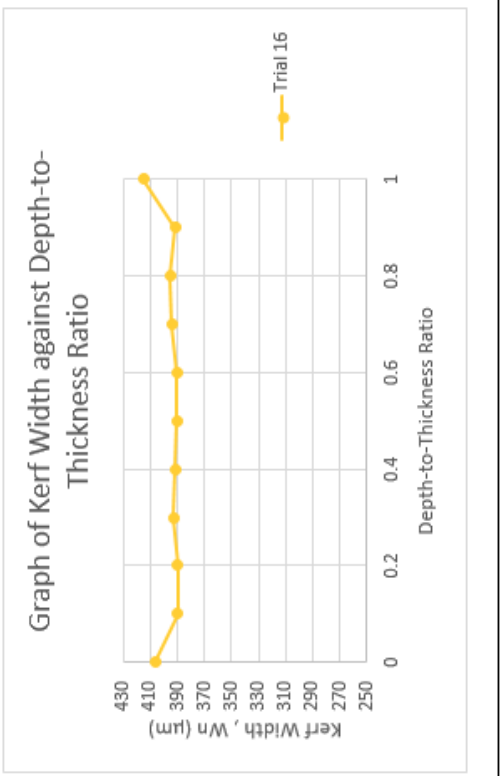
Trial 14



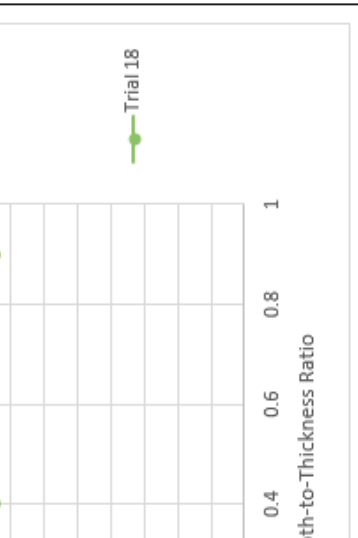
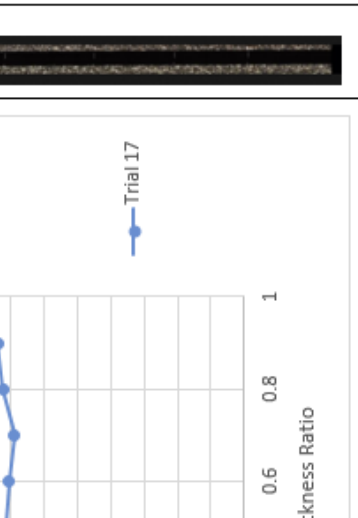



Trial 15

Trial 16

<p>Trial 17</p> 	<p>Trial 18</p> 	<p>Graph of Kerf Width against Depth-to-Thickness Ratio</p>  <table border="1"> <thead> <tr> <th>Depth-to-Thickness Ratio</th> <th>Kerf Width, W_n (μm)</th> </tr> </thead> <tbody> <tr><td>0.05</td><td>405</td></tr> <tr><td>0.1</td><td>400</td></tr> <tr><td>0.2</td><td>395</td></tr> <tr><td>0.3</td><td>390</td></tr> <tr><td>0.4</td><td>385</td></tr> <tr><td>0.5</td><td>380</td></tr> <tr><td>0.6</td><td>385</td></tr> <tr><td>0.7</td><td>390</td></tr> <tr><td>0.8</td><td>395</td></tr> <tr><td>0.9</td><td>400</td></tr> <tr><td>1.0</td><td>405</td></tr> </tbody> </table>	Depth-to-Thickness Ratio	Kerf Width, W_n (μm)	0.05	405	0.1	400	0.2	395	0.3	390	0.4	385	0.5	380	0.6	385	0.7	390	0.8	395	0.9	400	1.0	405	<p>Graph of Kerf Width against Depth-to-Thickness Ratio</p>  <table border="1"> <thead> <tr> <th>Depth-to-Thickness Ratio</th> <th>Kerf Width, W_n (μm)</th> </tr> </thead> <tbody> <tr><td>0.05</td><td>405</td></tr> <tr><td>0.1</td><td>400</td></tr> <tr><td>0.2</td><td>395</td></tr> <tr><td>0.3</td><td>390</td></tr> <tr><td>0.4</td><td>385</td></tr> <tr><td>0.5</td><td>380</td></tr> <tr><td>0.6</td><td>385</td></tr> <tr><td>0.7</td><td>390</td></tr> <tr><td>0.8</td><td>395</td></tr> <tr><td>0.9</td><td>400</td></tr> <tr><td>1.0</td><td>405</td></tr> </tbody> </table>	Depth-to-Thickness Ratio	Kerf Width, W_n (μm)	0.05	405	0.1	400	0.2	395	0.3	390	0.4	385	0.5	380	0.6	385	0.7	390	0.8	395	0.9	400	1.0	405
Depth-to-Thickness Ratio	Kerf Width, W_n (μm)																																																		
0.05	405																																																		
0.1	400																																																		
0.2	395																																																		
0.3	390																																																		
0.4	385																																																		
0.5	380																																																		
0.6	385																																																		
0.7	390																																																		
0.8	395																																																		
0.9	400																																																		
1.0	405																																																		
Depth-to-Thickness Ratio	Kerf Width, W_n (μm)																																																		
0.05	405																																																		
0.1	400																																																		
0.2	395																																																		
0.3	390																																																		
0.4	385																																																		
0.5	380																																																		
0.6	385																																																		
0.7	390																																																		
0.8	395																																																		
0.9	400																																																		
1.0	405																																																		

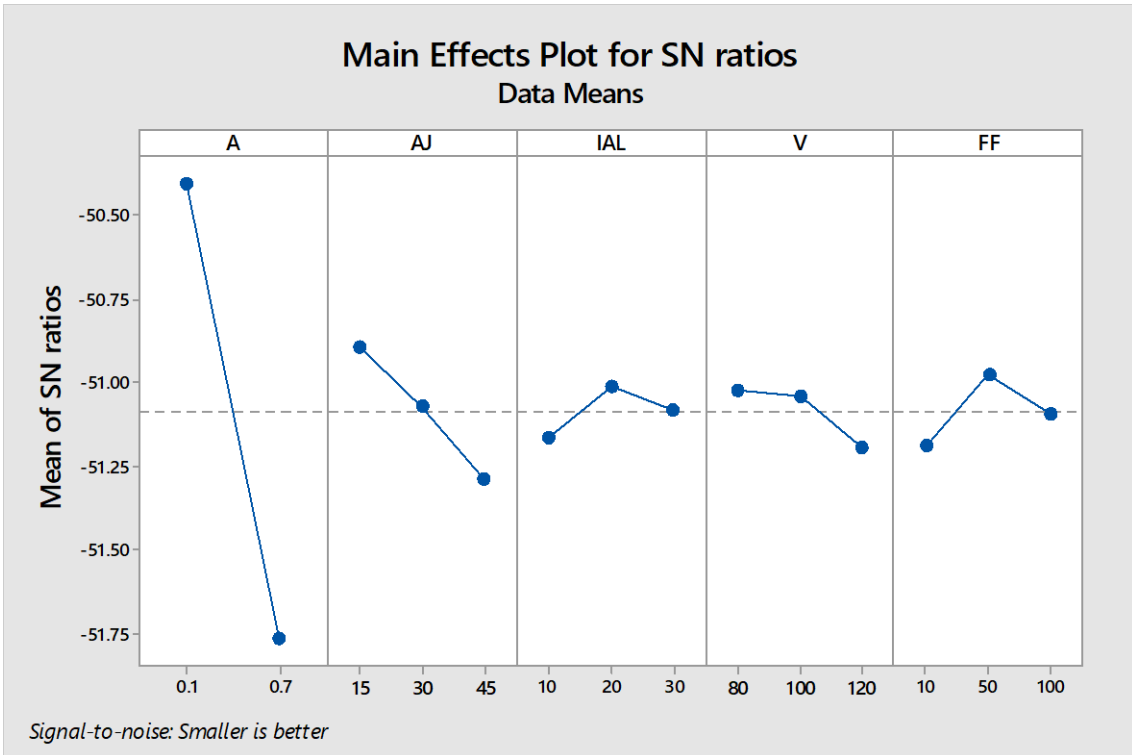


Figure 4.22: Main effect plot of S/N for WEDM kerf width.

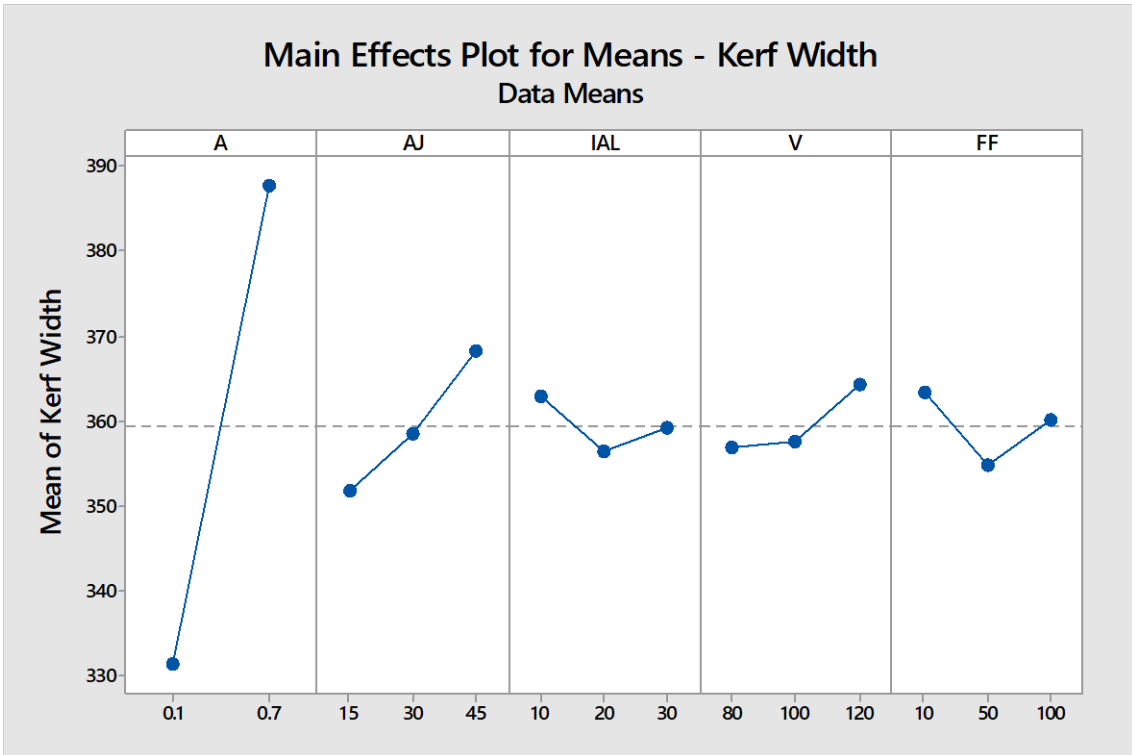


Figure 4.23: Main effect plot of Means for WEDM kerf width.

Table 4.22: ANOVA analysis of WEDM kerf width.

Factor Symbol	DOF	Sum of Square	Mean of Square	F- value	P- value	Contribution (%)
A μs	1	14342.2	14342.2	110.06	0.000	85.64
AJ V	2	802.4	401.2	3.08	0.102	4.79
IAL A	2	125.3	62.7	0.48	0.635	0.75
V V	2	206.8	103.4	0.79	0.485	1.23
FF %	2	227.9	113.9	0.87	0.453	1.36
Error	8	1042.5	130.3			6.22
Total	17	16747.1				100

A confirmation tests to predict the kerf width responses under optimum condition has been conducted as shown in Table 4.23. The predicted and experimental results demonstrated a close adherence to the model trends with an error of 0.3%. The experimental results confirmed the validity of Taguchi method.

4.23: Confirmation test results for WEDM kerf width.

Response	Mean		S/N ratio (dB)		Error %
	Predicted	Experiment	Predicted	Experiment	
Kerf width	313.20	320.20	-49.96	-50.11	0.30

4.2.3 Surface Roughness

1. 2D Surface Roughness

Table 4.24: Summary of the mean 2D surface roughness parameters results.

Trial No.	A μs	AJ V	IAL A	V V	FF %	Ra (μm)			Mean		
						6mm	18mm	Mean	Rsk	Rku	Rq
1	0.1	15	10	80	10	1.86	1.95	1.91	-0.39	2.96	2.38
2	0.1	15	20	100	50	1.81	1.94	1.87	-0.36	2.75	2.23
3	0.1	15	30	120	100	1.9	1.97	1.93	-0.37	2.95	2.40
4	0.1	30	10	80	50	1.83	1.97	1.9	-0.37	3.03	2.38
5	0.1	30	20	100	100	1.98	2.11	2.04	-0.22	3.04	2.54
6	0.1	30	30	120	10	1.88	1.89	1.88	-0.39	2.96	2.35
7	0.1	45	10	100	10	1.83	1.9	1.87	-0.34	2.99	2.34
8	0.1	45	20	120	50	1.89	1.96	1.92	-0.30	2.90	2.40
9	0.1	45	30	80	100	1.93	1.97	1.95	-0.21	2.99	2.44
10	0.7	15	10	120	100	3.29	3.37	3.33	-0.21	2.85	4.15
11	0.7	15	20	80	10	3.26	3.12	3.19	-0.27	2.62	3.91
12	0.7	15	30	100	50	3.12	3.35	3.24	-0.33	2.75	4.01
13	0.7	30	10	100	100	3.15	3.15	3.15	-0.16	2.75	3.90
14	0.7	30	20	120	10	3.15	2.94	3.04	-0.29	2.84	3.79
15	0.7	30	30	80	50	3.12	3.17	3.14	-0.24	2.70	3.89
16	0.7	45	10	120	50	3.42	3.35	3.38	-0.23	2.56	4.14
17	0.7	45	20	80	100	3.18	3.3	3.24	-0.25	2.8	4.03
18	0.7	45	30	100	10	3.06	3.16	3.11	-0.25	2.64	3.84

Table 4.24 exhibits the 2D surface roughness parameters. It has been noticed that the mean Ra of trial 1 to 9 are very close and in the range of 1.9 to 2.00 μm whilst the Ra of trial 10 to 18 are more than 1.5 times higher over 3.0 μm . This is mainly due to the increase in pulse-on time. According to the main effect plots in Figure 4.25, the optimal performance can be achieved to minimize Ra at pulse on time, A 0.1 μs (level 1), average machining voltage, AJ 30 V (level 2), ignition pulse current, IAL 30 A (level 3), open gap voltage, V 100 V (level 2) and function of frequency, FF 10 % (level 1). The optimum condition of design parameters for Ra is defined as $A_1B_2C_3D_2E_1$. From ANOVA analysis in Table 4.25, it was noticed that at 95% confidence level, only pulse on time is statistically significant in minimizing Ra. Smaller pulse on time, the discharge energy decreases, the volume of workpiece material removed is reduced, smaller spherical cavities are generated, smaller Ra.

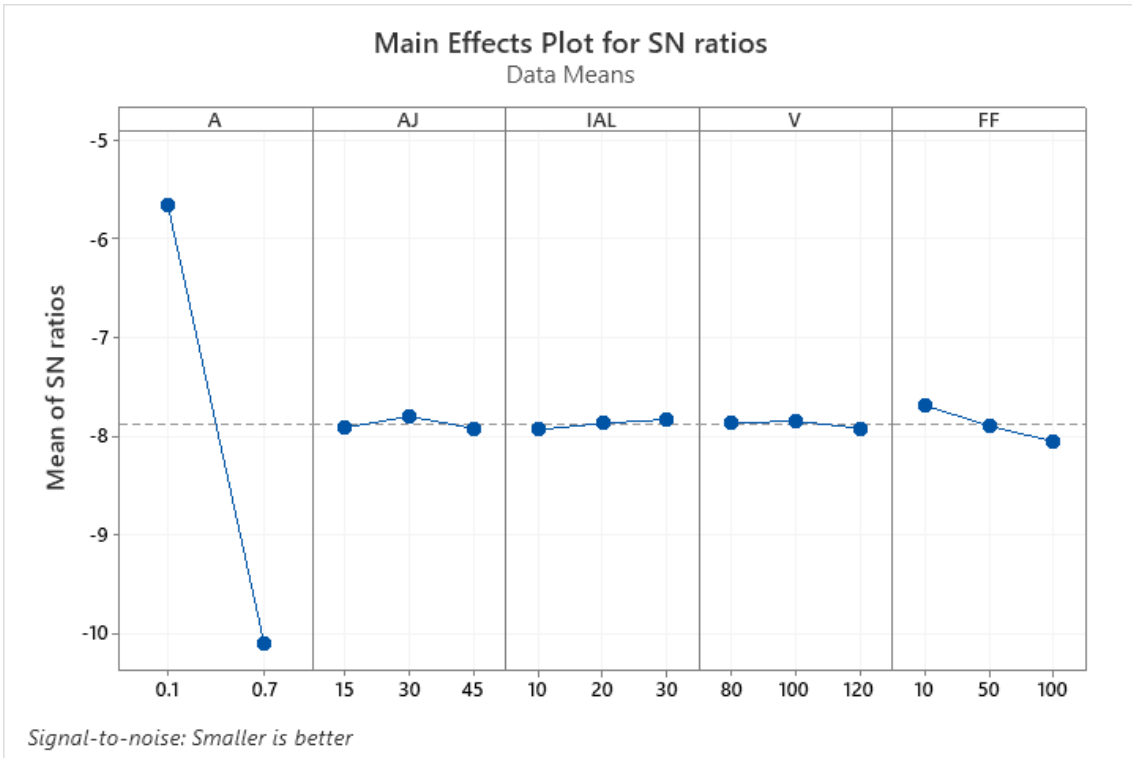


Figure 4.24: Main effect plot of S/N for WEDM Ra.

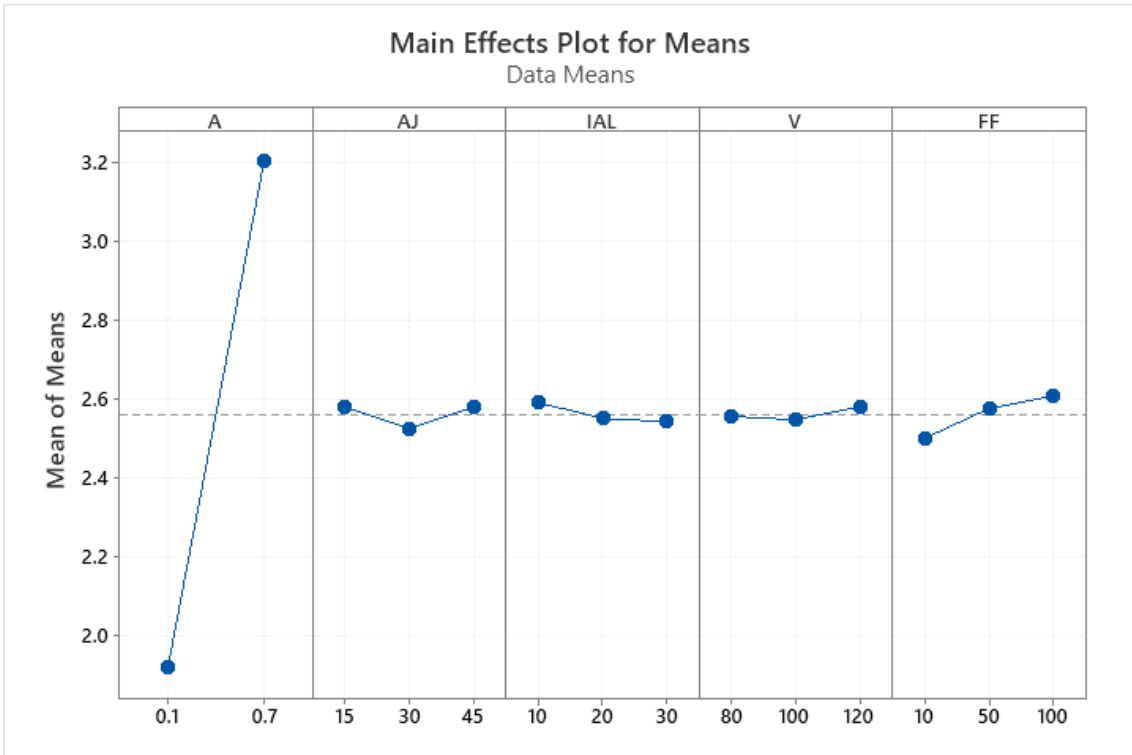


Figure 4.25: Main effect plot of Means for WEDM Ra.

Table 4.25: ANOVA analysis of WEDM Ra.

Factor Symbol	DOF	Sum of Square	Mean of Square	F-value	P- value	Contribution (%)
A μs	1	7.41125	7.41125	1061.91	0.000	98.47
AJ V	2	0.01138	0.00569	0.82	0.476	0.15
IAL A	2	0.00801	0.00401	0.57	0.585	0.11
V V	2	0.00361	0.00181	0.26	0.778	0.05
FF %	2	0.03601	0.01801	2.58	0.137	0.48
Error	8	0.05583	0.00698			0.74
Total	17	7.52609				100

Table 4.26: Confirmation test results for WEDM Ra.

Response	Mean		S/N ratio (dB)		Error %
	Predicted	Experiment	Predicted	Experiment	
Ra	1.79	1.82	-5.31	-5.20	2.07

2.

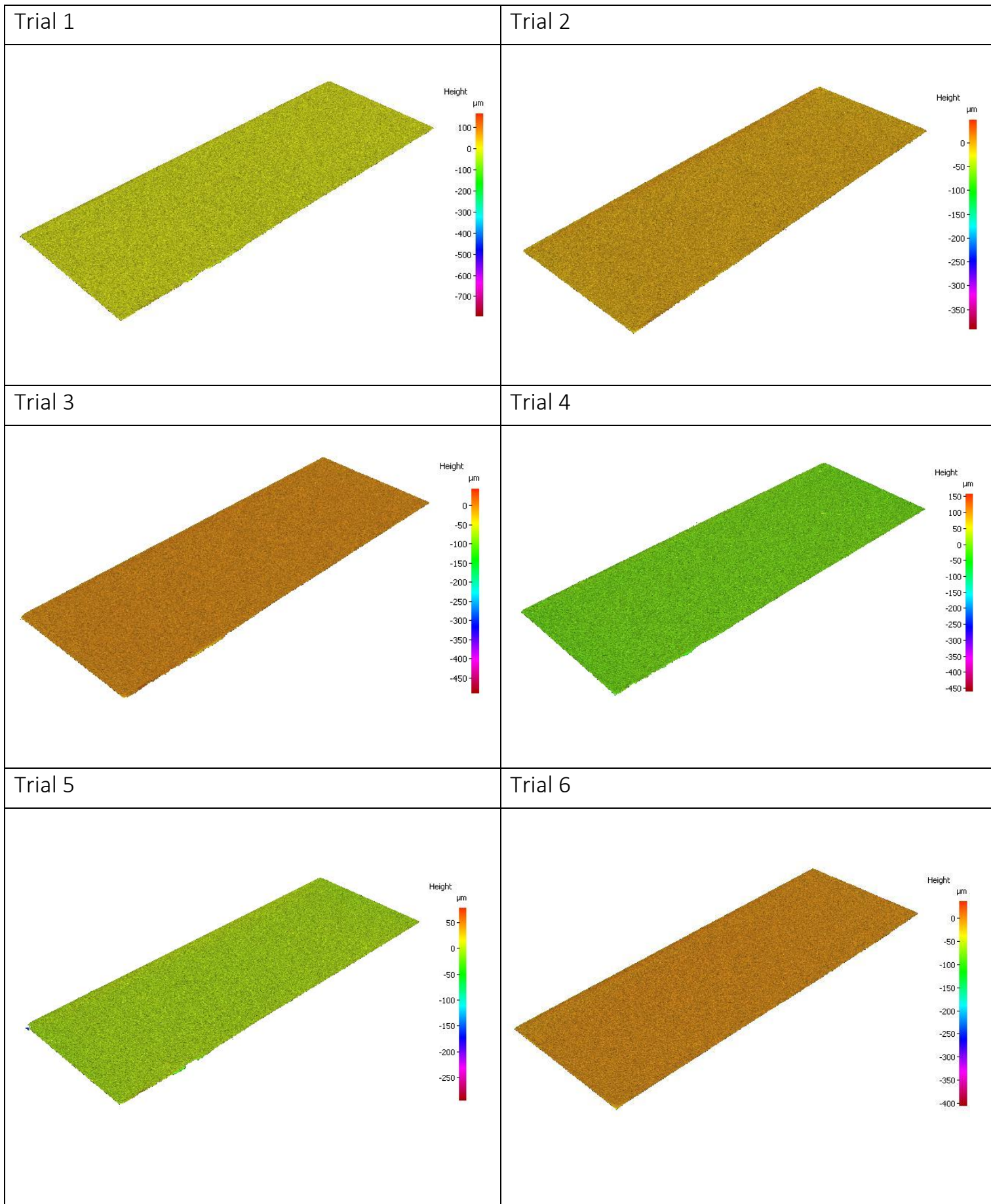
3. 3D surface roughness

Table 4.27: Summary of the mean 3D surface roughness parameters results.

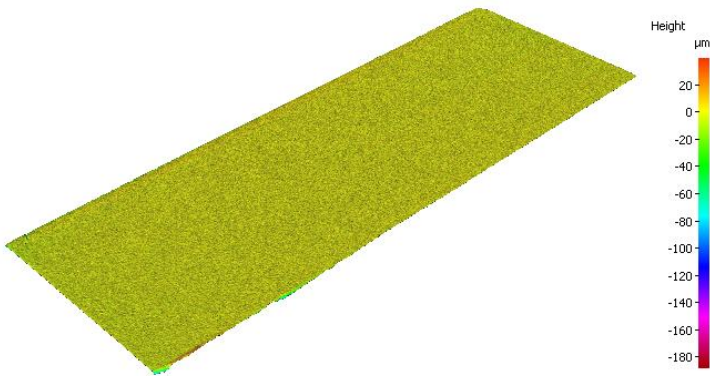
Trial No.	A μs	AJ V	IAL A	V V	FF %	Sa (μm)			Mean		
						Upper	Lower	Mean	Ssk	Sku	Sq
1	0.1	15	10	80	10	1.71	1.74	1.73	-0.235	3.885	2.17
2	0.1	15	20	100	50	1.72	1.75	1.74	-0.385	3.22	2.175
3	0.1	15	30	120	100	1.6	1.71	1.66	-0.345	3.19	2.075
4	0.1	30	10	80	50	1.84	1.82	1.83	-0.32	3.835	2.31
5	0.1	30	20	100	100	1.88	1.94	1.91	-0.03	6.965	2.43
6	0.1	30	30	120	10	1.78	1.85	1.82	-0.28	3.406	2.28
7	0.1	45	10	100	10	1.77	1.84	1.81	-0.17	3.105	2.26
8	0.1	45	20	120	50	1.8	1.81	1.81	-0.175	4.67	2.275
9	0.1	45	30	80	100	1.8	1.89	1.85	-0.4	3.175	2.315
10	0.7	15	10	120	100	3.31	3.34	3.33	-0.2	3.345	4.17
11	0.7	15	20	80	10	3.29	3.32	3.31	-0.3	2.99	4.125
12	0.7	15	30	100	50	3.24	3.3	3.27	-0.26	3.025	4.085
13	0.7	30	10	100	100	3.22	3.25	3.24	-0.255	3	4.04
14	0.7	30	20	120	10	3.08	3.12	3.10	-0.24	3.48	3.895
15	0.7	30	30	80	50	3.23	3.27	3.25	-0.245	2.965	4.055
16	0.7	45	10	120	50	3.24	3.29	3.27	-0.255	2.99	4.075
17	0.7	45	20	80	100	3.29	3.38	3.34	-0.315	3.02	4.17
18	0.7	45	30	100	10	3.13	3.13	3.13	-0.255	2.99	3.9

Table 4.28: Three-dimensional (3D) topography maps for the WEDM cutting

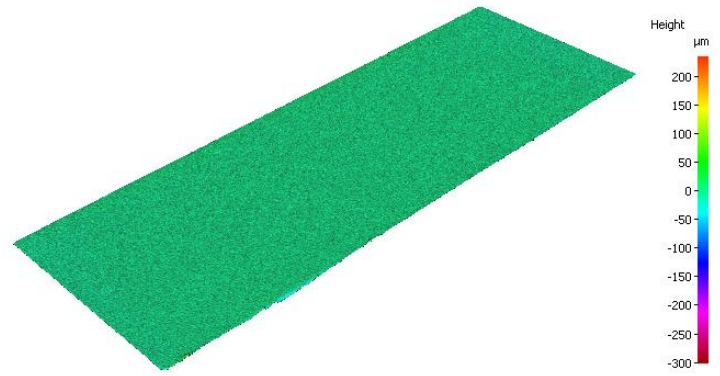
front Trial 1 to 18.



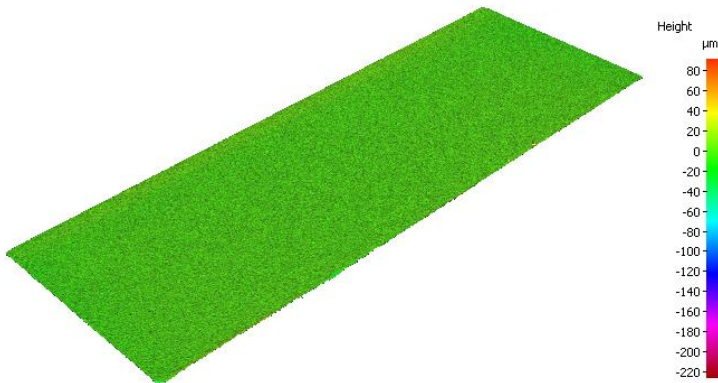
Trial 7



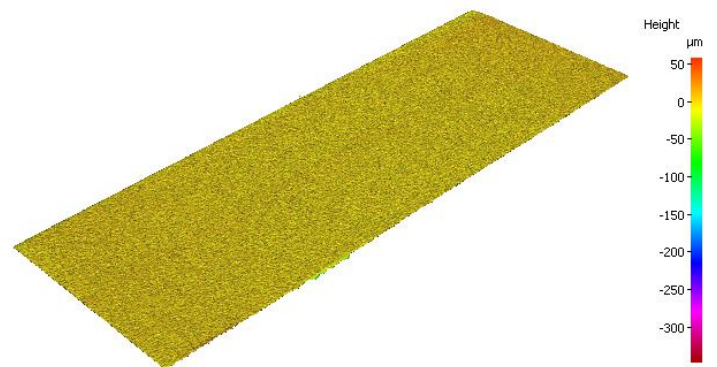
Trial 8



Trial 9



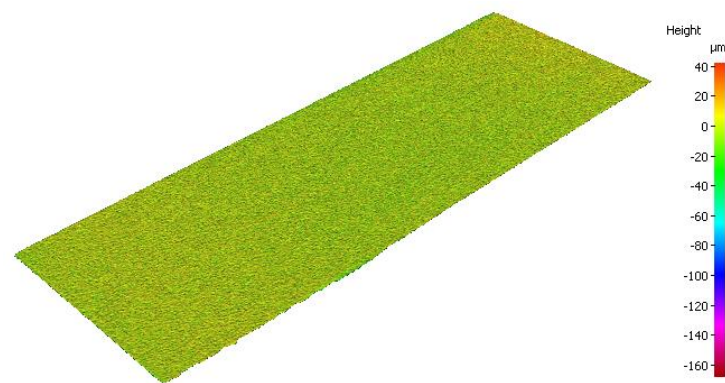
Trial 10



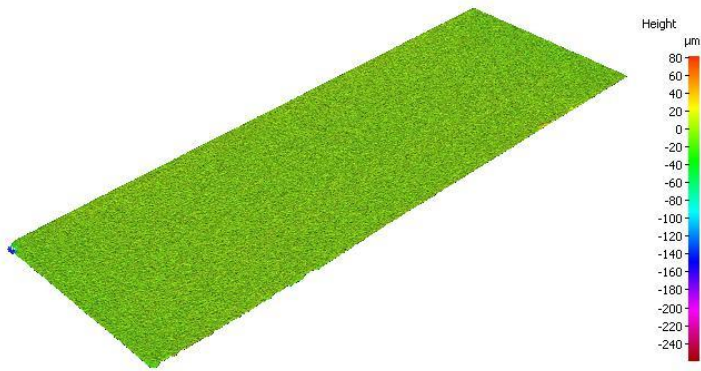
Trial 11



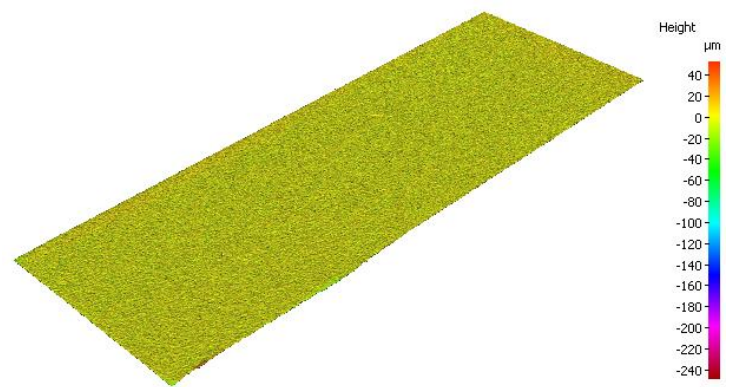
Trial 12



Trial 13



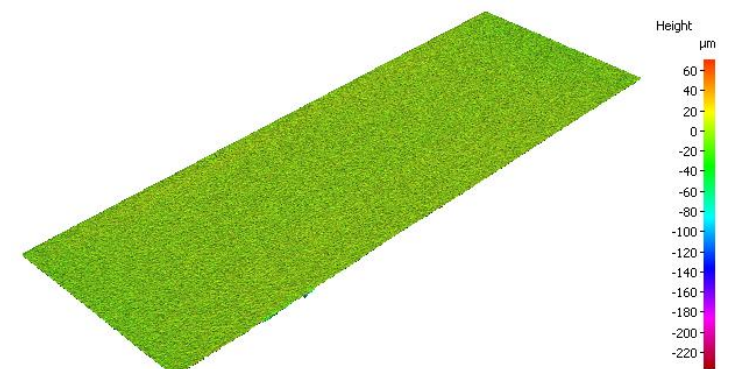
Trial 14



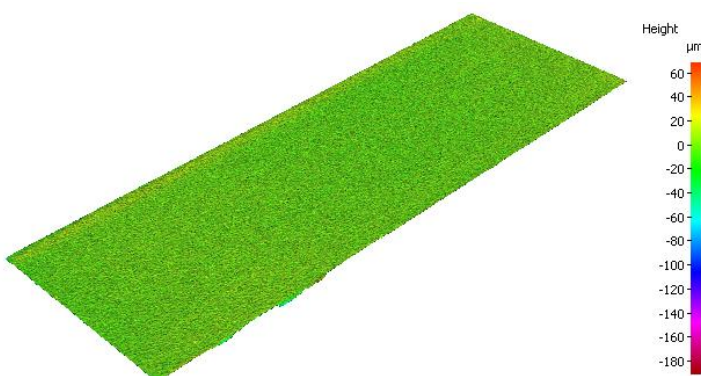
Trial 15



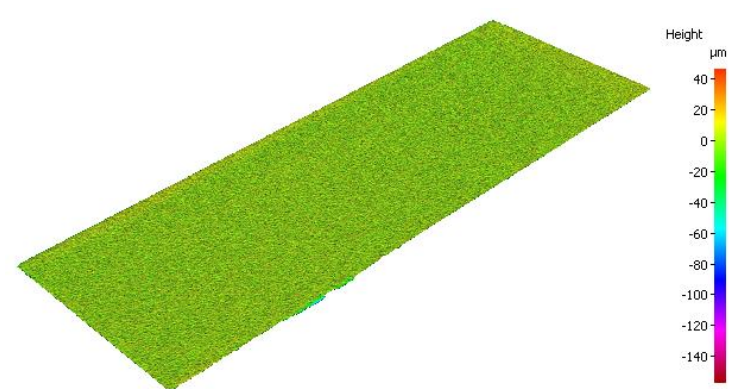
Trial 16



Trial 17



Trial 18



The surface topography map shows that the surface machined by the WEDM is considerably flat. The main effects plot for S/N ratio and means are shown in Figure 4.26 and Figure 4.27. It is clear that the maximum S/N ratio occurs at pulse on time, A 0.1 μ s (level 1), average machining voltage, AJ 15 V (level 1), ignition pulse current, I_{AL} 30 A (level 3), open gap voltage, V 120 V (level 3) and function of frequency, FF 10 % (level 1). The optimum condition of design parameters for S_a is defined as $A_1B_1C_3D_3E_1$. The pulse on time and average machining voltage increases, the discharge energy increases, the number of electrons striking the work surface increases, more material is eroded from the work surface per discharge, deeper craters were generated.

Similar to R_a , the ANOVA as shown in Table 4.29 revealed that only pulse on time is the significant factor in minimizing S_a with PCR=98.96%. The confirmation test was performed and the predicted and experimental results were reported in Table 30. The percentage of error between the predicted and experimental S/N ratio is $3.53 < 5\%$, hence, the Taguchi model is valid.

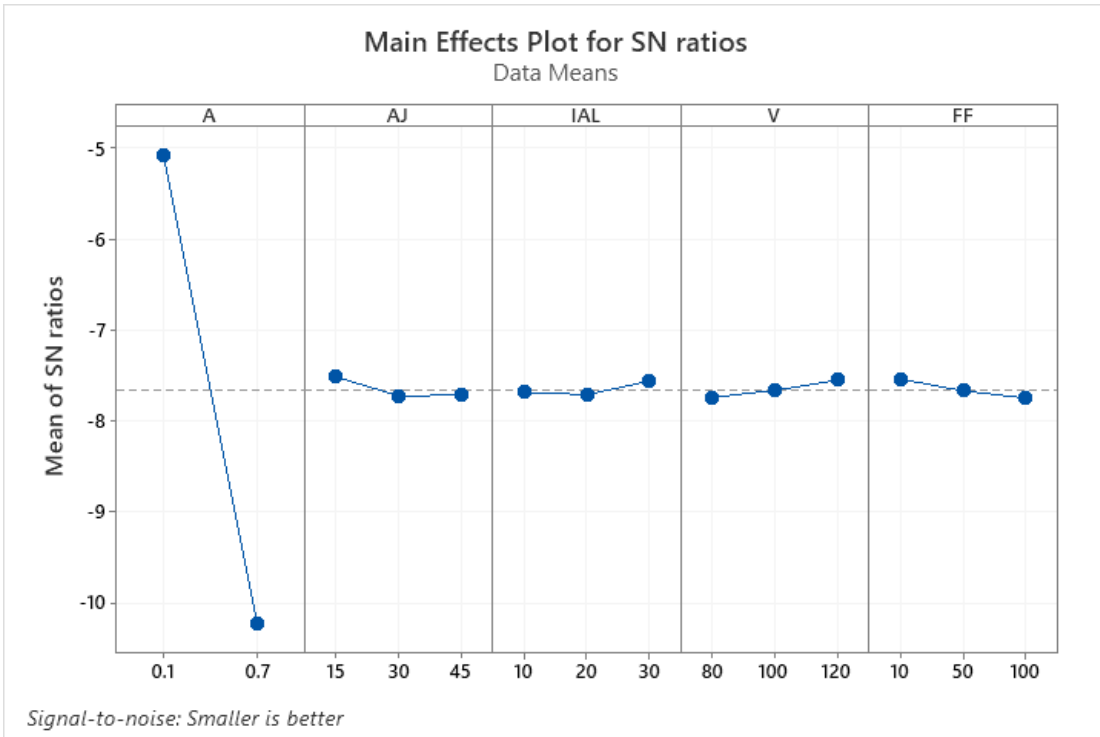


Figure 4.26 Main effect plot of S/N for WEDM Sa.

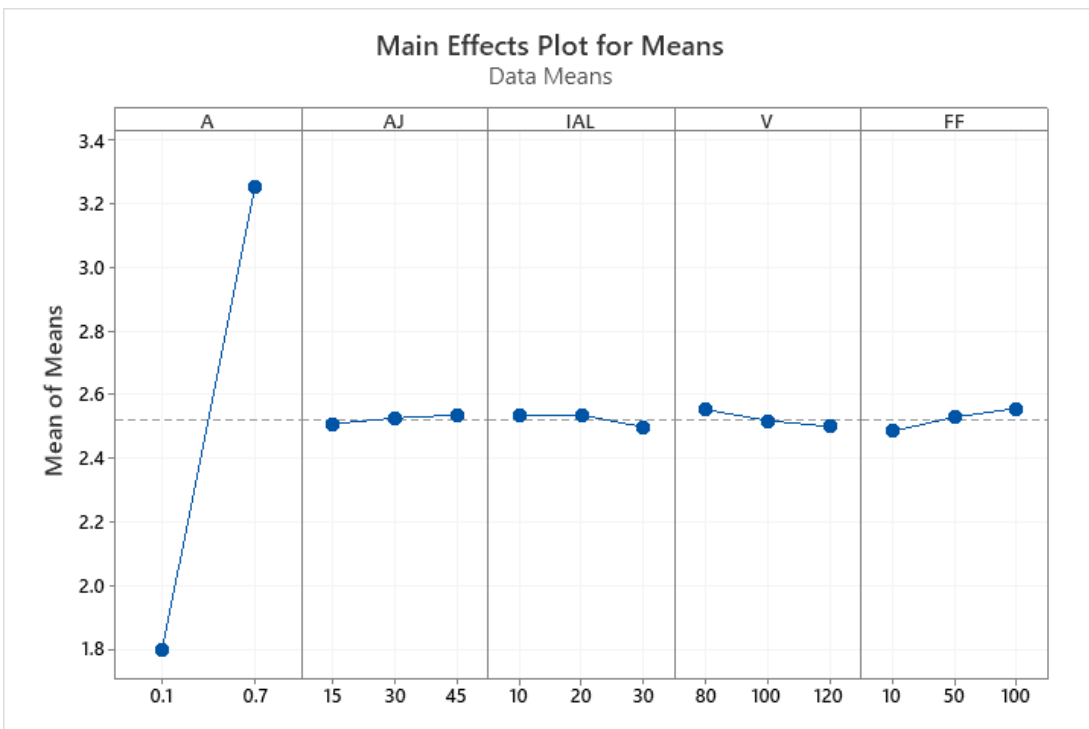


Figure 4.27: Main effect plot of Means for WEDM Sa.

Table 4.29: ANOVA analysis of WEDM Sa.

Factor Symbol	DOF	Sum of Square	Mean of Square	F-value	P- value	Contribution (%)
A μs	1	9.50480	9.50480	1134.90	0.000	98.96
AJ V	2	0.00248	0.00124	0.15	0.865	0.03
IAL A	2	0.00588	0.00294	0.35	0.714	0.06
V V	2	0.00881	0.00441	0.53	0.610	0.09
FF %	2	0.01574	0.00787	0.94	0.430	0.16
Error	8	0.06700	0.00838			0.70
Total	17	9.60471				100

Table 4.30: Confirmation test results for WEDM kerf Sa.

Response	Mean		S/N ratio (dB)		Error %
	Predicted	Experiment	Predicted	Experiment	
Sa	1.69	1.74	-4.64	-4.81	3.53

4.3.4 Micro-hardness

The microhardness plot showed that there is an increase of microhardness on the machined surface due to the heat affected zone. WEDM utilises thermal energy to melt and vaporised workpiece material. The thermal impact of rapid heating and cooling leads to quenching effect, resulting the molten material and electrode material solidify on the workpiece surface and increase in the bulk hardness of the material. Figure 4.29 shows the main effects plot for mean micro-hardness versus the factor parameters. The optimal machining parameters for microhardness: pulse on time, A 0.7 μ s (level 2), average machining voltage, AJ 30 V (level 2), ignition pulse current, IAL 30 A (level 3), open gap voltage, V 100 V (level 2) and function of frequency, FF 50 % (level 2). The optimum condition of design parameters for microhardness is defined as $A_2B_2C_3D_2E_2$. According to ANOVA analysis in Table 4.31, it is evident that the most significant factor in affecting the microhardness is pulse on time (PCR=60.78%) followed by average machining voltage (PCR=16.6%). The pulse-on time increases, the discharge energy increases. This allows more efficient of heating and quenching process and decreases the recast layer thickness. The average machining voltage at moderate level is desirable. Increase in the supply

voltage, a large percentage of the workpiece is heated to melting stage and redeposited on the surface as recast layer.

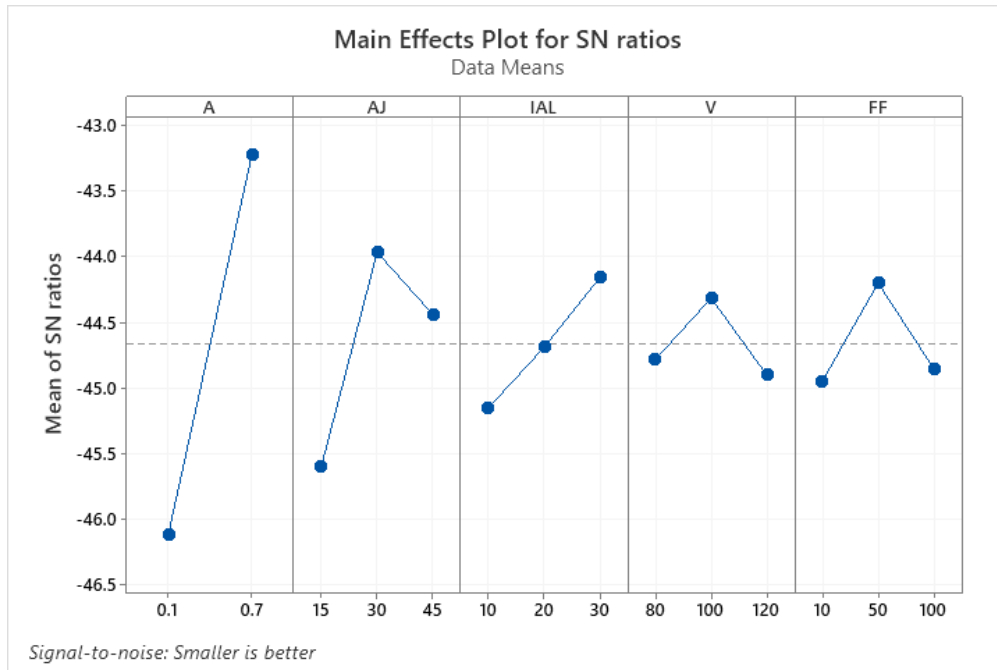


Figure 4.28: Main effect plot of S/N for WEDM microhardness.

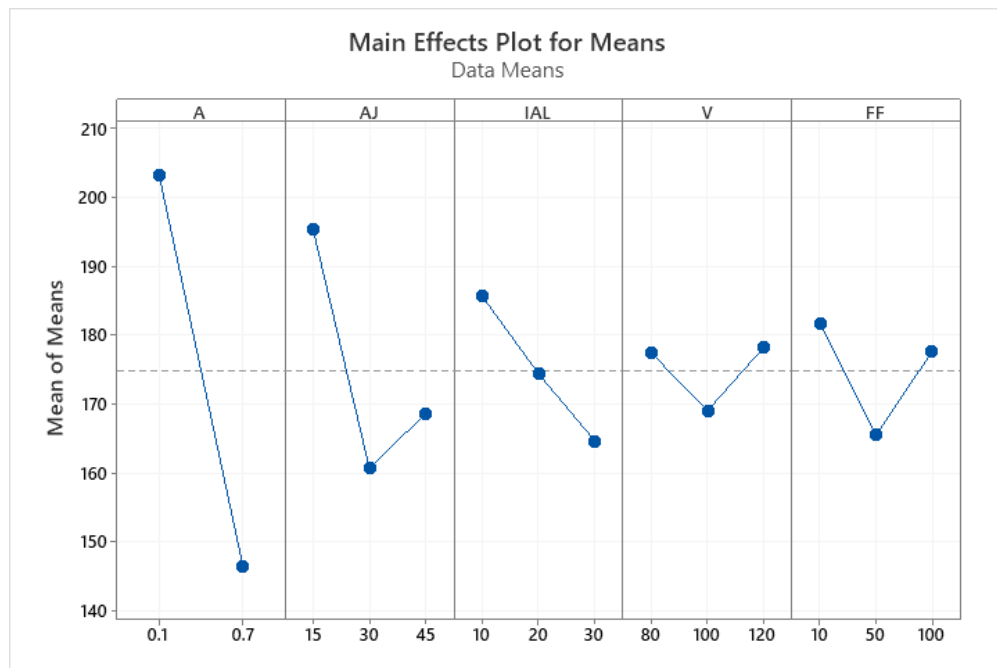


Figure 4.29: Main effect plot of Means for WEDM microhardness.

Table 4.31: ANOVA analysis of WEDM microhardness.

Factor Symbol	DOF	Sum of Square	Mean of Square	F- value	P- value	Contribution (%)
A μs	1	14534.0	14534.0	39.76	0.000	60.78
AJ V	2	3969.3	1984.6	5.43	0.032	16.6
IAL A	2	1330.2	665.1	1.82	0.223	5.56
V V	2	311.1	155.5	0.43	0.337	1.30
FF %	2	844.6	422.3	1.16	0.362	3.53
Error	8	2924.2	365.5			12.23
Total	17	23913.3				100.00

The predicted and experimental results of the confirmation test are given in Table 4.32. It is observed that the microhardness result was improved using the optimal machining parameters determined by Taguchi analysis.

Table 4.32: Confirmation test results for WEDM microhardness.

Response	Mean		S/N ratio (dB)		Error %
	Predicted	Experiment	Predicted	Experiment	
HK	106.78	120.52	-41.20	-41.62	1.01

4.4 Evaluation of surface microstructure

Further analysis using a high-resolution SEM microscope on the selected AWJ and WEDM machined samples. The highest and lowest surface roughness based on S_a , trial 3 $S_a=1.66\mu m$ (Parameters: $A=0.1\mu s$; $AJ=15V$; $IAL=30A$; $V=120V$ and $FF=100\%$) and trial 17 $S_a=3.34\mu m$ (Parameters: $A=0.7\mu s$; $AJ=45V$; $IAL=20A$; $V=80V$ and $FF=100\%$) were selected to study the surface morphology. Figure 4.30 shows the general appearance of the EDM machined surface. It can be seen that the surface consists of small craters and surface irregularities generated during the heating process. The surface generated by WEDM is considered homogeneous. The sizes of the voids ranges from 3 to $6\mu m$.

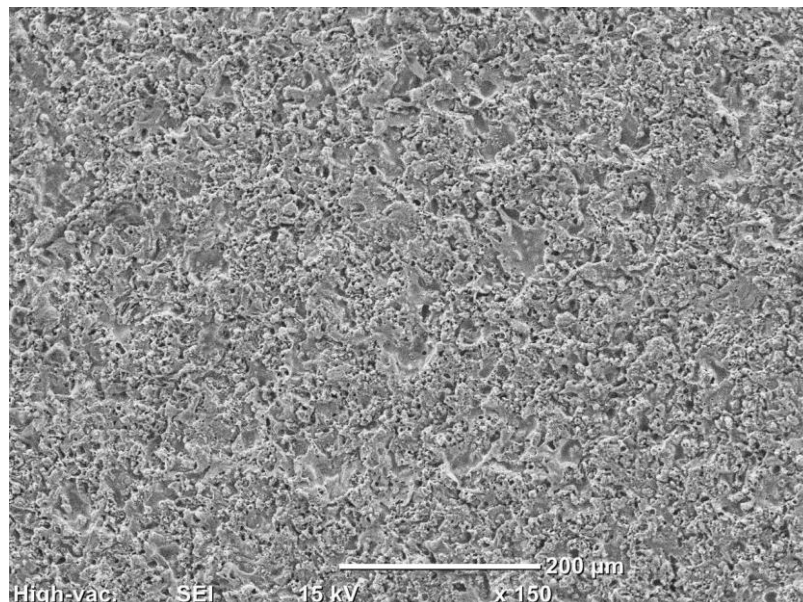


Figure 4.30: SEM image of WEDM machined surface trial 3 at magnification X150.

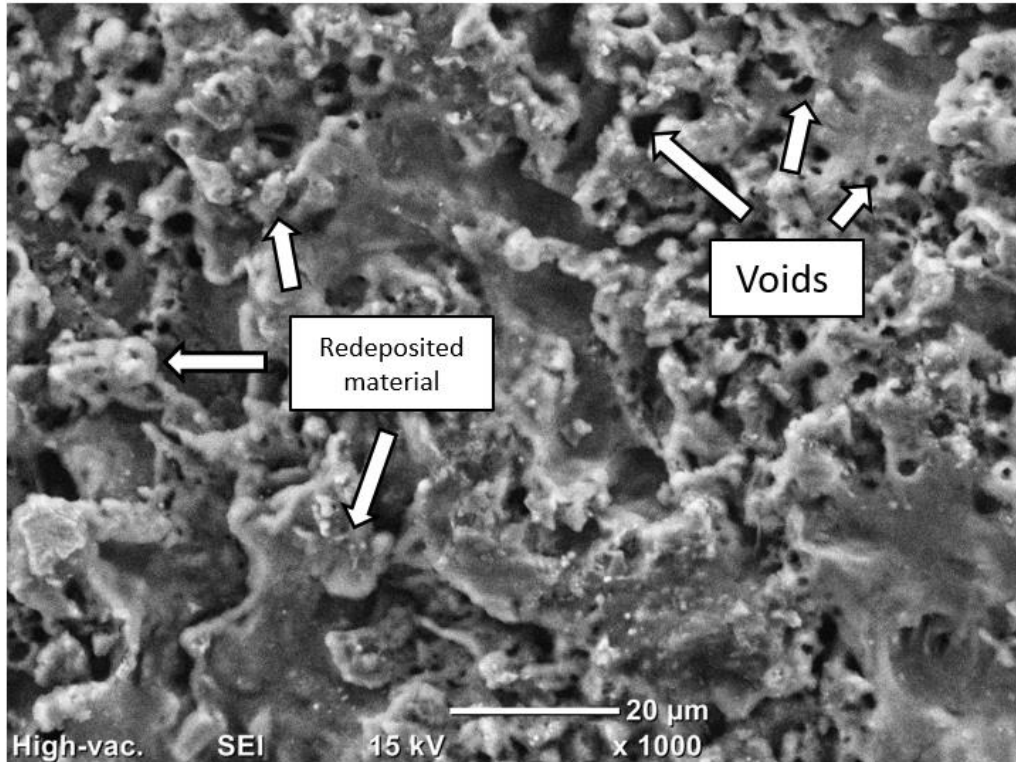


Figure 4.31: SEM image of WEDM machined surface trial 3 at magnification X1000.

Compared to Trial 3, the general appearance of trial 17 shows no major variation in surfaces machined by WEDM except for the larger craters.

Figure 4.32 (a) shows that the surface consists of voids under the magnification of x1000. Large craters up to 25-30 μm , which are 5 to 6 times larger than the craters in trial 3 due to high pulse-on time and micro-cracks can be seen on the redeposited material region. The large craters and cracks caused the surface to be rougher and the surface roughness increases,

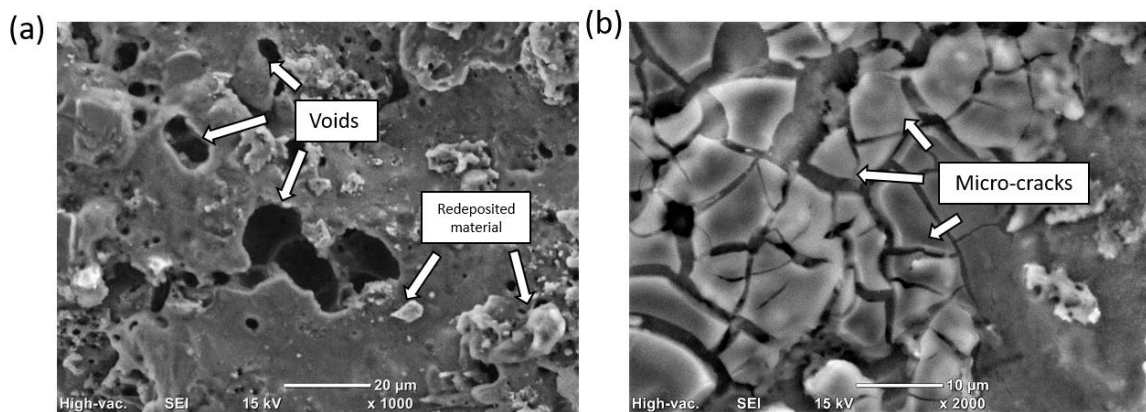


Figure 4.32: SEM image of Trial 17 at magnification of (a) X1000 and (b) X2000.

An EDS elemental analysis was carried out on the surface of Trial 17. The base material MMC which is made up of 85% Al matrix AA2618 only consists of 2.8% of Cu. The EDS analysis shows that it consists of 11.83% of Copper (Cu) and 5.25% Zinc (Zn) additional elements which detached from the wire were not flushed away and deposited on the material. The overlay of Al and SiC X-ray mapping is shown in Figure 4.34 (a). The red spots represents the SiC reinforced particles embedded in the Al blue-greenish contour matrix. From Figure 4.34 (b), It shows that the Cu and Zn deposited on the surface randomly.

Table 4.33: EDS chemical composition of scanned surface.

Element	(keV)	Mass %	Sigma	Atom %	Cation K
C K	0.277	1.01	0.01	2.10	0.4275
O K	0.525	25.27	0.31	39.30	26.2951
Al K	1.486	49.04	0.26	45.23	51.6378
Si K	1.739	7.61	0.15	6.74	3.5536
Cu K	8.040	11.83	0.34	4.63	12.5459
Zn K	8.630	5.25	0.29	2.00	5.5401
Total		100.00		100.00	

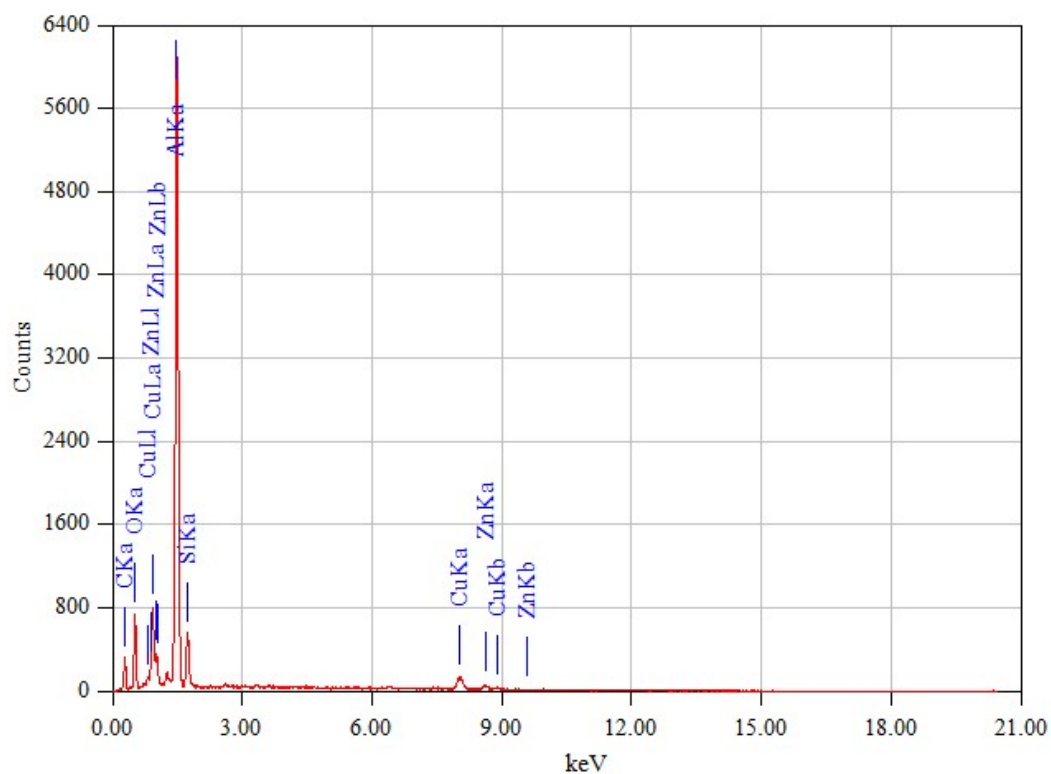


Figure 4.33: EDS spectrum of the chemical composition.

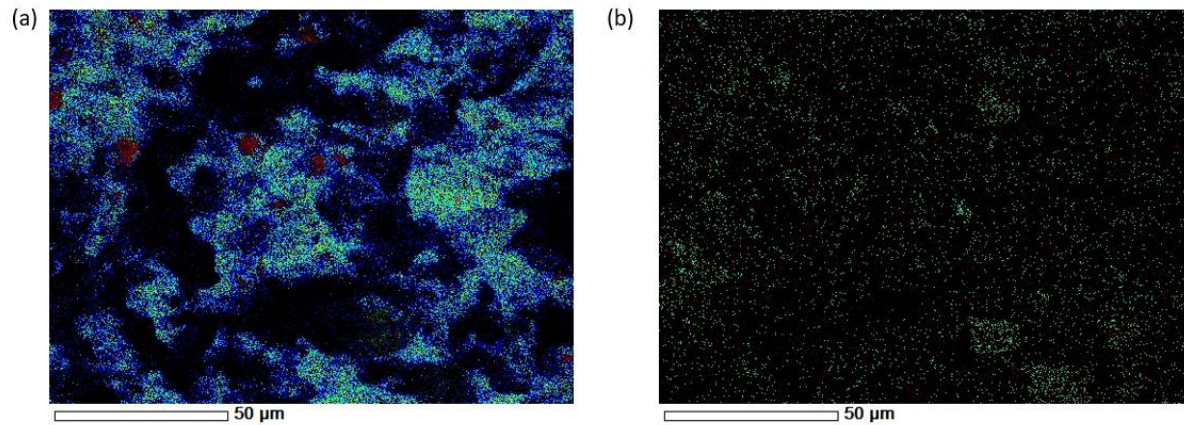


Figure 4.34: (a) Overlay of Al and SiC X-ray mapping and (b) map topography of Cu and Zn atoms.

A white bubble-like protrusion was discovered on the right bottom part of the cutting front of sample 5 on the 3D surface topography contour mapping. By using area analysis, the constituent chemical composition table shows that the oxygen element consists of 62.86%. It shows that oxygen from the deionized water and melting of Zn and Cu from the brass wire during spark erosion entrapped on the surface, which initiates globules. WEDM process is a strong exothermic reaction. Owing to the high chemical affinity of Al to O_2 under rapid oxidation process and high temperature above 1200°C , the oxide bubble will be formed simultaneously on the surface.

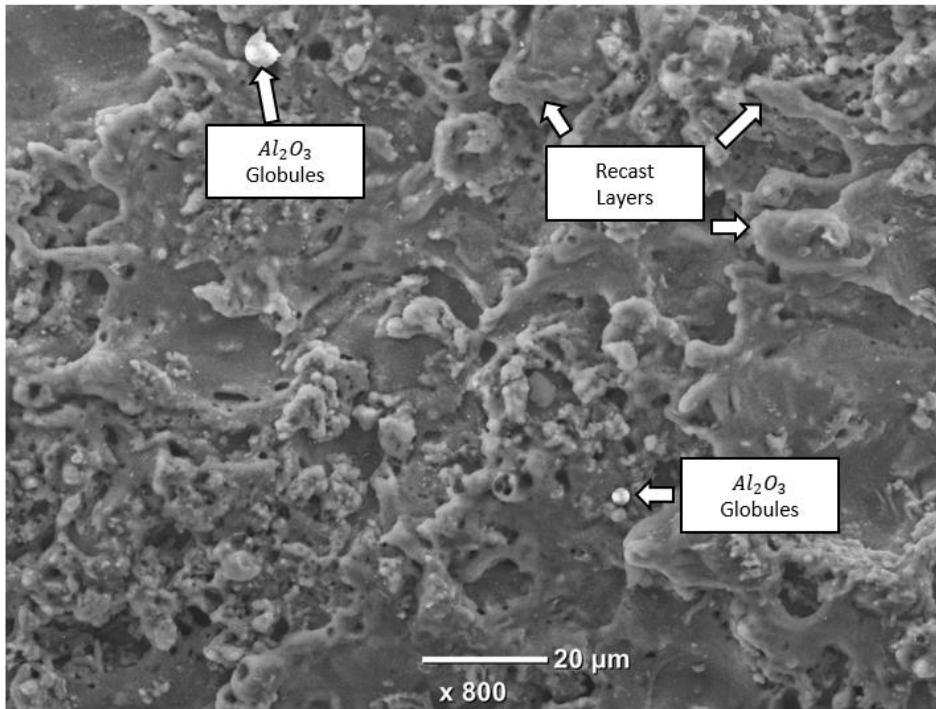


Figure 4.35: SEM image of WEDM machined surface at magnification X800.

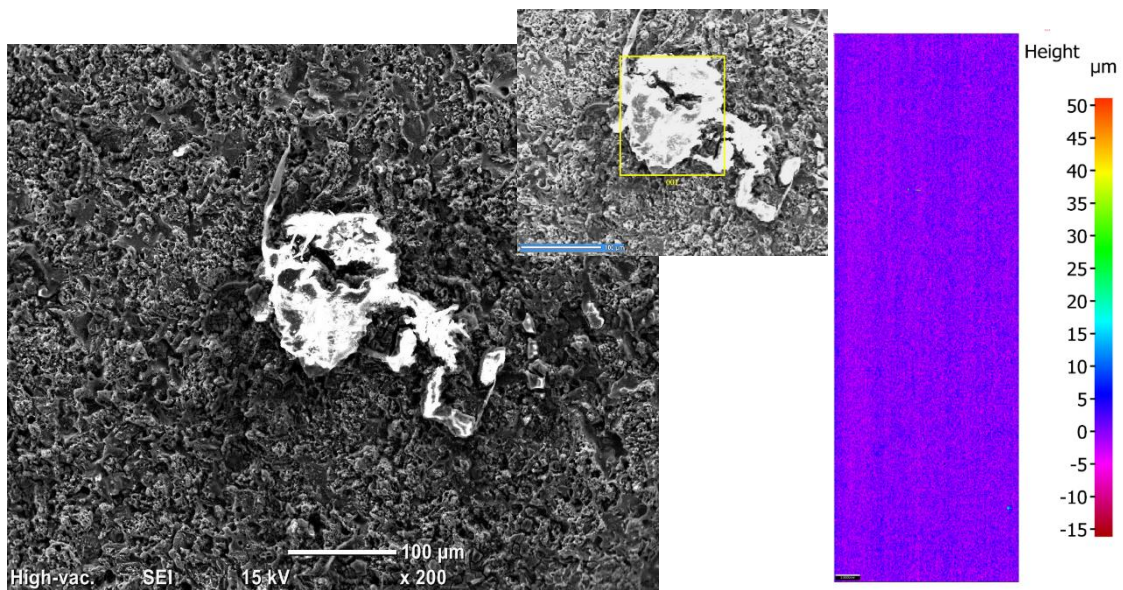


Figure 4.36: SEM image of the entrapped aluminium oxide and 3D topography of the analysed area.

Table 4.34: EDS chemical composition.

Element	(keV)	Mass %	Sigma	Atom %	Cation K
C K	0.277	2.66	0.02	4.18	1.5458
O K	0.525	62.86	0.64	74.19	73.2411
Al K	1.486	26.22	0.33	18.35	19.6724
Si K	1.739	2.22	0.14	1.49	0.9622
Cu K	8.040	5.19	0.40	1.54	3.9437
Zn K	8.630	0.84	0.27	0.24	0.6349
Total		100.00		100.0	

The material removal process of AWJ is due to the impact of solid particles by erosion. The material removal process are divided into two zones: micro-cutting zone which occurred at the top surface and deformation zone occurs at the bottom surface. In micro-cutting zone, the material is removed by sharp edged abrasive particles impacted by shallow angles. At the bottom surface, the particle attack angles become larger and ploughing marks are caused by the jet stream energy losses at the lower part of the cutting front. The SEM images in Figure 4.37 clearly indicates that ploughing deformation at the initial damage zone and rough cutting zone. Overlapping craters and abrasive track marks caused by ploughing of the abrasive particles can be observed. Grit embedment and lips are observed at the edges of the abrasive wears tracks in the rough cutting zone.

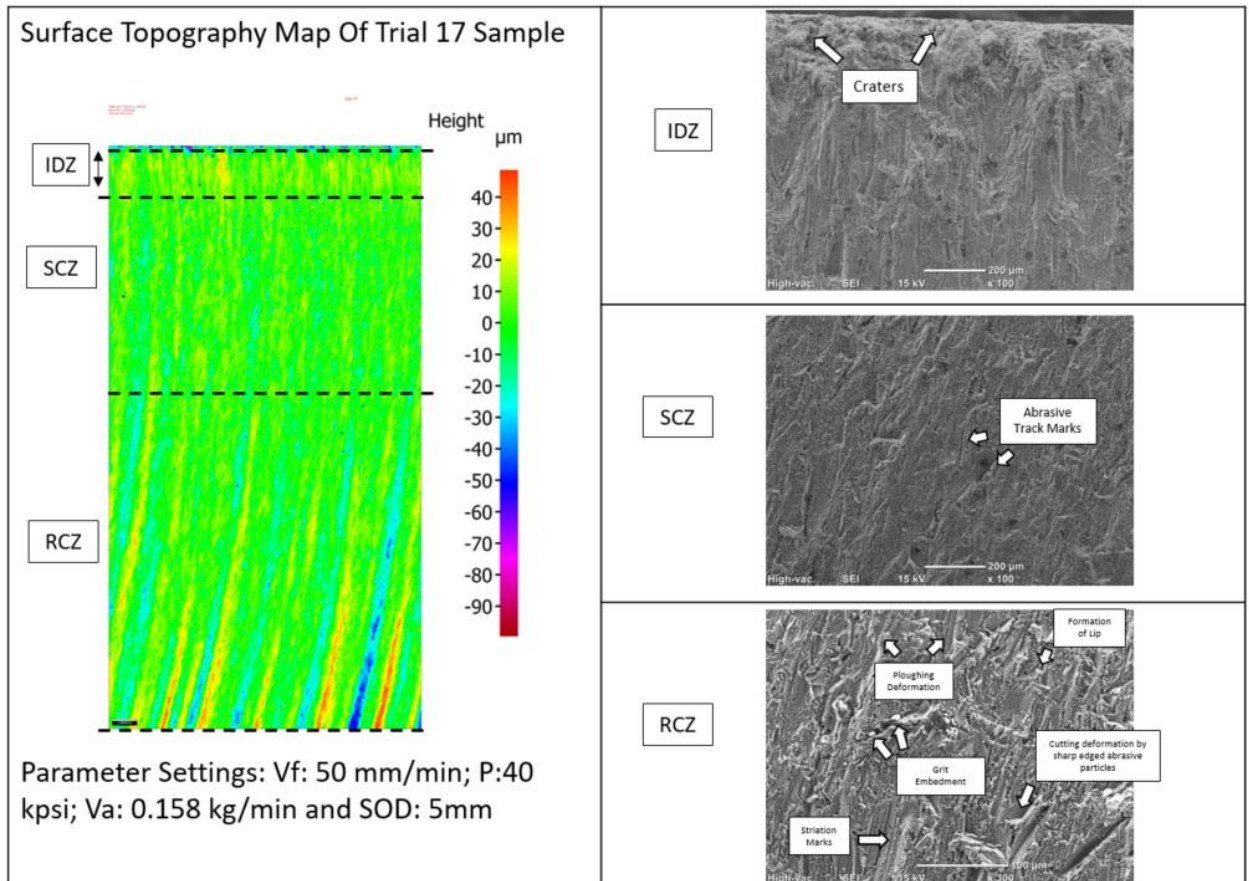


Figure 4.37: The different zones in the AWJ machined surfaces and deformations mechanism involved in the MMC.

It is clearly visible in Figure 4.38. that a grit is embedded along an abrasive track mark in the RCZ. This may be due to part of an abrasive particle broke during the cutting process and embedded in the surface while other part of the grit continues to plough on the surface. Similar to some of the researches reported, the grit embedment was not removed during the post cleaning process due to mechanical interlocking[135, 136]. In order to verify the existence of grit embedment, an EDS spot analysis was performed to obtain the chemical composition. Comparing the chemical composition of the

garnet tabulated in Table 3.1 obtained from the product data sheet, iron (Fe) and magnesium (Mg) are not the main elements of the garnet and were used to identify the presence of garnet. Figure 4.41 represents the chemical composition obtained from EDS analysis, it was found that it consists of 14.25 % of Fe and 3.07% of Mg.

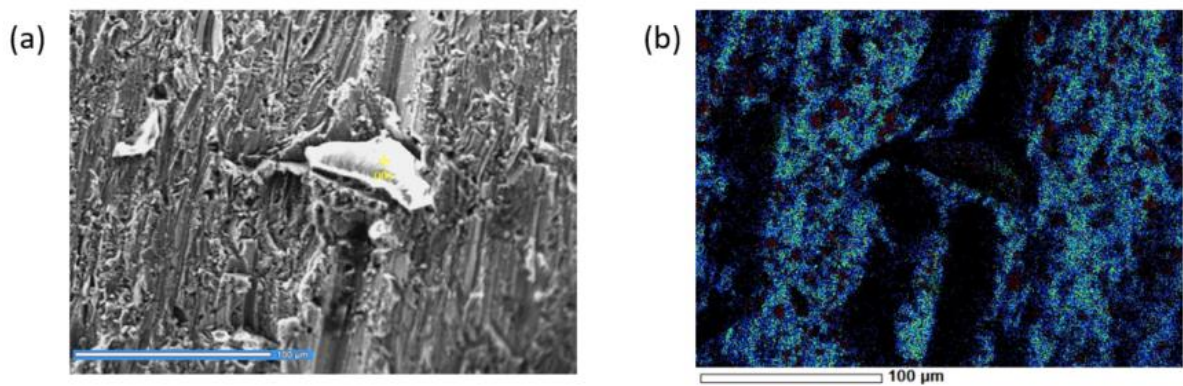


Figure 4.38: The EDS analysis using spot analysis and overlay of Al and SiC.

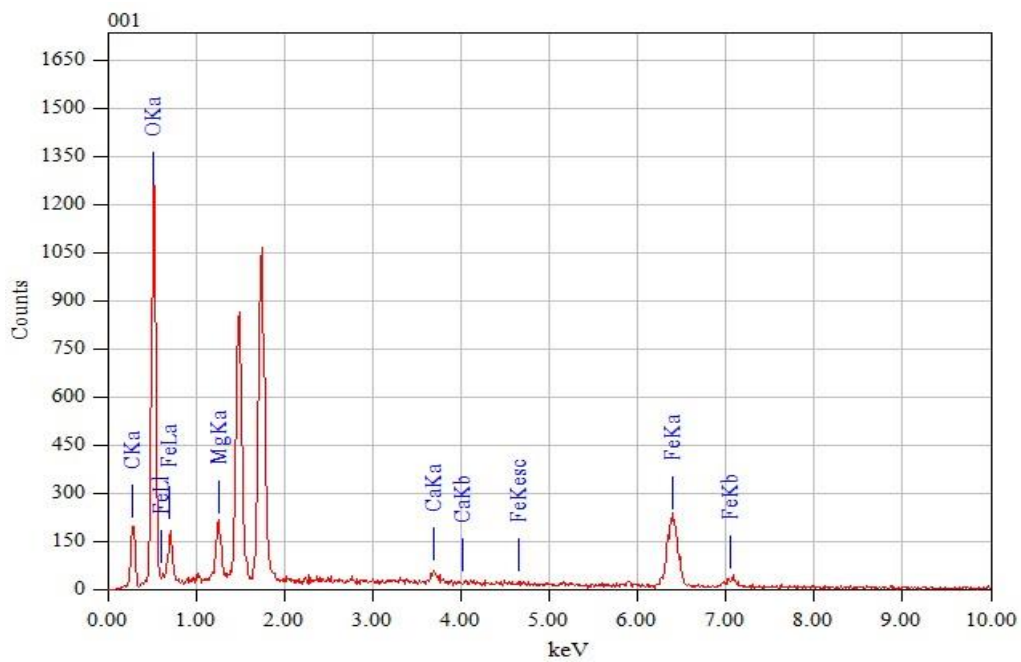


Figure 4.39: EDS spectrum of the chemical composition.

Table 4.35: EDS chemical composition of the spot analysis.

Element	(KeV)	Mass %	Sigma	Atom %	Cation K
C K	0.277	0.74	0.02	1.29	0.4362
O K	0.525	53.19	1.17	69.53	63.7594
Mg K	1.253	3.07	0.26	2.64	2.2256
Al K	1.486	10.98	0.42	8.51	8.9333
Si K	1.739	16.21	0.52	12.07	9.8019
Ca K	3.690	0.64	0.13	0.34	0.6518
Ti K	4.508	0.38	0.12	0.17	0.3572
Fe K	6.398	14.25	0.73	5.33	13.5188
Zr L	2.042	0.54	0.29	0.12	0.3157
Total		100.00		100.00	

Trial 6 has the smallest mean Sa. The SEM images shown in Figure 4.40. shows that the depth of IDZ is lower and less waviness compared to trial 17. The depth of SCZ is larger and the surface is smoother compared to trial 17, which contributed towards the small mean Sa. However, uniform wear tracks in the direction of jet traverse at the bottom part of the SCZ are presents. There is no obvious striation marks seen in the RCZ. The SEM images indicates presence of deformation surfaces such as abrasive wear tracks, ploughing marks, craters and abrasive particles embedment.

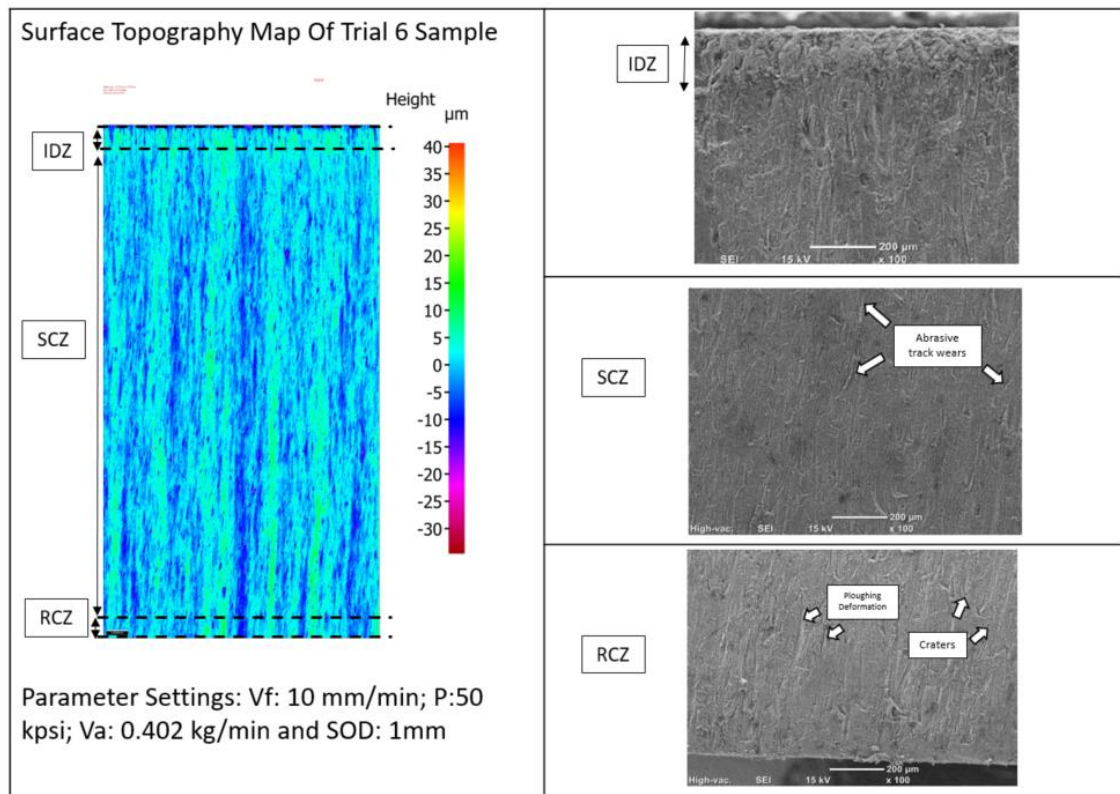


Figure 4.40: SEM images of the different zones in the AWJ machined surfaces of trial 6.

4.5 Phase Two: Wettability Analysis

In this experiment, static contact angle measurements were selected to characterise the wettability of the selected AWJ and WEDM machined surfaces. The preliminary static contact analysis was measured by JGW-360A contact angle measurement system. The base material surface was found to be hydrophilic as the static contact angle is $\sim 78.04^\circ$, $< 90^\circ$ due to the high energy of bulk material formed by Al metal. It was found that the AWJ

machined surfaces are hydrophilic and the WEDM machined surface are hydrophobic (see Figure 4.41).

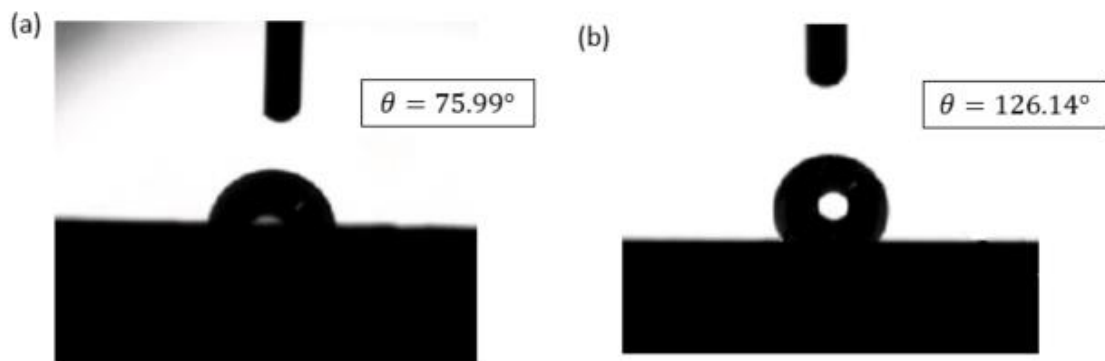


Figure 4.41: Static contact angle measurement of AWJ Trial 6 and WEDM Trial 3.

4.5.1 Static Contact Angle (CA) Results

The surface machined by AWJ is considered as heterogeneous. Hence, more measurements are taken as shown in Figure 4.42 (a) to better represent the entire surface: Three measurements are taken on the upper, middle and bottom section of the surface. As the WEDM machined surface is considered homogeneous: Three scans were conducted and averaged with each surface area of approximately 1.2mm^2 at two different regions: upper and bottom. The static contact angles and the factors affecting the surface wettability of AWJ and WEDM machined surfaces were further studied in the following

sections. The static contact angles changes are attributed to the modification of surface morphologies and surface chemistry of the surfaces.

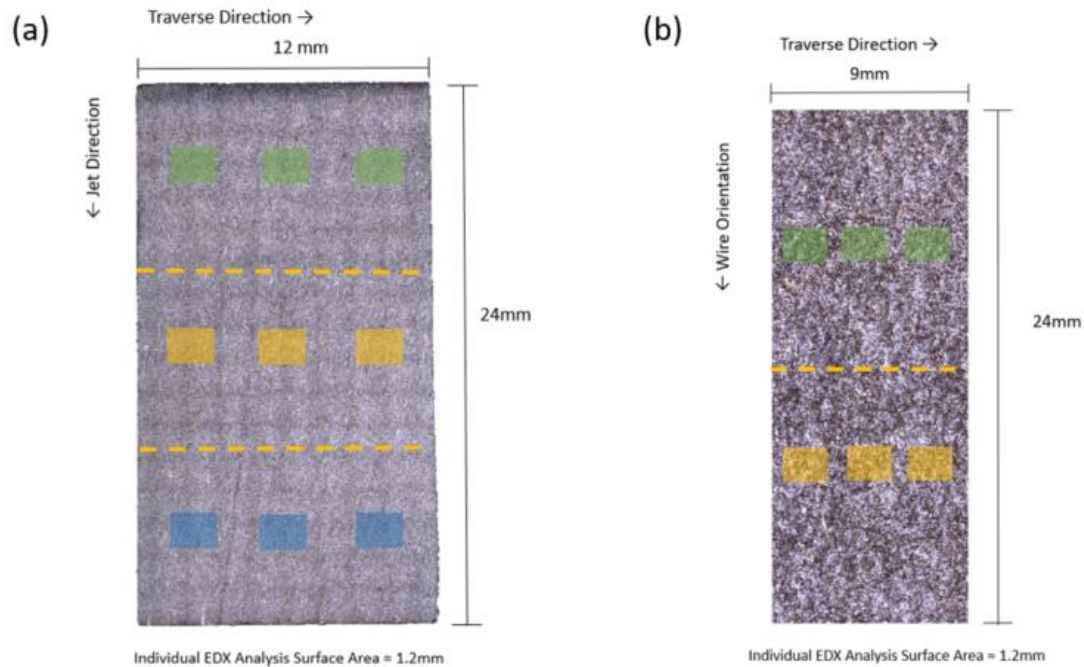


Figure 4.42: (a) 9 measurements taken on AWJ samples and (b) 6 measurements taken on WEDM samples.

The in-depth static contact angle analysis was carried out on the SciCity contact angle optical tensiometer. The intrinsic contact angle of the MMC was found to be 69.28° , which is consistent with the result found at the preliminary test. The mean CA measurements results of AWJ samples are summarised in Table 4.36. It can be observed that the majority of the AWJ machined surfaces are hydrophobic. Trial 15 and 17 (high Sa) are hydrophobic due to the striation marks generated on the cutting front. It

creates a “air pocket” effect based on Cassie-Baxter model. The pillars of the striation marks form support points to lift the water droplets up.

Table 4.36: Summary of CA measurement of AWJ samples.

Trial No.	Vf <i>mm/min</i>	P <i>kpsi</i>	Va <i>kg/min</i>	SOD <i>mm</i>	Contact Angle (°)			
					Ave. Upper	Ave. Middle	Ave. Bottom	Mean
1	5	30	0.158	1	81.34	59.44	58.44	66.41
2	5	40	0.340	3	37.30	60.64	61.56	53.17
3	5	50	0.402	5	58.56	89.55	89.64	79.25
4	10	30	0.158	3	89.63	46.44	30.59	55.55
5	10	40	0.340	5	89.14	51.06	73.37	71.19
6	10	50	0.402	1	93.12	105.41	101.34	99.96
7	20	30	0.340	1	48.78	80.94	90.30	73.34
8	20	40	0.402	3	87.77	71.99	67.78	75.85
9	20	50	0.158	5	74.50	76.42	58.71	69.88
10	30	30	0.402	5	63.03	71.30	64.87	66.40
11	30	40	0.158	1	70.52	67.43	94.71	77.55
12	30	50	0.340	3	85.31	75.93	72.73	77.99
13	40	30	0.340	5	70.90	85.71	98.17	84.93
14	40	40	0.402	1	83.33	89.36	81.40	84.70
15	40	50	0.158	3	92.21	107.42	95.16	98.26
16	50	30	0.402	3	93.39	88.00	87.51	89.63
17	50	40	0.158	5	102.12	98.38	91.08	97.19
18	50	50	0.340	1	76.54	68.00	80.28	74.94

The diameter of the water droplet can be calculated by using $V = \frac{\pi D^3}{24} \left(\frac{2 - 3 \cos \theta + \cos^3 \theta}{\sin^3 \theta} \right)$. The width and depth of the striation marks were measured using ProfileForm in Alicona software. It shows that the diameter of the water droplet is much larger than the width of the striation marks, hence, the water droplets were lifted by the pillars. ANOVA and Taguchi analysis show that there is no interaction between the process parameters and CA.

Trial 15 – Sa: **Mean:** 7.18 μ m **Bottom:** 9.22 μ m

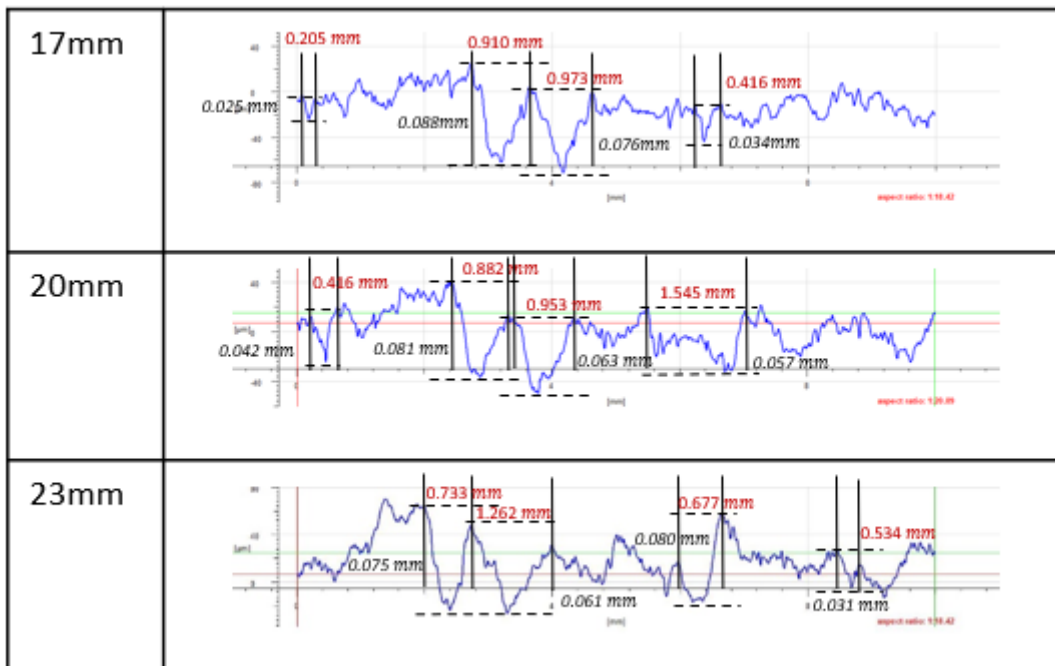
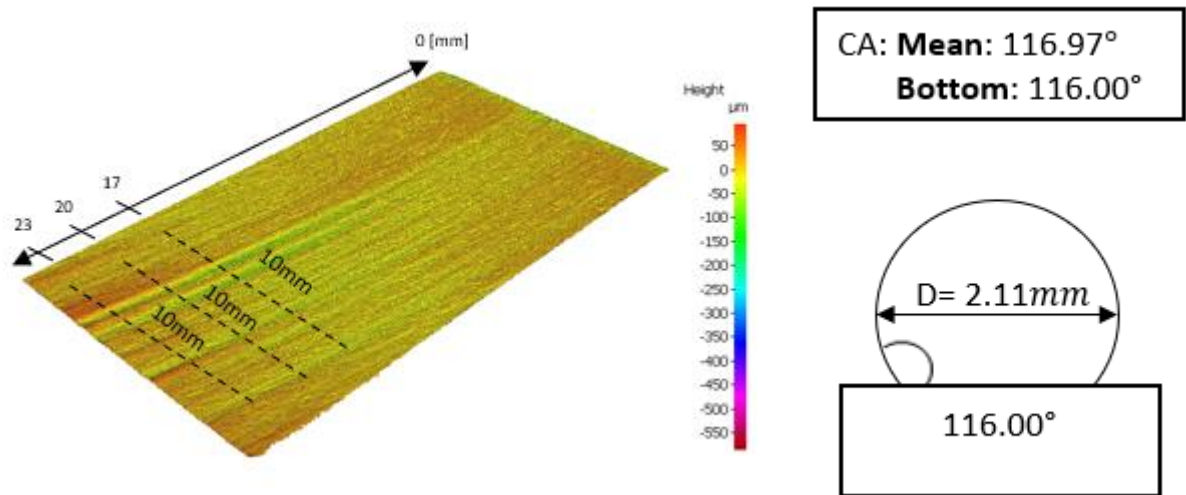


Figure 4.43: AWJ Trial 15 striation marks analysis based on the water droplet diameter.

Table 4.37: Mean CA of WEDM machined samples.

Trial No.	A μs	AJ V	IAL A	V V	FF %	Contact Angle ($^{\circ}$)		
						Upper	Lower	Mean
1	0.1	15	10	80	10	115.00	117.00	116.00
2	0.1	15	20	100	50	124.30	118.86	121.58
3	0.1	15	30	120	100	87.32	86.11	86.72
4	0.1	30	10	80	50	129.28	111.74	120.51
5	0.1	30	20	100	100	122.25	119.10	120.68
6	0.1	30	30	120	10	109.00	100.80	104.90
7	0.1	45	10	100	10	99.33	87.64	93.49
8	0.1	45	20	120	50	135.85	134.19	135.02
9	0.1	45	30	80	100	119.00	104.49	111.75
10	0.7	15	10	120	100	119.27	123.57	121.42
11	0.7	15	20	80	10	124.15	116.20	120.18
12	0.7	15	30	100	50	125.05	115.00	120.03
13	0.7	30	10	100	100	115.85	120.30	118.08
14	0.7	30	20	120	10	128.18	123.00	125.59
15	0.7	30	30	80	50	126.28	126.00	126.14
16	0.7	45	10	120	50	133.31	107.09	120.20
17	0.7	45	20	80	100	125.50	113.54	119.52
18	0.7	45	30	100	10	119.52	129.00	124.26

As it can be observed from Table 4.37, apart from Trial 3, contact angles on all the WEDM surfaces increases when compared with the intrinsic angle, which means that the surfaces are hydrophobic. Trial 3 shows the

hydrophilic characteristic as it has the lowest SA surface roughness. This is due to the droplets entering the shallow pores. The surface roughness increases, the craters generated by the WEDM process become larger, hence the air cushion effect increases, the surface becomes more hydrophobic. Similar to AWJ results, ANOVA and Taguchi analysis show that there is no interaction between the process parameters and CA.

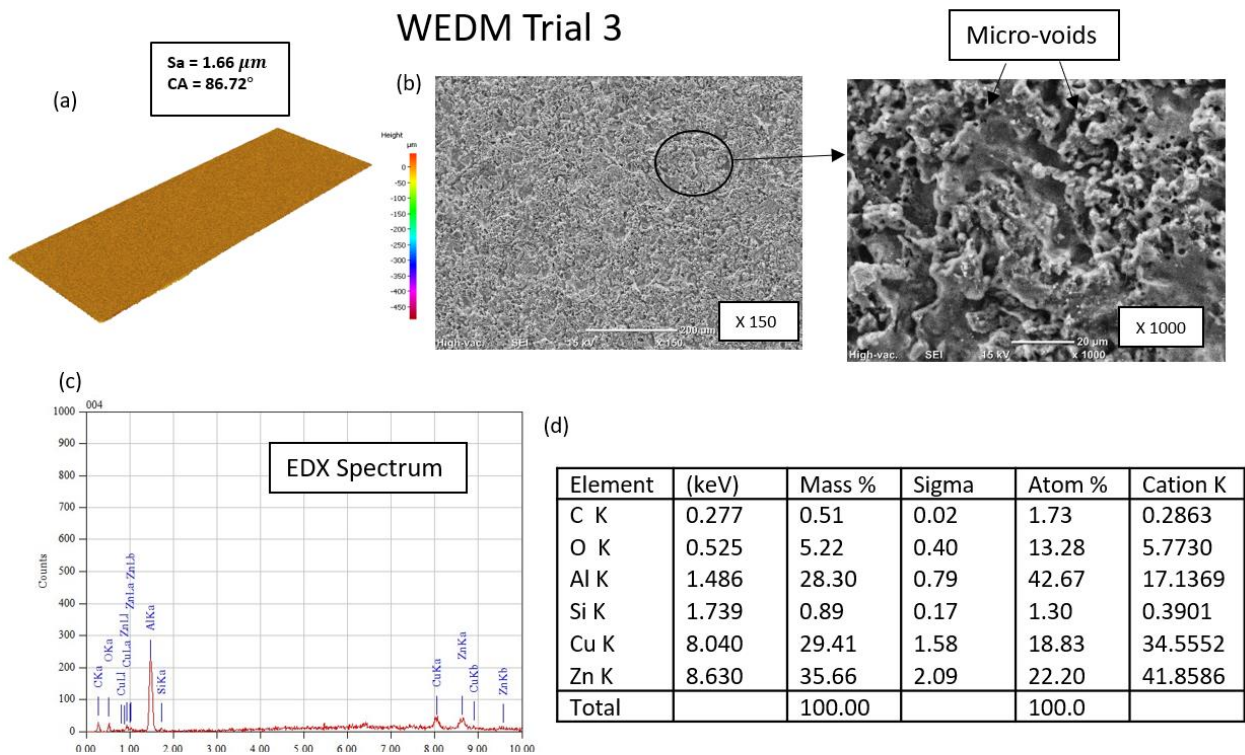


Figure 4.44: (a) WEDM Trial 3 3D surface topography (b) SEM image showing micro-voids (c) general surface EDX spectrum and (d) chemical composition analysis.

4.5.2 AWJ Regression Analysis

The anisotropic surface features generated by AWJ contributes to the complex behaviour of wetting behaviours. Due to the change in surface chemistry such as oxygen diffusion and grit embedment in AWJ, SEM and EDX analysis were carried out to analyse the chemical composition as the high porosity content adsorb organic compounds from air. Study suggested that an increase in the concentration of iron Fe within the surface layer increases the surface energy slight and therefore more reactive with water, while Cu reduces the surface energy, hence more hydrophobic[137].

The regression model was generated in Minitab to show that which factors are statistically significant. The regression equation was obtained: $CA = 11.0 + 8.41 S_a - 1.8 S_{sk} + 4.34 S_{ku} + 5.05 Fe - 0.239 O$. The Pareto charts were obtained to show the values of standardized effects with significance level $\alpha = 0.05$ with confidence level of 95%. The values on the x-axis of Pareto charts are so called standardized effects which is t values. The standardized effects of the independent parameters and their interactions on the dependent parameter are shown in the diagram. According to Figure 4.45, it shows that that S_a and S_{ku} cross the reference line (p value equal to 0.05), which indicates that they are significant.

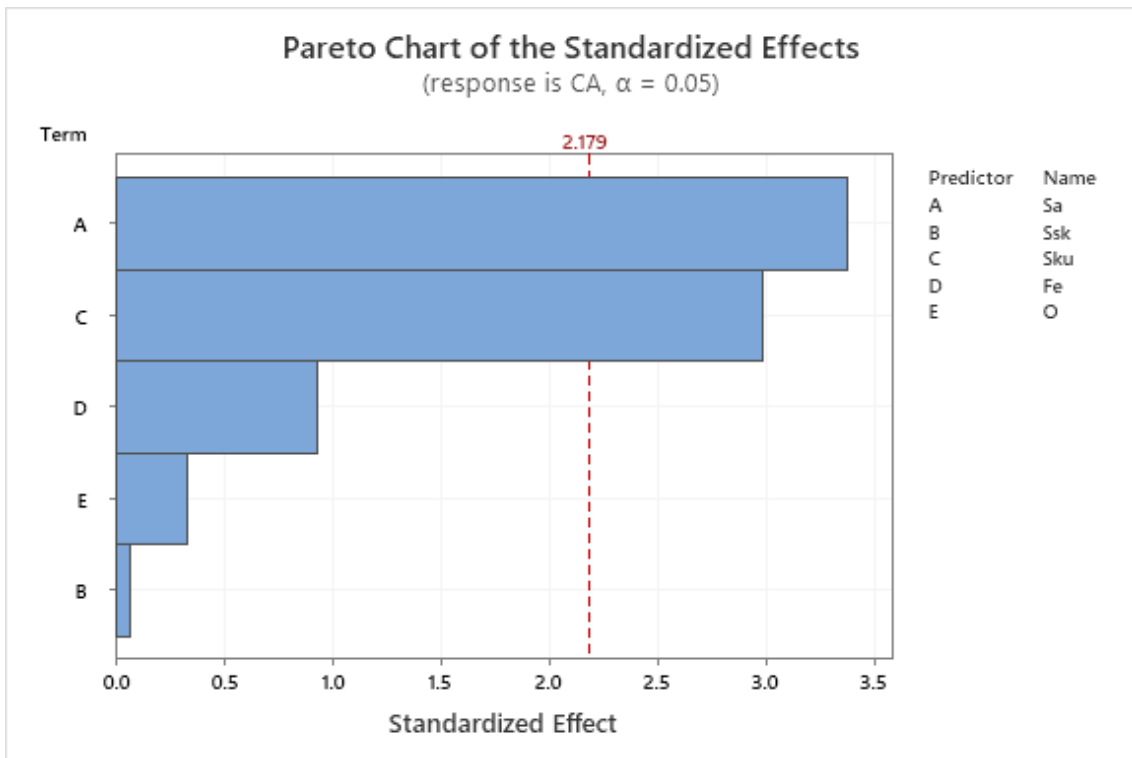


Figure 4.45: Pareto chart of AWJ variables and their interaction on the CA.

AWJ machined surfaces show anisotropic features and topography with large Sa and Sku exhibit better hydrophobicity due to the dominant textures such as the striation marks. ANOVA analysis was performed and the results were tabulated in Table 4.38. It indicates that there is no correlation between the wettability and Ssk, Fe and O content.

Table 4.38: ANOVA analysis of the regression analysis of AWJ.

Source	Sum of Squares (SS)	Degree of Freedom (DoF)	Mean Square (MS)	F-value	P-value
Regression	2220.88	5	444.175	6.05	0.005
Sa	838.72	1	838.719	11.41	0.005
Ssk	0.33	1	0.328	0.00	0.948
Sku	656.78	1	656.784	8.94	0.011
Fe	63.72	1	63.724	0.87	0.370
O	7.97	1	7.967	0.11	0.748
Error	881.72	12	73.476		
Total	3102.59	17			

4.5.3 WEDM Regression Analysis

Copper is the abundant material in the Broncocut wire used in the experiment. Some other elements diffused into the base material of MMC such as Cu and Zn from the Bronocut wire and O generated during the WEDM cutting process due to water decomposing in the discharge spark gap. It was used in EDX analysis to identify the percentage of the wire diffusion.

The wire diffusion percentage and oxygen content were analysed by using EDX to determine the effect on wettability. Regression equation was

obtained: $CA = 60.0 = 10.67 S_a - 69.7 S_{sk} + 10.49 S_{ku} + 1.00 \text{ Wire} - 1.330 O$.

The Pareto Chart in Figure 4.46 shows that S_a , S_{ku} and O content cross the reference line (p value equal to 0.05), which indicates that they are significant.

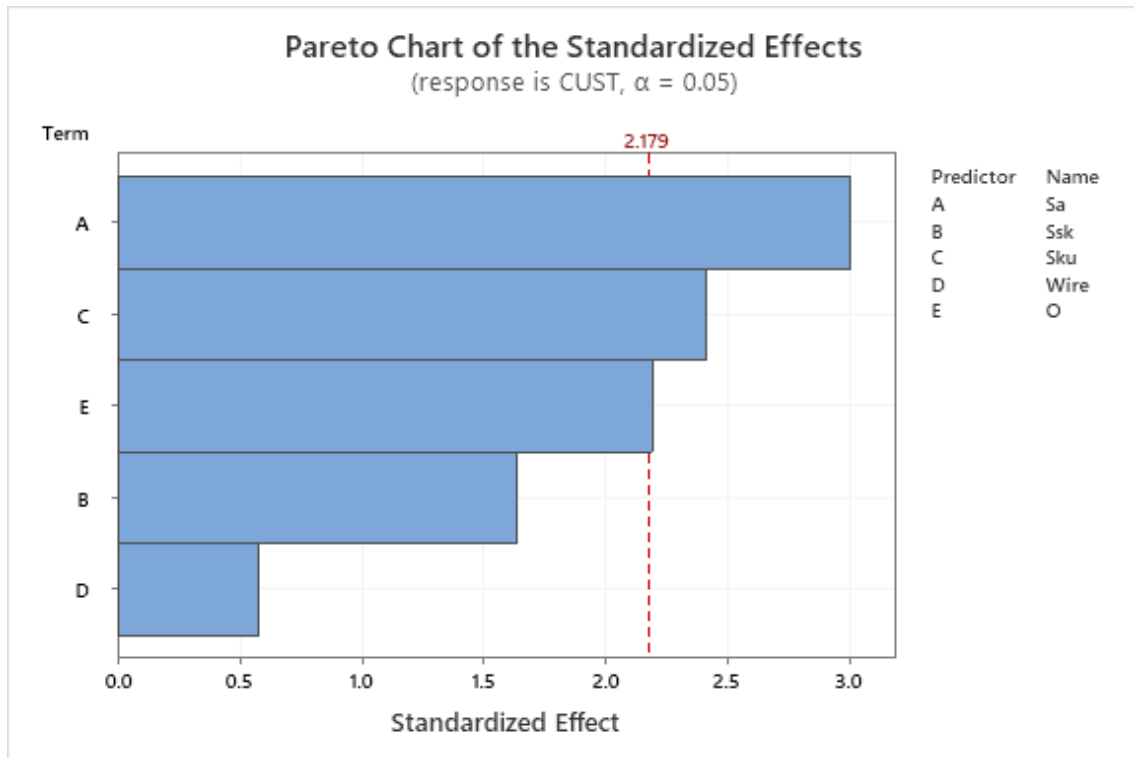


Figure 4.46: Pareto chart of WEDM variables and their interaction on the CA.

The analysis of variance ANOVA was performed and showed that there is no correlation between the machining parameters and increase of Cu, Zn and O contents. The relationship between wettability and 3D surface topography characteristics were explored. The formation of bulges and craters are due to the heat generated during WEDM. The higher the S_a and S_{ku} , the larger the CA. The bulges form support pillars to lift the water droplets and the

craters act as a gap with different pressure, which prevent the water droplet from entering the gap. Trial 8 ($S_a=1.81$; $S_{ku}=4.67$) indicates that the surface has dominant topography of deep craters, which promotes the “air pocket” effect. EDS chemical analysis show that the amount of oxygen increased compared to the surfaces prior to machining. The deionized water produces oxygen due to pyrolysis at high temperature and the unexpelled gas is trapped in the re-solidified material. The wettability study show that suitable surface roughness and topography can achieve improved hydrophobicity.

Table 4.39: ANOVA analysis of the regression analysis of WEDM.

Source	Sum of Squares (SS)	Degree of Freedom (DoF)	Mean Square (MS)	F-value	P-value
Regression	1437.84	5	287.57	4.08	0.021
Sa	635.97	1	635.97	9.03	0.011
Ssk	187.84	1	187.84	2.67	0.128
Sku	409.86	1	409.86	5.82	0.033
Wire	23.77	1	23.77	0.34	0.572
O	338.24	1	338.24	4.80	0.049
Error	844.91	12	70.41		
Total	2282.75	17			

4.5.4 XPS Analysis

Surface chemistry characterization using X-ray photoelectron spectroscopy to analyse the chemical bonds of oxygen containing functional groups within 10nm depth. The test is performed by a multifunctional X-ray photoelectron spectrometer Kratos Analytical Axis Supra. Due to the elimination of inorganic oxygen, the contact angle is only influenced by oxygen-containing polar group (C-OH, COO), which are the indicator on wettability. Narrow scan of carbon was acquired and the XPS Spectrogram at 1s is split and fitted by CasaXPS software as illustrated in the the Figure 4.47 below. The atom concentration of the oxygen containing functional groups can be obtained in the full-scan XPS spectrum and the carboxyl COO and carbonyl C=O can be obtained from their peak split results. The peak at 284.6 eV indicates hydrocarbons (C-H, C-C); the characteristics peak at 286.2 eV relates to phenol or ether carbon (C-O); the characteristic peak at 288.1 eV denotes carbonyl carbons (C=O); and the peak at 289.9eV is for carboxyl carbon (COO).

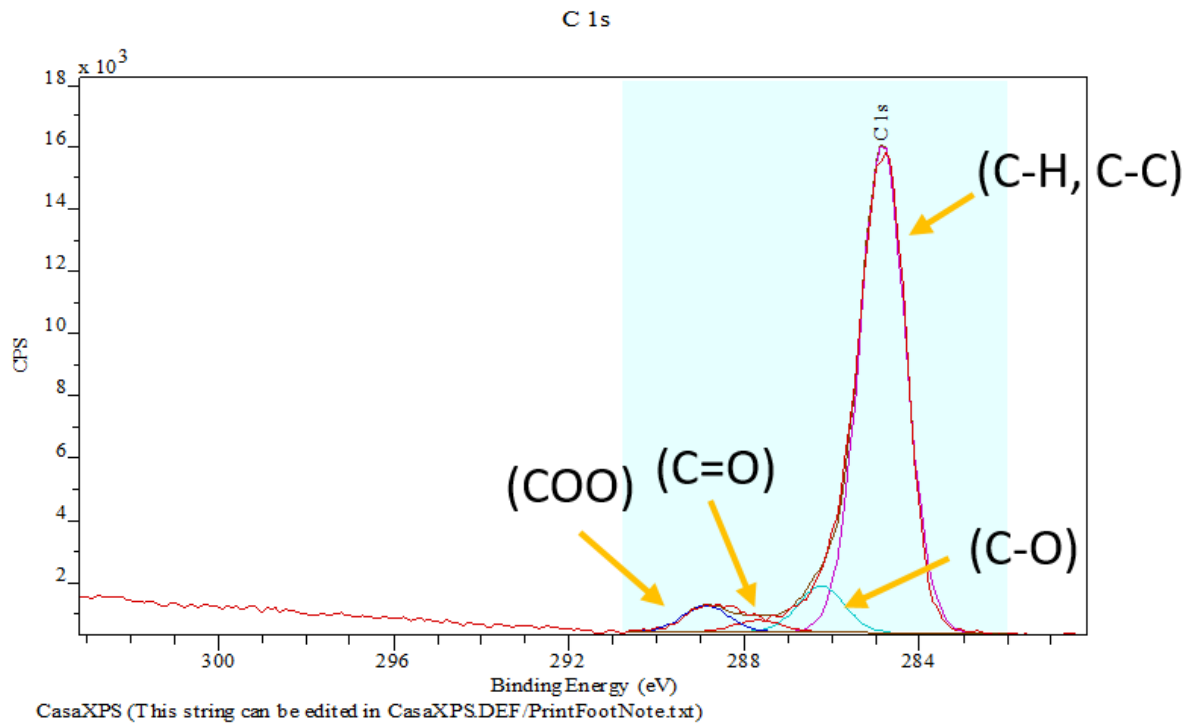


Figure 4.47: XPS Spectra of WEDM Trial 8.

Table 4.40: Relative concentration ratio of different forms of organic C/%.

Sample	COO	C=O	C-O	C-H,C-C
WEDM Trial 8	4.61	2.15	8.18	85.07
Sa=1.81				
Sku=4.67				
CA=135.02				
WEDM Trial 3	4.23	2.38	11.07	82.32
Sa=1.66				
Sku=3.19				
CA=86.72				
AWJ Trial 2	4.4	2.93	13.17	79.50
Sa=3.53				

Sk _u =5				
CA=53.17				
AWJ Trial 17	4.93	3.22	12.05	79.79
Sa=7.19				
Sk _u =3.43				
CA=111.22				

To illustrate the calculation process for the concentration of oxygen-containing functional groups:

The relative molar concentration of carboxyl group:

$$W_{mol}(COO) = 4.61 \times 80.34\% = 3.70\%$$

The relative molar concentration of carbonyl group:

$$W_{mol}(C = O) = 2.15 \times 80.34\% = 1.73\%$$

The relative molar concentration of ether and hydroxyl group is as follows:

- (a) The molar ratio of C-O bond to atoms in the oxygen-containing functional groups:

$$W_{mol}(C - O) = \frac{8.18}{(4.61 + 2.15 + 8.18)} \times 100\% = 54.75\%$$

- (b) The oxygen concentration of hydroxyl and ether group:

$$W_{mol}(O) = 54.75\% \times 18.22\% = 9.98\%$$

(c) The equation of the oxygen in C-O bond:

$$W_{mol}(-O-) + W_{mol}(-OH) = 9.98\%$$

(d) The equation of carbon in C-O bond:

$$W_{mol}(2C_{-o-}) + W_{mol}(C_{-OH}) = 80.34\% \times 8.18\% = 6.57\%$$

Solving the two equations from (c) and (d), the molar concentrations are obtained: $W_{mol}(-O-) = 3.41\%$ and $W_{mol}(-OH) = 6.57\%$

The calculation results of oxygen-containing functional groups are tabulated in Table 4.41. Among the polar oxygen-containing functional groups, hydroxyl group is considered the greater promoter to the surface wettability compared to carboxyl group. The results indicate that the content of polar oxygen groups is slightly higher in the AWJ samples compared to WEDM samples. However, the oxygen containing polar group is unevenly distributed on the surface of WEDM and AWJ machined MMC surface. Hence, the polar oxygen groups has no significant influence on the surface wettability.

Table 4.41: Molar content of polar oxygen groups of different samples.

Sample	COO	C=O	C-OH	C-O-C	Polar oxygen groups (C-OH,COO)
WEDM Trial 8 Sa=1.81 Sku=4.67 CA=135.02	3.70	1.73	6.57	3.41	10.27
WEDM Trial 3 Sa=1.66 Sku=3.19 CA=86.72	3.40	1.91	8.89	2.52	12.29
AWJ Trial 2 Sa=3.53 Sku=5 CA=53.17	3.53	2.35	10.58	1.13	14.11
AWJ Trial 17 Sa=7.19 Sku=3.43 CA=111.22	3.78	3.62	9.13	0.93	12.91

4.5.5 Summary

This chapter implies the optimisation of process parameters for WEDM and AWJ machining of Al-SiC MMC for Phase 1. Phase 2 provides an in-depth understanding of the behaviour of surface wettability. It was found that there is no interaction between the CA and process parameters. It shows that by exploring the surface topography, the surface wetting characteristics of MMC can be manipulated. Surface roughness is the most significant factor on wettability of engineering surfaces. The results show that isotropic features and topography with high surface roughness S_a and large kurtosis exhibits hydrophobic behaviour. It is mainly because the Cassie-Baxter or 'air cushion' effect; the larger the craters / pits, the larger the contact angle. The results of elemental analysis and XPS experiments indicate that the oxygen diffusion into the MMC surface is random and no significant influence on the surface wettability. The oxygen containing functional groups can be classified into three types: carbon-oxygen single bond (ether (C-O-C) and hydroxyl (C-OH)), carbonyl group (C=O), and carboxyl group (COO). Carboxyl and hydroxyl group are greatest promoter to surface wettability.

4.6 Phase Three: Case study – Strategy in creating anti-icing special purpose aircraft surfaces using hybrid machining method.

4.6.1 Design specification of ventral fins and anti-icing systems

This case study was designed based on one of the major applications of Al/SiC MMC. Two ventral fins on F-16 Fighting Falcon, located on the fuselage behind the wings. The original ventral fins were made of 2024-T4 aluminium. MMC can be used to replace conventional material to increase the specific stiffness of the fin by 40% due to aerodynamic buffeting which causes fatigue cracking[28]. The advantage of Al/SiC MMC are lighter weight and better strength, compared to conventional metallic materials.



Figure 4.48: Ventral fins of an F-16 Fighting Falcon.

Icing is a build-up of ice on the surface of an aircraft surfaces such as wings, tails and propellers, which leads to an increase of drag and reduce lift. This results in aerodynamic stalling which cause critical accidents. The common anti-icing systems: special process kinematics, coatings, multi-process steps. Chemical anti-icing applies a protective layer of chemicals onto the surface of the aircraft to prevent formation of ice. This method has disadvantages as the water is able to dilute the anti-icing agent to form a contaminant. A number of anti-icing systems have been reported[138]. This includes pneumatic de-icing, thermal anti-icing system and glycol-based fluid, which are complicated and require high maintenance.

4.6.2 Proposed machining method combining AWJ and WEDM

The hybrid machining process is defined as the combined process steps that are performed in two or more process steps to manufacture components to achieve better machining performance[139]. The main purpose of the development and application of a hybrid process is to maximize the advantages and address the limitation of the individual techniques. The development of hybrid non-traditional machining processes is continuously evolving and the examples of common techniques reported in the studies are: Electrochemical Discharge Machining and Laser-Chemical Machining [140].

4.6.3 Results Analysis

The rough cutting of the experiment was conducted and the material removal rate of the AWJ is $1543\text{mm}^3/\text{min}$. Three 3D measurements were taken on the upper middle and bottom part of the machined area. From Table 4.42, the mean S_a of $6.80\mu\text{m}$ and S_{ku} of 5.72 indicate that surface generated by the AWJ is considered rough and dominated by deep valleys due to the striation marks and ploughing effect of abrasive particles. The mean CA is 97.68° (SD=12.25). The AWJ machined surface was then polished by WEDM to generate EDM craters topographic features.

Table 4.42: Result analysis of S_a and S_{ku} after rough cutting of AWJ.

Parameter	S_a (μm)	S_{ku}
Upper	5.91	5.32
Middle	5.84	6.79
Bottom	8.64	5.06
Mean	6.80	5.72

The primary and secondary polishing process is shown in Figure 4.49 and it can be seen that the dominant features of AWJ such as the striation marks at the bottom part of the machined surface were removed.

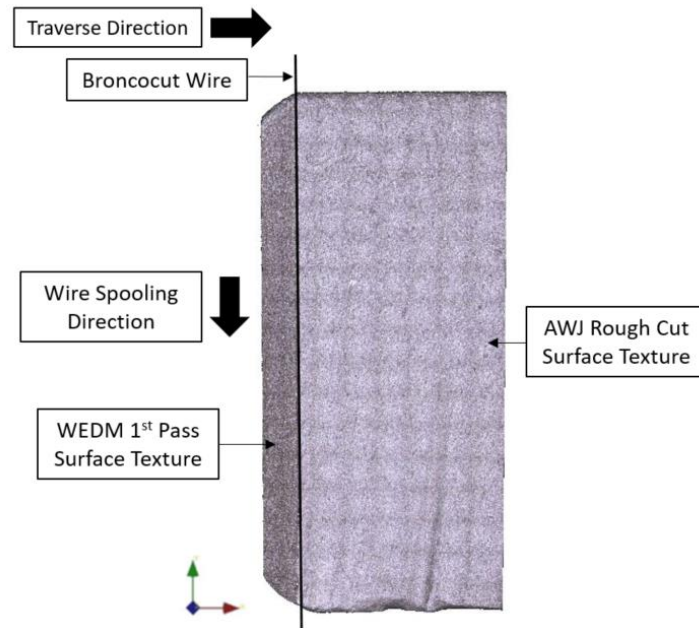


Figure 4.49: Schematic diagram of the primary and secondary polishing of WEDM.

The Sa and Sku decrease after primary WEDM polishing. This shows that the WEDM polishing improved the surface topography. Figure 4.50 shows that the increment in CA from the roughing process to primary and secondary polishing. As shown in Figure 4.50. it is evident that the contact angle increases dramatically from 97.68° (SD=12.25) to 126.68° (SD=10.20) after primary WEDM polishing. This means that the surface becomes more hydrophobic. From Table 4.43, it indicates that the mean Sa after primary and secondary polishing is considered identical ($\sim 3.2\mu m$) whereas the slight increase in Sku indicates that the surface generated after secondary polishing is dominated by deeper craters, which increases the 'air cushion'

effect, considering the WEDM surface is generated by random and repeated superposition of electrical discharge. The 3D surface topography map in Figure 4.51. shows that the surface generated after secondary polishing is more uniform and homogeneous. After secondary polishing, a close to superhydrophobic surface (CA=146.20°) was generated.

Table 4.43: Mean Sa and Sku after primary and secondary polishing.

Parameter	First Pass / Primary Polishing		Second Pass / Secondary Polishing	
	Sa (μm)	Sku	Sa (μm)	Sku
Upper	3.42	3.07	3.25	3.64
Middle	3.21	4.74	3.06	4.74
Bottom	3.21	3.17	3.25	3.70
Mean	3.28	3.66	3.19	4.03

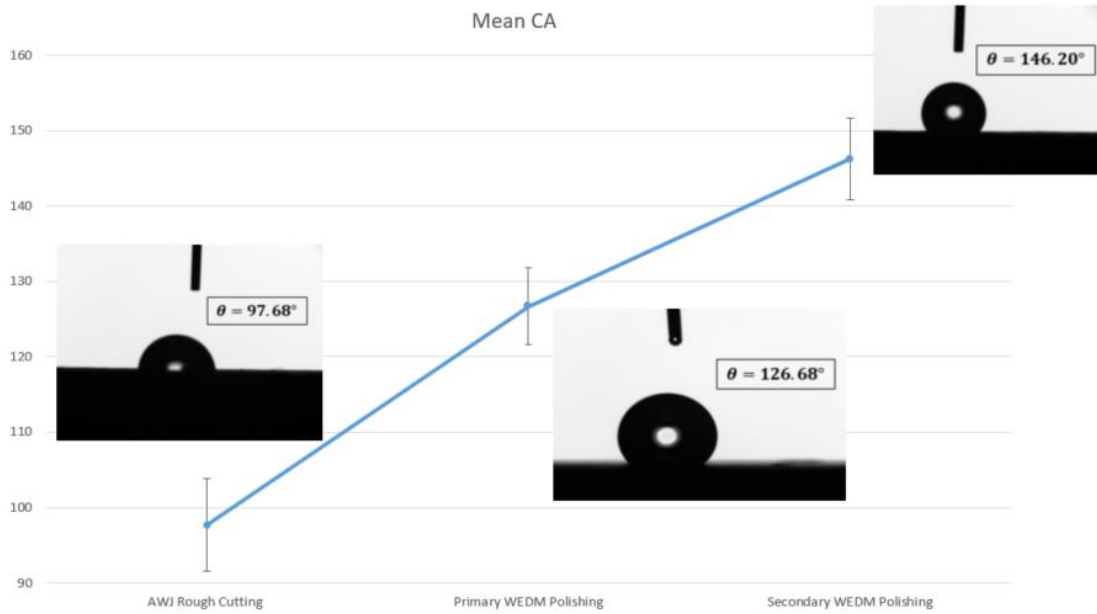


Figure 4.50: Increment in CA for WEDM rough cutting and dual passes WEDM polishing.

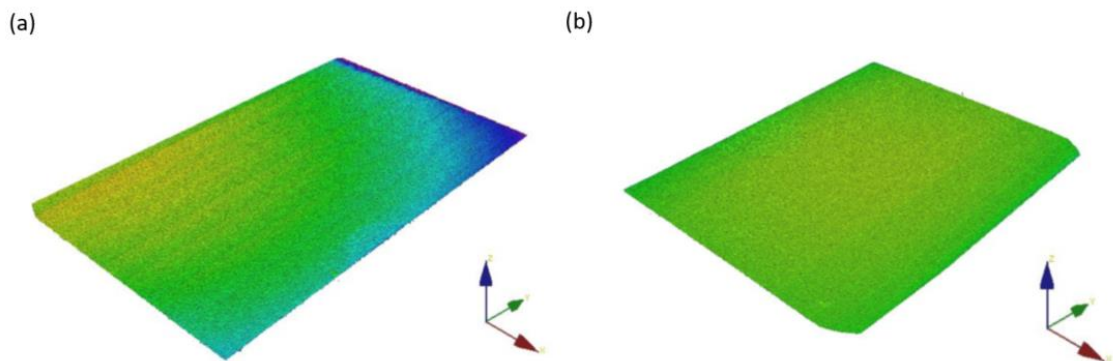


Figure 4.51: The 3D topography map of the (a) primary WEDM polishing and (b) secondary WEDM polishing surface.

CHAPTER 5: CONCLUSIONS

1. Phase One:

The objective of this phase was to identify the baseline operating process parameters for WEDM and AWJ of MMC and investigate the workpiece surface integrity.

- The optimisation of process parameters for AWJ and WEDM are detailed in Chapter 4. In general, it was determined that traverse rate is the dominant factor for AWJ; pulse-on time for WEDM.
- Despite significant progress has been made towards machinability of MMC using AWJ and WEDM by optimising the process parameters in literature, the in-depth understanding of the machined surface integrity was not evaluated.

2. Phase Two:

The objective of this phase was to evaluate the relationship between wettability and the cutting process parameters.

- For both WEDM and AWJ machined samples, Taguchi and ANOVA analysis suggest that there is no interaction between the static contact angle and the machining process parameters.

- Comparing the two different machining methods, samples machined by AWJ method has shown the better adhesion due to the rougher surface finish and oxygen adsorption.
- Sa and Sku are the major factors in affecting the wettability of the MMC.
- Isotropic features and topography with high surface roughness Sa and large kurtosis exhibits hydrophobic behaviour. The larger the craters/pits, the larger the contact angle due to the Cassie-Baxter or 'air-cushion' effect.
- The results of elemental analysis and XPS experiment indicate that the oxygen diffusion into the MMC surface is random and no significant influence on the surface wettability.

3. Phase Three:

The objective of this phase is to propose a hybrid machining strategy combining AWJ and WEDM in order to create a hydrophobic surface for special purpose aerospace application.

- The results show that the proposed strategy of conducting rough cutting using AWJ and dual passes of WEDM polishing to develop microscale features generated a close to superhydrophobic surface (CA= 146.20°).

- This hybrid machining concept highlights the significant potential of high MRR of AWJ and the rapid fabrication of close to superhydrophobic surface of dual passes WEDM polishing.
- The proposed methodology shows that the development of hybrid machining can save cost and elimination of additional coating for industrial implementation.

4. Key Project Contributions

- The Taguchi and ANOVA analysis showed that the DoE is valid in determining the optimum process parameters. The experiments confirmed that the process parameters optimisation provide reference for the selection of functional surface manufacturing methods in industrial application.
- In this present study, static contact angle is proved to be an effective mean for evaluating wettability of workpiece material., it can be concluded that surface roughness Sa is the major factor in affecting the wettability of the MMC.
- The state-of-the-art in hybrid machining WEDM and AWJ machining of MMC has been presented in this research. The case study demonstrated a novel and non-conventional hybrid machining application of abrasive waterjet and wire electrical discharge machining to generate a hydrophobic Al-SiC MMC surface.

CHAPTER 6: RECOMMENDATIONS FOR FUTURE WORKS

Several areas were highlighted during this research which the author recommended for future investigations.:

- Further studies should be carried out by using full factorial analysis on the significant parameters.
- Considering the thermal effect of WEDM on the machined surfaces, the analysis of material deformation behaviour, residual stress and influence of surface thermal damage on the wettability is necessary.
- The proposed hybrid machining strategy shows a huge potential and benefit in the aerospace industry especially in those applications where controlled surface finishing and higher dimensional precision are required. It is necessary to further improve the study of the proposed hybrid machining strategy and establish their applications in industrial settings.
- Future research needs to be continued to study the potential of improvement in tool design strategy (parallel hybrid machining), process monitoring and overall time and cost efficiency. The development of multiscale modelling of the hybrid machining process is another key for future studies.

REFERENCES

1. Ibrahim, I.A., F.A. Mohamed, and E.J. Lavernia, *Particulate reinforced metal matrix composites — a review*. Journal of Materials Science, 1991. **26**(5): p. 1137-1156.
2. Fan, J. and J. Njuguna, *An Introduction to Lightweight Composite Materials and Their Use in Transport Structures*. 2016. p. 3-34.
3. Callister, W.D. and D.G. Rethwisch, *Fundamentals of Materials Science and Engineering: An Integrated Approach*. 2012: Wiley.
4. Campbell, F.C., *Manufacturing technology for aerospace structural materials [electronic resource] / F.C. Campbell*. Aerospace engineering materials science. 2006, Amsterdam: Elsevier.
5. Le Roux, T., *The machining of a metal matrix composite / by Teresa Maria le Roux*. 1994, Thesis (M.Phil)-University of Birmingham, School of Metallurgy and Materials.
6. Clyne, T.W., *An introduction to metal matrix composites*, P.J. Withers, Editor. 1993, New York, NY, USA :: Cambridge [England] .:
7. Miracle, D.B., *Metal matrix composites – From science to technological significance*. Composites Science and Technology, 2005. **65**(15): p. 2526-2540.
8. Lee, KB., Kim, SH., Kim, DY , *Aluminum Matrix Composites Manufactured using Nitridation-Induced Self-Forming Process*. Scientific Reports, 2019. **9**(1): p. 20389.
9. Gupta, M. and M.K. Surappa, *Processing-Microstructure-Mechanical Properties of Al Based Metal Matrix Composites Synthesized Using Casting Route*. Key Engineering Materials, 1995. **104-107**: p. 259-274.

10. Divecha, A.P., S.G. Fishman, and S.D. Karmarkar, *Silicon Carbide Reinforced Aluminum—A Formable Composite*. JOM, 1981. **33**(9): p. 12-17.
11. Davim, J.P., *Application of Merchant theory in machining particulate metal matrix composites*. Materials & Design, 2007. **28**(10): p. 2684-2687.
12. Chawla, N., J.W. Jones, C. Andres, and J.E. Allison, *Effect of SiC volume fraction and particle size on the fatigue resistance of a 2080 Al/SiCp composite*. Metallurgical and Materials Transactions A, 1998. **29**(11): p. 2843-2854.
13. N. Chawla, C. Andes, L. C. Davis, J. E. Allison, and J. W. Jones, *The interactive role of inclusions and SiC reinforcement on the high-cycle fatigue resistance of particle reinforced metal matrix composites*. Metallurgical and Materials Transactions A, 2000. **31**(3): p. 951-957.
14. Milan, M.T. and P. Bowen, *Fatigue crack growth resistance of SiCp reinforced Al alloys: Effects of particle size, particle volume fraction, and matrix strength*. Journal of Materials Engineering and Performance, 2004. **13**(5): p. 612-618.
15. Hobi, A., H. Newal, M. Dawood, and N. Dawood, *Silicon Carbide Particle Reinforced Aluminum Matrix Composite Prepared by Stir-Casting*. 2012: p. ٤٤٢.
16. *CES Edupack Software*. 2009, Granta Design Limited.
17. Surappa, M.K., *Aluminium matrix composites: Challenges and opportunities*. Sadhana, 2003. **28**(1): p. 319-334.
18. Francis, N., M. Leonard, and K. John Baptist, *Novel Applications of Aluminium Metal Matrix Composites*, in *Aluminium Alloys and*

- Composites*, C. Kavian Omar, Editor. 2019, IntechOpen: Rijeka. p. Ch. 5.
19. Ajay Kumar, P., P. Rohatgi, and D. Weiss, *50 Years of Foundry-Produced Metal Matrix Composites and Future Opportunities*. International Journal of Metalcasting, 2020. **14**(2): p. 291-317.
 20. Stojanovic, B. and L. Ivanovic, *Application of aluminium hybrid composites in automotive industry*. Tehnicki Vjesnik, 2015. **22**: p. 247-251.
 21. Dev Srivyas, P. and M.S. Charoo, *Application of Hybrid Aluminum Matrix Composite in Automotive Industry*. Materials Today: Proceedings, 2019. **18**: p. 3189-3200.
 22. Amin, S.M. and B.F. Wollenberg, *Toward a smart grid: power delivery for the 21st century*. IEEE Power and Energy Magazine, 2005. **3**(5): p. 34-41.
 23. Singh, H., G. Singh Brar, H. Kumar, and V. Aggarwal, *A review on metal matrix composite for automobile applications*. Materials Today: Proceedings, 2021. **43**: p. 320-325.
 24. G B, V., C. Rao, and N. Selvaraj, *Mechanical and Tribological Behavior of Particulate Reinforced Aluminum Metal Matrix Composites – a review*. Journal of Minerals and Materials Characterization and Engineering, 2011. **10**.
 25. Ashok Kumar, S J Akash, S Arunkumar, V Balaji, M Balamurugan and A J Kumar, *Fabrication and Corrosion Behaviour of Aluminium Metal Matrix Composites – A Review*. IOP Conference Series: Materials Science and Engineering, 2020. **923**(1): p. 012056.
 26. European Commission, Directorate-General for Mobility and Transport, Directorate-General for Research and Innovation,

- Flightpath 2050 : Europe's vision for aviation : maintaining global leadership and serving society's needs*. 2011: Publications Office.
27. M'Saoubi, R., Axinte D., Soo S L, Nobel C, Attia H., Kappmeyer G., Engin S., Sim WM., *High performance cutting of advanced aerospace alloys and composite materials*. CIRP Annals, 2015. **64**(2): p. 557-580.
 28. STEPHENS, J. *High temperature metal matrix composites for future aerospace systems*. in *24th Joint Propulsion Conference*. 1987.
 29. Lino Alves, F.J., A.M. Baptista, and A.T. Marques, *3 - Metal and ceramic matrix composites in aerospace engineering*, in *Advanced Composite Materials for Aerospace Engineering*, S. Rana and R. Figueiro, Editors. 2016, Woodhead Publishing. p. 59-99.
 30. Rawal, S.P., *Metal-matrix composites for space applications*. JOM, 2001. **53**(4): p. 14-17.
 31. Lasance, C.J.M. and R. Simons, *Advances in High Performance Cooling for Electronics*. 2005. **11**.
 32. Berg, J.S., *Composite Material Advances in the Golf Industry*. 2000: Society of Manufacturing Engineers.
 33. Sidhu, S.S., S. Kumar, and A. Batish, *Metal Matrix Composites for Thermal Management: A Review*. Critical Reviews in Solid State and Materials Sciences, 2016. **41**(2): p. 132-157.
 34. Association, T.A. *Product Markets | The Aluminum Association,* Aluminum Association, 2020.; Available from: <https://www.aluminum.org/product-markets>.
 35. Dandekar, C.R. and Y.C. Shin, *Modeling of machining of composite materials: A review*. International Journal of Machine Tools and Manufacture, 2012. **57**: p. 102-121.

36. Khanna, N., et al., *Effect of Hybrid Machining Techniques on Machining Performance of In-House Developed Mg-PMMC*. Transactions of the Indian Institute of Metals, 2019. **72**(7): p. 1799-1807.
37. Rui-song, J., W. Wen-hu, S. Guo-dong, and W. Zeng-qiang, *Experimental investigation on machinability of in situ formed TiB₂ particles reinforced Al MMCs*. Journal of Manufacturing Processes, 2016. **23**: p. 249-257.
38. Danil Yu. P, Mozammel M, Munish K. G, Alisson R. Machado, Ítalo V. Tomaz, Murat S, Szymon W, T Mikolajczyk, W Kapłonek,, *Improvement of machinability of Ti and its alloys using cooling-lubrication techniques: A review and future prospect*. Journal of Materials Research and Technology, 2021. **11**: p. 719-753.
39. Przystacki, D., P. Szymanski, and S. Wojciechowski, *Formation of surface layer in metal matrix composite A359/20SiCP during laser assisted turning*. Composites Part A: Applied Science and Manufacturing, 2016. **91**: p. 370-379.
40. Bharat, N. and P.S.C. Bose, *A study on conventional and non-conventional machining behaviour of metal matrix composites: a review*. International Journal of Ambient Energy, 2022. **43**(1): p. 7600-7616.
41. N.K. Angwenyi, N.M. Senga, N.K. Ronoh, F.M. Mwema, E.T. Akinlabi, B. Tanya, *The effects of machining parameters on conventional machining: An overview*. Materials Today: Proceedings, 2021. **44**: p. 1540-1542.

42. Nicholls, C., B. Boswell, I. Davies, and N. Islam, *Review of machining metal matrix composites*. The International Journal of Advanced Manufacturing Technology, 2017. **90**: p. 2429-2441.
43. Ruisong JIANG, Xinfu CHEN, Renwei GE, Wenhui WANG, Guodong SONG, *Influence of TiB₂ particles on machinability and machining parameter optimization of TiB₂/Al MMCs*. Chinese Journal of Aeronautics, 2018. **31**(1): p. 187-196.
44. Jangali Satish, G., V.N. Gaitonde, and V.N. Kulkarni, *Traditional and non-traditional machining of nickel-based superalloys: A brief review*. Materials Today: Proceedings, 2021. **44**: p. 1448-1454.
45. Müller, F. and J. Monaghan, *Non-conventional machining of particle reinforced metal matrix composite*. International Journal of Machine Tools and Manufacture, 2000. **40**(9): p. 1351-1366.
46. Mehta, K.M., S. Kumar Pandey, and V.A. Shaikh, *Unconventional Machining of ceramic matrix Composites – A review*. Materials Today: Proceedings, 2021. **46**: p. 7661-7669.
47. Min Ao, Huimin Liu, Chaofang Dong, Shan Feng, Juncheng Liu, *Degradation mechanism of 6063 aluminium matrix composite reinforced with TiC and Al₂O₃ particles*. Journal of Alloys and Compounds, 2021. **859**: p. 157838.
48. Gunasekaran, T., S.N. Vijayan, P. Prakash, and P. Satishkumar, *Mechanical properties and characterization of Al7075 aluminum alloy based ZrO₂ particle reinforced metal-matrix composites*. Materials Today: Proceedings, 2020.
49. Mahaviradhan, N., S. Sivaganesan, N. Padma Sravya, and A. Parthiban, *Experimental investigation on mechanical properties of*

- carbon fiber reinforced aluminum metal matrix composite*. Materials Today: Proceedings, 2021. **39**: p. 743-747.
50. Sanjay Manghnani, Deepika Shekhawat, Chandramani Goswami, Tapan Kumar Patnaik, Tej Singh, *Mechanical and tribological characteristics of Si₃N₄ reinforced aluminium matrix composites: A short review*. Materials Today: Proceedings, 2021. **44**: p. 4059-4064.
51. Jaya Prasad, V., K. Narasimha Rao, and N. Kishore Babu, *Mechanical and tribological characterization of aluminum metal matrix composite reinforced with micro ceramic particles (TiB₂/SiC)*. Materials Today: Proceedings, 2020. **23**: p. 637-641.
52. Davim, J.P., *Machining of Metal Matrix Composites*. 2011: Springer London.
53. Sanikere, Prashantha & Veerasha, R.B. & Shashidhara, S.M. & Shivanna, Mallik & Shivasiddaramaiah, A.G., *A Study on Machining Characteristics of Al6061-Sic Metal Matrix Composite through Wire – Cut Electro Discharge Machining*. Materials Today: Proceedings, 2017. **4**(10): p. 10779-10785.
54. Younas, T., M. Manzoor, and J. Kumari. *Non-conventional machining processes as expedient alternatives for conventional machining processes*. in *2017 IEEE 3rd International Conference on Engineering Technologies and Social Sciences (ICETSS)*. 2017.
55. Zhao, Wansheng & Gu, Lin & Xu, H. & Li, L. & Xiang, X., *A Novel High Efficiency Electrical Erosion Process – Blasting Erosion Arc Machining*. Procedia CIRP, 2013. **6**: p. 621-625.
56. D. Palanisamy, N.Manikandan, R. Ramesh, M. Kathirvelan, D. Arulkirubakaran, *Machinability Analysis and Optimization of Wire-EDM Textured Conventional Tungsten Carbide Inserts in Machining of*

- 17–4 PH Stainless Steel. *Materials Today: Proceedings*, 2021. **39**: p. 359-367.
57. Vishnu Vardhana Naidu, B., K.C. Varaprasad, and K. Prahlada Rao, *Development of regression models for wire electrical discharge machining of aluminium metal matrix composites*. *Materials Today: Proceedings*, 2021. **39**: p. 236-239.
58. Uğur, A., E. Nas, and H. Gökkaya, *Investigation of the Machinability of SiC Reinforced MMC materials produced by Molten Metal Stirring and Conventional Casting Technique in Die-Sinking Electrical Discharge Machine*. *International Journal of Mechanical Sciences*, 2020. **186**: p. 105875.
59. Sivaprakasam, P. and P. Hariharan, *Surface characteristics of nano powder mixed micro-wire electrical discharge machining on inconel alloy*. *Materials Today: Proceedings*, 2021. **38**: p. 494-498.
60. J.J. Sha, Z.Z. Lv, G.Z. Lin, J.X. Dai, Y.F. Zu, Y.Q. Xian, W. Zhang, D. Cui, C.L. Yan, *Synergistic strengthening of aluminum matrix composites reinforced by SiC nanoparticles and carbon fibers*. *Materials Letters*, 2020. **262**: p. 127024.
61. Ulas, M., O. Aydur, T. Gurgenc, and C. Ozel, *Surface roughness prediction of machined aluminum alloy with wire electrical discharge machining by different machine learning algorithms*. *Journal of Materials Research and Technology*, 2020. **9**(6): p. 12512-12524.
62. F. Klocke, D. Welling, A. Klink, D. Veselovac, T. Nöthe, R. Perez, *Evaluation of Advanced Wire-EDM Capabilities for the Manufacture of Fir Tree Slots in Inconel 718*. *Procedia CIRP*, 2014. **14**: p. 430-435.

63. Yue, T.M. and V. Dai, *Wire electrical discharge machining of Al₂O₃ particle and short fibre reinforced aluminium based composites*. *Materials Science and Technology*, 1996. **12**(10): p. 831-836.
64. Antar, Mohammad & Soo, S.L. & Aspinwall, D.K. & Jones, D. & Perez, Roberto., *Productivity and Workpiece Surface Integrity When WEDM Aerospace Alloys Using Coated Wires*. *Procedia Engineering*, 2011. **19**: p. 3-8.
65. T. Masuzawa, M. Fujino, K. Kobayashi, T. Suzuki, N. Kinoshita., *Wire Electro-Discharge Grinding for Micro-Machining*. *CIRP Annals*, 1985. **34**(1): p. 431-434.
66. Karmakar, R. and P. Maji, *Research advancements in machining of metal matrix composites through wire electro discharge machining technique*. *Materials Today: Proceedings*, 2021. **44**: p. 4457-4461.
67. M.B.A. Shuvho, M.A. Chowdhury, M. Kchaou, B.K. Roy, A. Rahman, M.A. Islam, *Surface characterization and mechanical behavior of aluminum based metal matrix composite reinforced with nano Al₂O₃, SiC, TiO₂ particles*. *Chemical Data Collections*, 2020. **28**: p. 100442.
68. N.R. Prabhuswamy, S. Srinivas, Aref Vasli, M.V. Sheshashayan, S. Venkatesh, Yash Roongta, *Machinability Studies of Aluminium 6061 cut by Abrasive Water Jet*. *Materials Today: Proceedings*, 2018. **5**(1, Part 3): p. 2865-2870.
69. Suresh, V., A.D. Praneet, and J. Anoop, *Ingenious analysis on machining parameters of aluminium alloy (LM25)/graphite (Gr)/boron carbide (B₄C) hybrid composites using wire electrical discharge machining (WEDM)*. *Materials Today: Proceedings*, 2021. **37**: p. 3112-3117.

70. Griffiths, B., *3 - Surface Finish Measuring Methods*, in *Manufacturing Surface Technology*, B. Griffiths, Editor. 2001, Kogan Page Science: Oxford. p. 70-108.
71. Gururaja, S., M. Ramulu, and W. Pedersen, *MACHINING OF MMCs: A REVIEW*. *Machining Science and Technology*, 2013. **17**(1): p. 41-73.
72. Kulekci, M.K., *Processes and apparatus developments in industrial waterjet applications*. *International Journal of Machine Tools and Manufacture*, 2002. **42**(12): p. 1297-1306.
73. Hashish, M., *Optimization Factors in Abrasive-Waterjet Machining*. *Journal of Engineering for Industry*, 1991. **113**(1): p. 29-37.
74. Sureban, R., V.N. Kulkarni, and V.N. Gaitonde, *Modern Optimization Techniques for Advanced Machining Processes – A Review*. *Materials Today: Proceedings*, 2019. **18**: p. 3034-3042.
75. Razzell, A.G., *4.23 - Joining and Machining of Ceramic Matrix Composites*, in *Comprehensive Composite Materials*, A. Kelly and C. Zweben, Editors. 2000, Pergamon: Oxford. p. 689-697.
76. Maneiah, D., M. Shunmugasundaram, A. Raji Reddy, and B. Zareena, *Optimization of machining parameters for surface roughness during abrasive water jet machining of aluminium/magnesium hybrid metal matrix composites*. *Materials Today: Proceedings*, 2020. **27**: p. 1293-1298.
77. Matsumura, T., T. Muramatsu, and S. Fueki, *Abrasive water jet machining of glass with stagnation effect*. *CIRP Annals*, 2011. **60**(1): p. 355-358.
78. Natarajan, Y., P.K. Murugesan, M. Mohan, and S.A. Liyakath Ali Khan, *Abrasive Water Jet Machining process: A state of art of review*. *Journal of Manufacturing Processes*, 2020. **49**: p. 271-322.

79. Raissi, K., A. Cornier, D. Kremer, and O. Simonin. *Mixing tube geometry influence on abrasive waterjet flow*. in *BHR GROUP CONFERENCE SERIES PUBLICATION*. 1996. MECHANICAL ENGINEERING PUBLICATIONS LIMITED.
80. Labus, T., *High pressure equipment and systems*. An overview of waterjet fundamentals and applications, 5th Ed. Waterjet Technology Assoc., Saint Louis, 2001.
81. Vijay Kumar, K., T.S.A. Suryakumari, and V. Mohanavel, *A Review on methods used to optimize Abrasive Jet Machining parameters*. Materials Today: Proceedings, 2020.
82. Saurabh, Saket & Tiwari, Tanmay & Nag, Akash & Dixit, Amit & Mandal, Niladri & Das, Alok & Mandal, Amitava & Srivastava, Ashish, *Processing of alumina ceramics by abrasive waterjet- an experimental study*. Materials Today: Proceedings, 2018. **5**: p. 18061-18069.
83. Radovanovic, M., *Multi-Objective Optimization of Abrasive Water Jet Cutting Using MOGA*. Procedia Manufacturing, 2020. **47**: p. 781-787.
84. Paul, T. and I. Mandal, *Development and Parametric Optimization of Abrasive Jet Machining Setup*. Materials Today: Proceedings, 2020. **22**: p. 2306-2315.
85. Balaji, D.S. and T. Jeyapoovan, *Multi-objective optimization in abrasive water jet peening on AA6063 alloy*. Materials Today: Proceedings, 2021. **45**: p. 1928-1933.
86. Kumar, V., M. Kharub, R. Kumar, and P. Rakesh, *Process Parameters Optimization of Wire EDM on AISI 304 Using the Taguchi Method*. 2021. p. 363-371.

87. Singh, V. and S.K. Pradhan, *Optimization of WEDM Parameters Using Taguchi Technique and Response Surface Methodology in Machining of AISI D2 Steel*. Procedia Engineering, 2014. **97**: p. 1597-1608.
88. Sharma, D., R. Bhandari, A. Aherwar, and R. Rimasauskiene, *Matrix materials used in composites: A comprehensive study*. Materials Today: Proceedings, 2019. **21**: p. 1559-1562.
89. Ho, K.H., S.T. Newman, S. Rahimifard, and R.D. Allen, *State of the art in wire electrical discharge machining (WEDM)*. International Journal of Machine Tools and Manufacture, 2004. **44**(12): p. 1247-1259.
90. Alpas, A.T., S. Bhattacharya, and I.M. Hutchings, *4.5 Wear of Particulate Metal Matrix Composites*, in *Comprehensive Composite Materials II*, P.W.R. Beaumont and C.H. Zweben, Editors. 2018, Elsevier: Oxford. p. 137-172.
91. G. Agrawal, Y.S. Negi, S. Pradhan, M. Dash, S.K. Samal, *3 - Wettability and contact angle of polymeric biomaterials*, in *Characterization of Polymeric Biomaterials*, M.C. Tanzi and S. Farè, Editors. 2017, Woodhead Publishing. p. 57-81.
92. Lee, L.-H., *Surface Chemistry of Solid and Liquid Interfaces*, by H. Yildirim Erbil. The Journal of Adhesion, 2007. **83**(5): p. 507-508.
93. Q. Huang, C. Zhang, Qunying Liu, Yan Ning and Yongxing Cao, *New type of fiber optic sensor network for smart grid interface of transmission system*. in *IEEE PES General Meeting*. 2010.
94. Yukihiro Kusano, Masato Yoshikawa, Itsuo Tanuma, Kazuo Naito, Masuhiro Kogoma, Satiko Okazaki, *Plasma surface treatment of fluoropolymers at atmospheric pressure*, in *Advanced Materials '93*, 1994, Elsevier. p. 657-660.

95. Praveen, K.M., C.V. Pious, S. Thomas, and Y. Grohens, *Chapter 1 - Relevance of Plasma Processing on Polymeric Materials and Interfaces*, in *Non-Thermal Plasma Technology for Polymeric Materials*, S. Thomas, et al., Editors. 2019, Elsevier. p. 1-21.
96. Extrand, C.W. and S.I. Moon, *When Sessile Drops Are No Longer Small: Transitions from Spherical to Fully Flattened*. *Langmuir*, 2010. **26**(14): p. 11815-11822.
97. Alam, E.C.D.a.W., *CHAPTER 1 - Wettability*, in *Wettability*, E.C.D.a.W.B.T.-W. Alam, Editor. 2008, Eds. Gulf Publishing Company. p. 1-55.
98. Kleinhans, M.G, Markies, H., de Vet, S.J., Postema F.N., *Static and dynamic angles of repose in loose granular materials under reduced gravity*. *Journal of Geophysical Research Atmospheres*, 2011. **116**.
99. Miwa, Masashi & Nakajima, Akira & Fujishima, Akira & Hashimoto, Kazuhito & Watanabe, Toshiya, *Effects of the Surface Roughness on Sliding Angles of Water Droplets on Superhydrophobic Surfaces*. *Langmuir*, 2000. **16**(13): p. 5754-5760.
100. Pierce, E., F.J. Carmona, and A. Amirfazli, *Understanding of sliding and contact angle results in tilted plate experiments*. *Colloids and Surfaces A: Physicochemical and Engineering Aspects*, 2008. **323**(1): p. 73-82.
101. Ali, M.Y. and W.N.P. Hung, *1.11 Micromachining*, in *Comprehensive Materials Finishing*, M.S.J. Hashmi, Editor. 2017, Elsevier: Oxford. p. 322-343.
102. Abdulhadi, H., S. Aqida, and I. Ismail, *Tool Failure in Die Casting*. 2019.

103. Klemm, A., P. Sanjeevan, and P. Klemm, *The Effects of Laser Cleaning Process on Geometrical Microstructure of Cementitious Composites*. *Brittle Matrix Composites 9, BMC 2009*, 2009: p. 323-334.
104. K. Grundke, K. Pöschel, A. Synytska, R. Frenzel, A. Drechsler, M. Nitschke, A.L. Cordeiro, P. Uhlmann, P.B. Welzel, *Experimental studies of contact angle hysteresis phenomena on polymer surfaces — Toward the understanding and control of wettability for different applications*. *Advances in Colloid and Interface Science*, 2015. **222**: p. 350-376.
105. Nikola Slepickova, K., S. Petr, K. Zdenka, and S. Vaclav, *Wettability and Other Surface Properties of Modified Polymers*, in *Wetting and Wettability*, A. Mahmood, Editor. 2015, IntechOpen: Rijeka. p. Ch. 12.
106. Mohammed, A., D.L. Abang Haji Abdul Majid, M.R. Ishak, and U. Basheer, *A Brief Research Review for Improvement Methods the Wettability between Ceramic Reinforcement Particulate and Aluminium Matrix Composites*. Vol. 203. 2017. 012002.
107. Hashim, J., L. Looney, and M.S.J. Hashmi, *The enhancement of wettability of SiC particles in cast aluminium matrix composites*. *Journal of Materials Processing Technology*, 2001. **119**(1): p. 329-335.
108. Sarkar S, Sen S, Mishra SC, Kudelwar MK, Mohan S., *Studies on Aluminum — Fly-Ash Composite Produced by Impeller Mixing*. *Journal of Reinforced Plastics and Composites*, 2010. **29**(1): p. 144-148.
109. Singh, V.K., S. Chauhan, P.C. Gope, and A.K. Chaudhary, *Enhancement of Wettability of Aluminum Based Silicon Carbide Reinforced Particulate Metal Matrix Composite*. *High Temperature Materials and Processes*, 2015. **34**(2): p. 163-170.

110. Omrani, E., A.D. Moghadam, P.L. Menezes, and P.K. Rohatgi, *Influences of graphite reinforcement on the tribological properties of self-lubricating aluminum matrix composites for green tribology, sustainability, and energy efficiency—a review*. The International Journal of Advanced Manufacturing Technology, 2016. **83**(1): p. 325-346.
111. Gutema, E., V. Bazhin, and S. Fedorov, *Wettability enhancement of aluminum metal matrix composite reinforced with magnesium coated silicon carbide particles*. IOP Conference Series: Materials Science and Engineering, 2019. **560**: p. 012179.
112. Kennedy, A.R., *The microstructure and mechanical properties of Al-Si-B₄C metal matrix composites*. Journal of Materials Science, 2002. **37**(2): p. 317-323.
113. Kumar, A. and R. Rai, *Fabrication, Microstructure and Mechanical Properties of Boron Carbide (B₄C) Reinforced Aluminum Metal Matrix Composite - A Review*. IOP Conference Series: Materials Science and Engineering, 2018. **377**: p. 012092.
114. Hashim, J., L. Looney, and M.S.J. Hashmi, *Metal matrix composites: production by the stir casting method*. Journal of Materials Processing Technology, 1999. **92-93**: p. 1-7.
115. Kumar S, S. and S.S. Hiremath, *Surface topography and wettability of the metallic surface machined through abrasive flow finishing*. Advances in Materials and Processing Technologies, 2020. **6**(1): p. 115-132.
116. Edachery, V., S. R, and S.V. Kailas, *Influence of surface texture directionality and roughness on wettability, sliding angle, contact*

- angle hysteresis, and lubricant entrapment capability*. Tribology International, 2021. **158**: p. 106932.
117. Ablyaz, T.R., Shlykov, E.S., Muratov, K.R., Mahajan, A., Singh, G., Devgan, S., Sidhu, S.S., *Surface Characterization and Tribological Performance Analysis of Electric Discharge Machined Duplex Stainless Steel*. Micromachines, 2020. **11**(10): p. 926.
 118. Quarto, M., G. Bissacco, and G. D'Urso, *Machinability and Energy Efficiency in Micro-EDM Milling of Zirconium Boride Reinforced with Silicon Carbide Fibers*. Materials, 2019. **12**: p. 3920.
 119. F. Piscitelli, F. Tescione, L. Mazzola, G. Bruno, M. Lavorgna, *On a simplified method to produce hydrophobic coatings for aeronautical applications*. Applied Surface Science, 2019. **472**: p. 71-81.
 120. Thomas, S.K., R.P. Cassoni, and C.D. MacArthur, *Aircraft anti-icing and de-icing techniques and modeling*. Journal of aircraft, 1996. **33**(5): p. 841-854.
 121. Lein, H.L., *Chapter 9 - Coatings and surfaces with hydrophobic and anti-icing properties*, in *Frontiers of Nanoscience*, M. Benelmekki and A. Erbe, Editors. 2019, Elsevier. p. 257-269.
 122. Bairagi, S., Järrendahl, K., Eriksson, F., Hultman, L., Birch, J., Hsiao, C.-L., *Glancing Angle Deposition and Growth Mechanism of Inclined AlN Nanostructures Using Reactive Magnetron Sputtering*. Coatings, 2020. **10**(8): p. 768.
 123. Widyatmoko, D. and P. Dehdezi, *De-icing/Anti-icing agents and their effects on airfield asphalt pavements*. 2015.
 124. T. Bharathidasan, S. Vijay Kumar, M.S. Bobji, R.P.S. Chakradhar, Bharathibai J. Basu, *Effect of wettability and surface roughness on ice-*

- adhesion strength of hydrophilic, hydrophobic and superhydrophobic surfaces. Applied Surface Science, 2014. 314.*
125. Körpe, D., *Development of de-icing and anti-icing solutions for aircraft on ground and analysis of their flow instability characteristics.* 2008.
 126. Khan, A. and T. Akhtar, *Preparation, physico-chemical characterization and electrical conductivity measurement studies of an organic-inorganic nanocomposite cation-exchanger: Poly-*o*-toluidine Zr(IV) phosphate.* *Electrochimica Acta - ELECTROCHIM ACTA*, 2008. **53**: p. 5540-5548.
 127. Yilmaz, S., *The Geometric Resistivity Correction Factor for Several Geometrical Samples.* *Journal of Semiconductors*, 2015. **36**: p. 082001-1.
 128. *GMA Brochure Waterjet*, in *GMA Australian Garnet*. 2006.
 129. Charmilles, *Robofil X40 CC X40 SL X40 SLP 690 Reference Manual*, in 205 971 02. 2007.
 130. Satyanarayana, S. and N. Babu, *Penetration ability of abrasive waterjets in cutting of aluminum-silicon carbide particulate metal matrix composites.* *Machining Science and Technology*, 2012. **16**: p. 337-354.
 131. *The Sum of Our Experience A Guide to Materials Preparation and Analysis.* 4th Edition ed. 2013: Buehler SumMet.
 132. Deleanu, L., C. Georgescu, and C. Suci, *A comparison between 2D and 3D surface parameters for evaluating the quality of surfaces.* *Ann. "dunarea de Jos" Univ. Galati- Fascicle v*, 2012. **1**: p. 5-12.
 133. Puertas, I. and C. Luis, *A Study of Optimization of Machining Parameters for Electrical Discharge Machining of Boron Carbide.*

- Materials and Manufacturing Processes - MATER MANUF PROCESS, 2004. **19**: p. 1041-1070.
134. Garg, R.K., Singh, K.K., Sachdeva, A., *Review of research work in sinking EDM and WEDM on metal matrix composite materials*. The International Journal of Advanced Manufacturing Technology, 2010. **50**(5): p. 611-624.
 135. Niranjana, C.A., S. Srinivas, and M. Ramachandra, *Effect of process parameters on depth of penetration and topography of AZ91 magnesium alloy in abrasive water jet cutting*. Journal of Magnesium and Alloys, 2018. **6**(4): p. 366-374.
 136. Huang, L., P. Kinnell, and P.H. Shipway, *Parametric Effects on Grit Embedment and Surface Morphology in an Innovative Hybrid Waterjet Cleaning Process for Alpha Case Removal from Titanium Alloys*. Procedia CIRP, 2013. **6**: p. 594-599.
 137. Simpson DJ, Bredow T, Chandra AP, Cavallaro GP, Gerson AR, *The effect of iron and copper impurities on the wettability of sphalerite (110) surface*. J Comput Chem, 2011. **32**(9): p. 2022-30.
 138. Goraj, Z. *AN OVERVIEW OF THE DEICING AND ANTIICING TECHNOLOGIES WITH PROSPECTS FOR THE FUTURE*. 2004.
 139. Schuh, G., J. Kreysa, and S. Orilski, *Roadmap "Hybride Produktion": Wie 1+1=3-Effekte in der Produktion maximiert werden können*. Fraunhofer IPT, 2009. **104**.
 140. Liao, Z., la Monaca, A., Murray, J.W., Speidel, A., Ushmaev, D., Clare, A.T., Axinte, D.A., & M'Saoubi, R, *Surface integrity in metal machining - Part I: Fundamentals of surface characteristics and formation mechanisms*. International Journal of Machine Tools and Manufacture, 2021. **162**: p. 103687.

APPENDIX A: MICROHARDNESS PROFILE

Results of microhardness graphs of cutting trials presented in Chapter 4.2 are shown below:

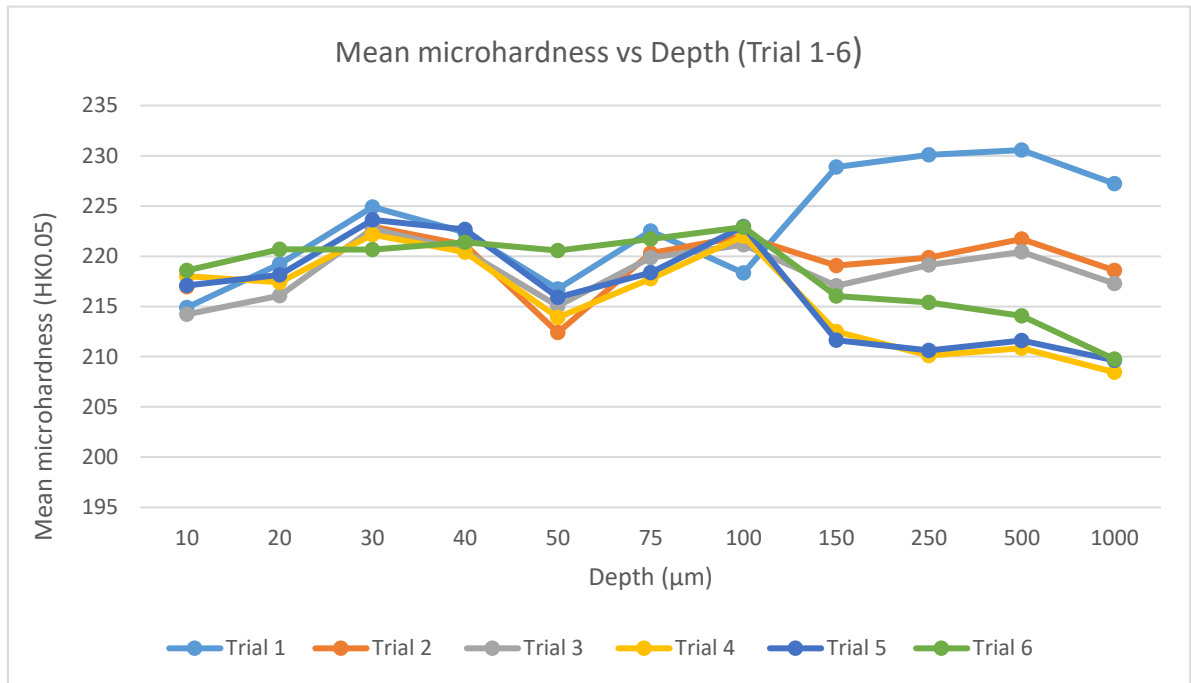


Figure A1: Microhardness profile of Trial 1 to Trial 6 of AWJ samples.

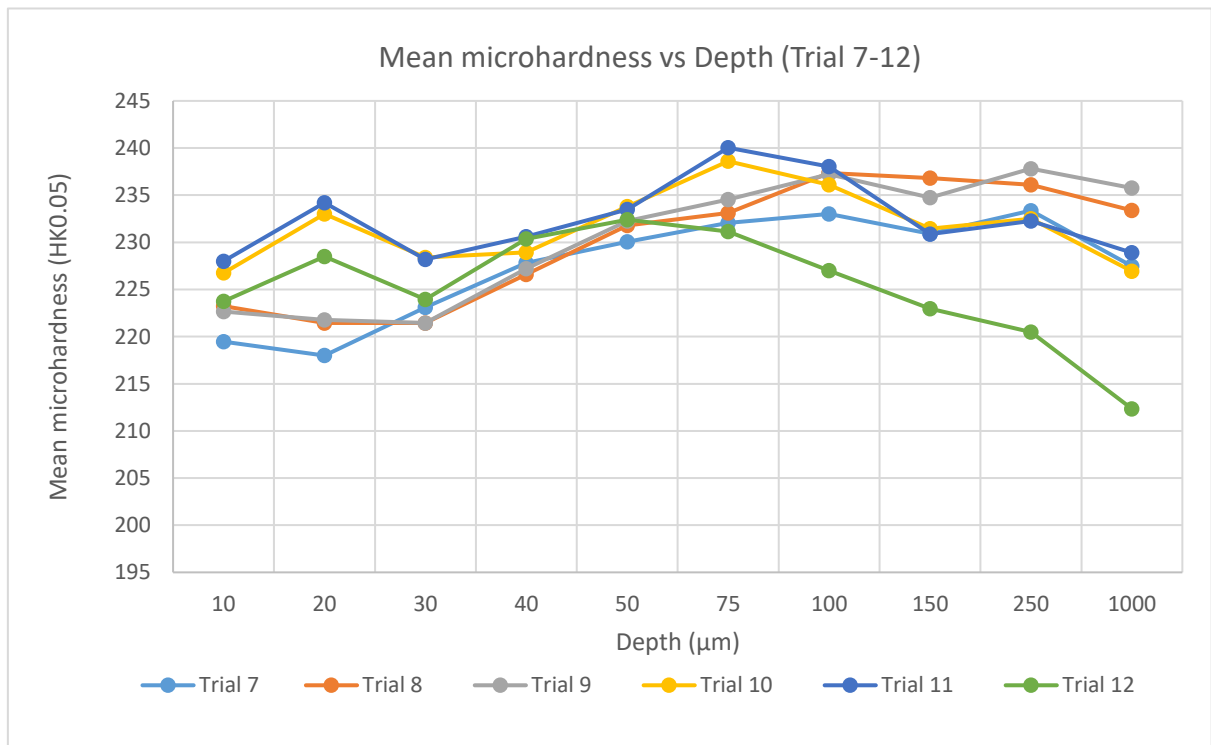


Figure A2: Microhardness profile of Trial 7 to Trial 12 of AWJ samples.

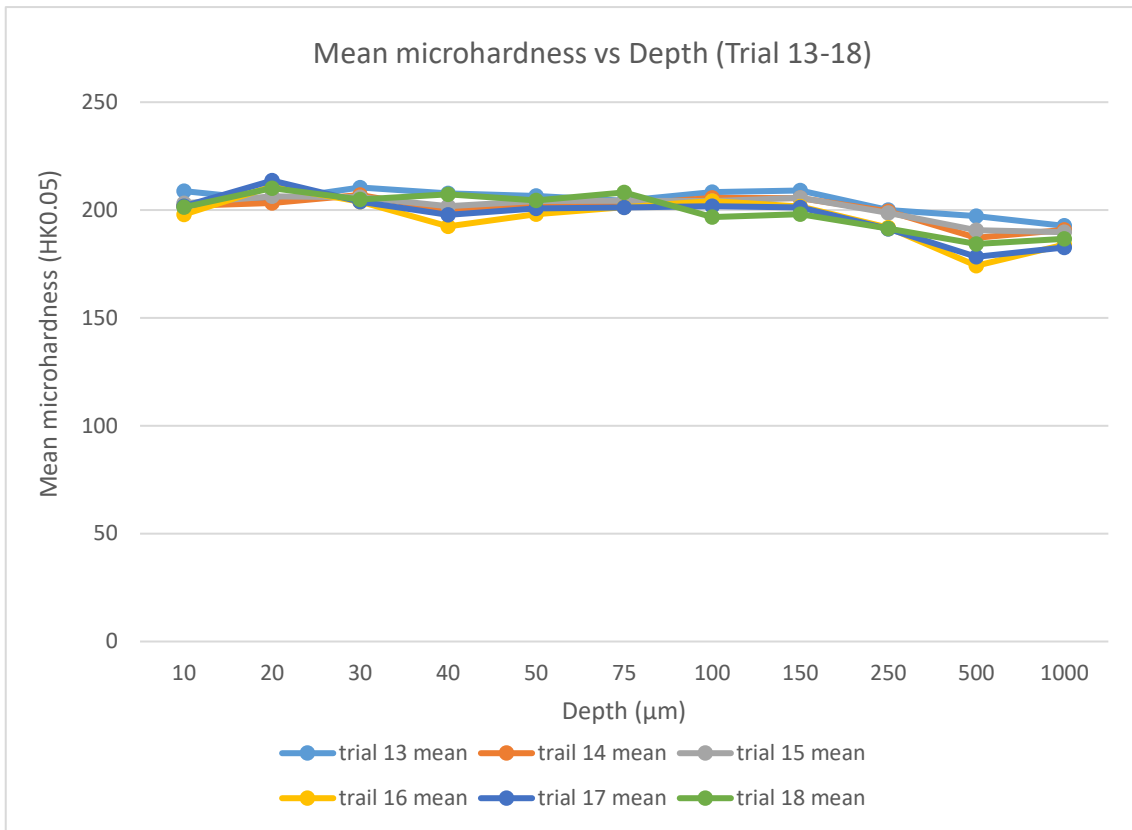


Figure A3: Microhardness profile of Trial 13 to Trial 18 of AWJ samples.

APPENDIX B: SEM IMAGES

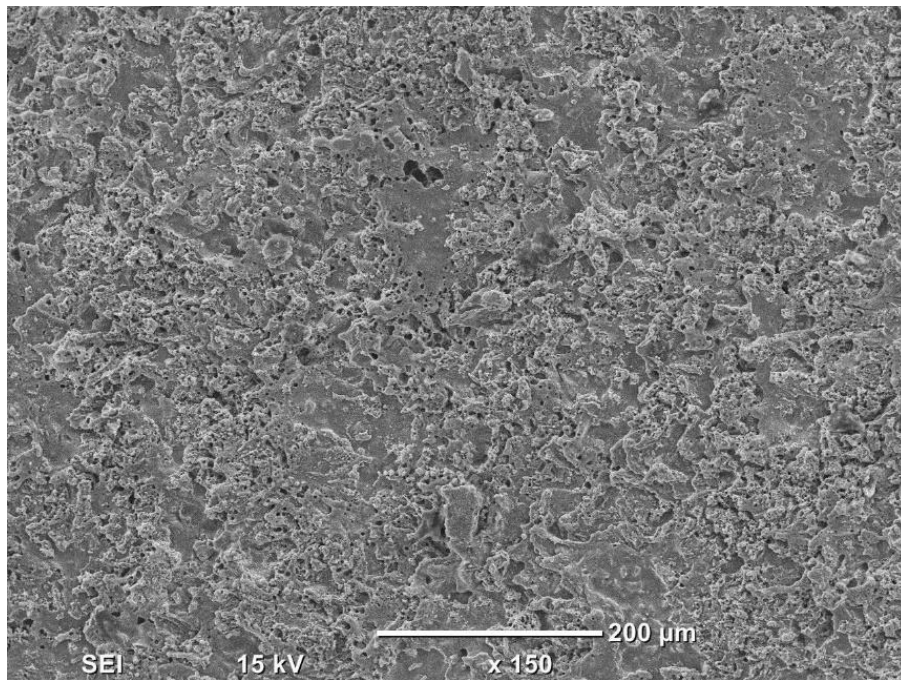


Figure B1: SEM of WEDM machined surface trial 17 at magnification X150.

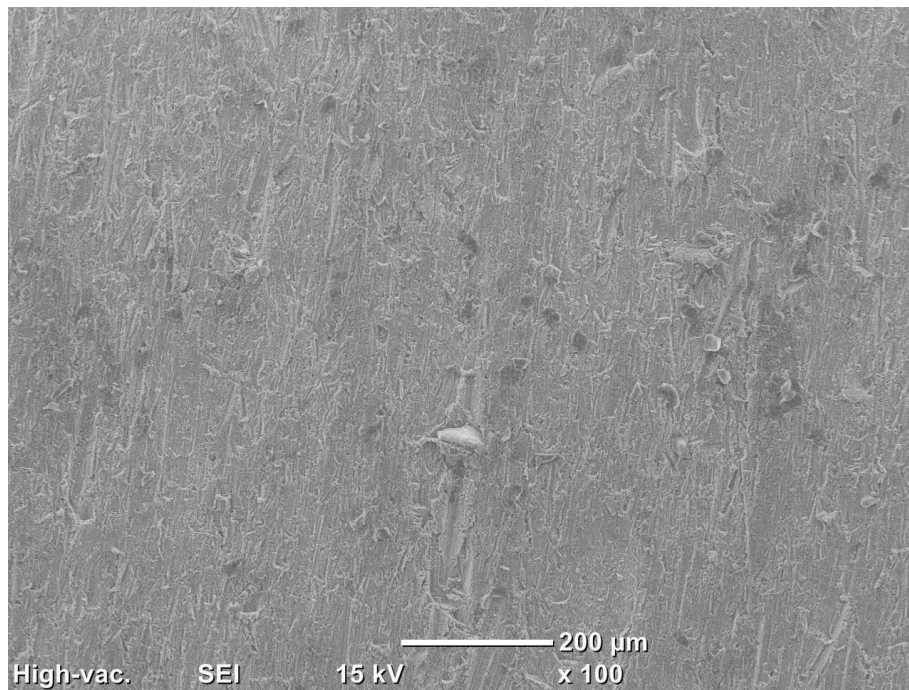


Figure B1: SEM of AWJ machined surface trial 15 at magnification X100.

APPENDIX C: CONTACT ANGLE

Details of the results data obtained from experiments and evaluated in wettability analysis are shown below:

Table C1: Summary of Mean CA and AWJ machining variables.

Trial No.	Vf	P	Va	SOD	Mean CA	Sa	Ssk	Sku	Fe	O
1	5	30	0.158	1	66.41	3.5	-0.49	4.99	4.94	28.08
2	5	40	0.340	3	53.17	3.53	-0.34	5	3.42	25.68
3	5	50	0.402	5	79.25	3.55	-0.32	4.45	3.05	31.87
4	10	30	0.158	3	55.55	4.38	-0.31	4.96	2.99	32.41
5	10	40	0.340	5	71.19	4.56	-0.25	4.04	3.08	22.48
6	10	50	0.402	1	99.96	2.87	-0.05	14.4	4.06	23.93
7	20	30	0.340	1	73.34	3.97	-0.52	3.9	3.55	23.44
8	20	40	0.402	3	75.85	3.67	-0.49	4.05	3.48	24.83
9	20	50	0.158	5	69.88	5.36	-0.43	4.22	3.55	22.99
10	30	30	0.402	5	66.40	4.6	-0.27	3.49	3.42	26.23
11	30	40	0.158	1	77.55	5.45	-0.41	3.77	3.48	20.89
12	30	50	0.340	3	77.99	4.86	-0.42	4.06	9.76	23.55
13	40	30	0.340	5	84.93	5.7	-0.29	3.66	2.91	21.05
14	40	40	0.402	1	84.70	4.13	-0.35	4.54	3.67	22.43
15	40	50	0.158	3	98.26	7.18	-0.46	4.1	3.10	21.81
16	50	30	0.402	3	89.63	5.09	-0.27	3.34	3.76	21.71
17	50	40	0.158	5	111.22	7.19	-0.21	3.43	3.04	23.84
18	50	50	0.340	1	76.50	5.15	-0.44	3.81	3.24	23.04

Table C2: Summary of Mean CA and WEDM machining variables.

Trial No.	A	AJ	IAL	V	FF	Mean CA	Sa	Ssk	Sku	Wire	O
1	0.1	15	10	80	10	116.00	1.73	-0.24	3.88 5	14.53	26.85
2	0.1	15	20	100	50	121.58	1.74	-0.39	3.22	13.53	31.04
3	0.1	15	30	120	100	86.72	1.66	-0.35	3.19	12.30	29.62
4	0.1	30	10	80	50	120.51	1.83	-0.32	3.83 5	12.38	33.45
5	0.1	30	20	100	100	120.68	1.91	-0.03	6.96 5	13.45	33.24
6	0.1	30	30	120	10	104.90	1.82	-0.28	3.40 6	14.55	33.19
7	0.1	45	10	100	10	93.49	1.81	-0.17	3.10 5	9.48	29.60
8	0.1	45	20	120	50	135.02	1.81	-0.18	4.67	14.65	27.42
9	0.1	45	30	80	100	111.75	1.85	-0.40	3.17 5	10.80	30.68
10	0.7	15	10	120	100	121.42	3.33	-0.2	3.34 5	12.22	28.82
11	0.7	15	20	80	10	120.18	3.31	-0.3	2.99	12.38	26.59
12	0.7	15	30	100	50	120.03	3.27	-0.26	3.02 5	12.66	26.25
13	0.7	30	10	100	100	118.08	3.24	-0.26	3	11.94	27.70
14	0.7	30	20	120	10	125.59	3.10	-0.24	3.48	11.81	27.26
15	0.7	30	30	80	50	126.14	3.25	-0.25	2.96 5	12.21	26.08
16	0.7	45	10	120	50	120.20	3.27	-0.26	2.99	12.43	26.25
17	0.7	45	20	80	100	119.52	3.34	-0.2	3.02	13.78	26.69
18	0.7	45	30	100	10	124.26	3.13	-0.26	2.99	10.53	23.47